

Håkon Mørkeseth

# Time Domain Vortex-Induced Motion Prediction of Spar-Type Floating Wind Turbine

Master's thesis in Marine Technology

Supervisor: Prof. Svein Sævik, NTNU, Prof. Bernt J. Leira, NTNU, Dr.  
Decao Yin, SINTEF Ocean, and Dr. Elizabeth Passano, SINTEF Ocean

June 2023



Håkon Mørkeseth

# **Time Domain Vortex-Induced Motion Prediction of Spar-Type Floating Wind Turbine**

Master's thesis in Marine Technology

Supervisor: Prof. Svein Sævik, NTNU, Prof. Bernt J. Leira, NTNU, Dr.  
Decao Yin, SINTEF Ocean, and Dr. Elizabeth Passano, SINTEF Ocean  
June 2023

Norwegian University of Science and Technology  
Faculty of Engineering  
Department of Marine Technology



Norwegian University of  
Science and Technology





## Master Thesis Description Spring 2023

for

**Stud. Tech. Håkon Mørkeseth**

### **Time domain Vortex Induced Motion prediction of Spar type floating wind turbine**

*Tidsplanbasert beregning av virvelinduserte bevegelser for flytende vindturbin*

Spars and Semis are attractive platforms for offshore wind power-and oil and gas industry. The platforms may obtain Vortex Induced Motions (VIM) due to ocean current. The motions can cause to fast accumulation of fatigue damage of slender structures connected to the platform, such as mooring lines, power cables and umbilicals. The VIM motion will also increase the drag loads on the platform which may cause increased offset and mean loads of these slender structures. Tow-out is often found to be a cost-effective installation method for both bottom fixed- and floating platforms. These platforms may also obtain similar VIM response problems. Today's VIM design practice is based on empirical methods where the platform motion amplitude is found based on parameters such as reduced velocity. Semi-empirical methods have for a long time been used for VIV design of risers, which are considered to be more scientific and generic approaches. Both frequency domain- (FD) and time domain (TD) methods have been developed. The idea of the present project proposal is to investigate the TD method with respect to improving VIM predictions. The master work to be performed during Spring 2023 represents a continuation of the project work performed in Fall 2022 and is to be carried out as follows:

1. Report the result of the literature review conducted during Fall 2022 into the master thesis document.
2. If deemed necessary, additional literature review into the fundamental theory of VIV & VIM, numerical prediction, tools, relevant standards. This is to further support the scope of work identified during the project thesis Fall 2022.
3. Replicate the Hywind Scotland FOWT as accurate as possible. This applies to all aspects of the FOWT including floater and tower geometry, mooring configuration and turbine unit.
4. Establish a representative environmental description considering the inherent correlations.
5. Analyse the full-scale measurements from Hywind Scotland where VIM should be looked for in particular. All available cases should be analysed with the TD VIV model and a calibration study should be performed to predict the motion, VIM or not, as accurately as possible. This includes a study of the relative importance of wave versus current conditions and their role with regard to onset of VIM.
6. Perform cases studies to e'



7. evaluate which environmental conditions that may trigger VIM and evaluate the effect of VIM with respect to fatigue and ULS design of the mooring system (including both the inline and cross-flow contributions.)
8. In agreement with the supervisors include more case scenarios.
9. Conclusions and recommendations for further work.

The work scope may prove to be larger than initially anticipated. Subject to approval from the supervisors, topics may be deleted from the list above or reduced in extent. This is to be notified to the reader in the introduction.

In the master report, the candidate shall present his/her personal contribution to the resolution of problems within the scope of the master work

Theories and conclusions should be based on mathematical derivations and/or logic reasoning identifying the various steps in the deduction.

The candidate should utilise the existing possibilities for obtaining relevant literature.

#### **Master report format**

The master report should be organised in a rational manner to give a clear exposition of results, assessments, and conclusions. The text should be brief and to the point, with a clear language. Telegraphic language should be avoided.

The report shall contain the following elements: A text defining the scope (this document to be included), preface, list of contents, summary, main body of thesis, conclusions with recommendations for further work, list of symbols and acronyms, references and (optional) appendices. All figures, tables and equations shall be numerated.

The supervisors may require that the candidate, in an early stage of the work, presents a written plan for the completion of the work.

The original contribution of the candidate and material taken from other sources shall be clearly defined. Work from other sources shall be properly referenced using an acknowledged referencing system.

The report shall be submitted in electronic format (.pdf):

- Signed by the candidate
- The text defining the scope shall be included (this document)
- Drawings and/or computer models that are not suited to be part of the report in terms of appendices shall be provided on separate (.zip) files.

#### **Ownership**

NTNU has according to the present rules the ownership of the master reports. Any use of the report has to be approved by NTNU (or external partner when this applies). The department has the right to use the report as if the work was carried out by a NTNU employee, if nothing else has been agreed in advance.



NTNU

Norwegian University of Science and Technology


Faculty of Engineering  
Department of Marine Technology

**Thesis supervisors:**

Prof. Svein Sævik, NTNU,  
Prof. Bernt J. Leira, NTNU  
Decao Yin, SINTEF Ocean  
Elizabeth Passano, SINTEF Ocean

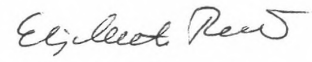
**Deadline: January, 2023, the exact date according to student web**

Trondheim, January , 2023

  
Svein Sævik

  
Bernt J. Leira

  
Decao Yin

  
Elizabeth Passano

Candidate – date and signature:

 8/2-23





# Preface

This report is the result of my master's thesis work at the Department of Marine Technology at the Norwegian University of Science and Technology during the spring semester of 2023. The master's thesis constitutes the entirety of the deliverables in the subject TMR4930 Marine Technology, Master's Thesis, with a scope of 30 credits, corresponding to the workload of a full semester. A preparatory study was performed in the autumn semester of 2022 in the subject TMR4500 Marine Structures, Specialization Project, with a scope of 7,5 credits. The results from the study were reported in a project thesis and the literature review in addition to the main findings are also reported in this master's thesis. The project thesis work was an educational introduction to the subject matter and provided me with valuable lessons to take into the master's thesis work.

A major part of the thesis work involved a deep dive into the vortex-induced vibration (VIV) and vortex-induced motion (VIM) research and literature. Different prediction tools and models were investigated, and a fair share of time was devoted to particular familiarization with the time domain (TD) VIV model recently developed at NTNU and SINTEF Ocean. Another crucial part of the thesis work included familiarization with the SIMA software workbench, and in particular the SIMO and RIFLEX modules, which are used to model the floating wind turbine and analyze the VIM response. The combined sum of this throughout the thesis work has provided me with both practical and theoretical knowledge on VIV and VIM, as well as a thorough methodology to analyze the phenomena and interpret the results. I have learned a lot through the process and am grateful for the challenge and opportunities the master's thesis work has provided.

I would like to express my sincere gratitude to my supervisors Prof. Svein Sævik, NTNU, Prof. Bernt J. Leira, NTNU, Dr. Decao Yin, SINTEF Ocean and Dr. Elizabeth Passano, SINTEF Ocean for weekly guidance, help and valuable discussions throughout the master's thesis work. Their unhesitating engagement, encouragement and commitment have been a great help and motivation. Their vast knowledge and expertise on VIM, floating wind and structural- and hydrodynamics in general have greatly enriched my thesis work and helped me develop a deeper understanding of the subject matter. I would also like to underline their high level of availability and reliability every single week throughout both the project and master's thesis work over the last year. Their guidance has been invaluable and I once again express my gratitude for their dedication to my master's thesis work.

It is an advantage for the readers of this thesis to be familiar with the basic concepts of structural- and hydromechanics. Particularly the fundamental theory of structural response and dynamic analysis in frequency and time domain would make understanding the context of the thesis easier. Some former knowledge on VIV and VIM would also be beneficial, although an introduction is provided.

**Håkon Mørkeseth**



---

June 11, 2023  
Trondheim

# Abstract

Floating wind is currently gaining popularity and the spar-type floating wind turbine shows great potential to emerge as an important piece in the global energy transition towards renewable sources. This structure may experience vortex-induced motion (VIM) due to ocean current, which refers to large oscillations of the floater caused by alternating vortex shedding. The motions are typically characterized by surge/sway or roll/pitch oscillations in the natural periods of the structure. These motions may in turn cause significant fatigue damage and consequently reduction of lifetime, and for this reason it is desirable to accurately predict the occurrence of VIM and the motion itself. This thesis investigates if a recently developed time domain (TD) vortex-induced vibration (VIV) model can be used as a VIM prediction tool. The TD VIV model considered in this thesis is a hydrodynamic load model recently developed at NTNU and SINTEF Ocean and is still a hot research topic undergoing constant refinement and improvement. The model adds two VIV load terms, one for the cross-flow (CF) and one for the in-line (IL) direction, in the classical Morison's equation in terms of coefficients and a synchronization model. The synchronization model is capturing the phase coupling between force and response to account for the phenomenon known as lock-in, where the vortex shedding frequency locks on to the natural frequency of the structure. The objectives of this thesis included validating the model for VIM prediction against full-scale measurements, evaluating the relative importance of environmental conditions with regard to onset of VIM and applying a representative environmental description to investigate the effect of VIM on the ultimate limit state (ULS) design and fatigue life of the mooring system.

The floating wind turbine (FWT) concept used throughout the thesis is the Hywind Scotland 6 MW spar-type FWT. Five of these wind turbines make up the 30 MW Hywind Scotland wind park and are currently in operation off the north-east coast of Scotland. This FWT concept is modelled in the SIMA workbench using a combination of SIMO, a program for simulation of motions and station-keeping behaviour of floating structures, and RIFLEX, a program for analysis of slender structures. Free decay tests were performed to determine the natural periods of the complete structure, which then were compared to stated periods by the operator, Equinor. Full-scale measurements including global x- and y-motion for cases with varying metocean conditions were also provided by Equinor in collaboration with ORE Catapult. The modelled FWT was then analyzed with and without the TD VIV model and the results were compared to the full-scale measurements for validation. It was found that the TD VIV model produces accurate results regarding the onset of VIM for all of the provided full-scale measurement cases, which builds on the potential of the TD VIV model to be used as a VIM prediction tool.

Furthermore, the same cases were used to evaluate the relative importance of wind and waves in combination with current with regards to onset of VIM. It was observed that the waves had little to no contribution with regards to VIM response of the FWT. In all cases, the wind loading proved to be the governing factor of the FWT response. When removing the wind completely, the cases with low current speeds were found to be unaffected with regards to VIM response. The cases with the highest current speeds were however experiencing small amounts of VIM which were not captured by the TD VIV model when wind was included. The VIM translation amplitudes were never exceeding the translation amplitudes from the full environment results including wind, current and waves.

Finally, a representative full year environmental description was established to investigate the effect of VIM on the ULS design and fatigue life of the mooring system. A set of different complete metocean conditions considering probability distributions of wind, waves and current were established, each with equal probability of occurrence over a full year. The conditions were analyzed with and without the TD VIV model and an ULS check was performed. It was found that the maximum stress in the mooring lines was increased due to predicted VIM by the TD VIV model. A fatigue analysis was also performed and it was found that the lifetime of the mooring lines was massively reduced due to VIM predicted by the TD VIV model. Both CF and IL contributions were found to be of significance. It was concluded that the validated TD VIV model produces substantial VIM and consequently fatigue damage on the mooring lines over a representative full year environmental condition. The lifetime reduction caused by VIM underlines the importance of an accurate prediction tool and the TD VIV model is showing great potential, however, additional validation and potentially calibration is needed in order to confidently predict accurate VIM.

# Sammendrag

Flytende vind øker for tiden i popularitet og den flytende spar-vindturbinen viser stort potensial til å tre frem som en viktig brikke i den globale energiomstillingen til fornybare kilder. Denne konstruksjonen kan oppleve virvel-induserte bevegelser (VIM) grunnet havstrømninger, som refererer til store oscillasjoner av flyteren forårsaket av alternerende virvelavløsning. Bevegelserne er typisk karakterisert av jag/svai eller rull/stamp oscillasjoner i de naturlige periodene til konstruksjonen. Disse bevegelserne kan så forårsake signifikant utmattingskade og følgelig redusert levetid, og på grunn av dette er det ønskelig å nøyaktig predikere forekomsten av VIM og bevegelsen i seg selv. Denne oppgaven undersøker om en nylig utviklet tidsplan (TD) virvel-indusert vibrasjons- (VIV) modell kan bli brukt som et VIM-prediksjonsverktøy. TD VIV-modellen betraktet i denne oppgaven er en hydrodynamisk lastmodell nylig utviklet ved NTNU og SINTEF Ocean og er fremdeles et hett forskningstema som undergår konstant forbedring. Modellen legger til to VIV lasttermer, en for tverrstrøms- (CF) og en for medstrøms- (IL) retningen, i den klassiske Morison's ligning i form av koeffisienter og en synkroniseringsmodell. Synkroniseringsmodellen fanger fasekoblingen mellom kraft og respons for å ta hensyn til fenomenet kjent som "lock-in", hvor virvelavløsningsfrekvensen låser seg til den naturlige frekvensen til konstruksjonen. Målene for denne oppgaven inkluderte å validere modellen for VIM prediksjon mot full-skala målinger, evaluere den relative betydningen av miljøforhold med hensyn til oppstart av VIM og anvende en representativ miljøbeskrivelse for å undersøke effekten av VIM på bruddgrensetilstanden (ULS) og utmattingslevetiden til fortøyningsystemet.

Det flytende vinturbin- (FWT) konseptet brukt gjennom denne oppgaven er Hywind Scotland 6 MW spar-FWTen. Fem av disse vindturbinene utgjør vindparken Hywind Scotland 30 MW og er for øyeblikket i drift utenfor nordøst-kysten av Skottland. Dette FWT-konseptet er modellert i SIMA arbeidsbenk ved bruk av en kombinasjon av SIMO, et program for simulering av bevegelser og fastholdingsoppførsel av flytende konstruksjoner, og RIFLEX, et program for analyse av slanke konstruksjoner. Tester ble utført for å fastslå de naturlige periodene til den komplette konstruksjonen, som så ble sammenlignet med oppgitte perioder fra operatøren, Equinor. Full-skala målinger inkludert global x- og y-bevegelse for tilfeller med varierende meteocean-forhold ble også utlevert av Equinor i samarbeid med ORE Catapult. Den modellerte FWTen ble så analysert med og uten TD VIV-modellen og resultatene ble sammenlignet med full-skala målinger for validering. Det ble funnet at TD VIV-modellen produserer nøyaktige resultater med hensyn til oppstart av VIM for alle de tilgjengelige full-skala målingstilfellene, som underbygger potensialet for TD VIV-modellen til å bli brukt som et VIM-prediksjonsverktøy.

Dessuten ble de samme tilfellene brukt til å evaluere den relative betydningen av vind og bølger i kombinasjon med strøm med hensyn til oppstart av VIM. Det ble observert at bølgene hadde liten til ingen påvirkning med hensyn til VIM-respons av FWTen. For all tilfellene viste vindlasten seg å være den styrende faktoren av FWT-responsen. Når vinden ble fjernet fullstendig, ble tilfellene med lav strømhastighet funnet å være upåvirket med hensyn til VIM-respons. Tilfellene med de høyeste strømhastighetene opplevde imidlertid små mengder VIM som ikke ble fanget opp av TD VIV-modellen når vinden var inkludert. VIM-translasjonsamplitudene oversteg aldri translasjonsamplitudene fra resultatene for den fulle miljøtilstanden inkludert vind, strøm og bølger.

Til slutt, en representativ helårs miljøbeskrivelse ble etablert for å undersøke effekten av VIM på ULS-design og utmattingslevetid av fortøyningsssystemet. Et sett av forskjellige komplette meteocean-tilstander som tar hensyn til sannsynlighetsfordelinger av vind, bølger og strøm ble etablert, hver med lik sannsynlighet av forekomst over et helt år. Tilstandene ble analysert med og uten TD VIV-modellen og en ULS-sjekk ble gjennomført. Det ble funnet at det maksimale stresset i fortøyningslinene økte grunnet predikert VIM av TD VIV-modellen. En utmattingsanalyse ble også gjennomført, og det ble funnet at levetiden til fortøyningslinene ble massivt redusert grunnet predikert VIM av TD VIV-modellen. Både CF- og IL-bidrag ble funnet å være av betydning. Det ble konkludert med at den validerte TD VIV-modellen produserer betydelig VIM og følgelig utmattingskade på fortøyningslinene over en representativ helårs miljøbeskrivelse. Reduksjonen i levetid forårsaket av VIM understreker viktigheten av et nøyaktig prediksjonsverktøy og TD VIV-modellen viser stort potensiale, men likevel, ytterligere validering og potensielt kalibrering er nødvendig for å selvsikkert kunne predikere nøyaktig VIM.

# Contents

<b>Problem definition</b>	<b>i</b>
<b>Preface</b>	<b>vi</b>
<b>Abstract</b>	<b>viii</b>
<b>Sammendrag</b>	<b>x</b>
<b>List of Figures</b>	<b>xxi</b>
<b>List of Tables</b>	<b>xxiv</b>
<b>Nomenclature</b>	<b>xxv</b>
<b>1 Introduction</b>	<b>1</b>
1.1 Background . . . . .	1
1.2 Objectives . . . . .	3
1.3 Thesis structure . . . . .	4
<b>2 Theoretical background</b>	<b>7</b>
2.1 Introduction to vortex-induced vibrations . . . . .	7
2.1.1 Fixed circular cylinder in steady flow . . . . .	7
2.1.2 Forced harmonic oscillation of a circular cylinder in steady flow . . . . .	11
2.1.3 Elastically mounted circular cylinder in steady flow . . . . .	13
2.2 Introduction to vortex-induced motions . . . . .	15
2.2.1 Reynolds number . . . . .	16
2.2.2 Mass ratio . . . . .	17
2.2.3 Aspect ratio . . . . .	17
2.2.4 Degrees of freedom . . . . .	18
2.3 Aerodynamics . . . . .	19
2.3.1 Steady wind . . . . .	19
2.3.2 Unsteady wind . . . . .	19
2.3.3 Spatially varying wind . . . . .	19
2.4 Fatigue . . . . .	20
<b>3 Prediction tools for vortex-induced vibrations/motions</b>	<b>23</b>

3.1	Existing vortex-induced vibration prediction models . . . . .	23
3.1.1	Computational fluid dynamics . . . . .	23
3.1.2	Semi-empirical frequency domain models . . . . .	24
3.1.3	Empirical time domain models . . . . .	25
3.2	Semi-empirical time domain model VIVANA-TD . . . . .	25
3.2.1	Hydrodynamic load formulation . . . . .	26
3.2.2	Synchronization of vortex shedding forces . . . . .	28
3.3	Engineering practice for vortex-induced motion prediction . . . . .	30
3.3.1	Regulations and recommended practice . . . . .	31
3.3.2	Model tests . . . . .	31
3.3.3	Numerical studies . . . . .	32
3.3.4	Review of field measurements . . . . .	32
<b>4</b>	<b>Modelling of floating wind turbine concept</b> . . . . .	<b>33</b>
4.1	Hywind Scotland wind turbine description . . . . .	33
4.2	Software . . . . .	37
4.2.1	SIMO . . . . .	37
4.2.2	RIFLEX . . . . .	38
4.2.3	TurbSim . . . . .	38
4.3	Modelling procedure . . . . .	39
4.3.1	Spar floater and tower structure . . . . .	39
4.3.2	Mooring system . . . . .	43
4.3.3	Turbine components . . . . .	46
4.3.4	Blades . . . . .	49
4.3.5	Ballast and weight distribution . . . . .	50
4.3.6	Integration and damping parameters . . . . .	50
4.4	Free decay tests . . . . .	51
4.5	Environmental loading . . . . .	53
4.6	Hydrodynamic load model . . . . .	55
4.7	Modelling challenges . . . . .	55
<b>5</b>	<b>Validation against full-scale measurements</b> . . . . .	<b>57</b>
5.1	Full-scale measurements description . . . . .	57
5.2	Metocean data of full-scale cases . . . . .	58
5.2.1	Wave condition . . . . .	59
5.2.2	Wind condition . . . . .	60
5.2.3	Current condition . . . . .	60
5.3	Discussion on the full-scale cases . . . . .	61
5.4	Results and discussion of validation . . . . .	63
<b>6</b>	<b>Case studies</b> . . . . .	<b>73</b>
6.1	Effect of wind and waves on VIM prediction . . . . .	73
6.2	Representative full year environmental conditions . . . . .	79
6.2.1	Wave condition . . . . .	79
6.2.2	Wind condition . . . . .	82
6.2.3	Current condition . . . . .	84
6.2.4	Complete full year environmental condition . . . . .	87
6.3	Results and discussion of the full year environmental conditions . . . . .	88
6.4	Effect on mooring system . . . . .	92



---

6.4.1	Ultimate limit state . . . . .	92
6.4.2	Fatigue life . . . . .	94
<b>7</b>	<b>Conclusions and further work</b>	<b>99</b>
7.1	Conclusions . . . . .	99
7.2	Recommendations for further work . . . . .	100
	<b>References</b>	<b>103</b>
	<b>Appendices</b>	<b>109</b>
<b>A</b>	<b>TurbSim example input file</b>	<b>111</b>
A.1	turbsim_case1.inp . . . . .	111
<b>B</b>	<b>Complete set of results</b>	<b>115</b>
B.1	Validation against full-scale measurements . . . . .	115
B.2	Effect of wind and waves on VIM response . . . . .	127
B.3	Full year environmental condition . . . . .	138



# List of Figures

1.1	Different floating wind turbine concepts. . . . .	1
1.2	Definition of components and rigid body motions of a spar-type floating wind turbine. . . . .	2
2.1	Flow around a stationary circular cylinder including the vortex shedding phenomenon. . . . .	9
2.2	Strouhal number vs. Reynolds number. . . . .	10
2.3	Lift and drag forces acting on a circular in steady flow. . . . .	11
2.4	Contour plots for pure CF excitation and added mass coefficients. . . . .	13
2.5	Typical VIV experiments for rigid, circular cylinders in steady flow: a) CF motion only, b) IL motion only, c) combined IL and CF motion. . . . .	13
2.6	CF response of an elastically mounted circular cylinder in steady air flow: a) dimensionless frequency, b) dimensionless amplitude, c) phase angle. . . . .	14
2.7	CF excitation force coefficient curve for a given non-dimensional frequency. . . . .	15
2.8	VIM can be treated as a subset of VIV, represented by high Reynolds numbers, small mass ratio, low aspect ratio and rigid body motion. . . . .	16
2.9	Collection of mean drag coefficients on a fixed circular cylinder for varying Reynolds number and roughness ratio. . . . .	16
2.10	CF cylinder response with 2 DOF motion for four different mass ratios. . . . .	17
2.11	2 DOF trajectories of combined CF and IL motion. . . . .	18
2.12	Fatigue load history and symbol definitions. . . . .	20
2.13	Strain time series and stress-strain response. . . . .	20
2.14	Pagoda roof rainflow analogy. . . . .	21
2.15	The Miner summation procedure. . . . .	22
3.1	3D cylinder strip in incoming flow. . . . .	27
3.2	Hydrodynamic force terms at the cylinder cross-section. . . . .	27
3.3	Phase angle relationship between CF vortex shedding force and relative structure velocity in local y-direction for CF synchronisation. . . . .	29
3.4	CF synchronization function. . . . .	30
3.5	A typical VIM design curve. . . . .	31
4.1	The Hywind Scotland wind park. . . . .	34
4.2	Hywind Scotland floater geometry. . . . .	35
4.3	Mooring arrangement for the Hywind Scotland wind turbines. . . . .	35
4.4	Naming of lines and bridles in the mooring system. . . . .	37
4.5	Overview of SIMO modules and structure. . . . .	37
4.6	Overview of RIFLEX modules and structure. . . . .	38

4.7	Nodal degrees of freedom for a RIFLEX beam element. . . . .	39
4.8	Definition of axisymmetric cross section coordinate system. . . . .	41
4.9	Heave added mass of spar with heave plate. . . . .	43
4.10	RIFLEX bar element in initial and deformed configuration. . . . .	43
4.11	The modelled floating wind turbine with mooring system before and after static analysis. . . . .	44
4.12	Outline of a wind turbine model in SIMA. . . . .	46
4.13	Outline of the rotor and shaft system with local coordinate systems. . . . .	47
4.14	The modelled hub and nacelle arrangement. . . . .	47
4.15	Definition of yaw misalignment between wind direction and shaft orientation. . . . .	48
4.16	Outline of yaw controller model in SIMA. . . . .	48
4.17	A modelled blade indicating different foil sections. . . . .	50
4.18	Free decay tests for the six degrees of freedom. . . . .	52
4.19	Definition of environmental directions in SIMA. . . . .	53
4.20	A TurbSim generated wind field. . . . .	54
5.1	Definition of environmental directions in the Equinor data. . . . .	59
5.2	Location of HS4 and the wave buoy in the Hywind Scotland wind park. . . . .	60
5.3	Cumulative Weibull distributions of current speeds at different depths at Buchan Deep. . . . .	62
5.4	Translation in x- and y-direction for case 1. The full-scale measurements from Equinor and the SIMA results both with and without the TD VIV model are shown. . . . .	64
5.5	Fast Fourier transform of translation in x- and y-direction for case 1. The full-scale measurements from Equinor and the SIMA results both with and without the TD VIV model are shown. . . . .	65
5.6	Translation in x- and y-direction for case 3. The full-scale measurements from Equinor and the SIMA results both with and without the TD VIV model are shown. . . . .	66
5.7	Fast Fourier transform of translation in x- and y-direction for case 3. The full-scale measurements from Equinor and the SIMA results both with and without the TD VIV model are shown. . . . .	67
5.8	Translation in x- and y-direction for case 6. The full-scale measurements from Equinor and the SIMA results both with and without the TD VIV model are shown. . . . .	68
5.9	Fast Fourier transform of translation in x- and y-direction for case 6. The full-scale measurements from Equinor and the SIMA results both with and without the TD VIV model are shown. . . . .	69
5.10	Translation in x- and y-direction for case 11. The full-scale measurements from Equinor and the SIMA results both with and without the TD VIV model are shown. . . . .	70
5.11	Fast Fourier transform of translation in x- and y-direction for case 11. The full-scale measurements from Equinor and the SIMA results both with and without the TD VIV model are shown. . . . .	71
6.1	Translation in x- and y-direction for case 1. All lines show results with the TD VIV model for different metocean environments. Full environment consists of current, wind and waves. . . . .	74
6.2	Fast Fourier transform of translation in x- and y-direction for case 1. All lines show results with the TD VIV model for different metocean environments. Full environment consists of current, wind and waves. . . . .	75

6.3	Translation in x- and y-direction for case 2. All lines show results with the TD VIV model for different metocean environments. Full environment consists of current, wind and waves. . . . .	76
6.4	Fast Fourier transform of translation in x- and y-direction for case 2. All lines show results with the TD VIV model for different metocean environments. Full environment consists of current, wind and waves. . . . .	76
6.5	Translation in x- and y-direction for case 3. All lines show results with the TD VIV model for different metocean environments. Full environment consists of current, wind and waves. . . . .	77
6.6	Fast Fourier transform of translation in x- and y-direction for case 3. All lines show results with the TD VIV model for different metocean environments. Full environment consists of current, wind and waves. . . . .	77
6.7	Translation in x- and y-direction for case 8. All lines show results with the TD VIV model for different metocean environments. Full environment consists of current, wind and waves. . . . .	78
6.8	Fast Fourier transform of translation in x- and y-direction for case 8. All lines show results with the TD VIV model for different metocean environments. Full environment consists of current, wind and waves. . . . .	79
6.9	Weibull distribution of significant wave height at Buchan Deep. . . . .	80
6.10	Spectral peak period for given significant wave height at Buchan Deep. . . . .	81
6.11	All-year wave rose at Buchan Deep for the period 1958 - 2010. . . . .	81
6.12	Weibull distribution of wind speed at 10 meters above sea level at Buchan Deep. . . . .	82
6.13	Computed turbulence intensity compared to turbulence intensity measurements at 100 m above sea level at FINO 3. . . . .	83
6.14	Wind roses for the 1 hour average wind speed at different height above sea level at Buchan Deep for the period 1958 - 2010. . . . .	84
6.15	Cumulative Weibull distributions of current speeds at different depths at Buchan Deep. The distributions are divided in ten intervals with equal probability of occurrence and the expected value within each interval is presented. . . . .	85
6.16	Current roses for different depths at Buchan Deep for the period November 2013 - February 2014. . . . .	86
6.17	Translation in x- and y-direction for full year environment 4. Results both with and without the TD VIV model are shown. . . . .	88
6.18	Fast Fourier transform of translation in x- and y-direction for full year environment 6. Results both with and without the TD VIV model are shown. . . . .	89
6.19	Translation in x- and y-direction for full year environment 7. Results both with and without the TD VIV model are shown. . . . .	89
6.20	Fast Fourier transform of translation in x- and y-direction for full year environment 7. Results both with and without the TD VIV model are shown. . . . .	90
6.21	Fast Fourier transform of translation in x- and y-direction for full year environment 8. Results both with and without the TD VIV model are shown. . . . .	90
6.22	Fast Fourier transform of translation in x- and y-direction for full year environment 9. Results both with and without the TD VIV model are shown. . . . .	91
6.23	Translation in x- and y-direction for full year environment 10. Results both with and without the TD VIV model are shown. . . . .	91
6.24	Fast Fourier transform of translation in x- and y-direction for full year environment 10. Results both with and without the TD VIV model are shown. . . . .	92
6.25	Stress in main mooring line 141 for full year environment 10 with and without the TD VIV model. . . . .	93

6.26	Stress in main mooring line 142 for full year environment 10 with and without the TD VIV model. . . . .	93
6.27	Stress in main mooring line 143 for full year environment 10 with and without the TD VIV model. . . . .	94
6.28	S-N curve for different mooring lines. . . . .	95
6.29	Fatigue damage distribution with and without the TD VIV model for all the mooring lines. . . . .	96
6.30	Overview of the floating wind turbine with incoming environmental directions and fatigue lifetimes with and without the TD VIV model indicated. . . . .	97
B.1	Translation in x- and y-direction for case 1. The full-scale measurements from Equinor and the SIMA results both with and without the TD VIV model are shown. 116	
B.2	Fast Fourier transform of translation in x- and y-direction for case 1. The full-scale measurements from Equinor and the SIMA results both with and without the TD VIV model are shown. . . . .	116
B.3	Translation in x- and y-direction for case 2. The full-scale measurements from Equinor and the SIMA results both with and without the TD VIV model are shown. 117	
B.4	Fast Fourier transform of translation in x- and y-direction for case 2. The full-scale measurements from Equinor and the SIMA results both with and without the TD VIV model are shown. . . . .	117
B.5	Translation in x- and y-direction for case 3. The full-scale measurements from Equinor and the SIMA results both with and without the TD VIV model are shown. 118	
B.6	Fast Fourier transform of translation in x- and y-direction for case 3. The full-scale measurements from Equinor and the SIMA results both with and without the TD VIV model are shown. . . . .	118
B.7	Translation in x- and y-direction for case 4. The full-scale measurements from Equinor and the SIMA results both with and without the TD VIV model are shown. 119	
B.8	Fast Fourier transform of translation in x- and y-direction for case 4. The full-scale measurements from Equinor and the SIMA results both with and without the TD VIV model are shown. . . . .	119
B.9	Translation in x- and y-direction for case 5. The full-scale measurements from Equinor and the SIMA results both with and without the TD VIV model are shown. 120	
B.10	Fast Fourier transform of translation in x- and y-direction for case 5. The full-scale measurements from Equinor and the SIMA results both with and without the TD VIV model are shown. . . . .	120
B.11	Translation in x- and y-direction for case 6. The full-scale measurements from Equinor and the SIMA results both with and without the TD VIV model are shown. 121	
B.12	Fast Fourier transform of translation in x- and y-direction for case 6. The full-scale measurements from Equinor and the SIMA results both with and without the TD VIV model are shown. . . . .	121
B.13	Translation in x- and y-direction for case 7. The full-scale measurements from Equinor and the SIMA results both with and without the TD VIV model are shown. 122	
B.14	Fast Fourier transform of translation in x- and y-direction for case 7. The full-scale measurements from Equinor and the SIMA results both with and without the TD VIV model are shown. . . . .	122
B.15	Translation in x- and y-direction for case 8. The full-scale measurements from Equinor and the SIMA results both with and without the TD VIV model are shown. 123	

B.16	Fast Fourier transform of translation in x- and y-direction for case 8. The full-scale measurements from Equinor and the SIMA results both with and without the TD VIV model are shown. . . . .	123
B.17	Translation in x- and y-direction for case 9. The full-scale measurements from Equinor and the SIMA results both with and without the TD VIV model are shown. . . . .	124
B.18	Fast Fourier transform of translation in x- and y-direction for case 9. The full-scale measurements from Equinor and the SIMA results both with and without the TD VIV model are shown. . . . .	124
B.19	Translation in x- and y-direction for case 10. The full-scale measurements from Equinor and the SIMA results both with and without the TD VIV model are shown. . . . .	125
B.20	Fast Fourier transform of translation in x- and y-direction for case 10. The full-scale measurements from Equinor and the SIMA results both with and without the TD VIV model are shown. . . . .	125
B.21	Translation in x- and y-direction for case 11. The full-scale measurements from Equinor and the SIMA results both with and without the TD VIV model are shown. . . . .	126
B.22	Fast Fourier transform of translation in x- and y-direction for case 11. The full-scale measurements from Equinor and the SIMA results both with and without the TD VIV model are shown. . . . .	126
B.23	Translation in x- and y-direction for case 1. All lines show results with the TD VIV model for different metocean environments. Full environment consists of current, wind and waves. . . . .	127
B.24	Fast Fourier transform of translation in x- and y-direction for case 1. All lines show results with the TD VIV model for different metocean environments. Full environment consists of current, wind and waves. . . . .	127
B.25	Translation in x- and y-direction for case 2. All lines show results with the TD VIV model for different metocean environments. Full environment consists of current, wind and waves. . . . .	128
B.26	Fast Fourier transform of translation in x- and y-direction for case 2. All lines show results with the TD VIV model for different metocean environments. Full environment consists of current, wind and waves. . . . .	128
B.27	Translation in x- and y-direction for case 3. All lines show results with the TD VIV model for different metocean environments. Full environment consists of current, wind and waves. . . . .	129
B.28	Fast Fourier transform of translation in x- and y-direction for case 3. All lines show results with the TD VIV model for different metocean environments. Full environment consists of current, wind and waves. . . . .	129
B.29	Translation in x- and y-direction for case 4. All lines show results with the TD VIV model for different metocean environments. Full environment consists of current, wind and waves. . . . .	130
B.30	Fast Fourier transform of translation in x- and y-direction for case 4. All lines show results with the TD VIV model for different metocean environments. Full environment consists of current, wind and waves. . . . .	130
B.31	Translation in x- and y-direction for case 5. All lines show results with the TD VIV model for different metocean environments. Full environment consists of current, wind and waves. . . . .	131
B.32	Fast Fourier transform of translation in x- and y-direction for case 5. All lines show results with the TD VIV model for different metocean environments. Full environment consists of current, wind and waves. . . . .	131

B.33	Translation in x- and y-direction for case 6. All lines show results with the TD VIV model for different metocean environments. Full environment consists of current, wind and waves. . . . .	132
B.34	Fast Fourier transform of translation in x- and y-direction for case 6. All lines show results with the TD VIV model for different metocean environments. Full environment consists of current, wind and waves. . . . .	132
B.35	Translation in x- and y-direction for case 7. All lines show results with the TD VIV model for different metocean environments. Full environment consists of current, wind and waves. . . . .	133
B.36	Fast Fourier transform of translation in x- and y-direction for case 7. All lines show results with the TD VIV model for different metocean environments. Full environment consists of current, wind and waves. . . . .	133
B.37	Translation in x- and y-direction for case 8. All lines show results with the TD VIV model for different metocean environments. Full environment consists of current, wind and waves. . . . .	134
B.38	Fast Fourier transform of translation in x- and y-direction for case 8. All lines show results with the TD VIV model for different metocean environments. Full environment consists of current, wind and waves. . . . .	134
B.39	Translation in x- and y-direction for case 9. All lines show results with the TD VIV model for different metocean environments. Full environment consists of current, wind and waves. . . . .	135
B.40	Fast Fourier transform of translation in x- and y-direction for case 9. All lines show results with the TD VIV model for different metocean environments. Full environment consists of current, wind and waves. . . . .	135
B.41	Translation in x- and y-direction for case 10. All lines show results with the TD VIV model for different metocean environments. Full environment consists of current, wind and waves. . . . .	136
B.42	Fast Fourier transform of translation in x- and y-direction for case 10. All lines show results with the TD VIV model for different metocean environments. Full environment consists of current, wind and waves. . . . .	136
B.43	Translation in x- and y-direction for case 11. All lines show results with the TD VIV model for different metocean environments. Full environment consists of current, wind and waves. . . . .	137
B.44	Fast Fourier transform of translation in x- and y-direction for case 11. All lines show results with the TD VIV model for different metocean environments. Full environment consists of current, wind and waves. . . . .	137
B.45	Translation in x- and y-direction for full year environment 1. Results both with and without the TD VIV model are shown. . . . .	138
B.46	Fast Fourier transform of translation in x- and y-direction for full year environment 1. Results both with and without the TD VIV model are shown. . . . .	138
B.47	Translation in x- and y-direction for full year environment 2. Results both with and without the TD VIV model are shown. . . . .	139
B.48	Fast Fourier transform of translation in x- and y-direction for full year environment 2. Results both with and without the TD VIV model are shown. . . . .	139
B.49	Translation in x- and y-direction for full year environment 3. Results both with and without the TD VIV model are shown. . . . .	140
B.50	Fast Fourier transform of translation in x- and y-direction for full year environment 3. Results both with and without the TD VIV model are shown. . . . .	140



---

B.51 Translation in x- and y-direction for full year environment 4. Results both with and without the TD VIV model are shown. . . . .	141
B.52 Fast Fourier transform of translation in x- and y-direction for full year environment 4. Results both with and without the TD VIV model are shown. . . . .	141
B.53 Translation in x- and y-direction for full year environment 5. Results both with and without the TD VIV model are shown. . . . .	142
B.54 Fast Fourier transform of translation in x- and y-direction for full year environment 5. Results both with and without the TD VIV model are shown. . . . .	142
B.55 Translation in x- and y-direction for full year environment 6. Results both with and without the TD VIV model are shown. . . . .	143
B.56 Fast Fourier transform of translation in x- and y-direction for full year environment 6. Results both with and without the TD VIV model are shown. . . . .	143
B.57 Translation in x- and y-direction for full year environment 7. Results both with and without the TD VIV model are shown. . . . .	144
B.58 Fast Fourier transform of translation in x- and y-direction for full year environment 7. Results both with and without the TD VIV model are shown. . . . .	144
B.59 Translation in x- and y-direction for full year environment 8. Results both with and without the TD VIV model are shown. . . . .	145
B.60 Fast Fourier transform of translation in x- and y-direction for full year environment 8. Results both with and without the TD VIV model are shown. . . . .	145
B.61 Translation in x- and y-direction for full year environment 9. Results both with and without the TD VIV model are shown. . . . .	146
B.62 Fast Fourier transform of translation in x- and y-direction for full year environment 9. Results both with and without the TD VIV model are shown. . . . .	146
B.63 Translation in x- and y-direction for full year environment 10. Results both with and without the TD VIV model are shown. . . . .	147
B.64 Fast Fourier transform of translation in x- and y-direction for full year environment 10. Results both with and without the TD VIV model are shown. . . . .	147



# List of Tables

2.1	Regimes of flow around a smooth, circular cylinder in steady current. . . . .	8
4.1	Main properties of a Hywind Scotland wind turbine, floating substructure and mooring configuration. . . . .	34
4.2	Properties of the complete HS4 structure including wind turbine, tower, substructure and mooring system. . . . .	36
4.3	Properties of the mooring system. . . . .	36
4.4	Spar floater and tower structure modelled in SIMA. . . . .	40
4.5	Hydrodynamic force coefficients for the spar floater. . . . .	42
4.6	Main mooring line element sections. . . . .	45
4.7	Bridle element sections. . . . .	45
4.8	Hydrodynamic force coefficients for the mooring lines. . . . .	46
4.9	Modelled yaw controller parameters. . . . .	49
4.10	Blade element sections. . . . .	49
4.11	Numerical integration parameters. . . . .	50
4.12	Structural damping parameters. . . . .	51
4.13	Natural periods in the six DOFs stated by Equinor and calculated by free decay tests in SIMA, as well as the difference between the two. . . . .	52
4.14	Empirical hydrodynamic coefficients and parameters used for the TD VIV model. . . . .	55
5.1	Metocean data for the 11 operational cases from the Hywind Scotland wind park. . . . .	58
5.2	Wave conditions for the 11 operational cases divided in wind sea and swell contributions. The total wave conditions are also provided. . . . .	59
5.3	Wind conditions for the 11 operational cases. . . . .	61
5.4	Current conditions for the 11 operational cases at four different depths relative to the sea surface. . . . .	61
6.1	Weibull parameters for significant wave height at Buchan Deep. . . . .	80
6.2	Parameters in the peak period Weibull distribution given significant wave height. . . . .	80
6.3	Weibull parameters for wind speed at 10 meters above sea level at Buchan Deep. . . . .	82
6.4	Weibull parameters for current speed at different depths at Buchan Deep. . . . .	84
6.5	Complete representative full year environmental conditions for wave and wind parameters. . . . .	87
6.6	Complete representative full year environmental conditions for current parameters. . . . .	87
6.7	Maximum stresses in the mooring lines for full year environment 10 with and without the TD VIV model. . . . .	94

6.8	Fatigue life for the different mooring lines with and without the TD VIV model. . .	97
-----	---	----

# Nomenclature

## List of acronyms

2D	Two-dimensional
3D	Three-dimensional
CF	Cross-flow
CFD	Computational fluid dynamics
DNS	Direct numerical simulation
DOF	Degree of freedom
DOI	Digital object identifier
FD	Frequency domain
FEM	Finite element method
FFT	Fast Fourier transform
FSI	Fluid-structure interaction
FWT	Floating wind turbine
GPS	Global positioning system
IL	In-line
LES	Large eddy simulation
RANS	Reynolds-averaged Navier-Stokes
TD	Time domain
ULS	Ultimate limit state
UTC	Coordinated universal time
VIM	Vortex-induced motion
VIV	Vortex-induced vibration

## List of symbols

$\alpha_1$	Mass proportional damping coefficient
$\alpha_2$	Stiffness proportional damping coefficient
$\beta$	Inverse numerical integration parameter
$\Delta f_x$	In-line synchronization range
$\Delta f_y$	Cross-flow synchronization range
$\Delta S$	Stress range
$\epsilon$	Damping parameter
$\gamma$	Numerical integration parameter
$\gamma$	Shape parameter in Weibull distribution
$\nu$	Kinematic viscosity
$\omega$	Circular frequency
$\omega_s$	Circular Strouhal frequency
$\phi$	Phase angle
$\phi_{exc,x}$	Instantaneous in-line phase of vortex shedding force
$\phi_{exc,y}$	Instantaneous cross-flow phase of vortex shedding force
$\phi_{\dot{x}_{rel}}$	Instantaneous phase of in-line cylinder velocity
$\phi_{\dot{y}_{rel}}$	Instantaneous phase of cross-flow cylinder velocity
$\Psi_m$	Stability function
$\rho$	Fluid density
$\sigma$	Standard deviation
$\theta$	Numerical integration parameter
$\theta$	Scale parameter in Weibull distribution
$\theta_x$	Phase difference between in-line cylinder velocity and vortex shedding force
$\theta_y$	Phase difference between cross-flow cylinder velocity and vortex shedding force
$\epsilon$	Location parameter in Weibull distribution
$A$	Amplitude
$A$	Area
$A_R$	Aspect ratio
$C$	Damping matrix

---

$c$	Damping
$C_A$	Added mass coefficient
$C_D$	Drag coefficient
$C_d$	Drag coefficient
$C_l$	Lift coefficient
$C_M$	Inertia coefficient
$\overline{C_x}$	Mean drag coefficient
$\overline{C_y}$	Mean lift coefficient
$CA_x$	Added mass coefficient in tangential direction
$CA_y$	Added mass coefficient in normal direction
$CL_x$	Linear drag coefficient in tangential direction
$CL_y$	Linear drag coefficient in normal direction
$CQ_x$	Quadratic drag coefficient in tangential direction
$CQ_y$	Quadratic drag coefficient in normal direction
$D$	Damage sum in fatigue analysis
$D$	Diameter
$F$	Force
$f$	Frequency
$\hat{f}$	Non-dimensional frequency
$\mathbf{F}$	Hydrodynamic force
$\hat{f}_{0,x}$	Non-dimensional in-line frequency of maximum energy transfer
$\hat{f}_{0,y}$	Non-dimensional cross-flow frequency of maximum energy transfer
$F_A$	Added mass force
$\mathbf{F}_D$	Drag force
$F_E$	Excitation force
$f_{exc,x}$	Instantaneous in-line frequency
$\hat{f}_{exc,x}$	Non-dimensional instantaneous in-line frequency
$f_{exc,y}$	Instantaneous cross-flow frequency
$\hat{f}_{exc,y}$	Non-dimensional instantaneous cross-flow frequency
$\mathbf{F}_{FK}$	Froude-Kriloff force

---

$F_H$	Hydrodynamic force
$F_{H,0}$	Hydrodynamic force amplitude
$f_i$	External forces
$F_m$	Measured driving force
$\mathbf{F}_{M_a}$	Added mass force
$\hat{f}_{max,x}$	Maximum non-dimensional in-line synchronization frequency
$\hat{f}_{max,y}$	Maximum non-dimensional cross-flow synchronization frequency
$\hat{f}_{min,x}$	Minimum non-dimensional in-line synchronization frequency
$\hat{f}_{min,y}$	Minimum non-dimensional cross-flow synchronization frequency
$f_n$	Natural frequency
$f_s$	Vortex shedding frequency
$\mathbf{F}_{v,x}$	In-line vortex shedding force
$\mathbf{F}_{v,y}$	Cross-flow vortex shedding force
$F_x$	In-line fluid force
$\overline{F_x}$	Mean in-line fluid force
$F_y$	Cross-flow fluid force
$\overline{F_y}$	Mean cross-flow fluid force
$H_s$	Significant wave height
$I_u$	Turbulence intensity
$\mathbf{j}_3$	Unit vector in axial cylinder direction
$k$	Stiffness
$k_s$	Mean surface protrusion height
$K_t$	Tangential stiffness matrix
$L$	Length
$m$	Mass
$m^*$	Mass ratio
$m_a$	Added mass
$M_t$	Tangential mass matrix
$N$	Number of cycles to failure
$n_i$	Number of cycles



---

$p$	Pressure
$PLexp$	Power-law exponent
$q$	Wake parameter
$\dot{\mathbf{r}}_n$	Transverse structure velocity
$\ddot{\mathbf{r}}_n$	Transverse structure acceleration
$Re$	Reynolds number
$St$	Strouhal number
$t$	Time
$Tp$	Peak period
$U$	Incident flow velocity
$\bar{u}$	Mean wind speed
$\mathbf{u}$	Incident flow velocity
$U_0$	Wind speed at reference elevation
$u_i$	Velocity component in i-direction
$u_j$	Velocity component in j-direction
$\mathbf{u}_n$	Transverse fluid velocity
$\dot{\mathbf{u}}_n$	Transverse fluid acceleration
$U_R$	Reduced velocity
$\mathbf{u}_t$	Tangential fluid velocity
$U_{ref}$	Reference wind speed
$v$	Velocity
$\mathbf{v}_n$	Transverse relative velocity
$x_i$	i-direction
$x_j$	j-direction
$\dot{x}_{rel}$	Relative structure velocity in local x-direction
$y$	Cross-flow direction or displacement
$\dot{y}$	Cross-flow velocity
$\ddot{y}$	Cross-flow acceleration
$y_0$	Cross-flow oscillation amplitude
$\dot{y}_{rel}$	Relative structure velocity in local y-direction

$z$	Height
$Z_0$	Surface roughness
$z_r$	Reference elevation
$z_{ref}$	Reference height

# Chapter 1

## Introduction

### 1.1 Background

The world is looking to transition its energy sources from traditional fossil fuels to more renewable sources. This is often referred to as the global energy transition and several new energy sources have to emerge, or existing ones have to largely increase in extent in order to reduce the effects of global warming and climate change. Floating wind is currently gaining popularity and could emerge as an important piece in the global energy transition towards renewable sources. Up until now most offshore wind turbines have been bottom-fixed and floating wind turbines are still in a development phase where several challenges have to be overcome in order to make it economically beneficial to invest in, as well as to operate. Several different floating wind turbine concepts exist, and some of them are illustrated in Fig. 1.1.

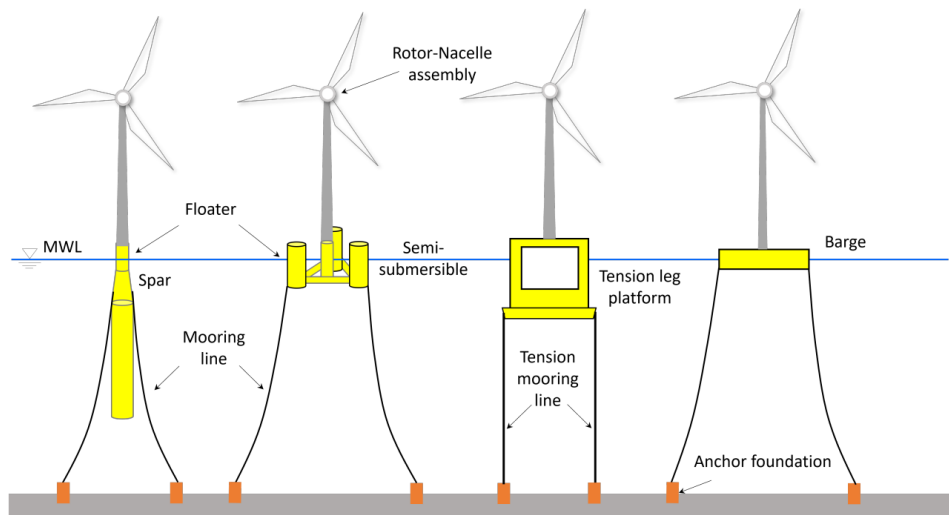
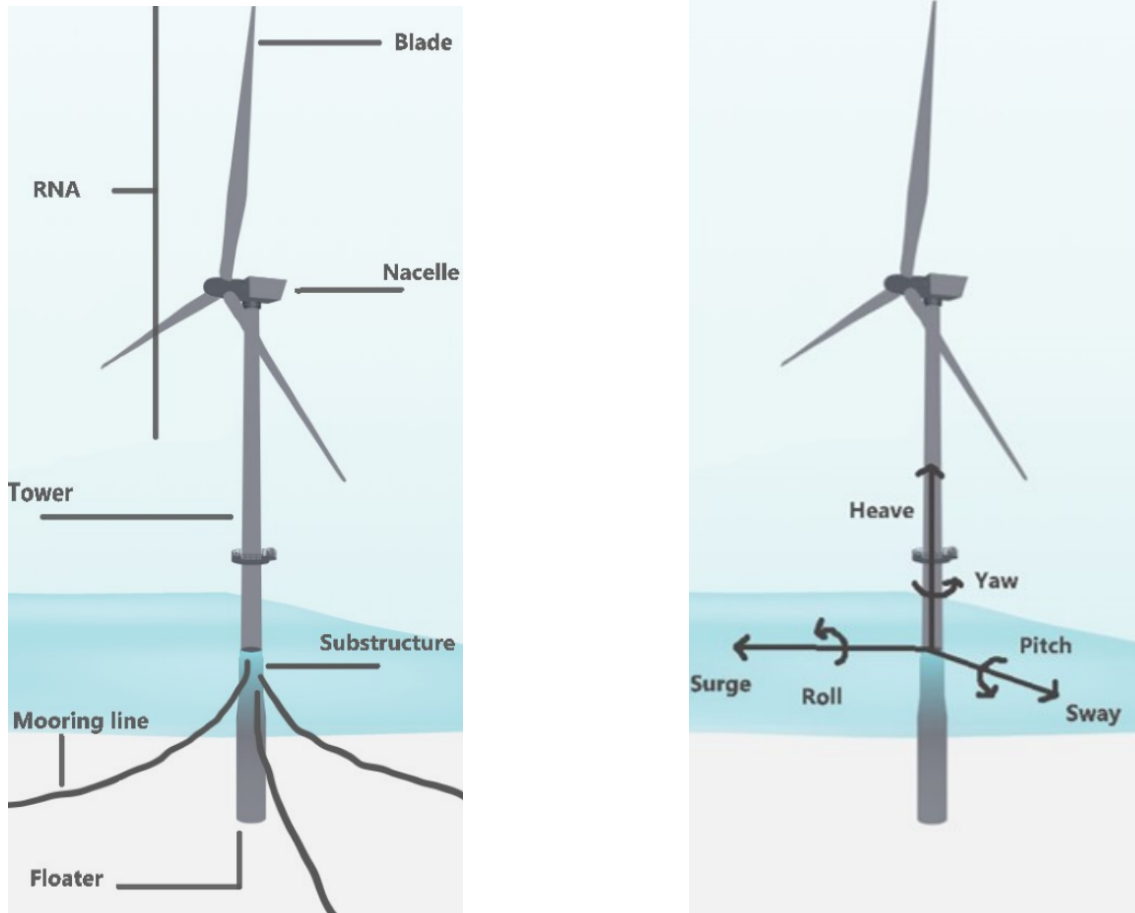


Figure 1.1: Different floating wind turbine concepts. The figure is from [1].

The figure illustrates a spar, semi-submersible, tension leg platform and a barge, which are some of the most popular concepts for floating wind turbines today. In this thesis a spar-type floating wind turbine is investigated. A spar-type floating wind turbine is also illustrated in Fig. 1.2, where the different components making up the total wind turbine structure are shown in Fig. 1.2a and the six degrees of freedom rigid body motion are shown in Fig. 1.2b. Some of these conventions are frequently used throughout this thesis and reference is made to this figure for the definitions.



(a) Components of a spar-type floating wind turbine.

(b) Six degrees of freedom rigid body motion of a spar type floating wind turbine.

Figure 1.2: Definition of components and rigid body motions of a spar-type floating wind turbine. The figures are from [2].

In any way, the spar-type floating wind turbine shows great potential to emerge as an important piece in the global energy transition. This structure may however experience vortex-induced motion (VIM) due to ocean current, which refers to large oscillations of the floater caused by alternating vortex shedding. The motions are typically characterized by surge/sway or roll/pitch oscillations in the natural periods of the structure. These motions may in turn cause significant fatigue damage and consequently reduction of lifetime, and for this reason it is desirable to accurately predict the occurrence of VIM and the motion itself. The current engineering practice for VIM prediction

is based on empirical methods found from model tests, numerical studies and review of full-scale field measurements. Regarding vortex-induced vibration (VIV) prediction, there exists several semi-empirical tools which are considered as a more scientific and accurate approach than the current practice for VIM prediction. In recent years a time domain (TD) VIV model, VIVANA-TD, referred to as the TD VIV model in this thesis, has been developed at NTNU which shows great promise as a VIV prediction tool. This thesis investigates if this TD VIV model can be used as a VIM prediction tool.

## 1.2 Objectives

The main and overall objective of this thesis was to investigate if the TD VIV model could be used as a VIM prediction tool. To answer this question several smaller objectives and subgoals were defined, some in closer correlation to the main objective, but all contributing to an overall answer to the proposed question. These objectives included:

- Present fundamental theory on VIV and VIM including a literature review and an introduction to the fundamental aspects relevant for understanding the matters discussed and presented in this thesis.
- Present an overview of the existing VIV prediction tools and the current engineering practice for VIM prediction.
- In particular, describe the TD VIV model in more detail.
- Replicate the Hywind Scotland spar-type floating wind turbine as accurately as possible in SIMA using SIMO and RIFLEX, and report the modelling procedure.
- Introduce full-scale measurements and respective metocean data for the cases.
- Analyse the modelled FWT considering the full-scale environmental cases with and without the TD VIV model and compare the results to the full-scale measurements to validate the model.
- Perform case studies to investigate the effect of wind and waves on the VIM predicted by the TD VIV model.
- Establish a representative full year environmental condition.
- Analyze the modelled FWT considering the representative full year environmental condition with and without the TD VIV model and present the results.
- Investigate the effect the predicted VIM with the full year environmental condition has on the mooring system in terms of ULS design and fatigue life.
- Present the important findings, conclusions and recommendations for further work.

## 1.3 Thesis structure

The thesis is structured in the following way:

**Chapter 2** provides a theoretical background and literature review of VIV and VIM, including an introduction to the fundamental aspects relevant for this thesis. The chapter is structured in such a way that a novice reader with basic knowledge on structural analysis and hydromechanics should be able to follow the train of thought in the chapter. Short introductions to relevant aerodynamics and fatigue are also included in the chapter.

**Chapter 3** describes the existing VIV prediction tools including computational fluid dynamics (CFD), semi-empirical frequency domain models as well as some empirical time domain models. The semi-empirical time domain model VIVANA-TD for VIV prediction, referenced to in this thesis as the TD VIV model, is the main focus throughout the thesis and is described in more detail. In addition, the chapter also includes information in the current engineering practice for VIM prediction.

**Chapter 4** introduces the Hywind Scotland spar-type floating wind turbine which is the concept used in this thesis. The software used to model the floating wind turbine is introduced, and the modelling procedure is outlined. A description of the modelled structure is also included, as well as verification of the model in terms of free decay test to calculate natural periods which then were compared to stated periods. In addition, some notes on the modelling and challenges along the way are discussed in the chapter.

**Chapter 5** gives an introduction to full-scale measurement cases from a Hywind Scotland wind turbine. The full-scale measurements themselves are presented, as well as the metocean conditions for each of the cases. The modelled floating wind turbine is then analyzed with the same environmental conditions as the full-scale measurements, both with and without the TD VIV model, and the results are compared the full-scale measurements and presented in the chapter. This was done to validate the TD VIV model as a VIM prediction tool and a discussion on the validation is also included in the chapter.

**Chapter 6** includes results from several case studies. First, the effect of wind and waves on the VIM prediction was investigated and the results are presented. Next, a representative full year environmental condition was established in order to investigate the effect of VIM on the ULS design and fatigue life of the mooring system. The procedure for establishing the representative environmental condition is presented in the chapter and the specific value are listed. The modelled floating wind turbine is analyzed with the environmental condition both with and without the TD VIV model, and the results are presented and discussed. Finally, the effect on the mooring system with regards to the ultimate limit state and fatigue life is presented.

**Chapter 7** summarizes the key findings, concludes and provides recommendations for further work.

**Appendix A** shows an example of a TurbSim-input file used to generate spatially varying turbulent wind fields.

---

**Appendix B** contains complete sets of results from the validation against the full-scale measurements, from the investigation on the effect of wind and waves on the VIM response predicted by the TD VIV model, and from the representative full year environmental conditions. The results are presented in terms of time series plots of the translational motion in x- and y-directions, as well as frequency spectra of the translational motions.





## Chapter 2

# Theoretical background

This chapter presents the results of a literature review on the fundamental theory of VIV and VIM. Parts of previous work and research on the topic are also presented. There has been extensive research on particularly VIV over several decades, and hence only parts of the available literature are presented. The chapter should also serve as an introduction to VIV and VIM for readers not already familiarized with the phenomena.

### 2.1 Introduction to vortex-induced vibrations

The following introduction to VIV is based on the book by Sumer and Fredsøe [3]. The introduction is built on the example of a rigid, circular cylinder. Firstly the cylinder is fixed and placed in steady flow, where different flow regimes and the vortex shedding phenomena are introduced. Forces on the cylinder are also discussed. Then the cylinder is forced to oscillate harmonically in steady flow where added mass and excitation are investigated. Lastly the cylinder is elastically mounted in steady flow where lock-in of the frequency and response amplitude is looked into.

#### 2.1.1 Fixed circular cylinder in steady flow

To get a proper understanding of VIV it is important to initially understand the vortex shedding phenomenon, here exemplified by a fixed circular cylinder in steady incoming flow. A characteristic property of the flow regime around the cylinder is given by the Reynolds number. The non-dimensional parameter gives the ratio of inertial to viscous forces and is defined as:

$$Re = \frac{UD}{\nu}, \quad (2.1)$$

where  $Re$  is the Reynolds number,  $U$  is the velocity of the undisturbed incoming flow,  $D$  is the cylinder diameter and  $\nu$  is the kinematic viscosity of the fluid. As seen from Eq. (2.1), the Reynolds number gives the ratio of inertial forces to viscous forces. The viscous forces develop as a result of large velocity gradients in the radial direction close to the cylinder. The no-slip boundary condition, which must be satisfied at all times when fluid is in contact with a solid surface, states that the fluid at the surface will have zero velocity relative to the surface. This boundary condition

gives rise to a thin boundary layer, which is characterized by the mentioned velocity gradients, forming around the cylinder in consideration.

An overview of the different Reynolds number flow regimes around a circular cylinder is shown in Tab. 2.1. When  $Re < 5$ , the flow is unseparated from the cylinder. With reference to the definition of the Reynolds number in Eq. (2.1), the viscous forces dominate in this flow regime. Flow separation starts occurring at  $Re \approx 5$ , and a shear layer is formed at each side of the cylinder which ends up as vortices. See Fig. 2.1 for an illustration of flow around a stationary circular cylinder including the vortex shedding phenomenon. The figure also includes a schematic definition of some relevant terms. For  $5 \leq Re < 40$ , the pair of vortices remains stable behind the cylinder in the provisionally laminar steady flow. These vortices are often referred to as Föppl vortices. An instability occurs when  $Re \approx 40$ , which causes one of the vortices to grow larger than the other. This divergent geometry of the flow environment behind the cylinder causes an adverse pressure gradient which draws the smaller vortex across the wake and towards the larger vortex. Due to the opposite vorticity directions of the two vortices, the vorticity supply to the larger vortex from its boundary layer is cut off as the smaller vortex with vorticity of the opposite sign is approaching. This consequently leads to the phenomenon of vortex shedding where the larger vortex is released from the boundary layer. As the larger vortex now is a free vortex, it is convected downstream by the flow, and in its place a new vortex starts to form. The previously smaller vortex will now grow larger and eventually draw the new vortex across the wake. This leads to the shedding of the previously smaller, now larger vortex, and the process will repeat itself in an alternate manner between the sides of the cylinder [4]. The alternating vortex shedding gives the wake an appearance of a vortex street consisting of two rows of vortices. This is often referred to as a von Kármán vortex street.

Table 2.1: Regimes of flow around a smooth, circular cylinder in steady current. The table is adapted from [3].

Reynolds number	Description
$Re < 5$	No separation. Creeping flow.
$5 \leq Re < 40$	A fixed pair of symmetric vortices.
$40 \leq Re < 200$	Laminar vortex street.
$200 \leq Re < 300$	Transition to turbulence in the wake.
$300 \leq Re < 3 \cdot 10^5$	<b>Subcritical.</b> Wake completely turbulent. Laminar boundary separation.
$3 \cdot 10^5 \leq Re < 3.5 \cdot 10^5$	<b>Critical (Lower transition).</b> Laminar boundary layer separation on one side. Turbulent boundary layer separation, but laminar boundary layer on the other side.
$3.5 \cdot 10^5 \leq Re < 1.5 \cdot 10^6$	<b>Supercritical.</b> Turbulent boundary layer separation. Partly turbulent, partly laminar boundary layer.
$1.5 \cdot 10^6 \leq Re < 4.5 \cdot 10^6$	<b>Upper transition.</b> Boundary layer completely turbulent at one side.
$4.5 \cdot 10^6 \leq Re$	<b>Transcritical.</b> Boundary layer completely turbulent at both sides.

For the range  $40 \leq Re < 200$ , the vortex street is laminar and the shedding does not vary in the spanwise direction [6]. As the Reynolds number is further increased, a transition to turbulence transpires in the wake region. In the range  $200 \leq Re < 300$ , the turbulence region moves towards the cylinder with increasing Reynolds number [7]. At  $Re = 300$ , the wake is completely turbulent. The spanwise vortex shedding correlation, which essentially is a two-dimensional feature, observed

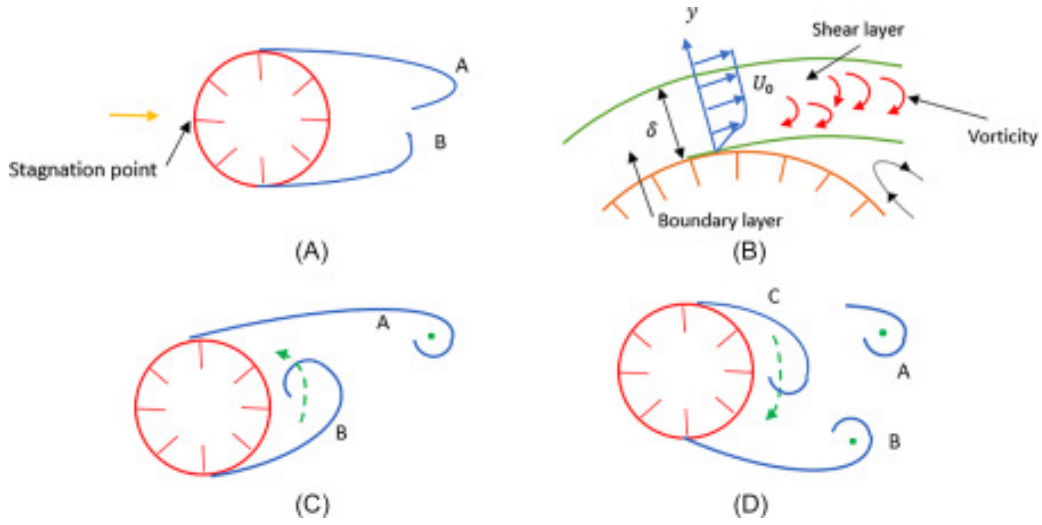


Figure 2.1: Flow around a stationary circular cylinder including the vortex shedding phenomenon. The figure is from [5].

in the range  $40 \leq Re < 200$ , becomes distinctly three-dimensional in the range  $200 \leq Re < 300$ , i.e. the vortices are shed in blocks in the spanwise direction [8]. This three-dimensional feature of the vortex shedding prevails for all  $Re > 300$ , and the wake remains completely turbulent. When the Reynolds number is within the wide range  $300 \leq Re < 3 \cdot 10^5$ , known as the subcritical flow regime, the boundary layer over the cylinder remains laminar, even though the wake is turbulent. As the Reynolds number is further increased, the transition to turbulence occurs also in the boundary layer. In the narrow range  $3 \cdot 10^5 \leq Re < 3.5 \cdot 10^5$ , known as the critical (or lower transition) flow regime, the boundary layer becomes turbulent at the separation point on one side of the cylinder. On the separation point at the other side of the cylinder the flow in the boundary layer remains laminar. This asymmetry in the flow causes a non-zero mean lift force on the cylinder. However, the side at which the turbulent separation occurs is alternating occasionally, causing the lift force to change direction [9]. As the Reynolds number is increased further, the boundary layer separation becomes turbulent at both sides of the cylinder, however the whole boundary layer is not yet turbulent. In the range  $3.5 \cdot 10^5 \leq Re < 1.5 \cdot 10^6$ , known as the supercritical flow regime, the boundary layer is still laminar to a transition point between the stagnation point and the separation point. Further downstream (including the separation point) the boundary layer is turbulent. When the Reynolds number reaches  $1.5 \cdot 10^6$ , the boundary layer becomes fully turbulent on one side of the cylinder, while it remains partly laminar on the opposite side. This behaviour prevails over the range  $1.5 \cdot 10^6 \leq Re < 4.5 \cdot 10^6$ , known as the upper transition flow regime. Finally, when  $Re \geq 4.5 \cdot 10^6$ , known as the transcritical flow regime, the boundary layer is completely turbulent over the whole cylinder surface.

The vortex shedding phenomenon is the key feature of all the flow regimes described above, when  $Re \geq 40$ . The vortex shedding frequency,  $f_s$ , is the frequency at which the vortex shedding occurs, and is closely related to the relevant dimensionless parameter, the Strouhal number, defined as:

$$St = \frac{f_s D}{U}. \quad (2.2)$$

Given the Strouhal number, the vortex shedding frequency of a fixed cylinder with diameter  $D$  in

steady incoming flow of velocity  $U$ , can be calculated as:

$$f_s = \frac{StU}{D}. \quad (2.3)$$

The Strouhal number varies with the surface roughness of the cylinder, as well as the Reynolds number [10]. Fig. 2.2 shows the relationship of the Strouhal number and Reynolds number for a circular cylinder. The original  $St$  versus  $Re$  curve collated by [11] is shown as solid grey in the background. The upper curve, with the abrupt increase of  $St$ , denotes a smooth surface, while the lower curve denotes a rough surface. The open circles denote the bulk of data discussed and presented in [12], while the squares denote some of the data used by [11] in the development of the original  $St$  versus  $Re$  curve. As seen from Fig. 2.2, in the subcritical range,  $St \approx 0.2$ . This is also a well known approximation stated by many, e.g. [13]. It is also seen in the figure that for a smooth cylinder in the upper part of the subcritical, as well as in the critical, supercritical and the lower parts of the upper transition flow regimes,  $St$  increases to a maximum value of around 0.45. When  $Re$  is further increased in the upper transition flow regime,  $St$  drops to around 0.25 and is in the range 0.25 – 0.3 for the remainder of the upper transition, as well as the transcritical flow regime.

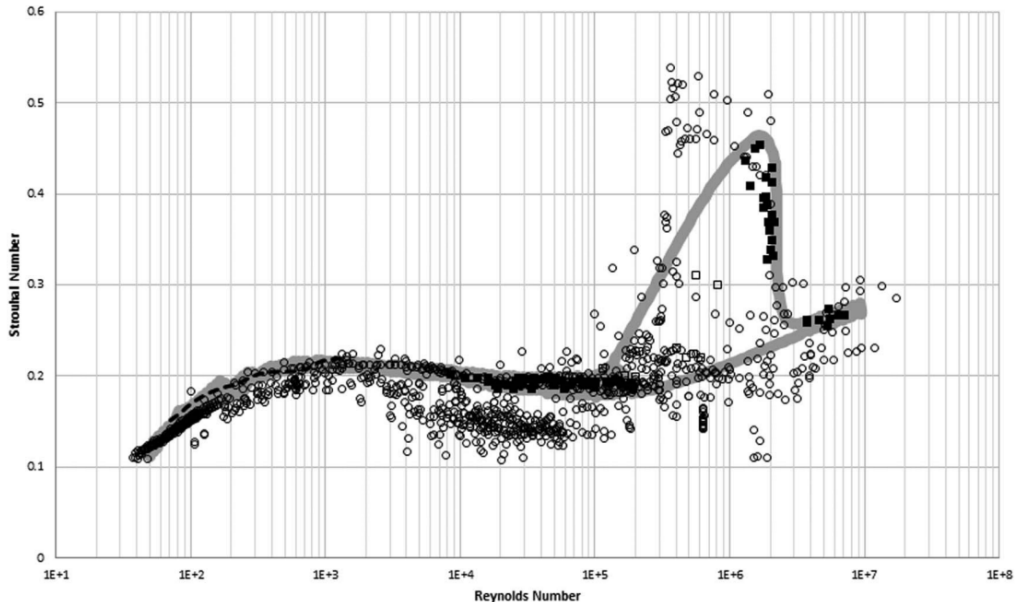


Figure 2.2: Strouhal number vs. Reynolds number. The figure is from [12].

It should be noted that the vortex shedding frequency is not always well defined in a narrow-banded spectrum with a sharply defined and dominant peak. On the contrary the vortex shedding frequency may consist of several frequency components [9]. In the subcritical flow regime the vortex shedding is regular and occurs in an orderly and well defined manner. This corresponds to a narrow-banded frequency spectrum and is also the case for the supercritical flow regime. In the upper transition flow regime, the vortex shedding is however irregular and disorderly, resulting in a broad-banded frequency spectrum. As described in Tab. 2.1, the boundary layer is completely turbulent at one side of the cylinder, but partly turbulent, partly laminar on the other side in the upper transition flow regime. This asymmetry with regard to the vortex formation partially

inhibits the interaction between the vortices, and is the reason for the disordered vortex shedding. In the transcritical flow regime, the narrow banded frequency spectrum and regular vortex shedding is re-established.

Varying fluid pressure and shear stress arise around the fixed circular cylinder due to the flow around it when placed in steady flow as previously described. The resulting force on the cylinder can be split into two components, one in the in-line (IL) direction called drag, and one in the cross-flow (CF) direction called lift (see Fig. 2.3). These force components can be expressed as dimensionless coefficients on the form:

$$C_d = \frac{F_x}{\frac{1}{2}\rho DU^2} \quad (2.4)$$

and:

$$C_l = \frac{F_y}{\frac{1}{2}\rho DU^2} \quad (2.5)$$

for the IL and CF directions respectively. Here,  $\rho$  is the fluid density,  $x$  denotes the IL direction and  $y$  denotes the CF direction.  $C_d$  and  $F_x$  are drag coefficient and IL fluid force per unit length respectively, while  $C_l$  and  $F_y$  are the lift coefficient and CF fluid force per unit length respectively. The drag coefficient and IL fluid force have significant mean components,  $\overline{C_d}$  and  $\overline{F_x}$ , which has two contributions, one due to pressure (IL mean pressure force) and one due to friction (IL mean friction force). The mean components of the lift coefficient and CF fluid force,  $\overline{C_l}$  and  $\overline{F_y}$ , is zero due to symmetry. The instantaneous lift is however non-zero and its value can be quite substantial.

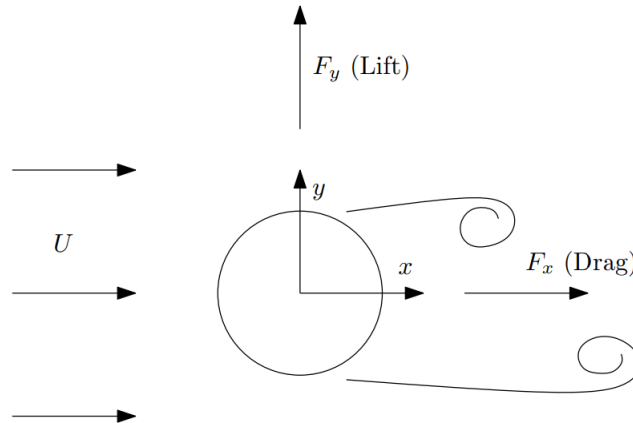


Figure 2.3: Lift and drag forces acting on a circular in steady flow. The figure is from [14].

### 2.1.2 Forced harmonic oscillation of a circular cylinder in steady flow

Now, consider a rigid circular cylinder in steady incoming flow forced to oscillate harmonically. The driving force can be applied either in the CF or IL direction, or as a combination of the two. The issue of forcing pure CF oscillation by a driving frequency  $f$ , was first experimentally investigated in [15]. For  $f$  far from the vortex shedding frequency given by the Strouhal relationship,  $f_s$ , the researchers found that the lift force oscillates with  $f_s$ . When  $f$  approaches  $f_s$  however, it was found that the lift force starts to oscillate with  $f$ , rather than  $f_s$ . This means that the lift force becomes synchronized with the motion and  $f_s$  no longer exists. This synchronization was observed over a

range of driving frequencies and is of great importance for the vortex-induced forces as shall be seen later.

When performing forced harmonic oscillation experiments in the CF direction, the displacement can be described as:

$$y = y_0 \sin(2\pi ft) = y_0 \sin(\omega t), \quad (2.6)$$

where  $y_0$  is the oscillation displacement amplitude,  $f$  is the oscillation frequency and  $\omega$  is the circular oscillation frequency. Consequently the velocity and acceleration can be described as:

$$\dot{y} = \omega y_0 \cos(\omega t) \quad (2.7)$$

and:

$$\ddot{y} = -\omega^2 y_0 \sin(\omega t) \quad (2.8)$$

respectively. The equation of motion for free oscillation in the CF direction can be written as:

$$m\ddot{y} + c\dot{y} + ky = F_H, \quad (2.9)$$

where  $m$  is the mass,  $c$  is the damping,  $k$  is the stiffness and  $F_H$  is the total hydrodynamic force on the cylinder. This hydrodynamic force can generally be decomposed into two main components. One component in phase with the velocity and the other component in phase with the acceleration of the cylinder. The former component acts as excitation or damping corresponding to positive or negative energy transfer to the system respectively. The latter component does not have any contribution to the energy transfer, but rather acts as an inertia force. Mathematically the hydrodynamic force can be written as:

$$F_H = F_{H,0} \sin(\omega t + \phi) = F_{H,0} \cos(\omega t) \sin(\phi) + F_{H,0} \sin(\omega t) \cos(\phi), \quad (2.10)$$

where  $F_{H,0}$  is the hydrodynamic force amplitude and  $\phi$  is the phase angle between the hydrodynamic force and the motion of the cylinder. The hydrodynamic force can also be rewritten as:

$$F_H = F_E \cos(\omega t) + F_A \sin(\omega t), \quad (2.11)$$

where  $F_E$  is the excitation force in phase with the velocity and  $F_A$  is the added mass force in phase with the acceleration. Now the equation of motion in Eq. (2.9) can be written as:

$$m(-\omega^2 y_0 \sin(\omega t)) + c(\omega y_0 \cos(\omega t)) + k(y_0 \sin(\omega t)) = F_E \cos(\omega t) + F_A \sin(\omega t). \quad (2.12)$$

For the case of forced harmonic oscillation the system has no restoring and damping and thus the cylinder only experiences inertial and hydrodynamic forces. These has to be equal to the measured driving forces throughout the experiment. The equation of motion then becomes:

$$m(-\omega^2 y_0 \sin(\omega t)) - F_E \cos(\omega t) - F_A \sin(\omega t) = F_m, \quad (2.13)$$

where  $F_m$  is the measured driving force. Rewriting the added mass force to an added mass gives:

$$(m + m_a)(-\omega^2 y_0 \sin(\omega t)) - F_E \cos(\omega t) = F_m, \quad (2.14)$$

where  $m_a$  is the added mass. Now the added mass and excitation coefficients can be found experimentally. A frequently used hydrodynamic coefficient database for pure CF was established in [16]. Examples of contour plots for pure CF excitation and added mass coefficients are shown in Fig. 2.4 for  $Re = 10,000$ . The non-dimensional frequency is defined as:

$$\hat{f} = \frac{fD}{U}, \quad (2.15)$$

and the amplitude ratio is defined as  $y_0/D$ .

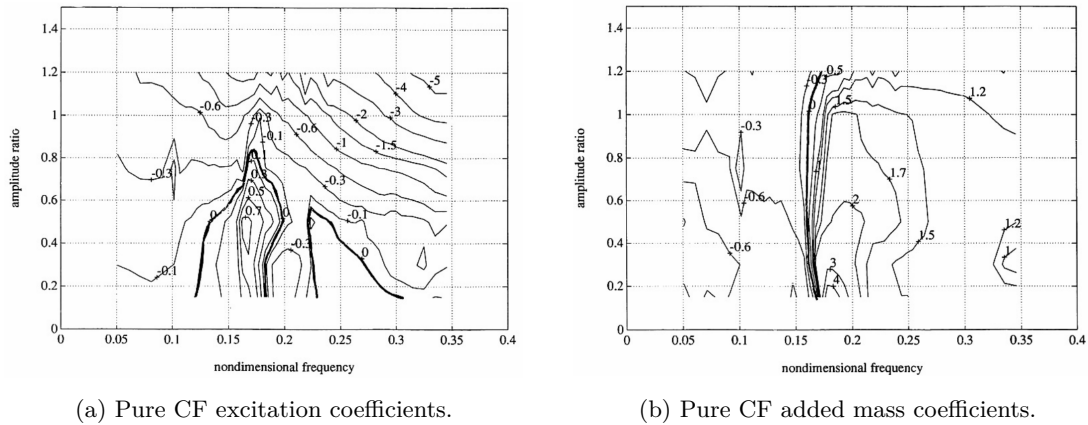


Figure 2.4: Contour plots for pure CF excitation and added mass coefficients. The figures are from [16].

### 2.1.3 Elastically mounted circular cylinder in steady flow

If a rigid, circular cylinder is mounted on elastic supports such as springs, it will start to oscillate when placed in steady incoming flow as a response to the vortex shedding forces. This oscillating motion is called VIV. The vortex shedding triggers the vibration and the vibration is altering the flow, thus also altering the fluid forces. This makes VIV a resonant fluid-structure interaction (FSI) phenomenon. If the cylinder is elastically mounted in both the IL and CF direction, the VIV motion may be observed as a combination of IL and CF displacements. A typical VIV displacement pattern in the combined CF and IL direction is the figure eight motion, where the cylinder is following a figure eight trajectory as a response to the vortex shedding forces. Naturally, this figure eight pattern is observed when the IL motion frequency is double the CF motion frequency. However, the cylinder can also be restrained to only move in the IL or CF direction and would naturally only experience VIV motion in its respective degree of freedom (DOF) in which the cylinder can move. See Fig. 2.5 for a simple sketch of the experimental setups for the three scenarios.

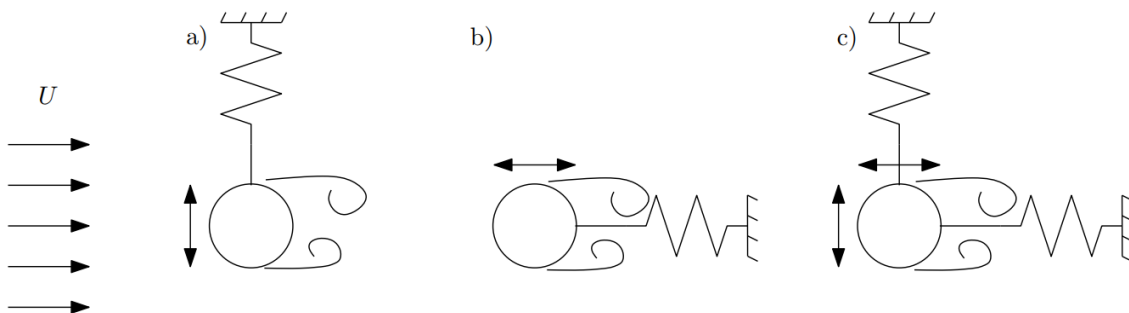


Figure 2.5: Typical VIV experiments for rigid, circular cylinders in steady flow: a) CF motion only, b) IL motion only, c) combined IL and CF motion. The figure is from [14].

Experiments investigating the vortex shedding frequency, oscillation frequency and displacement amplitude of a spring mounted cylinder were carried out in [17]. A variable in the experiments

was the dimensionless flow velocity, now known as the reduced velocity, defined as:

$$U_R = \frac{U}{f_n D}, \quad (2.16)$$

where  $f_n$  is the natural frequency of the cylinder. Since the experiments were conducted in air, the added mass was negligible and consequently the natural frequency constant. Some findings are shown in Fig. 2.6 and it can be seen that the cylinder did not oscillate for low reduced velocities when the vortex shedding frequency followed the preciously defined Strouhal relationship. When  $U_R$  was increased to above 5, the vortex shedding frequency locked on to natural frequency of the cylinder and remained constant up to  $U_R \approx 7$ . This phenomenon is referred to as lock-in or synchronization, and the reduced velocity region at which it occurs is known as the lock-in region or synchronization region. It is important to emphasize the fact that the added mass is negligible for the air test. If the test was conducted in water, added mass would play a crucial part and alter the natural frequency with change in the reduced velocity. However, the air test serves as a good introduction to the phenomenon. With further increase of  $U_R$ , the vortex shedding frequency started to deviate from the natural frequency, and rather follows the Strouhal relationship again. Lock-in causes the lift force to oscillate with the same frequency as the cylinder motion and hence the cylinder vibration reaches large amplitudes as seen in Fig. 2.6b).

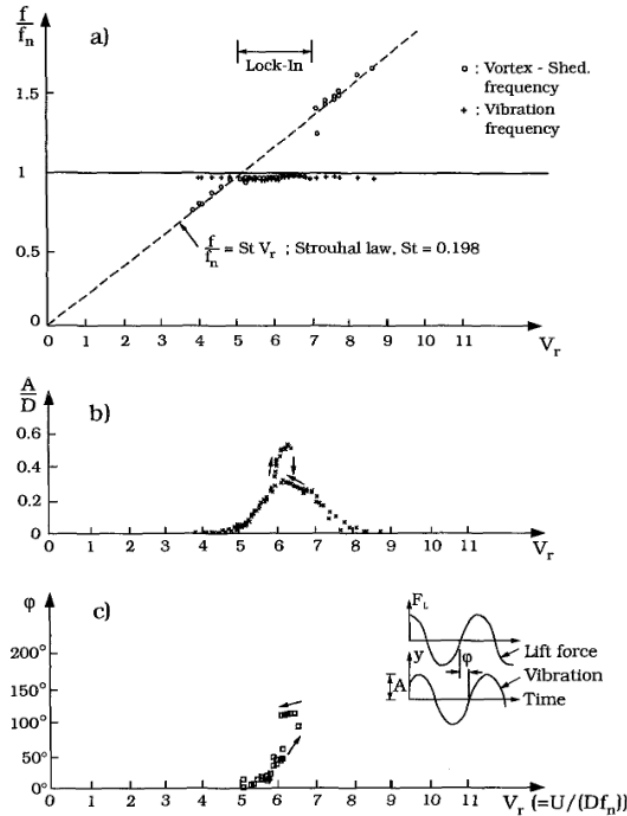


Figure 2.6: CF response of an elastically mounted circular cylinder in steady air flow: a) dimensionless frequency, b) dimensionless amplitude, c) phase angle. The experiments were carried out by [17]. The figure is from [3].



Another feature identified by free oscillation experiments is that VIV is a self-limiting process. This means that the displacements amplitude will reach a steady state condition after a transient response for all initial conditions. This feature is observed due to the excitation force coefficient being dependent on the response amplitude, as can be seen in Fig. 2.7 for a given non-dimensional frequency. The curve is defined from the three points, A, B and C, where point A gives the excitation coefficient when the response is zero. Point B gives the maximum value of the excitation coefficient, while point C gives the amplitude ratio when the excitation coefficient is zero. On the left hand side of point C the excitation coefficient is positive, while on the right hand side it is negative. A positive excitation coefficient will supply energy to the system and increase the amplitude ratio, while a negative excitation coefficient will subtract energy from the system and reduce the amplitude ratio, thus explaining the self-limiting feature of VIV.

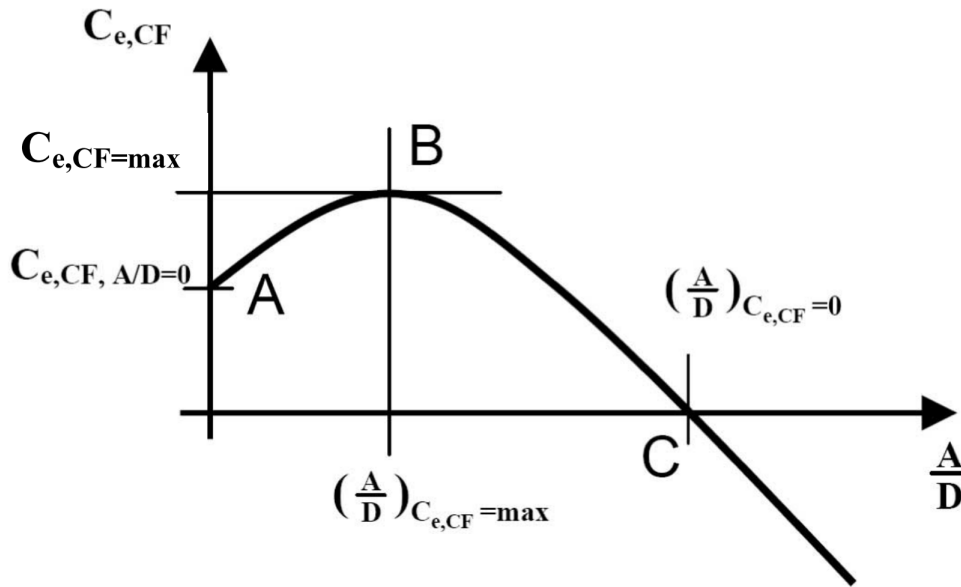


Figure 2.7: CF excitation force coefficient curve for a given non-dimensional frequency. The figure is from [18].

## 2.2 Introduction to vortex-induced motions

VIM is essentially a special subset of VIV, as both are resonant FSI phenomena. VIV regards motion and vibration of all types of structures, but in the literature and industry the primary focus has been towards slender structures, such as risers, pipelines, mooring lines and power cables. VIM is however often treated with regard to rigid body motion of larger floating structures such as spars and semi-submersibles. There exists no clear distinction between VIV and VIM, but generally speaking, VIM can be treated as a type of VIV, represented by small mass ratio and aspect ratio, high Reynolds numbers and at least two degrees of freedom (DOF) rigid body motion (see Fig. 2.8) [1]. The importance of these four parameters and aspects with regards to VIM are briefly described in the following. It is however important to understand the connection and the many similarities between VIV and VIM, as much of the following discussion also applies for VIV.

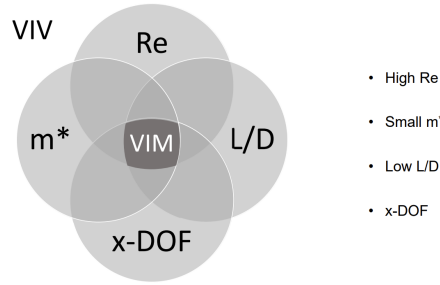


Figure 2.8: VIM can be treated as a subset of VIV, represented by high Reynolds numbers, small mass ratio, low aspect ratio and rigid body motion. The figure is from [1].

### 2.2.1 Reynolds number

The Reynolds number,  $Re$ , is already defined in Eq. (2.1) and treated with regard to VIV in Sec. 2.1.1. VIM is however occurring under higher Reynolds numbers than VIV. This comes from the significantly larger diameter or characteristic length of the structures under consideration, compared to the slender marine structures under consideration for VIV. There exists a large Reynolds number dependence on several important VIM parameters. Fig. 2.9 shows a collection of mean drag coefficients on a fixed circular cylinder with varying Reynolds number and surface roughness ratio. The surface roughness ratio is defined as the ratio between the mean height of the surface protrusions and the dimension of the cross section,  $k_s/D$ . The large drop in  $C_d$  observed around the critical flow regime is called the drag crisis and is caused by the separation point moving towards the rear of the cylinder with increasing Reynolds number. This is consequently causing a narrower wake and reduced drag coefficient.

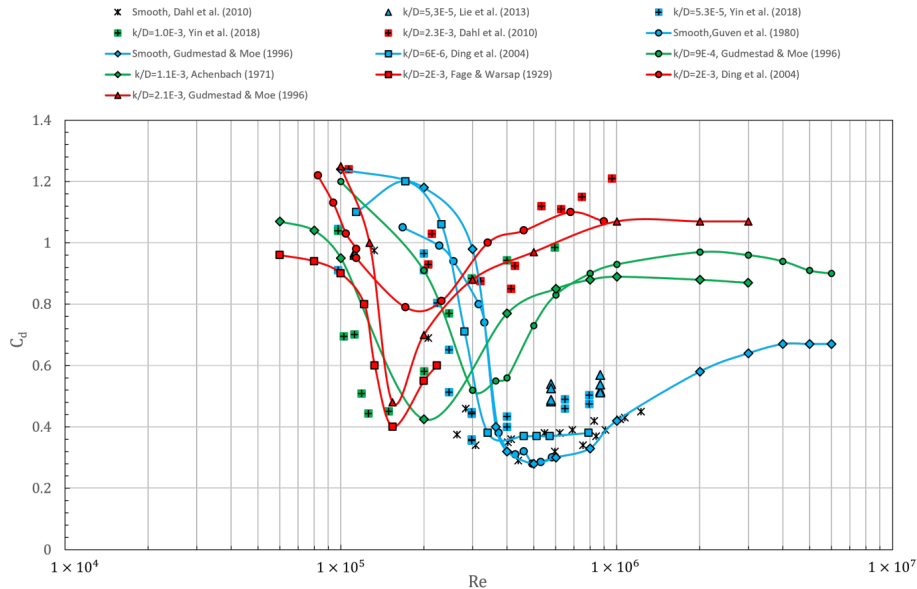


Figure 2.9: Collection of mean drag coefficients on a fixed circular cylinder for varying Reynolds number and roughness ratio. Reference is made to [1] for the data origin. The figure is from [1].

### 2.2.2 Mass ratio

The mass ratio is defined as:

$$m^* = \frac{m}{\frac{\pi}{4}\rho D^2}, \quad (2.17)$$

where  $m$  is mass per unit length. It can be seen from the definition that the mass ratio represents the ratio of structural mass in oscillation to fluid mass displaced by the structure. For VIM the mass ratio is small, such as for spar and semi-submersible floaters. Slender marine structures are no floaters and hence the structural mass can be several times the displaced fluid mass. The effect of varying mass ratio was investigated for a wide range in [19]. Fig. 2.10 shows the CF cylinder response with 2 DOF motion for four different mass ratios. It is observed that the maximum response increases and moves to higher reduced velocities with decreasing mass ratio.

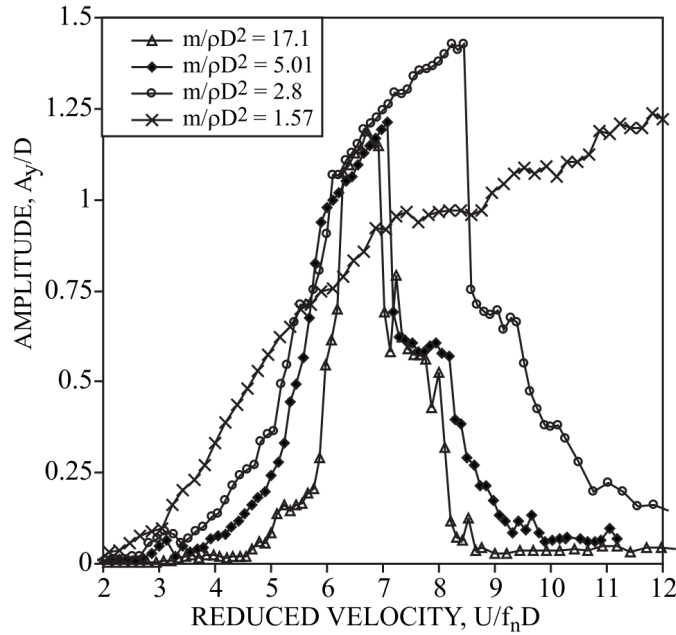


Figure 2.10: CF cylinder response with 2 DOF motion for four different mass ratios. The figure is from [19].

### 2.2.3 Aspect ratio

The aspect ratio is defined as:

$$A_R = \frac{L}{D}, \quad (2.18)$$

where  $L$  is the effective immersed length. For VIM the aspect ratio is low, as opposed to for slender marine structures where the aspect ratio is much higher. The effect of varying aspect ratio with regards to VIM has been scarcely studied according to [1] and [20]. However, [21] and [22] did find the Strouhal number to increase with the aspect ratio, due to the von Kármán vortex shedding, and [23] found this to be valid only for  $A_R > 2.0$ . Therefore a critical aspect ratio of  $\approx 2.0$  was suggested by [23], which is of importance for low aspect ratio floaters. Another effect to take into account for low aspect ratios is what happens at the free end. This was investigated in [24] and it was found that free end only affected VIV behaviour for surface-piercing cylinders with  $A_R < 0.5$ .

### 2.2.4 Degrees of freedom

Oscillation in at least 2 DOF plays an important part in the VIM response of floating units. Although most of the research is based on VIV acting on cylinders with only 1 or 2 DOF [20], the 2 DOF response is capturing striking changes to the dynamic behaviour. This simply comes from the coexistence of CF and IL oscillations. Some 2 DOF trajectories of combined CF and IL motion are shown in Fig. 2.11, and illustrates the complexity of the dynamic behaviour for 2 DOF motion.

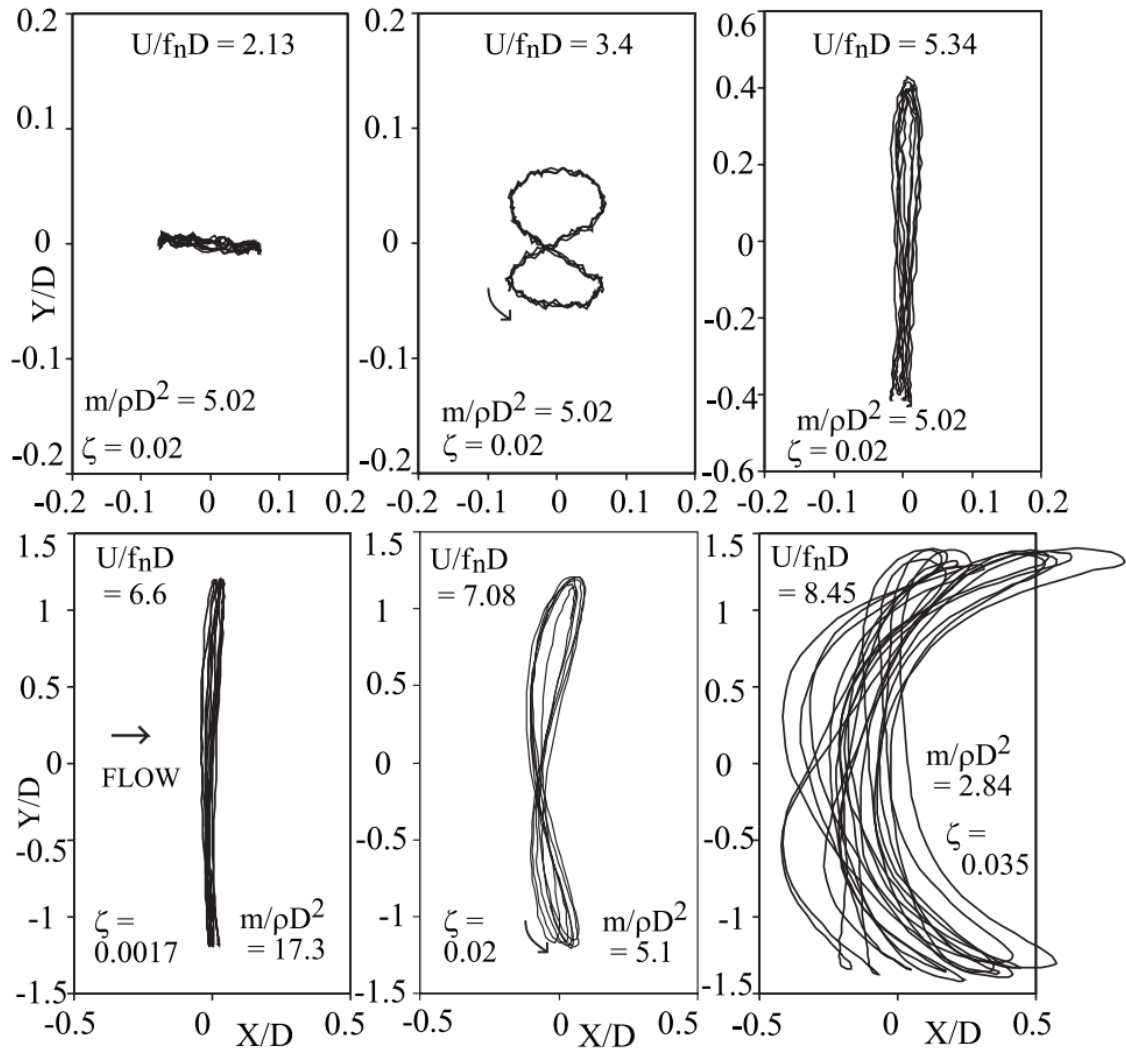


Figure 2.11: 2 DOF trajectories of combined CF and IL motion. Velocity increases from left to right. The figure is from [19].

## 2.3 Aerodynamics

The aerodynamic forces acting on a structure can only be calculated with a given wind environment description. This environment contains information on the movement of air through the given spatial domain. An important factor in the wind environment description is the turbulence. The turbulence can be modeled with different degrees of complexity ranging from steady wind where no incoming turbulence is assumed, to two-dimensional (2D) unsteady wind and three-dimensional (3D) spatially varying wind.

### 2.3.1 Steady wind

The simplest wind environment description is steady incoming wind with a constant velocity and direction. As introduced in Sec. 2.1.1, the no-slip boundary condition which states that when a fluid is in contact with a solid surface, the fluid at the surface will have zero velocity relative to the surface, is also valid for air. The velocity profile can hence not be considered constant through the height of the wind environment. Several different profiles exist to describe the changing velocity over the environment height. One such profile is the power-law profile described as:

$$\bar{u}(z) = \bar{u}(z_{ref}) \left( \frac{z}{z_{ref}} \right)^{PLe xp}, \quad (2.19)$$

where  $\bar{u}(z)$  is the mean wind speed at height  $z$  and  $\bar{u}(z_{ref})$  is the known mean wind speed at a reference height  $z_{ref}$  above ground.  $PLe xp$  is the power-law exponent. Another common wind profile is the logarithmic profile defined as:

$$\bar{u}(z) = \bar{u}(z_{ref}) \frac{\ln\left(\frac{z}{Z_0}\right) - \Psi_m}{\ln\left(\frac{z_{ref}}{Z_0}\right) - \Psi_m}, \quad (2.20)$$

where  $Z_0$  is the surface roughness and  $\Psi_m$  is a stability function often equal to zero.

### 2.3.2 Unsteady wind

The assumption of the wind being steady is not physical as wind in general is unsteady. The fact that air has low density and viscosity suggests that even small disturbances in the flow can cause turbulence. Turbulence is measured as variance or standard deviation around a mean wind speed. The turbulence is often described by a turbulence intensity,  $I_u$ , which is defined as:

$$I_u = \frac{\sigma}{\bar{u}}, \quad (2.21)$$

where  $\sigma$  is the standard deviation and  $\bar{u}$  is the mean wind speed. The turbulence in the unsteady wind is typically modelled by a turbulence spectrum. Several such spectra exists, and one commonly used example is the IEC Kaimal spectrum [25]. A definition of the spectrum can be found in [26].

### 2.3.3 Spatially varying wind

In addition to unsteady wind which varies in time, the wind can also vary in space, which is called spatially varying wind. This means the incoming wind speed on a wind turbine is not modelled constant over the rotor disc, but rather with spatially varying components, in addition the unsteady components with regards to time. This gives a much better representation of reality and should produce accurate response patterns, given good refinement and accurately defined environmental parameters.

## 2.4 Fatigue

Fatigue is damage to a structure due to cyclic loading over time. An example of a fatigue load history with symbol definitions is shown in Fig. 2.12. An S-N curve is defining the relationship between the stress range,  $\Delta S$ , and the number of cycles to failure,  $N$ , and the S-N curve is defined as:

$$N \cdot (\Delta S)^m = \text{constant}, \quad (2.22)$$

where  $m$  is constant defining the slope of the S-N curve.

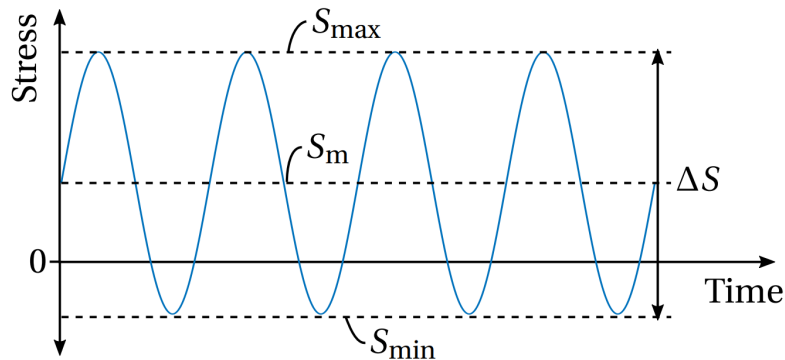


Figure 2.12: Fatigue load history and symbol definitions. The figure is from [27].

For cumulative damage analysis with variable amplitude loading, the stress-time history is divided into individual cycles which then are summed up to a distribution of stress ranges. Several different cycle counting techniques exist, but one commonly used is the rainflow counting method. This counting method is based upon counting cycles in accordance with the material's stress-strain response pattern which can be illustrated by hysteresis loops. An example of a strain time series as well as the stress-strain path forming hysteresis loops are plotted in Fig. 2.13.

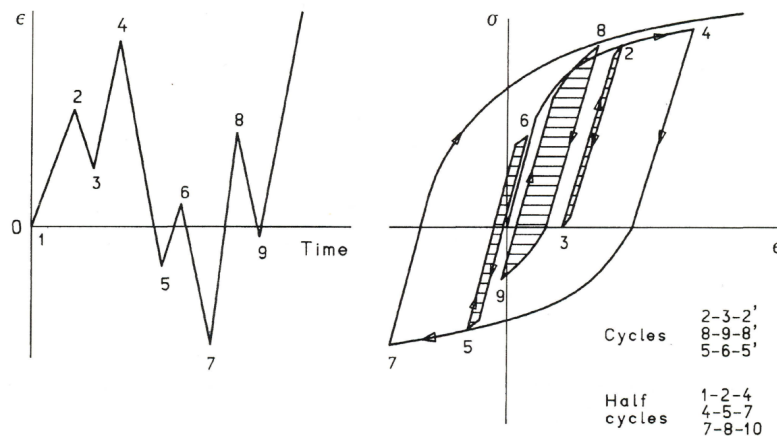


Figure 2.13: Strain time series and stress-strain response. The figure is from [27].

The rainflow counting method has gotten its name from an analogy of rain flowing down a pagoda roof. Fig. 2.14 illustrates the pagoda roof rainflow analogy with the same strain time series as illustrated in Fig. 2.13, but rotated 90 degrees.

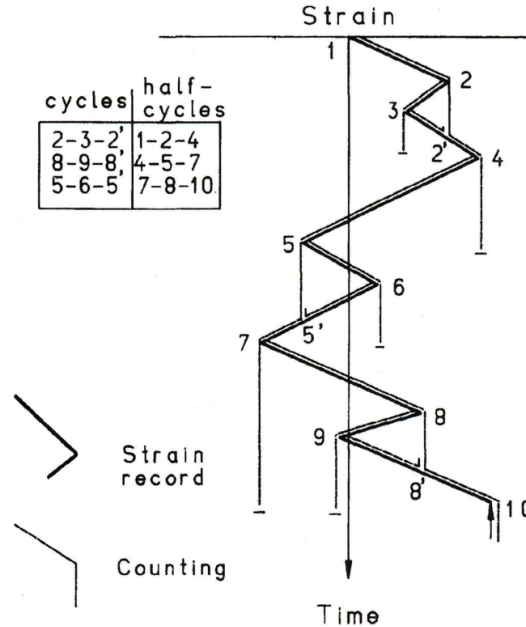


Figure 2.14: Pagoda roof rainflow analogy. The figure is from [27].

The rainflow counting technique can be described by three rules as listed in [27]:

1. Rain will flow down the roof initiating at the inside of each peak or valley. When it reaches the edge it will drip down.
2. The rain is considered to stop, and a cycle is completed, when it meets another flow from above.
3. Starting from a peak, the flow also stops when it comes opposite a more positive peak than that from which it started. Starting from a valley, the flow stops when it comes opposite a more negative valley than that from which it started.

Fatigue design is based on constant amplitude S-N data, while a floating wind turbine is experiencing a stochastic load history due to waves, wind and current. In order to calculate the fatigue damage under stochastic loading, the Miner summation can be used. The assumption in the Miner summation procedure is that the damage on the structure for each cycle is constant at a given stress range and defined as:

$$D = \frac{1}{N}, \quad (2.23)$$

where  $D$  is the damage and  $N$  is the constant amplitude endurance for the stress range in consideration. When several stress ranges are present in the load spectrum, the failure criterion is

defined as  $D = 1$ , and the damage sum is calculated as:

$$D = \sum_i \frac{n_i}{N_i}, \quad (2.24)$$

where  $i$  is the number of stress ranges and  $n_i$  is the number of cycles with stress range  $\Delta S_i$ . The Miner summation procedure is also illustrated in Fig. 2.15.

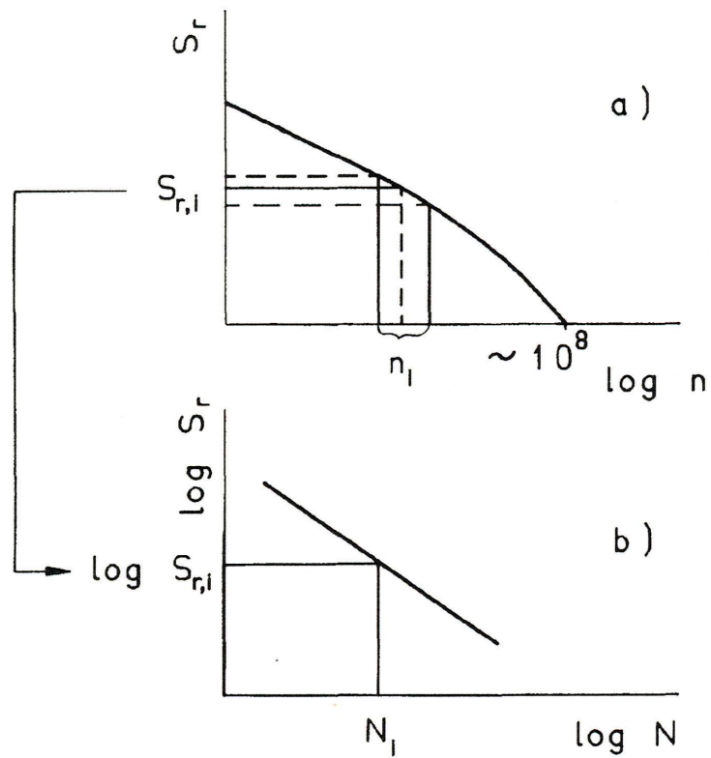


Figure 2.15: The Miner summation procedure. The figure is from [27].



## Chapter 3

# Prediction tools for vortex-induced vibrations/motions

The ability to predict VIV and VIM is important in design to reduce large safety factors and increased costs. There exists several prediction tools for VIV, both numerical and empirical. Some methods operate in the frequency domain (FD), while other operate in the time domain (TD). For VIM there is no existing pure VIM prediction tool, but the engineering practice is however relied on model tests, numerical studies and review of field measurements.

### 3.1 Existing vortex-induced vibration prediction models

To fully predict VIV it is essential to establish both a structural model as well as a hydrodynamic model. The structural model is representing the structural response due to the hydrodynamic forces. This is typically done by applying the well known and widely used finite element method (FEM). The hydrodynamic model is representing the loads acting on the structure. Some existing VIV prediction tools for the hydrodynamic model will be discussed in the following.

#### 3.1.1 Computational fluid dynamics

The flow around a circular cylinder can be analytically described by the Navier-Stokes equations. These equations are partial differential equations consisting of three momentum equations, which for an incompressible Newtonian fluid can be written with tensor notation as:

$$\frac{\partial u_i}{\partial t} + u_j \frac{\partial u_i}{\partial x_j} = -\frac{1}{\rho} \frac{\partial p}{\partial x_i} + \nu \frac{\partial^2 u_i}{\partial x_j^2} + f_i, \quad (3.1)$$

and the continuity equation as:

$$\frac{\partial u_i}{\partial x_i} = 0. \quad (3.2)$$

Here,  $u_i$  and  $u_j$  are the velocity components in the  $i$ - and  $j$ -direction respectively,  $x_i$  and  $x_j$  are the  $i$ - and  $j$ -direction respectively,  $p$  is the pressure and  $f_i$  is external forces. The Navier-Stokes

equations have never been solved analytically, due to their extreme complexity. However, they can be solved numerically, which forms the basis for the field of study known as computational fluid dynamics (CFD). In CFD, the Navier-Stokes equations are solved to calculate the entire flow field around the object under consideration. There exists several CFD methods, differing in how the domain is discretized and how the turbulence is modeled. Some examples of discretization methods are the finite difference method, the finite volume method and the finite element method. Regarding the turbulence modeling some examples are Reynolds-averaged Navier-Stokes (RANS), large eddy simulation (LES) and direct numerical simulation (DNS). The RANS models are mathematical models based on average values of variables for the flow and can again be divided into zero-equation models, one-equation models and two-equation models. An example of a zero-equation model is the mixing length model, examples of one-equation models are the  $k-l$  model and Spalart-Allmaras model, and examples of two-equation models are the  $k-\varepsilon$  model, the  $k-\omega$  model and the SST  $k-\omega$  model. DNS is listed as a turbulence model, but in fact the method does actually solve the Navier-Stokes equations directly without any specific turbulence model. Instead, the entire space and time domains are discretized, and requires an extremely fine mesh and small time step. LES is an average turbulence model where the filtered Navier-Stokes equations are used for the large-scale eddies, while an appropriate model is used for the smaller-scale eddies. The short introduction to CFD given above is meant to illustrate the complexity and width of the entire scientific discipline that is CFD.

CFD has been attempted applied as a method for VIV prediction in several studies, e.g. [28] and [29]. Both these studies conclude that two dimensional CFD simulations are less accurate than semi-empirical models, and it is therefore deduced that fully three dimensional CFD simulations are necessary to obtain results of high-quality. Such three dimensional simulations were conducted in [30] using DNS, and they provide realistic and detailed results for both the flow and structural response. CFD is therefore a promising prediction tool for VIV and other FSI problems. The drawback with CFD is however the huge computational cost. Even with state-of-the-art supercomputers the practical applications for the industry regarding VIV prediction are limited due to the extremely small resolution and time step needed to capture all scales in the vortex-shedding [31]. CFD is however a very useful and important research tool, and with the future increase in available computing power, CFD has great potential.

### 3.1.2 Semi-empirical frequency domain models

There exists several semi-empirical FD tools for VIV prediction and many of them are widely used in the offshore industry. Examples of such tools are VIVA [32], SHEAR7 [33], and VIVANA [18]. All of these three models uses hydrodynamic coefficients for the added mass, damping and excitation, which typically are found from forced oscillation experiments of rigid, circular cylinders. The coefficients are chosen from the database, corresponding to the non-dimensional oscillation frequency and amplitude for the cross section under consideration.

The FD models are useful and efficient for several types of analyses and hence they are popular and frequently used in the industry. Nevertheless, the models have their limitations and are not applicable for all types of analyses. In the FD the response can only be stationary and harmonic, and the structural model must be linearized. This linearization implies that any non-linearity cannot be handled by the FD models. For simple linear analyses, this is obviously not a problem, but the moment non-linearities are introduced, the FD models are unable to handle them and loses accuracy. Examples of non-linearities are time varying boundary conditions, e.g. seabed contact, large responses, tension variations and coupling between axial and lateral vibrations.

Another limitation with the FD models is that each frequency has to be considered individually. For cases with varying incoming velocity, e.g. sheared current, the interaction between different frequencies can be significant, but is not handled in the FD [34]. In addition, the FD models are having problems accounting for interaction with other dynamic external loads. In order to account for all these effects, a step-by-step time integration of the dynamic equilibrium equation must be performed. This is the basis for the TD models.

### 3.1.3 Empirical time domain models

There also exist some empirical TD models, which differs significantly from the FD models. Instead of operating in the FD, solving for the response at a given frequency, the TD models perform a stepwise time integration to simulate the response. In this way, the TD models can capture and simulate the non-linear effects. One example of such a model is ABAVIV [35], [36], where the presence of lock-in is determined from the predicted response at each time step. Before and after lock-in, the lift force oscillates with the Strouhal frequency, but as lock-in takes place, the force gradually changes its frequency towards being in phase with the cylinder velocity. Another empirical TD model was suggested by [37], which uses a neural network to predict the forces. The artificial intelligence was trained by a large database of rigid cylinder oscillation experiments. This method proved to give realistic predictions for several cases, but also experienced some serious stability issues.

A fundamentally different semi-empirical TD model is the wake oscillator [38]. There exist several variants of the wake oscillator as stated in [39], but the essence of the models builds on describing the lift force by a forced van der Poel equation. The differential equation can be written as

$$\frac{d^2q}{dt^2} + \epsilon\omega_s(q^2 - 1)\frac{dq}{dt} + \omega_s^2q = F, \quad (3.3)$$

where  $q$  is a single DOF dimensionless parameter describing the wake,  $\epsilon$  is a damping parameter and  $F$  is the external forcing. The parameter  $\omega_s$  is the Strouhal circular frequency defined as

$$\omega_s = 2\pi \frac{StU}{D}. \quad (3.4)$$

The van der Poel equation is able to capture the oscillating behaviour of the lift force which can be seen from the damping term in the equation. For  $q < 1$  the damping will be negative and increase the amplitude, while for a large  $q$  the damping will be positive and decrease the amplitude.

## 3.2 Semi-empirical time domain model VIVANA-TD for vortex-induced vibration prediction

In the recent years a very promising TD VIV model, VIVANA-TD, has been developed at NTNU. The model was first presented as parts of the PhD work of Thorsen in [40], and was further evolved with changes and improvements in his additional PhD publications [41], [42] and [43]. Later, the PhD work of Ulveseter, [44], [45], [46], [47], and Kim, [48], [49], [50] has also validated and improved the model.

### 3.2.1 Hydrodynamic load formulation

The TD VIV load model originates from the generalized Morison equation:

$$\mathbf{F} = C_M \rho \frac{\pi D^2}{4} \dot{\mathbf{u}}_n - (C_M - 1) \rho \frac{\pi D^2}{4} \ddot{\mathbf{r}}_n + \frac{1}{2} \rho D C_D |\mathbf{v}_n| \mathbf{v}_n, \quad (3.5)$$

where  $\mathbf{F}$  is the hydrodynamic force acting on the cylinder,  $C_D$  is the non-dimensional drag coefficient and  $C_M$  is the non-dimensional inertia coefficient, related to the non-dimensional added mass coefficient,  $C_A$ , as:

$$C_M = C_A + 1. \quad (3.6)$$

The parameter  $\dot{\mathbf{u}}_n$  is the fluid acceleration in the transverse direction,  $\ddot{\mathbf{r}}_n$  is the structure acceleration in the transverse direction and  $\mathbf{v}_n$  is the relative velocity in the transverse direction defined as:

$$\mathbf{v}_n = \mathbf{u}_n - \dot{\mathbf{r}}_n, \quad (3.7)$$

where  $\mathbf{u}_n$  is the fluid velocity in the transverse direction and  $\dot{\mathbf{r}}_n$  is the structure velocity in the transverse direction. The generalized Morison equation consists of three force contribution terms, that is the Froude-Kriloff force,  $\mathbf{F}_{FK}$ , defined as:

$$\mathbf{F}_{FK} = C_M \rho \frac{\pi D^2}{4} \dot{\mathbf{u}}_n, \quad (3.8)$$

the added mass force,  $\mathbf{F}_{M_a}$ , defined as:

$$\mathbf{F}_{M_a} = -(C_M - 1) \rho \frac{\pi D^2}{4} \ddot{\mathbf{r}}_n, \quad (3.9)$$

and the drag force,  $\mathbf{F}_D$ , defined as:

$$\mathbf{F}_D = \frac{1}{2} \rho D C_D |\mathbf{v}_n| \mathbf{v}_n. \quad (3.10)$$

The hydrodynamic load model is combining these force terms from the Morison equation with additional force terms from the vortex shedding, including both CF and IL contributions. Consequently, the model is based on strip theory and the incoming flow velocity,  $\mathbf{u}$ , should be decomposed into a component normal to cylinder axis,  $\mathbf{u}_n$ , and a component tangential to the cylinder axis,  $\mathbf{u}_t$ . The tangential component is neglected, as only the normal component gives a force contribution following strip theory. Fig. 3.1 shows a 3D cylinder strip in incoming flow as well as the velocity decomposition. Fig. 3.2 shows a cross section of the cylinder with local coordinate system and relevant vectors. The hydrodynamic force terms acting on the cross section are also shown.

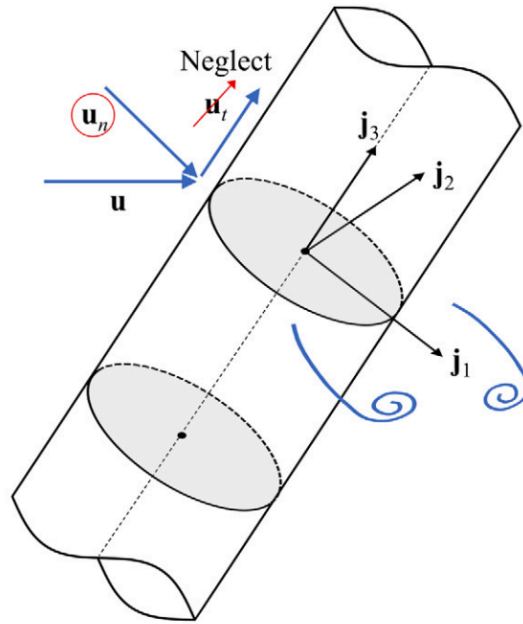


Figure 3.1: 3D cylinder strip in incoming flow. The figure is from [48].

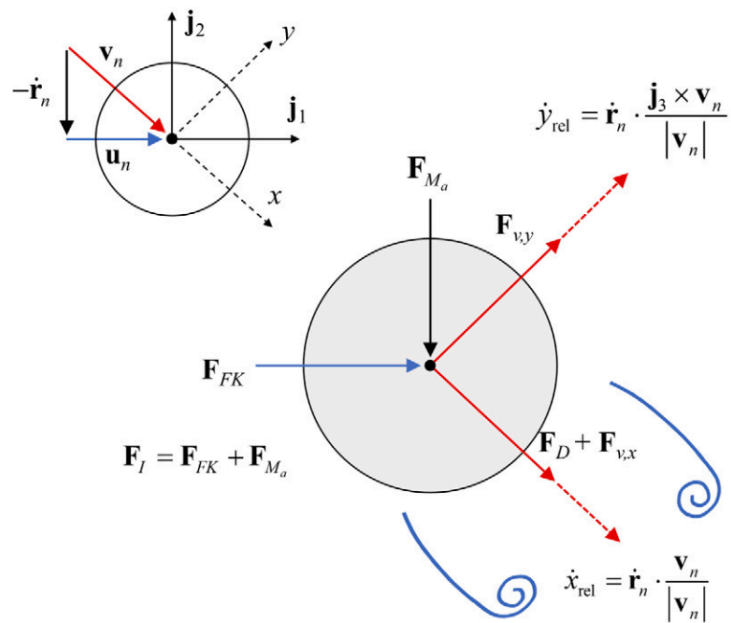


Figure 3.2: Hydrodynamic force terms at the cylinder cross-section. The figure is from [48].

The total hydrodynamic load model including both CF and IL vortex shedding terms is formulated as:

$$\begin{aligned}
 \mathbf{F}_n = & \underbrace{\underbrace{C_M \rho \frac{\pi D^2}{4} \dot{\mathbf{r}}_n}_{\text{Froude-Kriloff force}} - \underbrace{(C_M - 1) \rho \frac{\pi D^2}{4} \ddot{\mathbf{r}}_n}_{\text{Added mass force}} + \underbrace{\frac{1}{2} \rho DC_D |\mathbf{v}_n| \mathbf{v}_n}_{\text{Drag force}}}_{\text{Morison's equation}} \\
 & + \underbrace{\frac{1}{2} \rho DC_{v,x} |\mathbf{v}_n| \mathbf{v}_n \cos \phi_{exc,x}}_{\text{IL vortex shedding force}} + \underbrace{\frac{1}{2} \rho DC_{v,y} |\mathbf{v}_n| (\mathbf{j}_3 \times \mathbf{v}_n) \cos \phi_{exc,y}}_{\text{CF vortex shedding force}} \\
 & \underbrace{\hspace{10em}}_{\text{Vortex shedding force}}
 \end{aligned} \tag{3.11}$$

where the parameters  $\phi_{exc,x}$  and  $\phi_{exc,y}$  are the IL and CF instantaneous phases of the vortex shedding forces respectively, and  $\mathbf{j}_3$  is the unit vector in the axial direction of the cylinder. The first three terms constitute the Morison equation and the last two terms are the additional vortex shedding terms, and hence the equation can be written as:

$$\mathbf{F}_n = \mathbf{F}_{FK} + \mathbf{F}_{Ma} + \mathbf{F}_D + \mathbf{F}_{v,x} + \mathbf{F}_{v,y}, \tag{3.12}$$

where  $\mathbf{F}_{v,x}$  is the IL vortex shedding force defined as:

$$\mathbf{F}_{v,x} = \frac{1}{2} \rho DC_{v,x} |\mathbf{v}_n| \mathbf{v}_n \cos \phi_{exc,x}, \tag{3.13}$$

and  $\mathbf{F}_{v,y}$  is the CF vortex shedding force defined as:

$$\mathbf{F}_{v,y} = \frac{1}{2} \rho DC_{v,y} |\mathbf{v}_n| (\mathbf{j}_3 \times \mathbf{v}_n) \cos \phi_{exc,y}. \tag{3.14}$$

The CF vortex shedding force corresponds to a lift force in the local y-direction which is normal to the relative flow vector  $\mathbf{v}_n$ . The IL vortex shedding force corresponds to a drag force in the local x-direction which is equal to relative flow vector direction,  $\mathbf{v}_n$ . It should be noted that the vortex shedding forces are in phase with the relative structure velocities in local x- and y-direction. The relative structure velocity in local x-direction is defined as:

$$\dot{x}_{rel} = \dot{\mathbf{r}}_n \cdot \frac{\mathbf{v}_n}{|\mathbf{v}_n|}, \tag{3.15}$$

and the relative structure velocity in local y-direction is defined as:

$$\dot{y}_{rel} = \dot{\mathbf{r}}_n \cdot \frac{\mathbf{j}_3 \times \mathbf{v}_n}{|\mathbf{v}_n|}. \tag{3.16}$$

### 3.2.2 Synchronization of vortex shedding forces

An essential part of the TD VIV model is the synchronization of the vortex shedding forces. This synchronization model is capturing the phase coupling between force and response to account for the lock-in phenomenon. For the model to obtain lock-in, the vortex shedding frequency is changed to match the frequency of the relative structure velocity. This is illustrated in Fig. 3.3 for CF synchronization for both slow down and speed up. When the phase angle of the vortex shedding force is in front of the phase angle for the relative structure velocity, the instantaneous vortex

shedding frequency is reduced. This is the case termed slow down and is done to minimize the phase difference. The opposite case is termed speed up and has the same objective of minimizing the phase difference. For this case the phase angle of the vortex shedding force lags behind the phase angle of the relative structure velocity, and the instantaneous vortex shedding frequency is increased.

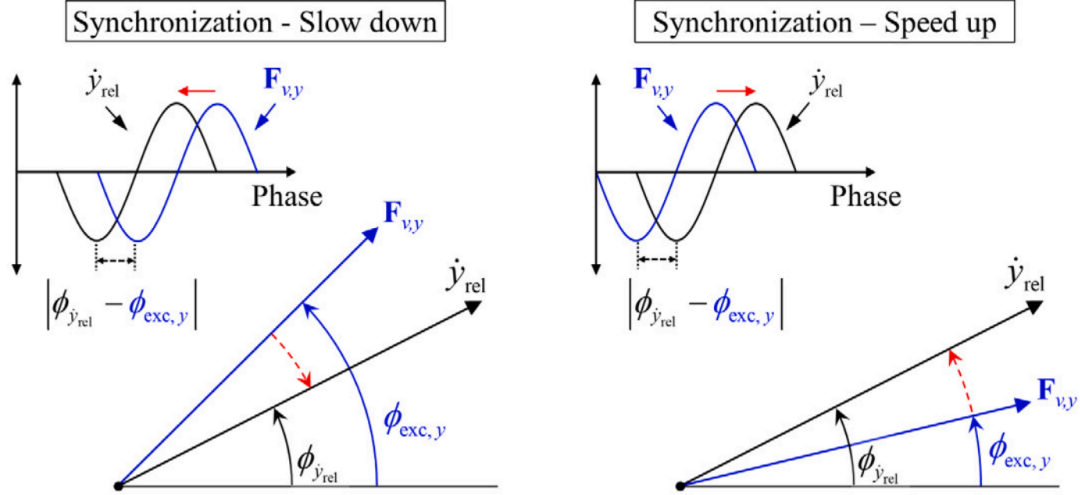


Figure 3.3: Phase angle relationship between CF vortex shedding force and relative structure velocity in local  $y$ -direction for CF synchronisation. The figure is from [48].

An important feature of the synchronization model is the requirement for synchronization to only happen within the synchronization range. The synchronization range is determined by experimental data and the resulting synchronization function for CF is illustrated in Fig. 3.4.

The relationship between the instantaneous frequency and the phase angle is given as:

$$\frac{d\phi_{exc,y}}{dt} = 2\pi f_{exc,y} = \frac{2\pi|\mathbf{v}_n|}{D} \hat{f}_{exc,y}, \quad (3.17)$$

where  $\hat{f}_{exc,y}$  is defined as:

$$\hat{f}_{exc,y} = \hat{f}_{0,y} + \Delta\hat{f}_y \sin\theta_y, \quad (3.18)$$

and  $\theta_y$  is the phase difference between CF cylinder velocity and CF vortex shedding force defined as:

$$\theta_y = \phi_{\dot{y}_{rel}} - \phi_{exc,y}. \quad (3.19)$$

Here,  $\Delta f_y$  is CF synchronization range and  $\hat{f}_{0,y}$  is the non-dimensional frequency of maximum energy transfer in the CF direction. The CF cylinder velocity is approximated numerically at each time step. Similarly for the IL responses, the relationship between the instantaneous frequency and the phase angle is given as:

$$\frac{d\phi_{exc,x}}{dt} = 2\pi f_{exc,x} = \frac{2\pi|\mathbf{v}_n|}{D} \hat{f}_{exc,x}, \quad (3.20)$$

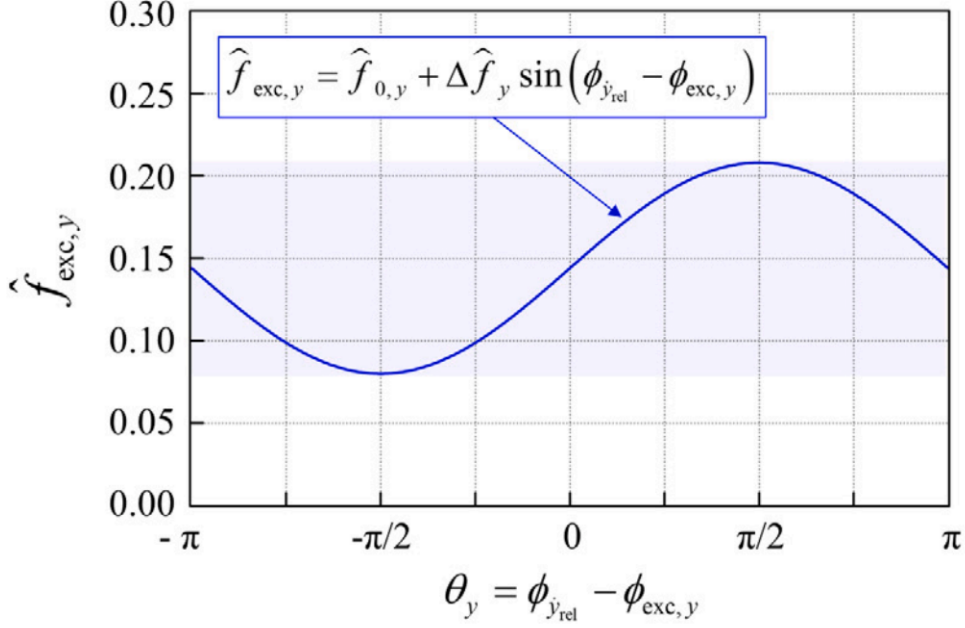


Figure 3.4: CF synchronization function. The figure is from [48].

where  $\hat{f}_{exc,x}$  is defined as:

$$\hat{f}_{exc,x} = \hat{f}_{0,x} + \Delta \hat{f}_x \sin \theta_x, \quad (3.21)$$

and  $\theta_x$  is the phase difference between IL cylinder velocity and IL vortex shedding force defined as:

$$\theta_x = \phi_{\dot{x}_{rel}} - \phi_{exc,x}. \quad (3.22)$$

Here,  $\Delta f_x$  is IL synchronization range and  $\hat{f}_{0,x}$  is the non-dimensional frequency of maximum energy transfer in the IL direction.

### 3.3 Engineering practice for vortex-induced motion prediction

There is no well-established analytical prediction tool for VIM response, although the industry is in need of an accurate and consistent method for VIM prediction in order to ensure integrity of floating structures while keeping the costs down. The current engineering practice is typically based on model tests which can be used to calibrate numerical methods. For the rare cases where full-scale field measurements are available, these can also be used in design to improve VIM prediction. A practical and often used method for VIM design criterion is the VIM design curve. A typical VIM design curve is shown in Fig. 3.5. This curve gives the design amplitude ratio,  $A/D$ , as a function of reduced velocity.



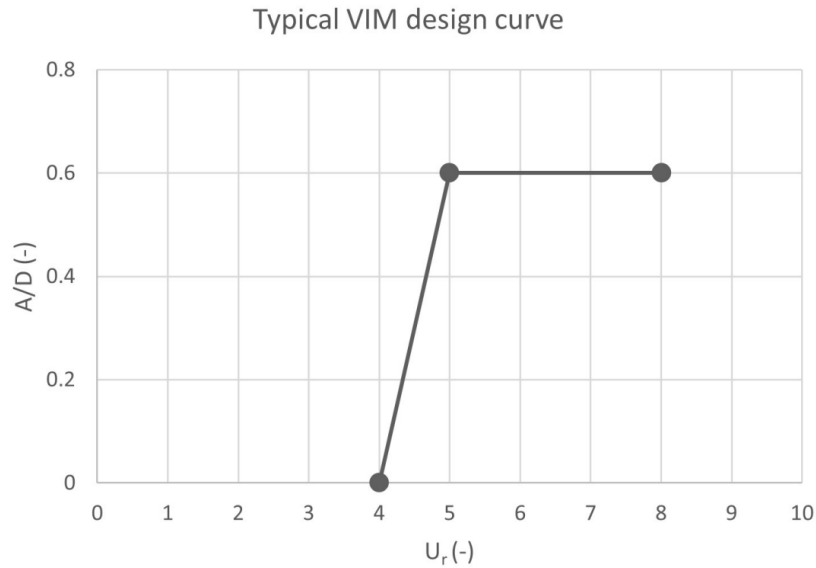


Figure 3.5: A typical VIM design curve. The figure is from [1] which adapted it from [51].

### 3.3.1 Regulations and recommended practice

The existing regulations and recommended practice regarding VIM are fragmentary and there is no available framework purely dedicated for VIM. However, VIM is partially treated in several documents including, but not limited to:

- DNV-RP-C205 Environmental Conditions and Environmental Loads [52]. This recommended practice includes guidance and information on environmental loads and conditions such as current modelling, including VIV and VIM.
- DNV-ST-0119 Floating wind turbine structures [53]. This standard specifies general principles and requirements for the structural design of floating wind turbine structures.
- ISO19901-7 Specific requirements on stationkeeping systems for floating offshore structures and mobile offshore units [54]. This document specifies methodologies and requirements for the design, analysis and evaluation of stationkeeping systems for floating structures.

### 3.3.2 Model tests

Model testing is recommended in design of floating structures to determine VIM response in terms of amplitude, frequency and drag coefficient, and is frequently used due to the lack of analytical methods. The model tests are typically separated in two categories, i.e. sub-critical Reynolds number model tests and super-critical Reynolds number model tests, and are carried out in a towing tank. Both experiments with surface piercing models floating vertically, or fully submerged models positioned vertically or horizontally are relevant for VIM response. During the development of floating offshore structures, especially by the oil and gas industry in the last decades, and more recently by the renewable energy industry, extensive VIM model testing has been carried out. A recently published state-of-the-art review of VIM is diving in to the literature and presents obtained knowledge from VIM model testing over the years [1].

### 3.3.3 Numerical studies

Numerical studies are sometimes used for VIM prediction, but compared to model testing the use is very limited. Some numerical studies have been carried out on FWTs in the recent years and the most notable are presented in the state-of-the-art review of VIM [1]. CFD has been used for VIM prediction especially for simpler structures such as a spar-type floater. Most of the CFD application comes from recent years due to the high demand of computational power during simulations, and even then the grid resolution has been relatively coarse. Some CFD publications focusing on VIM on spar-type floaters are also discussed in the state-of-the-art-review of VIM [1].

### 3.3.4 Review of field measurements

Full-scale field measurements, when available, offers a great way to validate numerical simulations or check scaling effects from experimental model tests. However, not many field measurements are published or even exists. Some of the measurements that are published are presented in the state-of-the-art review of VIM [1]. This includes full-scale measurements from the Hywind Scotland wind park which are obtained as a part of this thesis and will be presented in Ch. 5.

## Chapter 4

# Modelling of floating wind turbine concept

The Hywind Scotland 6 MW spar-type floating wind turbine is the concept to be analyzed in this thesis. This specific floating wind turbine concept is however only an exemplification of the wide range of concepts on which the TD VIV model potentially can be used to predict VIM. It is expected that the TD VIV model produces similar results for similar spar-type floating wind turbine concepts, but further research on the topic is highly recommended. The SIMA workbench, containing the software packages SIMO and RIFLEX among others, was used for modelling the floating wind turbine and running the TD VIV analyses. SIMA is developed by SINTEF Ocean and is a simulation and analysis tool for marine operations and floating systems. It covers the entire process from modelling to interpretation and documentation of results. In the current chapter, an introduction to the Hywind Scotland spar-type floating wind turbine concept and the software used for modelling and analysis, as well as the methodology for the modelling procedure, will be given.

### 4.1 Hywind Scotland wind turbine description

The world's first floating wind park, Hywind Scotland, has already over 5 years in operation since the electricity production began in October 2017 [55]. The 30 MW wind park is located around 25 km off the coast of Peterhead in Aberdeenshire north-east in Scotland and consists of 5 turbines, each rated at 6 MW. Fig. 4.1 illustrates the location and layout of the wind park, as well as some main dimensions for a unit. The turbines are placed in two rows going approximately northwest-southeast where the units have a distance of nine rotor diameters to each of their neighbouring units. The rotor diameter is 154 m with a hub height of 98 m above mean sea level. Siemens Wind Power (now Siemens Gamesa Renewable Energy) delivered the turbines of model SWT-6.0-154 with a top head mass of approximately 400 tons. The steel substructure is a spar-type floater with a diameter of 14.4 m at the keel and 9.45 m at the base of the tower. The total height of the floater is 85 m with a draft of approximately 78 m. Fig. 4.2 provides a simple sketch of the floater geometry and dimensions. The unit is ballast-stabilized and the total structure has a displacement

of around 11 200 tons. Each floater is moored by three mooring chains connected to the seabed by suction anchors. To provide sufficient yaw stiffness, each mooring chain is connected to the floater by two bridles as shown in Fig. 4.3. The complete mooring arrangement from floater to suction anchor with corresponding terminology is also illustrated. Tab. 4.1 provides a summary of the approximate main properties of the Hywind Scotland wind turbine, floating substructure and mooring configuration for any of the FWTs in the wind park. The individual properties of each unit installed on site can vary slightly from these values.

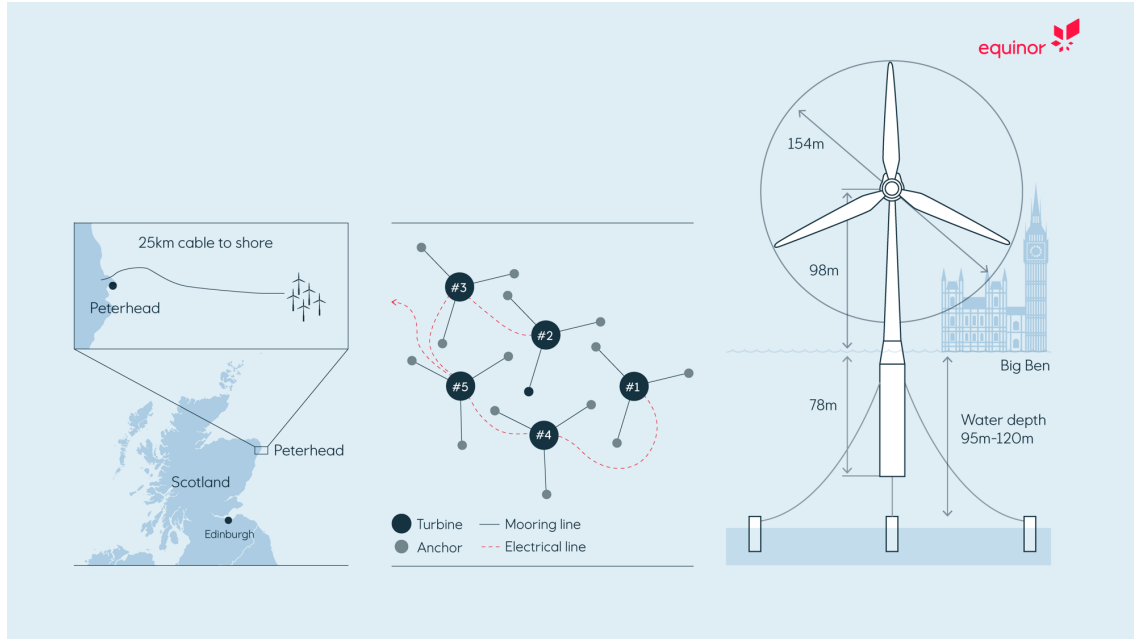


Figure 4.1: The Hywind Scotland wind park. The figure is from [56].

Table 4.1: Main properties of a Hywind Scotland wind turbine, floating substructure and mooring configuration. The table is adapted from [57].

Parameter	Value
Displacement	~ 11 200 tons
Draft hull	~ 78 m
Water depth	95-120 m
Diameter at keel	14.4 m
Anchor	Suction anchor
Mooring	3 lines with crowfoot
Maximum power	6 MW
Number of blades	3
Rotor diameter	154 m
Hub height	~ 98 m
Top head mass	~ 400 tons

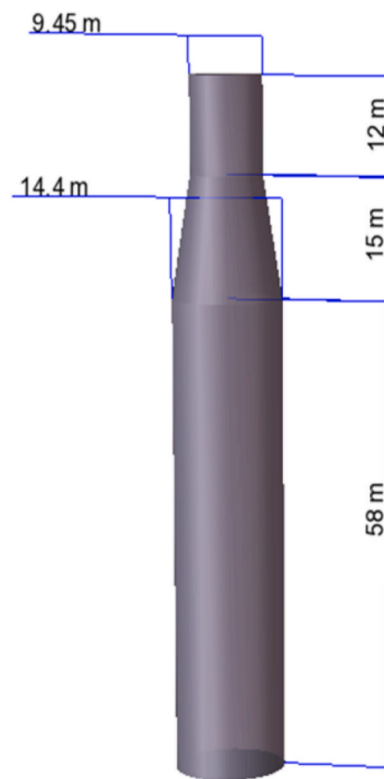


Figure 4.2: Hywind Scotland floater geometry. The figure is from [58].

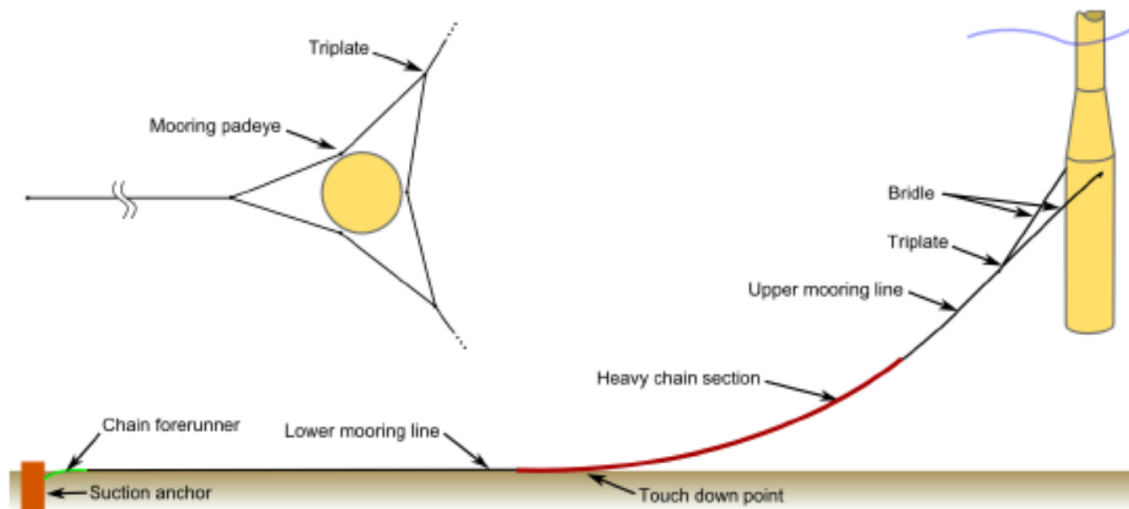


Figure 4.3: Mooring arrangement for the Hywind Scotland wind turbines. The figure is from [59].

One specific unit in the Hywind Scotland wind park is chosen to be modelled as accurately as possible in SIMA. This unit is the one marked #4 in Fig. 4.1, also referred to as HS4 for Hywind Scotland 4. HS4 is the southern most unit in the wind park and has one mooring line going directly in the southern direction, while the two other lines are evenly spread out with 120 degrees between each of the lines. This specific unit is chosen because full-scale measurements are provided by the operator Equinor along with more specific properties and characteristics of the different components [60]. Dynamic properties of the complete HS4 structure including substructure, tower, wind turbine and mooring system are listed in Tab. 4.2.

Table 4.2: Properties of the complete HS4 structure including wind turbine, tower, substructure and mooring system. The table is adapted from [60].

Property	Value		
Draft [m]	77.6		
Displacement [tons]	11 754		
Dry mass [tons]	11 483		
Mooring tension [tons]	270.9		
	X	Y	Z
Center of gravity [m]	-0.14	0	-50.03
Center of buoyancy [m]	0	0	-42.04
Eigenperiod surge [s]	96		
Eigenperiod sway [s]	96		
Eigenperiod heave [s]	25.8		
Eigenperiod roll [s]	33.7		
Eigenperiod yaw [s]	13.0		

Additional properties of the mooring system are also provided. In the initial condition the vertical load from the whole system is approximately 2660 kN. The tension in the upper end of a bridle is approximately 590 kN and the tension in the upper end of the main line is approximately 760 kN. The mooring system properties are given in Tab. 4.3. The geometry provided in the table is for an idealized system for all the FWTs in the wind park, and is not adjusted for the actual installed values for the HS4 unit which is the one to modelled in this work. The idealized system is producing higher tension in "Line 1, bridle 1" and "Line 3, bridle 2" compared to measurements. The line and bridle naming is illustrated in Fig. 4.4. For the other bridles, the agreement is good.

Table 4.3: Properties of the mooring system. The table is adapted from [60].

Property	Value	
Water depth [m]	100	
Radius of the anchors [m]	640	
Draft of mooring point [m]	20.6	
Number of lines	3	
Connection point outside wall [m]	0.8	
Segment name	Bridle	Main line
Segment length [m]	50	609.7
Nominal diameter [mm]	132	147
Young's modulus [MPa]	53 941	43 624
Segment dry mass per meter [kg/m]	348.5	432.2
Weight in water per meter [kN/m]	3.4030	3.8707

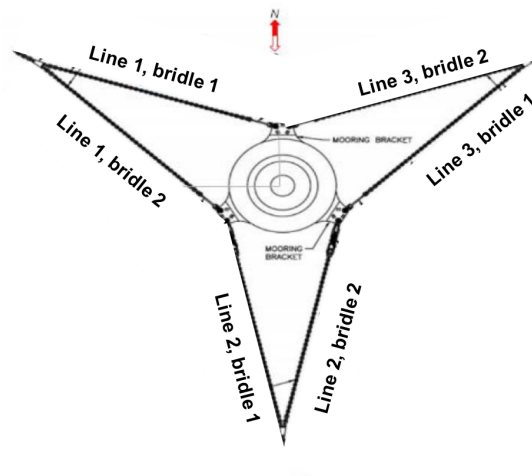


Figure 4.4: Naming of lines and bridles in the mooring system. The figure is from [60].

## 4.2 Software

The main software used to model and analyze the FWT concept with the TD VIV model was the SIMA software workbench. SIMA is developed by SINTEF Ocean and is a simulation and analysis tool for marine operations and floating systems. It covers the entire process from modelling to interpretation and documentation of results, and contains the software packages SIMO and RIFLEX, among others. These two packages are the ones utilized from the SIMA workbench in the modelling and analysis procedure are introduced in the following. In addition, the TurbSim software was used to generate input wind files for the analysis and is also introduced below.

### 4.2.1 SIMO

SIMO is a software package integrated into the SIMA workbench developed by SINTEF Ocean. SIMO is used for simulation of motions and station-keeping behaviour of complex systems consisting of floating vessel as well as suspended loads. It includes key features such as flexible modelling of multibody systems, nonlinear TD simulation of wave frequency and low frequency forces, environmental forces from wind, waves and current as well as active and passive control forces. The program is built up by five modules communicating via a shared file system as shown in Fig. 4.5. Details on the SIMO software package can be found in the user guide [61] and theory manual [62].

SIMO	INPMOD	File system for communication between modules	Input generation and presentation, interface to external sources of data
	STAMOD		Read input data, static analyses, define initial condition
	DYNMOD		Dynamic analyses, generation of time series
	OUTMOD		Post-processing of time series
	S2XMOD		Export of time series

Figure 4.5: Overview of SIMO modules and structure. The figure is from [61].

### 4.2.2 RIFLEX

RIFLEX is a software package implemented in SIMA for analysis of slender marine structures such as flexible risers, mooring lines, fish cage systems, pipelines, steel risers, power cables and more. Slender structures are characterized by:

- Small bending stiffness
- Large deflection
- Nonlinear cross section properties
- Complex cross section structure
- Large upper end motion excitation

RIFLEX can calculate both static and dynamic properties of the structure in consideration. The static analysis consists of an equilibrium configuration as well as parameter variations of position or tension, current velocity and direction. The dynamic analysis consists of an eigenvalue analysis giving the natural frequencies and mode shapes. It also gives response to harmonic motion and wave excitation or irregular wave and motion excitation. RIFLEX is built on a nonlinear finite element formulation, and includes key features such as nonlinear time domain solution and cross section properties as well as flexible modelling of both simple and complex systems. The program consists of five modules, similar to SIMO. The five modules communicate via a shared file system as shown in Fig. 4.6. Details on the RIFLEX software package can be found in the user guide [63], theory manual [64] and input reference [65].

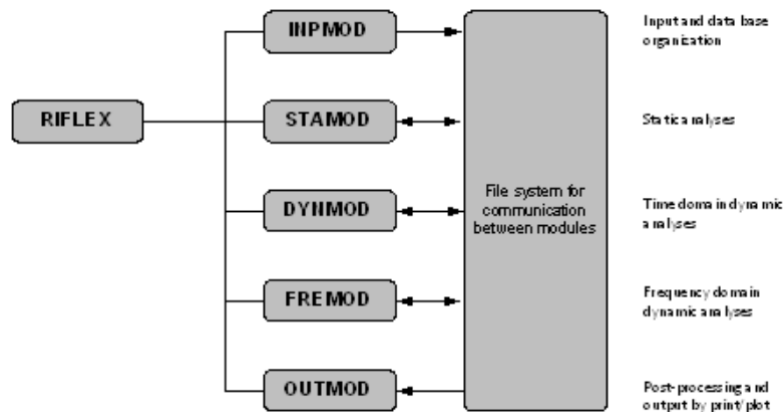


Figure 4.6: Overview of RIFLEX modules and structure. The figure is from [65].

### 4.2.3 TurbSim

TurbSim is a stochastic, full-field, turbulence simulator used to generate wind fields to input in simulation tools such as SIMA. The TurbSim software was developed by Kelley and Jonkman of the National Renewable Energy Laboratory, and is a flexible tool allowing to simulate wind fields with several customizable parameters, including the turbulence model. The program is command prompt operated and requires a text input files containing the user defined input parameters. An example input file can be found in App. A. Details on TurbSim can be found in the user guide [26].



### 4.3 Modelling procedure

The Hywind Scotland spar-type floating wind turbine was modelled using a combination of the SIMO and RIFLEX modules introduced in the previous sections. The different parts of the FWT are modelled as either SIMO bodies or RIFLEX elements.

#### 4.3.1 Spar floater and tower structure

The spar floater and tower is modelled as RIFLEX beam elements with axisymmetric cross sections. The RIFLEX beam element has six degrees of freedom at each node, three translational and three rotational. These nodal degrees of freedom are illustrated in Fig. 4.7. The main assumptions defining the RIFLEX beam elements are [64]:

- A plane section of the beam which initially is normal to the x-axis, remains plane and normal to the x-axis during deformations.
- Lateral contraction caused by axial elongation is neglected.
- The strains are small.
- Shear deformations due to lateral loading are accounted for by modifying the bending stiffness.
- St. Venant torsion model is applied.
- Torsional warping resistance is neglected.
- Coupling between torsion and bending is accounted for by a second order approximation of torsion and bending curvature, however, the coupling is not reflected in the stiffness matrix.

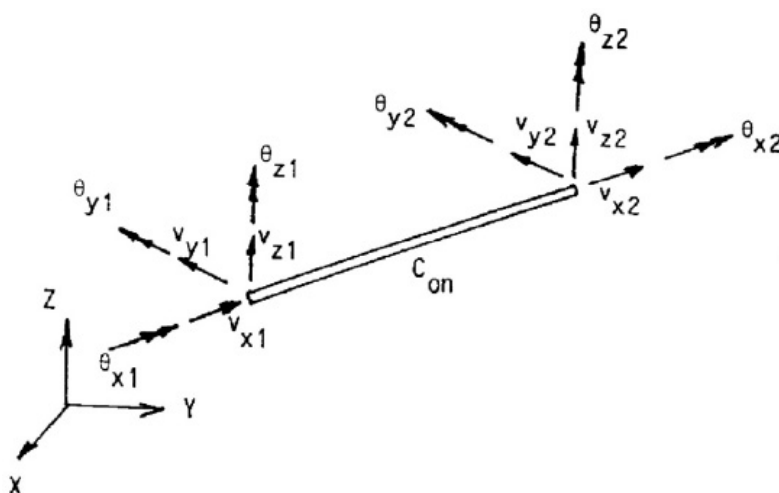


Figure 4.7: Nodal degrees of freedom for a RIFLEX beam element. The figure is from [64].

These RIFLEX elements with axisymmetric cross sections are circular and have a constant diameter. The Hywind Scotland spar floater does however have a conical frustum section where the diameter is changing over a certain height of the floater. This sections can be seen in Fig. 4.2. To model this section the diameter at the top and bottom is used to generate the average diameter over section. This average diameter is then used over the whole conical frustum section. In the transition of the spar-floater to the tower, another conical frustum section exists which is modelled in the same way. The complete tower structure is also a conical frustum section in itself. This is however modelled as 10 different section with constant diameter. The diameters are found by taking the diameter at the top and bottom of the tower and interpolating the average diameter over each of the 10 sections. Each section of the spar floater and tower structure is also divided into elements. The spar sections are modelled with an elements length 1.0 m to capture the vortex shedding on the structure accurately. The tower sections are modelled with larger element lengths as these are not submerged in water and experience vortex shedding from the ocean current. By increasing the elements length the computational time is reduced, and throughout the whole modelling process a trade-off between accuracy and computational cost has to be done. It should also be noted that the structure is modelled to never have sections were the adjacent elements increase or decrease with a factor greater then two. The total modelled spar floater and tower structure is listed in Tab. 4.4. The sections are listed from top top to bottom of the structure, i.e. Tower10 is located at the top of the tower and Spar1 is located at the bottom of the spar floater.

Table 4.4: Spar floater and tower structure modelled in SIMA.

Section	Diameter [m]	Section length [m]	Number of elements	Element length [m]
Tower10	4.20	8.3	1	8.3
Tower9	4.57	8.3	1	8.3
Tower8	4.93	8.3	1	8.3
Tower7	5.30	8.3	1	8.3
Tower6	5.67	8.3	1	8.3
Tower5	6.03	8.3	1	8.3
Tower4	6.40	8.3	1	8.3
Tower3	6.77	8.3	2	4.15
Tower2	7.13	8.3	3	2.77
Tower1	7.50	8.3	5	1.66
Transition	8.475	5.6	6	0.93
Spar3	9.45	12	12	1.0
Spar2	11.925	15	15	1.0
Spar1	14.4	58	58	1.0
Total	-	173.6	108	-

Hydrodynamic force coefficients for drag and added mass are determined for each floater section. All of the coefficients are non-dimensional and the hydrodynamic diameters are taken to be the same as the outer diameters of the modelled cross sections. The quadratic drag coefficients are used over the linear. The coefficients are defined in a local coordinate system where the x-direction is tangential to the cross section and the y-direction is normal to the cross section. Fig. 4.8 illustrates the axisymmetric cross section coordinate system definition. The quadratic drag coefficients in the normal direction,  $CQ_y$ , are obviously dependent on the Reynolds number, surface roughness and other factor, but are taken to be 1.0 for simplicity and consistency for all the spar sections and the transition section to the tower. In the tangential direction, the quadratic drag coefficients,  $CQ_x$ ,

are initially taken to be zero for all sections. However, the effect of the bottom, as well as the discs were two sections of different diameters are adjacent, have to be taken into account. These effects are implemented into the quadratic drag coefficients in the tangential direction. The drag force on a the bottom,  $F_{bottom}$ , is calculated as:

$$F_{bottom} = \frac{1}{2}\rho A_{bottom}v^2, \quad (4.1)$$

where  $A_{bottom}$  is the area of the spar-bottom, and  $v$  is the velocity of the spar relative to the fluid. The drag force on the disc between two sections with different diameter,  $F_{disc}$ , can be found as:

$$F_{disc} = \frac{1}{2}\rho(A_{large} - A_{small})v^2, \quad (4.2)$$

where  $A_{large}$  is the area of the largest cross section and  $A_{small}$  is the area of the smallest cross section. The tangential drag force on the cylinder section without any end effects,  $F_{cylinder}$ , can be found as:

$$F_{cylinder} = \frac{1}{2}\rho C_D A_{surface}v^2, \quad (4.3)$$

where  $A_{surface}$  is the total surface area of the cylinder in contact with water, excluding the ends, and can be found as:

$$A_{surface} = \pi DL, \quad (4.4)$$

where  $D$  is the diameter of the cross section and  $L$  is the length of the section. The quadratic drag coefficient in the tangential direction,  $CQ_x$ , for spar section 1, incorporating the effects of the bottom and the disc, can then be found as:

$$CQ_x = \frac{F_{bottom} + F_{disc}}{2 \cdot F_{cylinder}}. \quad (4.5)$$

The factor 2 comes from fact that only the disc or the bottom is contributing to the tangential drag at a time, depending on whether the spar is moving up or down in the water. To account for this, the two contributions are simply averaged.

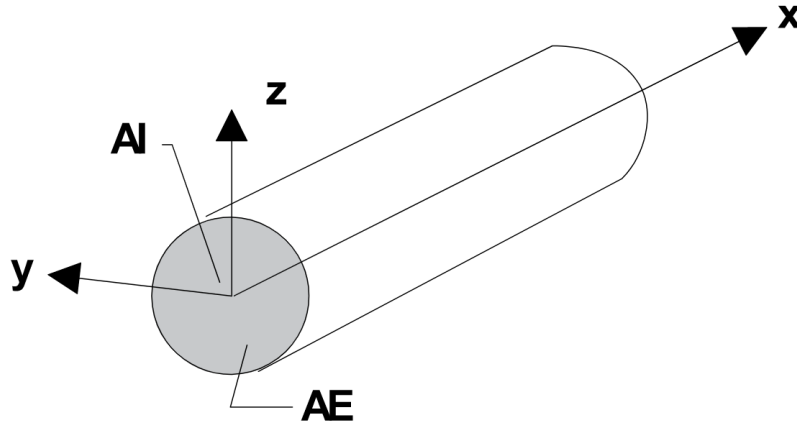


Figure 4.8: Definition of axisymmetric cross section coordinate system. The figure is from [65].

For spar section 2, a similar effect has to be taken into account, however, for this section only the disc at the top is contributing to the tangential drag as the bottom effect and disc at spar section

1 is taken into account on the coefficient of spar section 1. The quadratic drag coefficient in the tangential direction for spar section 2 can be found as:

$$CQ_x = \frac{F_{disc}}{2 \cdot F_{cylinder}}. \quad (4.6)$$

Again, the factor 2 comes from the fact that the disc is only contributing to the tangential drag when the spar is moving in the upwards direction. For spar section 3 and the transition section, the disc at the top is above the mean surface, and is not contributing to the tangential drag, with the exception of fractions of time when the structure is experiencing large heave motion or large waves. This effect is neglected, and the quadratic drag coefficients in the tangential direction for these sections are taken to be zero.

The added mass coefficients in the normal direction,  $CA_y$ , like the drag coefficients, are dependent on several parameters, but taken to be 1.0 for simplicity and consistency for all spar sections in addition to the transition section. The added mass coefficients in the tangential direction,  $CA_x$ , does however have to take into account the added mass appearing from effect of the bottom and the submerged discs in the areas where sections of different diameters are adjacent. Fig. 4.9 illustrates the added mass from the bottom as well as the added mass from a heave plate. Although the spar floater of the Hywind Scotland wind turbine does not have heave plates, the principle for determining the added mass at the discs is the same. The theoretical added mass,  $m_a$ , for the spar with the heave plate is given as:

$$m_a = \frac{1}{3}\rho D_s^3 - \left( \frac{1}{6}\rho D_s^3 - (D_s^2 - D_d^2)\sqrt{D_s^2 - D_d^2} \right), \quad (4.7)$$

where  $D_s$  is the diameter of the heave plate and  $D_d$  is the diameter of the spar. The relation:

$$m_a = \frac{1}{3}\rho D_s^3, \quad (4.8)$$

is the added mass of a submerged plate, assumed to be equivalent to the spherical volume enclosing the submerged plate. From this the added mass coefficients in the tangential direction for spar section 1 and 2 can be calculated, where spar section 1 includes the added mass from the bottom and first disc, and spar section 2 includes the added mass from the second disc. Spar section 3 and the transition section does not contribute to added mass in the tangential direction for the same reason as the drag coefficients. All the hydrodynamic force coefficients and diameters for the spar sections as well as the transition section can be found in Tab. 4.5.

Table 4.5: Hydrodynamic force coefficients for the spar floater.

Section	$CQ_x$	$CQ_y$	$CL_x$	$CL_y$	$CA_x$	$CA_y$	Hydrodynamic diameter [m]
Transition	0.0	1.0	0.0	0.0	0.0	1.0	8.475
Spar3	0.0	1.0	0.0	0.0	0.0	1.0	9.45
Spar2	0.0370	1.0	0.0	0.0	0.0187	1.0	11.925
Spar1	0.0408	1.0	0.0	0.0	0.0475	1.0	14.4

The nondimensional aerodynamic drag coefficient of the tower is varying significantly with different Reynolds number, i.e. wind speeds and tower diameters. The coefficient is however taken to be 0.5 for all tower sections for simplicity and consistency.

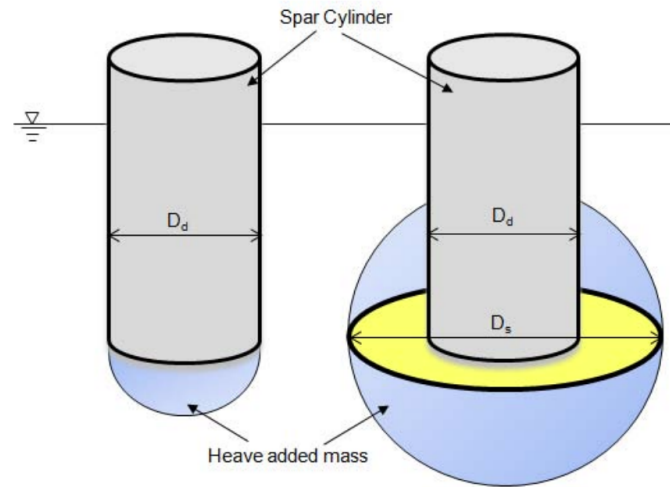


Figure 4.9: Heave added mass of spar with heave plate. The figure is from [66].

### 4.3.2 Mooring system

The mooring system is modelled as RIFLEX bar elements. The bar elements are assumed to be straight with an initial cross-sectional area,  $A_0$ , which is constant along the length of the element. Each of the two nodes of the element has three translational degrees of freedom, and no rotational degrees of freedom. This means the bar elements have zero bending stiffness and can only take loading the axial direction. This distinguishes the bar element from the beam element significantly. The element length is denoted  $L_0$  in the initial and  $L$  in deformed configuration, and Fig. 4.10 illustrates the RIFLEX bar element in an initial and deformed configuration.

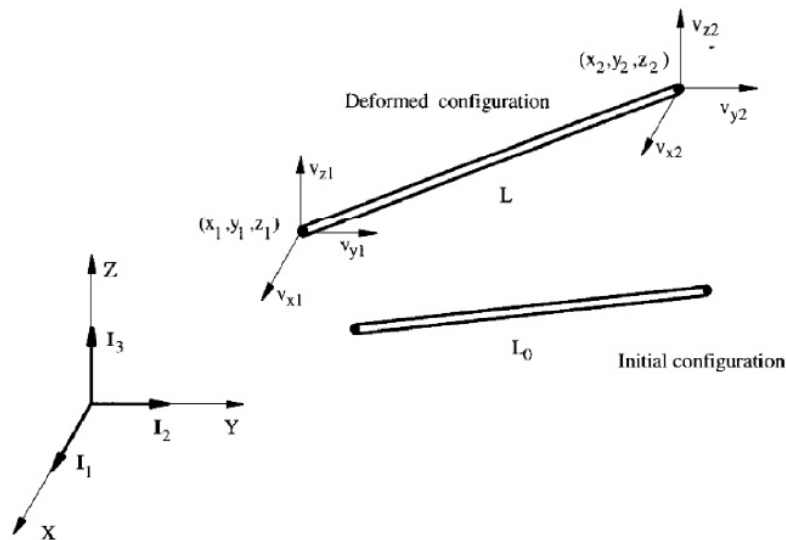
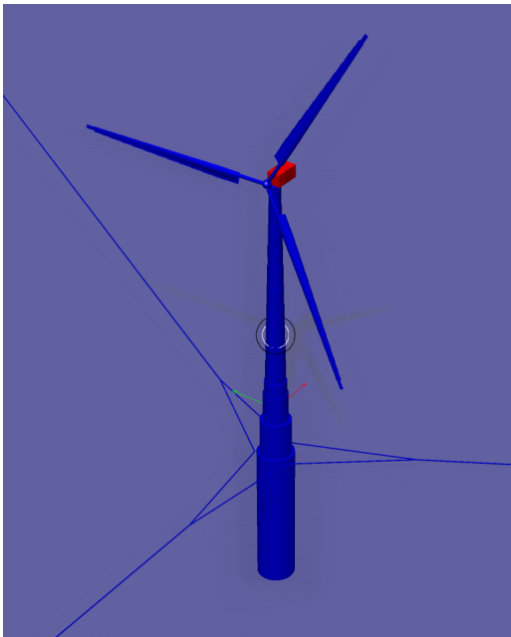
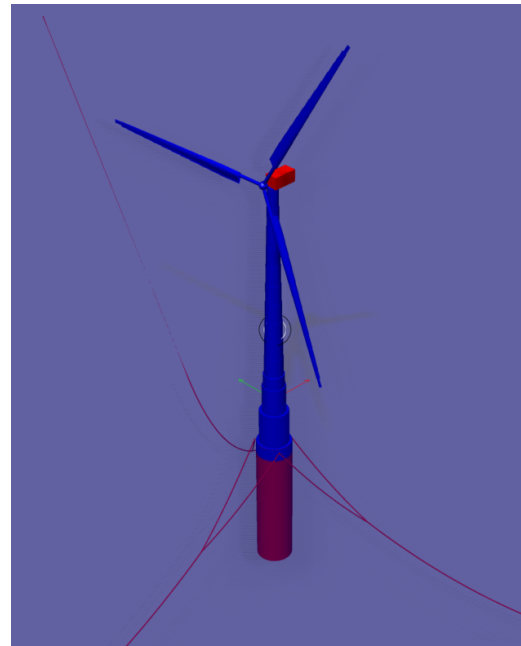


Figure 4.10: RIFLEX bar element in initial and deformed configuration. The figure is from [64].

The Hywind Scotland mooring system consists of three individual mooring lines connected to each floating wind turbine. Each line is anchored to the sea bed by a suction anchor, which is modelled as a fixed supernode in SIMA. The fixed anchor location is inputted as well as an initial position where the mooring line is completely straight. The initial position is necessary for the software to generate the mooring line. After the line is generated, the anchor is moved from the initial to the fixed position on the seabed in the static analysis. The modelled floating wind turbine before and after the static analysis can be seen in Fig. 4.11. The initial position of the mooring lines, where the lines are straight, can clearly be seen in Fig. 4.11a, while the physical position with all static forces applied and the anchor fixed to the seabed can be seen in Fig. 4.11b.



(a) The modelled floating wind turbine with mooring system before static analysis.



(b) The modelled floating wind turbine with mooring system after static analysis.

Figure 4.11: The modelled floating wind turbine with mooring system before and after static analysis.

Each mooring line consists of a main mooring line connected to the anchor at the seabed, as well as two bridles which are connected to the floating wind turbine. The bridles are connected in a crowfoot configuration to add yaw stiffness to the structure. The main mooring line and the bridles have different properties and are modelled accordingly in SIMA. The given mass coefficient is entered directly, while the axial stiffness is calculated from the cross sectional area and Young's modulus. The mooring system consists of studless steel chains and the given nominal diameter of the mooring lines is the diameter of the steel cross section of a chain link. This is 0.147 m for the main mooring line and 0.132 m for the bridles. The area used to calculate the axial stiffness is twice the area calculated from a circular cross section with the nominal diameter due to the layout of a chain link with equal cross sections on each side of the link. This area is also the modelled area of the bar elements.

The modelled mooring lines are divided into sections of different lengths to optimize the relation between accuracy and computational cost. Due to the long length of the mooring lines, small element lengths can quickly skyrocket the computational power needed for the analyses. However, a small element length is needed, especially in certain areas, to maintain good accuracy. It was desirable to have small element lengths in the proximity to connection points, i.e. close to the anchor, close to the connection between main mooring line and bridles, close to the connection between the bridles and the spar, and close to the seabed contact point. All of these areas are known point, except the seabed contact point. This point will move, potentially significantly, with the motions of the floating wind turbine. For this reason, a relatively large section of the mooring line is modelled with small elements here. This ensures that the movement of the mooring line on the seabed and transition to the water column is captured accurately. The complete list of mooring line sections with number of elements and element lengths can be found in Tab. 4.6 for the main mooring lines and in Tab. 4.7 for the bridles.

Table 4.6: Main mooring line element sections.

Section	Section length [m]	Number of elements	Element length [m]
Main1	10.0	10	1.0
Main2	2.9	1	2.0
Main3	4.0	1	4.0
Main4	8.0	1	8.0
Main5	4.0	1	4.0
Main6	2.0	1	2.0
Main7	370.0	370	1.0
Main8	2.0	1	2.0
Main9	4.0	1	4.0
Main10	8.0	1	8.0
Main11	171.7	11	15.609
Main12	8.0	1	8.0
Main13	4.0	1	4.0
Main14	2.0	1	2.0
Main15	10.0	10	1.0
Total	609.7	412	-

Table 4.7: Bridle element sections.

Section	Section length [m]	Number of elements	Element length [m]
Bridle1	10.0	10	1.0
Bridle2	10.0	5	2.0
Bridle3	10.0	3	3.3333
Bridle4	10.0	5	2.0
Bridle5	10.0	10	1.0
Total	50.0	33	-

The hydrodynamic force coefficients for drag and added mass of mooring liens are taken to be the same for the main mooring lines and the bridles. The hydrodynamic diameters of the mooring chains are taken to be  $0.9 \cdot 2d$ , where  $d$  is the nominal diameter. This is taking into account the chain geometry [67]. The added mass coefficient in the normal direction,  $CA_y$ , is taken be 1.0

and in the tangential direction,  $CA_x$ , it is taken to be 0.5. The quadratic drag coefficient in the normal direction,  $CQ_y$ , is taken to be 0.8, and in the tangential direction,  $CQ_x$ , it is taken to be zero. The linear drag coefficients,  $CL_x$  and  $CL_y$ , are taken to be zero. All the hydrodynamic force coefficients for the mooring lines as well as the hydrodynamic diameters are listed in Tab. 4.8.

Table 4.8: Hydrodynamic force coefficients for the mooring lines.

Line	$CQ_x$	$CQ_y$	$CL_x$	$CL_y$	$CA_x$	$CA_y$	Hydrodynamic diameter [m]
Main	0.0	0.8	0.0	0.0	0.5	1.0	0.2646
Bridle	0.0	0.8	0.0	0.0	0.5	1.0	0.2376

### 4.3.3 Turbine components

The wind turbine itself is modelled after the SIMA wind turbine specification found in [65]. The turbine is modelled by a group of lines that make up the blades and shaft of the wind turbine. An outline of the model can be found in Fig. 4.12. The supernode at the hub is the connecting point for the blades and the shaft. The shaft is modelled with RIFLEX elements and consists of two elements, one rotating, and one non-rotating. The connection between the two elements is made up of a flex-joint. An outline of the rotor and shaft system with local coordinate systems can be found in Fig. 4.13.

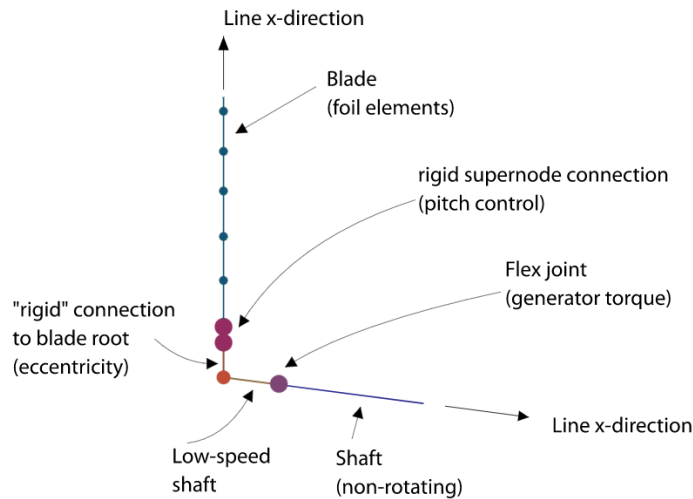


Figure 4.12: Outline of a wind turbine model in SIMA. The figure is from [65].

The hub and nacelle are modelled as 6 DOF - time domain SIMO bodies. That means the total motion of the bodies are simulated in the time domain and the bodies have six degrees of freedom. The hub is modelled as a sphere with radius 1.5 m, located at the top of the tower. The hub mass is free to rotate, but it should be noted that some of the hub mass is distributed to the shaft. The nacelle is modelled as a box with 10.0 m length, 5.0 m width and 5.0 m height, and is also placed at the top of the tower, but behind the hub. The modelled hub and nacelle arrangement can be found in Fig. 4.14. In this figure, the nacelle is red, the hub is pink and the tower and blades are green.



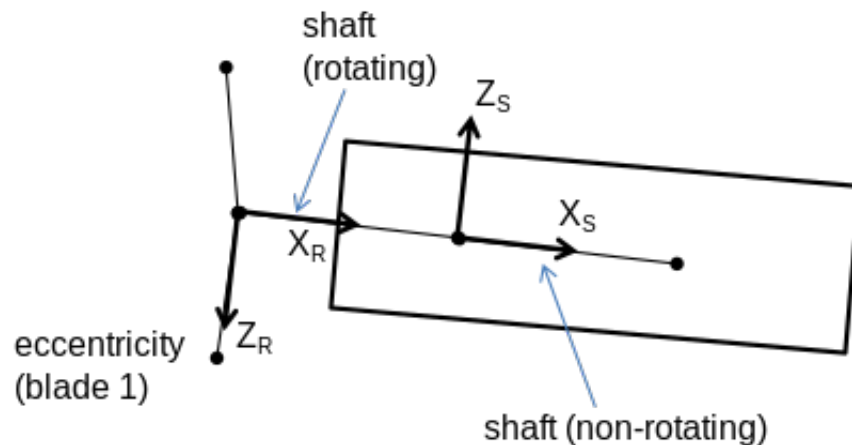


Figure 4.13: Outline of the rotor and shaft system with local coordinate systems. The figure is from [63].

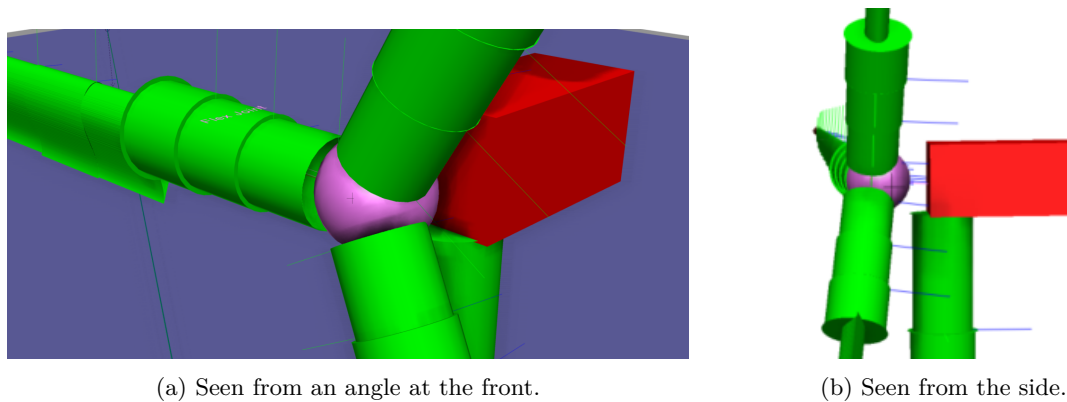


Figure 4.14: The modelled hub and nacelle arrangement.

The control system, which controls the generator torque and blade pitch, was not possible to obtain for the Hywind Scotland wind turbine. Instead the controller for a similar spar-type floating wind turbine was chosen and used as controller for the Hywind Scotland model. This will obviously not replace the actual controller of the Hywind Scotland wind turbine, but it is the only viable option, as no data is published on the actual controller. The similar wind turbine used for this was the 5 MW reference wind turbine for offshore system development [68]. All the parameters used for the controller can be found in the reference. This controller was also already implemented in SIMA on the OC3 Hywind-spar wind turbine [69] as an example floating wind turbine. The controller is modelled as an internal controller. It should be noted that the modelled controller was intended for a 5 MW wind turbine, while the Hywind Scotland wind turbine is a 6 MW wind turbine.

An internal control system for nacelle yaw also had to be implemented. This enables the wind turbine to rotate its hub, nacelle and blades into the wind direction. Fig. 4.15 defines the misalignment between the wind direction and the shaft orientation. With the yaw control system, environments with different wind directions can be utilized, while ensuring that the blades are

always faced towards the wind. The turbine orientation is upwind. The nacelle yaw controller was modelled by appending an extra line as an extension to the top of the tower, called the yaw line. Then the yaw correction is given as a rotation of the yaw line, relative to the tower line. The top of the tower line and bottom of the yaw line are modelled in the same location, but with two different supernodes. An outline of the yaw controller model is illustrated in Fig. 4.16. The modelled yaw controller parameters are listed in Tab. 4.9.

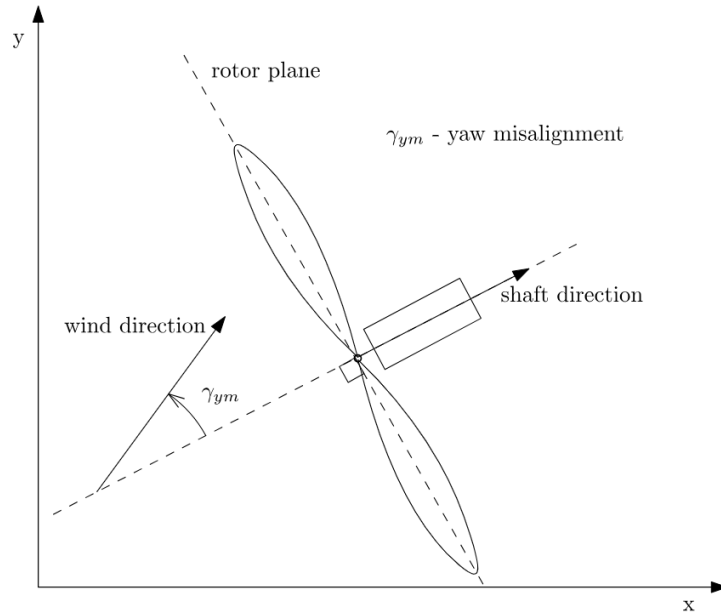


Figure 4.15: Definition of yaw misalignment between wind direction and shaft orientation. The figure is from [65].

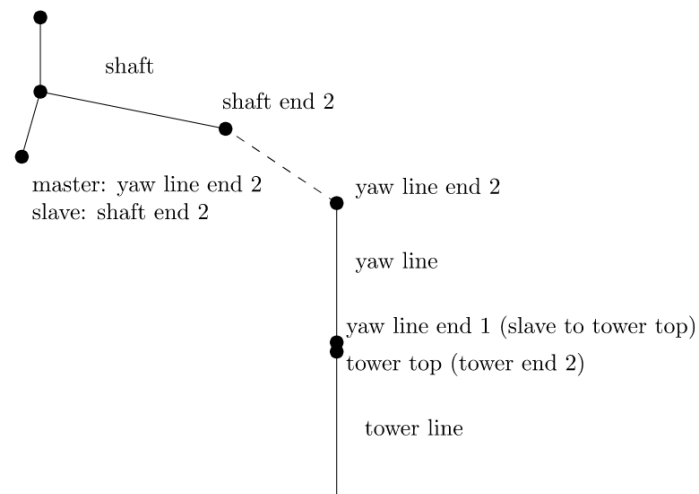


Figure 4.16: Outline of yaw controller model in SIMA. The figure is from [65].

Table 4.9: Modelled yaw controller parameters.

Time step [s]	Set point [deg]	Yaw rate [deg/s]	Error tres- hold [deg <sup>2</sup> s]	Fast low pass filter period [s]	Slow low pass filter period [s]
0.005	0.0	0.5	1.0	1.0	60.0

#### 4.3.4 Blades

A description of the Hywind Scotland blades and foil profiles geometries and properties were not possible to obtain, as with the control system. Therefore, the blades defined in the 5 MW reference wind turbine for offshore system development [68] were used as a measure. The blades consists of 17 different foil sections, each with different geometry and properties. Reference is made to [68] for the specific values. These blades were obviously intended for a 5 MW turbine, while the Hywind Scotland turbine is a 6 MW turbine. The blade lengths and rotor diameter were therefore altered to the given values of the Hywind Scotland wind turbine. Each foil section is modelled with RIFLEX double symmetric cross section elements. The modelled blade sections, with foil cross sections, number of elements and element length are listed in Tab. 4.10.

Table 4.10: Blade element sections.

Section	Foil	Section length [m]	Number of elements	Element length [m]
Blade1	Foil1	3.3556	1	3.3556
Blade2	Foil2	3.3556	1	3.3556
Blade3	Foil3	3.3556	1	3.3556
Blade4	Foil4	5.0333	1	5.0333
Blade5	Foil5	5.0333	1	5.0333
Blade6	Foil6	5.0333	1	5.0333
Blade7	Foil7	5.0333	1	5.0333
Blade8	Foil8	5.0333	1	5.0333
Blade9	Foil9	5.0333	1	5.0333
Blade10	Foil10	5.0333	1	5.0333
Blade11	Foil11	5.0333	1	5.0333
Blade12	Foil12	5.0333	1	5.0333
Blade12	Foil13	5.0333	1	5.0333
Blade14	Foil14	5.0333	1	5.0333
Blade15	Foil15	3.3556	1	3.3556
Blade16	Foil16	3.3556	1	3.3556
Blade17	Foil17	3.3556	1	3.3556
Total	-	75.5	17	-

The blades consists of two lines, as can be seen in Fig. 4.12. The inner line represents an eccentricity, while the outer line is the actual blade. Tab. 4.10 is only presenting the actual blade sections, not the eccentricity. The eccentricity is modelled as one single RIFLEX element with axisymmetric cross section and length 1.5 m. A modelled blade is shown in Fig. 4.17, where the different foil sections and elements can be seen.

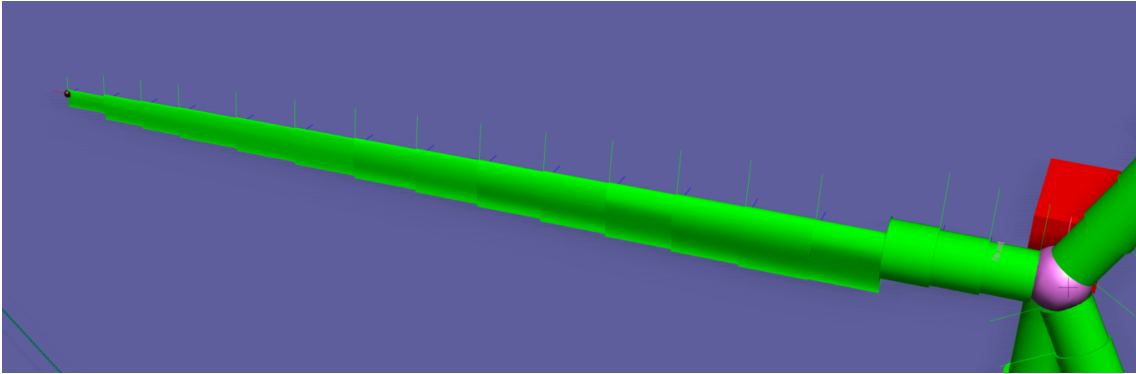


Figure 4.17: A modelled blade indicating different foil sections.

### 4.3.5 Ballast and weight distribution

Each component of the floating wind turbine structure was modelled with its prescribed weight. This was either done by calculating a mass coefficient per unit length for each of the different RIFLEX cross sections or by including a structural mass for the SIMO components. After all of the components were given a mass, the total mass of structure was calculated. A given dry mass of the structure was provided by Equinor [60], and difference between the two was found. This value gave the total mass of the ballast which then had to be modelled. The ballast was modelled as a SIMO body in the center of spar floater in the horizontal plane. The vertical position of the ballast SIMO body was determined to give a correct center of gravity of the total structure. This center of gravity was also provided by Equinor [60]. To determine the correct position, the center of gravity and mass of all modelled components were taken into account and the total center of gravity could be calculated. To obtain a correct center of gravity in the horizontal direction, the local center of gravity of the nacelle was adjusted. All other components was modelled to have its center of gravity in the geometric center.

### 4.3.6 Integration and damping parameters

The numerical time integration in RIFLEX is based on the Newmark- $\beta$  procedure. The integration parameters can be found in Tab. 4.11, where  $\beta$ ,  $\gamma$  and  $\theta$  are parameters defining the functional change in displacement, velocity and acceleration vectors over the time step.

Inverse $\beta$	$\gamma$	$\theta$
3.9	0.505	1

Table 4.11: Numerical integration parameters.

A structural damping model is applied in terms of the global Rayleigh damping model. This damping modal consists of two damping terms, one mass proportional and one stiffness proportional. The terms are defined as coefficients,  $\alpha_1$  and  $\alpha_2$ , where  $\alpha_1$  is the mass proportional damping coefficient and  $\alpha_2$  is the stiffness proportional damping coefficient. The total damping matrix,  $C$ , is defined as:

$$C = \alpha_1 M_t + \alpha_2 K_t, \quad (4.9)$$

where  $M_t$  is the tangential mass matrix and  $K_t$  is the tangential stiffness matrix. The mass proportional damping is taken to be zero, while the stiffness proportional damping is applied to remove high-frequency noise and disturbances from the analyses. The structural damping parameters used are listed in Tab. 4.12.

$\alpha_1$	$\alpha_2$
0.0	0.0159

Table 4.12: Structural damping parameters.

## 4.4 Free decay tests

When all components of the floating wind turbine were modelled, free decay tests were performed to determine the natural periods of the modelled structure. The free decay tests were performed in the six degrees of freedom to determine the natural periods in surge, sway, heave, roll, pitch and yaw motion. All the free decay tests are plotted in Fig. 4.18. Natural periods in combined motions were not investigated. It should be noted the all the motions are plotted around the nodes static position and local coordinate system. This implies that all plots are oscillating around zero. The free decay tests in surge, sway and heave were performed by applying a force in the center of gravity of the structure in the respective direction of the free decay test. The force was applied in an incremental order of 5000 N/s for 200 seconds. After the full force was applied, it was instantaneously removed and the structure was free to oscillate. The motions in the respective directions were then recorded and plotted against time. The free decay tests for surge, sway and heave are plotted in Figs. 4.18a, 4.18b and 4.18c respectively.

For roll and pitch free decay tests, a force with equal magnitude was applied with the same approach, only for these two degrees of freedom the force was applied in the hub. This was done to provoke the roll and pitch motion over the sway and surge, respectively. The was force removed instantaneously as for the surge, sway and heave cases, and the motions were plotted. The roll motion was plotted as translation of the hub in y-direction and is shown in Fig. 4.18d. The pitch motions was plotted as translation of the hub in x-direction and is shown in Fig. 4.18e.

Finally, for the yaw free decay test, the motion was not as easily provoked as for the five other degrees of freedom. A force was applied in each of the three attachment points for the bridles on the spar floater. The directions were 30 degrees off the tangential direction in each point to rotate the structure in the yaw direction a considerable amount and provoke the motion clearly in the oscillation after the forces were removed. The force in each point had to be decomposed into two vectors, one i x- and one in y-direction. The total force in each point equalled 5000 N/s for 200 seconds. The yaw motion is plotted as translation of the connection point for bridle 2 from mooring line 141 and bridle 1 from mooring line 142 in x-direction and is shown in Fig. 4.18f.

The natural periods were calculated from the free decay tests by counting the number of oscillations and the total time it took to reach that number. Then the average period over this time was calculated and used as the natural period of the modelled floating wind turbine structure. The time or number of oscillations used for the calculations were determined for each individual free decay tests. The reason for this was that the motions died out or merged into a combined motion with other degrees of freedom at different times for the different tests. When all the natural periods were calculated, they were compared with stated natural periods from the operator of the

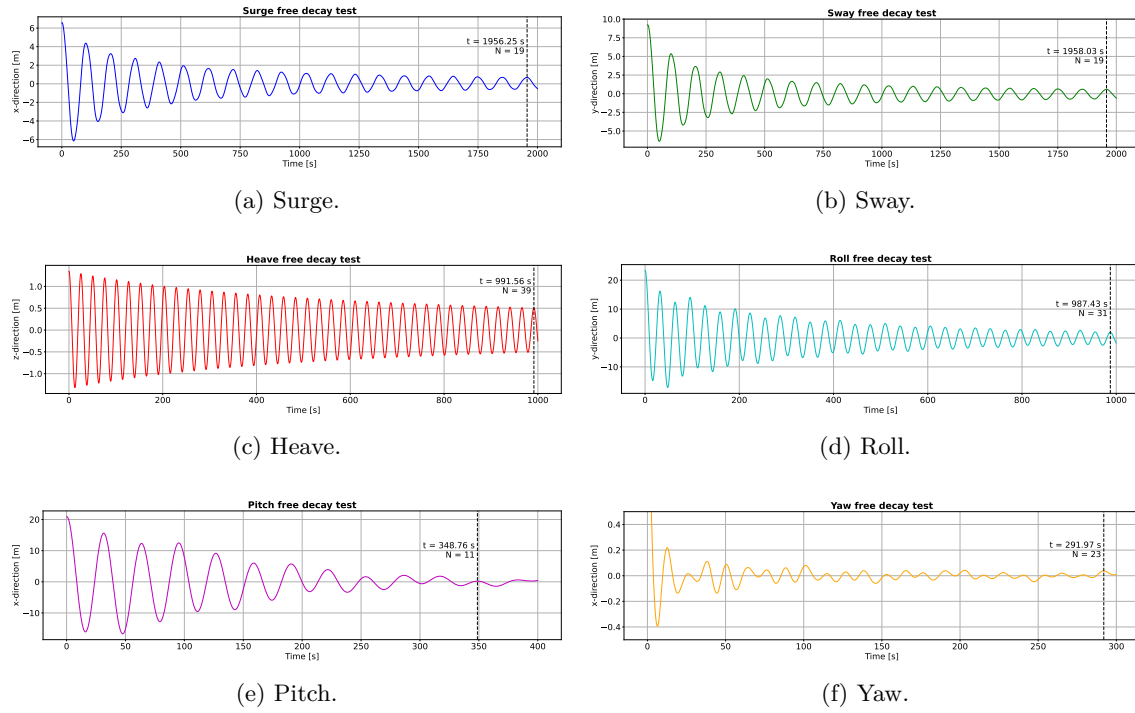


Figure 4.18: Free decay tests for the six degrees of freedom.

Hywind Scotland wind park, Equinor [60]. The differences between the calculated periods of the modelled structure and the stated periods of the actual full-scale structure were also calculated. All the calculated periods from the free decay tests, the stated periods from Equinor as well as the difference between the two are listed in Tab. 4.13. It can be seen from the table that all of the degrees of freedom gave calculated natural periods within  $\pm 7.5\%$  of the stated natural periods from Equinor. This confirmed the floating wind turbine model was modelled with a reasonable degree of accuracy and realistic response of the modelled structure was to be expected.

Table 4.13: Natural periods in the six DOFs stated by Equinor and calculated by free decay tests in SIMA, as well as the difference between the two.

DOF	Equinor stated period [s]	SIMA free decay period [s]	Difference [%]
Surge	96	103.0	7.29
Sway	96	103.1	7.40
Heave	25.8	25.42	-1.47
Roll	33.7	31.85	-5.49
Pitch	33.7	31.71	-5.91
Yaw	13.0	12.69	-2.38

## 4.5 Environmental loading

The environmental loading was applied as wind, waves and current according to the case in consideration. It should be noted that the definitions of the environmental directions in SIMA are different from the environmental directions in the full-scale measurements introduced later in the thesis. The different conventions will be addressed later, but is worth mentioning here as well, to avoid confusion. However, in this section, the SIMA directions will be introduced. The x-direction is defined positive towards the north and the y-direction positive towards the west. This gives a positive z-direction upwards. The wind, wave and current directions are conveniently all defined in the same manner. Wind, waves and current directions are defined as the direction from which the wind, waves and current are coming from, where 0 degrees is coming from the negative x-axis, moving towards the positive x-axis. Thus, waves, wind and current coming from the south have a direction defined as 0 degrees and waves, wind and current coming from the east have a wave direction defined as 90 degrees. The definition of the environmental directions in SIMA are illustrated in Fig. 4.19. All directions modelled in SIMA are following this convention.

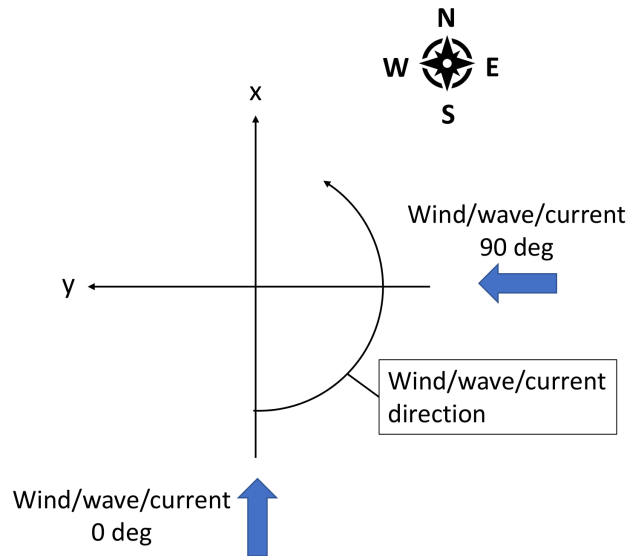


Figure 4.19: Definition of environmental directions in SIMA.

Both wind waves and swell waves were applied when applicable. These two wave components were modelled in an equal manner, but obviously with individual parameters for the significant wave height, peak period and wave direction. All the waves were however modelled using a 3-parameter Jonswap spectrum. A unidirectional spreading type, with 11 number of directions in the spreading function, was utilized. The peakedness parameter,  $\gamma$ , was calculated directly in the software as described in [65]. The current was modelled as regular current defined at a given number of points through the water column. Both direction and velocity was determined for the current at each level. The spacing between the levels through the water column was also user defined. These were determined considering the available information for each case.

The wind was modelled using the TurbSim software introduced in Sec. 4.2.3. An example TurbSim input file containing the parameters used for a case is included in App. A. From this input file, a turbulent wind field was generated over the prescribed domain and time. The wind field contains wind velocity and direction for each of the time steps through the total analysis time. A TurbSim generated wind field for a single time step is illustrated in Fig. 4.20. The spatial domain used for the wind modelling was 196 meters in height and 250 meters in width. This ensured that the floating wind turbine was free to move in response to the environmental loading and still be inside the wind field domain. The number of grid points in the vertical direction was 39 and in the horizontal direction 49. This gave a grid size of approximately  $5 \times 5$  meters. The IEC Kaimal model was used as the spectral turbulence model in the wind modelling. Details on the turbulence model can be found in [26]. The velocity wind profile type used was a power-law profile on the rotor disk, and a logarithmic profile elsewhere. The time step used for the wind modelling was 0.05 seconds.

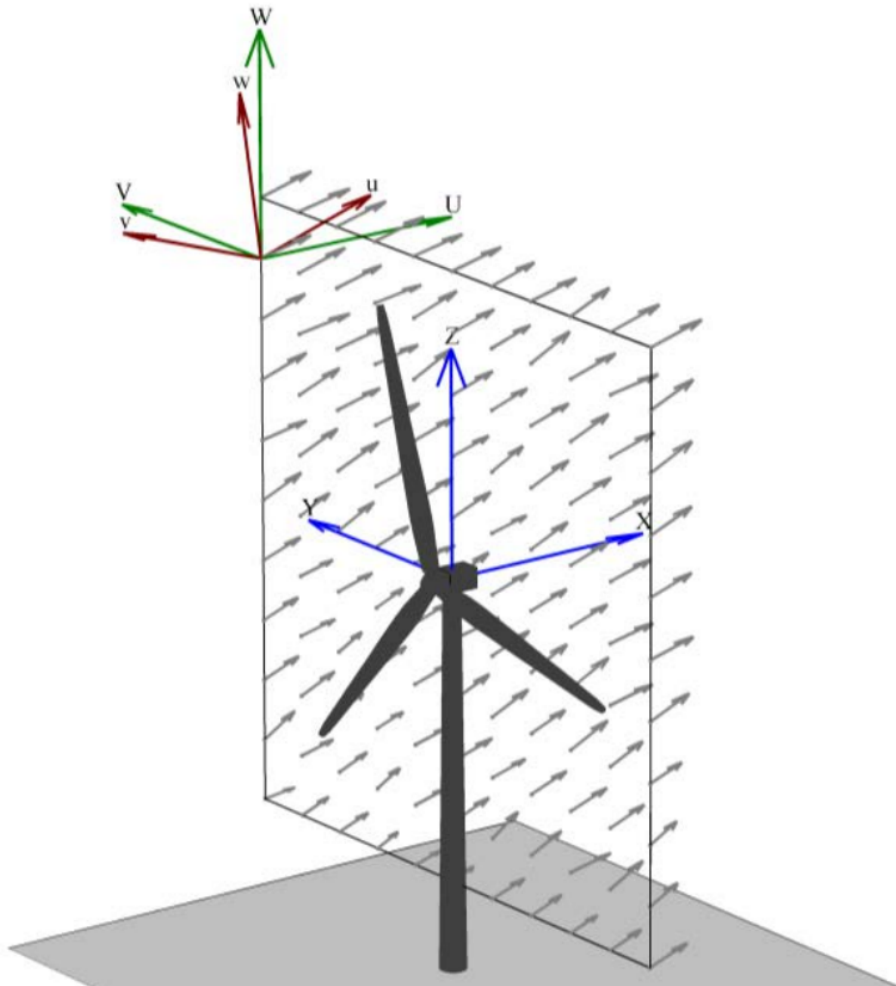


Figure 4.20: A TurbSim generated wind field. The figure is from [26].



## 4.6 Hydrodynamic load model

The main hydrodynamic load model used for the analyses was the TD VIV model introduced in Sec. 3.2. The empirical hydrodynamic coefficients and parameters of the TD VIV model have not been calibrated with regards to VIM cases in previous studies. Instead, the empirical values from a recent study on riser VIV [49] are used here. The hydrodynamic VIV coefficients and parameters used are listed in Tab. 4.14. The CF and IL loads are calculated separately, and all coefficients used are nondimensional. The option for a higher order VIV coefficient is not utilized, i.e. set to zero.

Parameter	
$C_{v,y}$	0.85
$\hat{f}_{0,y}$	0.144
$\hat{f}_{min,y}$	0.08
$\hat{f}_{max,y}$	0.208
$C_{v,x}$	0.75
$\hat{f}_{0,x}$	0.288
$\hat{f}_{min,x}$	0.16
$\hat{f}_{max,x}$	0.416

Table 4.14: Empirical hydrodynamic coefficients and parameters used for the TD VIV model.

When analyses were performed without the use of the TD VIV model, the hydrodynamic load model based on the generalized Morison's equation was used. This load model includes the same load terms as the TD VIV model, except the CF and IL VIV terms as described in Sec. 3.2. By comparing analyses with these two load models, the effect of the VIV load terms can easily be distinguished. The hydrodynamic diameters, as well as the drag and added mass coefficients used for the different cross sections are equal for the two hydrodynamic load models utilized in this work.

## 4.7 Modelling challenges

During modelling and validation of the floating wind turbine in SIMA, several unforeseen challenges emerged. One of these appeared during the modelling of the blades. As described in the modelling procedure of the blades in Sec. 4.3.4, blades from the 5 MW reference wind turbine for offshore system development [68] was used with adjusted blade length to give the the modelled turbine blades the rotor diameter of the Hywind Scotland wind turbine. The stiffness of blades were also initially adjusted with an increase of the same order as the increase in blade length. This did however cause the dynamic simulations to fail due to too large displacements of the blade tips when realistic wind speeds were applied. In other words, the blades were too soft, and the stiffness had to be additionally adjusted. Several stiffness values were applied and tested and the relative blade tip displacements were compared to the blade tip displacements of the reference wind turbine with exposed to similar wind speeds. This resulted in a total stiffness increase of factor two.

Another major modelling challenge appeared during testing and validation of the model with different environmental conditions. When wind was applied in the dynamic analyses, obviously the turbine starts to rotate. This increases the loading on the blades, and the force is pushing the turbine from its initial static position, to a new mean position were the mooring lines are tightened

and slacked off, depending on the line in question and the environment loading directions. When the floating wind turbine is moving through the water from its initial to its new mean position, the relative velocity between the water and the spar floater is significant. This caused the TD VIV model to produce VIM, even though no current forces were applied in the environment. The motion also used a considerable amount of time to die out, creating a need for a much longer transient period, before a realistic time series could be extracted from the results. Combined with the complexity of the model and total number of elements, the computational time to run a single case had reached an unacceptable level for the resources available in the current work. Several possibilities were looked into in order to counter the VIM occurring in the transient phase.

One attempt to limit the transient VIM was done by introducing the wind environment in an incremental order, instead of unleashing the full wind speed at an instance. Initially, it was attempted to do this directly in the SIMA software, but it was not found an adequate way to do this. Instead, the TurbSim-generated wind files had to be altered. The files were altered to increase the wind speed using several on-loading functions and over various amounts of time. After the wind transient phase had passed, the normal wind environment were applied. However, none of these attempts eliminated the problem with VIM in transient of the dynamic analyses. For some cases, the significance was reduced, but not enough to be of sufficiency, and the reduction was not consistent when considering different environmental conditions. For this reason, this attempt to limit the transient VIM was dismissed, and alternative possible solutions were investigated.

Next, it was instead attempted to move the complete wind turbine structure in the direction of the wind before any wind was applied, in order to reduce the occurring transient motion. This was done by applying a force in the center of gravity of the structure in an incremental order of 5000 N/s for 200 seconds. Then the wind environment was applied in such a way that the turbine started rotating when the full force in the center of gravity was applied. At the same time, the force in the center of gravity was removed in an equal but opposite incremental order of -5000 N/s for 200 seconds. By doing this, it was ensured that much of the movement of the spar floater from its initial position to its new mean position was done in a controlled manner. Testing also showed that this removed almost all transient VIM previously seen from the same environmental conditions. It was therefore decided to use this procedure for all the analyses in this work. The force applied to the center of gravity is always in the same direction as the wind for the case in consideration. This implies that the force is decomposed into two force vector, one in x-direction and one in y-direction, which combined gives a total force vector of the given magnitude in the wind direction. Although the complete procedure to avoid the transient VIM problem is somewhat tedious, this gives the most accurate time series and results with the computational resources available.

## Chapter 5

# Validation against full-scale measurements

To validate the TD VIV model as a VIM prediction tool, full-scale measurement data from the HS4 floating wind turbine unit in the Hywind Scotland wind park was utilized. The data were provided by Equinor, Masdar and ORE Catapult, and includes 11 operational cases for one of the floating wind turbines in the wind park [60]. The full-scale measurements are sometimes referred to as the Equinor data in the following. The cases were selected by the supplier based upon finding stationary environmental conditions which makes them relevant for simulating the same events. The cases should also represent typical operational conditions within a range of metocean parameters, according to the supplier. These full-scale measurements were compared with the simulation and analyses results from the modelled HS4 structure in SIMA. The full-scale measurements are compared both to results with and without the use of the TD VIV model to investigate the effect of the VIV load terms on the VIM response.

### 5.1 Full-scale measurements description

The full-scale measurements provided by Equinor included various field measurements. These are:

- Environmental conditions including wind, waves and current
- Nacelle yaw direction and roll/pitch motions
- Floater roll/pitch/yaw motions
- Global Positioning System (GPS) measurements of surge and sway motions
- Tension in mooring system

The measurements utilized in this thesis are all the environmental conditions, as well as the GPS measurements of surge and sway motions. VIM can easily be seen in the surge and/or sway motion of the structure, if present, and is for that reason a very useful measurement to look into when VIM response is a focus. It should be noted that tension in mooring system might also indicate VIM motion, but due to the complexity of the mooring system, this is not as reliable as the GPS measurements. The GPS antenna on the HS4 wind turbine is located at platform level at 15.3 meters above sea level. Due to this, some of the translational motions in surge and sway captured by the GPS might actually be due to rotations in roll and pitch.

## 5.2 Metocean data of full-scale cases

The 11 operational cases from the Hywind Scotland wind park with varying environmental conditions are presented in Tab. 5.1. The metocean data parameters includes significant wave height,  $H_s$ , peak period,  $T_p$ , and direction of the wave loads. The magnitude and direction of the wind and current loads are also included. The time references are given in Coordinated Universal Time (UTC) format. Each operational case contains 30 minutes of data where the date specified in Tab. 5.1 represents the midpoint in the interval. It should also be noted the table only serves as a compact overview of the environmental conditions and more specific environmental data will be presented for each of the wave, wind and current conditions in the following.

Table 5.1: Metocean data for the 11 operational cases from the Hywind Scotland wind park. The table is adapted from [60].

Case	Date	Wave			Wind		Current		Comment
		Hs [m]	Tp [s]	Dir. [deg]	Magn. [m/s]	Dir. [deg]	Magn. [m/s]	Dir. [deg]	
1	2018-03-26 23:30	2.2	10.6	14	8.5	172	0.24	16	
2	2018-01-14 15:40	4.2	8.7	165	20.4	174	0.32	24	
3	2018-04-14 00:40	2.1	10.5	107	5.2	171	0.32	195	
4	2018-02-13 01:20	2.1	6.5	201	15.5	174	0.27	187	
5	2018-02-24 04:50	2.5	7.3	164	14.1	161	0.17	150	
6	2018-01-09 09:40	3.2	9.3	131	13.9	146	0.09	303	
7	2018-01-06 08:00	4.4	10.9	17	13.7	11	0.21	19	
8	2018-07-29 04:00	3.0	7.9	161	16.6	179	0.33	44	
9	2018-05-02 04:00	2.3	6.5	185	15.6	175	0.12	233	
10	2018-01-24 11:30	3.9	8.3	174	30.0	212	0.27	27	Idle
11	2018-01-24 11:40	3.9	8.3	175	30.3	213	0.30	37	Idle

The definition of the environmental directions are different in the Equinor data then in the SIMA software used for the analyses. Recall the definition of the environmental directions in SIMA presented in Sec. 4.5 and illustrated in Fig. 4.19. In the Equinor data, however, the positive x-direction is defined towards the east, and the positive y-direction is defined towards the north. This gives a positive z-direction upwards. The wave direction is defined as the direction from which the waves are coming from., where 0 degrees is coming from the positive y-direction, going towards the negative y-direction. Thus, waves coming from the north have a wave direction defined as 0 degrees and waves coming from the east have a wave direction defined as 90 degrees. The wind direction is also defined as the direction from which the wind is coming from. Thus, wind coming from the north has a wind direction defined as 0 degrees and wind coming from the east has a wind direction defined as 90 degrees. The current direction is however defined as the direction to

which the current is going towards. Thus, current coming from the south has a current direction defined as 0 degrees and current coming from the west has a current direction defined as 90 degrees. The definition of the environmental directions in the Equinor data are illustrated in Fig. 5.1. All directions used in this section uses this definition.

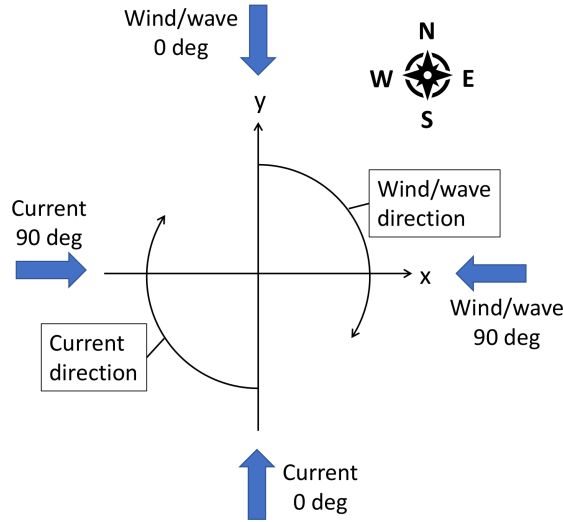


Figure 5.1: Definition of environmental directions in the Equinor data.

### 5.2.1 Wave condition

The wave conditions for the 11 operational cases are listed in Tab. 5.2. Wind sea and swell contributions are provided, as well as the total wave contribution. The wave conditions are measured by a wave buoy located on the southwest side of the wind park, as illustrated in Fig. 5.2. The figure also indicated the location of the HS4 unit relative to the wave buoy and the rest of the wind park.

Table 5.2: Wave conditions for the 11 operational cases divided in wind sea and swell contributions. The total wave conditions are also provided. The table is adapted from [60].

Case	Sign. wave height, $H_s$ [m]			Peak period, $T_p$ [s]			Wave direction [deg]		
	Total	Wind sea	Swell	Total	Wind sea	Swell	Total	Wind sea	Swell
1	2.23	0.94	2.03	10.6	7.95	10.6	14	313	14
2	4.21	2.93	3.02	8.7	8	8.7	165	168	163
3	2.07	1.48	1.44	10.5	8	10.5	107	111	103
4	2.13	2.09	0.4	6.5	6.5	14.6	201	201	61
5	2.51	2.45	0.52	7.3	7.3	8.3	164	164	174
6	3.25	2.32	2.29	9.3	7.55	9.3	131	134	127
7	4.41	2.42	3.68	10.9	7.7	10.9	17	19	16
8	3.02	2.74	1.27	7.85	7.85	8.3	161	163	148
9	2.28	2.26	0.3	6.5	6.5	8.3	185	185	170
10	3.87	3.06	2.36	8.3	8	8.3	174	184	160
11	3.85	3.07	2.32	8.3	8	8.3	175	186	157

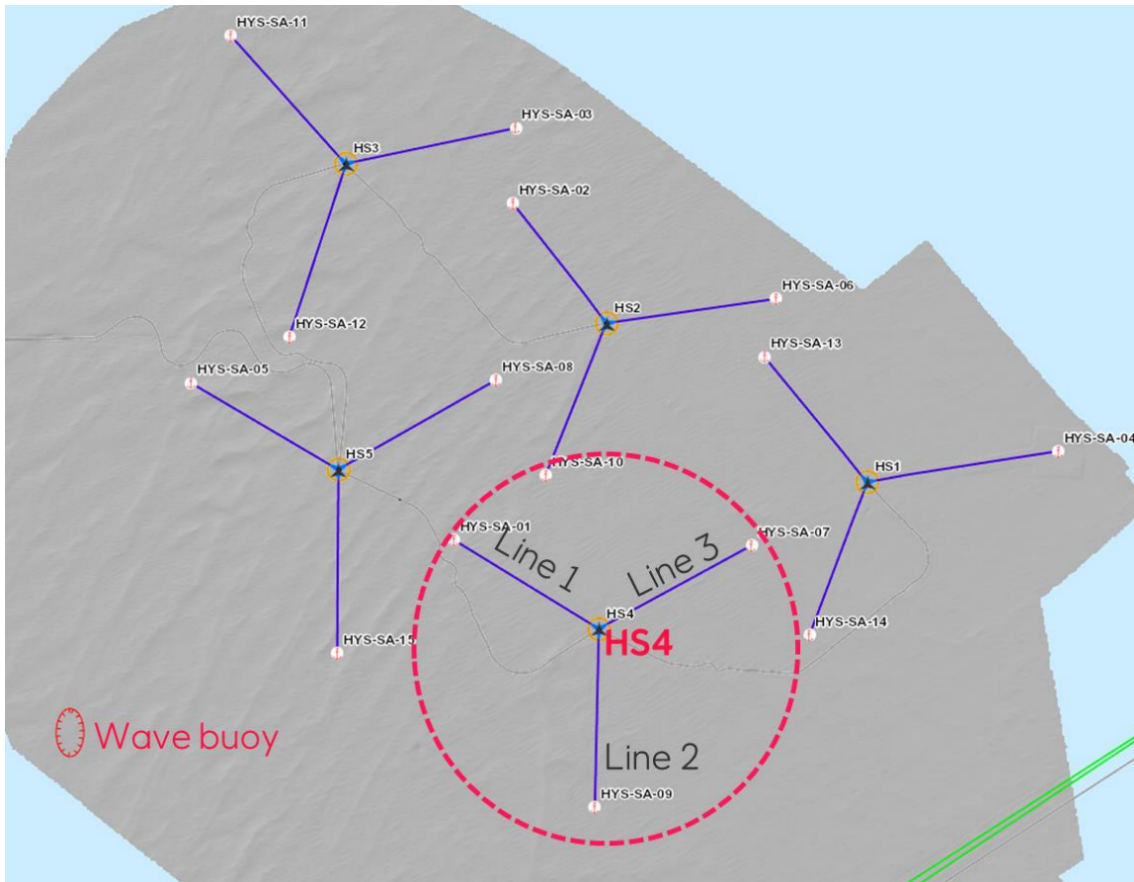


Figure 5.2: Location of HS4 and the wave buoy in the Hywind Scotland wind park. The figure is from [60].

### 5.2.2 Wind condition

The wind conditions for the 11 operational cases are listed in Tab. 5.3. Mean wind speed, standard deviation and wind direction are provided. The parameters are estimated based upon the turbines wind anemometer. Moments when the blade was covering the anemometer were removed from the idling cases, i.e. case 10 and 11. The wind turbine anemometer is located approximately 99 m above the mean sea level.

### 5.2.3 Current condition

The current conditions for the 11 operational cases are listed in Tab. 5.4. The current speeds and directions are measured at four different depths relative to the sea surface. The depths are -3.72 m, -11.72 m, -31.72 m and -67.72 m, and the conditions are measured by the wave buoy.

Table 5.3: Wind conditions for the 11 operational cases. The table is adapted from [60].

Case	Mean wind speed [m/s]	Standard deviation [m/s]	Wind direction [deg]
1	8.49	0.75	172
2	20.44	2.07	174
3	5.24	0.74	171
4	15.53	1.36	174
5	14.1	1.12	161
6	13.89	1.3	146
7	13.72	1.33	11
8	16.62	1.41	179
9	15.61	1.07	175
10	29.96	3.47	212
11	30.35	3.41	213

Table 5.4: Current conditions for the 11 operational cases at four different depths relative to the sea surface. The table is adapted from [60].

Case	Current speed [m/s]				Current direction [deg]			
	-3.72 m	-11.72 m	-31.72 m	-67.72 m	-3.72 m	-11.72 m	-31.72 m	-67.72 m
1	0.25	0.27	0.24	0.21	11	174	16	16
2	0.28	0.37	0.21	0.43	22	17	57	26
3	0.37	0.38	0.33	0.21	187	196	194	211
4	0.31	0.23	0.28	0.25	188	185	186	203
5	0.19	0.17	0.19	0.13	140	143	157	187
6	0.11	0.14	0.08	0.06	311	324	296	52
7	0.23	0.21	0.22	0.19	19	32	17	18
8	0.2	0.26	0.27	0.58	47	41	34	79
9	0.12	0.12	0.14	0.09	224	241	242	32
10	0.31	0.22	0.28	0.28	28	27	18	33
11	0.34	0.27	0.28	0.33	38	36	29	47

### 5.3 Discussion on the full-scale cases

The statement from Equinor and ORE Catapult which was provided together with the measurement data claimed that the cases were selected by the supplier based upon finding stationary environmental conditions which makes them relevant for simulating the same events. It was also claimed that the cases should represent typical operational conditions with a range in wind speed and wave height [70]. However, quite cunningly, nothing is said about the current speed. The current speed is, as we know, the determining factor for the VIM response and a certain current speed has to be present in order for the structure to experience significant VIM. It is also noted that the current speeds in the 11 cases presented in Tab. 5.4 seems quite low, however it is not so easy to tell without grounds to compare it. Therefore, it was determined to investigate if the current speeds in the provided case gave an accurate representation of the actual current conditions on the site of the Hywind Scotland wind park.

The Hywind Buchan Deep metocean design basis includes probability distributions of the different environmental conditions at Buchan Deep [71]. Buchan Deep is the site where the Hywind Scotland wind park is located. An Weibull distribution of the current speed at different depths at Buchan Deep is provided in the report. The general cumulative Weibull distribution is given as:

$$F(u) = 1 - \exp - \left( \frac{u - \varepsilon}{\theta} \right)^\gamma, \quad (5.1)$$

where  $u$  is the current speed  $\varepsilon$  is a location parameter,  $\theta$  is a scale parameter and  $\gamma$  is a shape parameter. The current data is obtained using an Acoustic Doppler current profiler located at the site. It should be noted that the current measurements does not include a full year, but ranges from November 2013 to March 2014. This includes the winter season which historically contains the harshest environmental conditions, so the measurements should be conservative. The Weibull distributions at Buchan Deep are plotted in Fig. 5.3 for different measurements point in the water column. The water depth levels for the measurement points does not correspond to the same

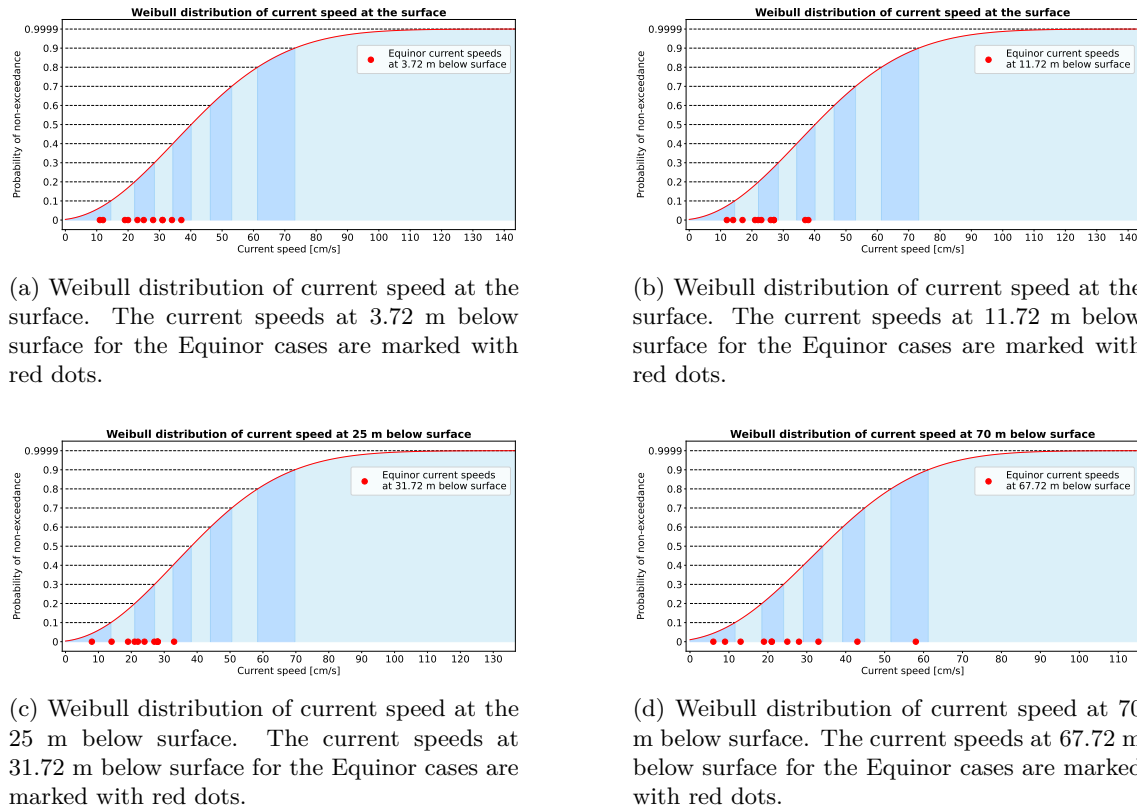


Figure 5.3: Cumulative Weibull distributions of current speeds at different depths at Buchan Deep. The distributions are divided in ten intervals with equal probability of occurrence and the current speeds at different depths for the Equinor cases are marked with red dots.

depth levels in the full-scale measurements cases, so a comparison is done on the closest values. The current speeds in the full-scale measurement cases are marked in the Weibull distributions to illustrate the likelihood of the given current speed to be found at the Hywind Scotland site.



The Weibull distributions are also divided into ten different intervals with equal probability of occurrence to easier illustrate to placement of the full-scale measurement points.

It is observed that, as expected by the wording of the provider, the full-scale measurement cases almost exclusively contains cases with current speeds in the lower half of the probability distributions. In fact, only three full-scale measurement points of all the 44 total points are in the top half of the probability distributions. This shows a strikingly clear tendency of the provider to only share case data with low current speeds. The reason for this unknown and it would only be speculation to provide explanations for this, but the takeaway is that significantly more VIM is expected than the full-scale measurement cases include. Increasing the current speed also increases the probability of VIM to occur so more VIM is expected when the current speeds reaches the part of the probability distribution not covered by the full-scale measurements.

## 5.4 Results and discussion of validation against full-scale measurements

The 11 operational full-scale cases introduced in section 5.2 were then modelled as different environments in SIMA. The modelling procedure of the environmental loading was described in Sec. 4.5. Each case was then analyzed with and without the TD VIV model and compared to the full-scale measurements. The results from the SIMA simulations of the full-scale cases are presented in this section and compared to the full-scale measurements provided by Equinor. The translation of the complete floating wind turbine structure in x- and y-direction is used for this purpose, as VIM can easily be captured as oscillations around the surge and sway natural periods in these time series. The translations are also converted to frequency spectra through a fast Fourier transform (FFT). Here, the natural periods are marked and frequency components around them can easily be spotted if present. In the following, results for a few of the interesting cases will be presented and discussed. A complete set of the full-scale measurements compared the results from SIMA with and without the TD VIV model can be found in App. B.1.

All the results are presented in similar format throughout this section. The translation plots are showing x-direction at the top and y-direction at the bottom. The motions are then plotted over time. All time series are plotted over 1800 seconds which constitutes to half an hour. This covers the entirety of the provided full-scale measurements. It should be noted that all simulations done SIMA have an initial transient removed. In addition to the adjustments mentioned in Sec. 4.7, a transient of 1200 seconds is removed all time series. Each SIMA simulation is in other words run over at least 3000 seconds. The simulations with and without the TD VIV model are presented in the same figures as the full-scale measurements. It is also worth mentioning that the x- and y-direction convention used for all of the presented results follows the definition illustrated in Fig. 4.19. That means positive x-motion is towards the north and positive y-motion is towards the west. The Equinor data is also corrected to follow this directional convention for easier comparison. To give an introduction to how the results are presented, the translation in x- and y-direction for case 1 is shown in Fig. 5.4. The case numbering refers to the full-scale cases presented in Sec. 5.2 and listed in Tab. 5.1. The full-scale measurements are labelled "Equinor" in the figure and are plotted in red and green for x- and y-directions respectively. The motion simulated with the TD VIV model are labeled "TD VIV model" and are plotted in blue and purple for the x- and y-directions respectively, while the motions simulated without the TD VIV model are labeled "No TD VIV model" and are plotted in orange and brown for x- and y-directions respectively. All the

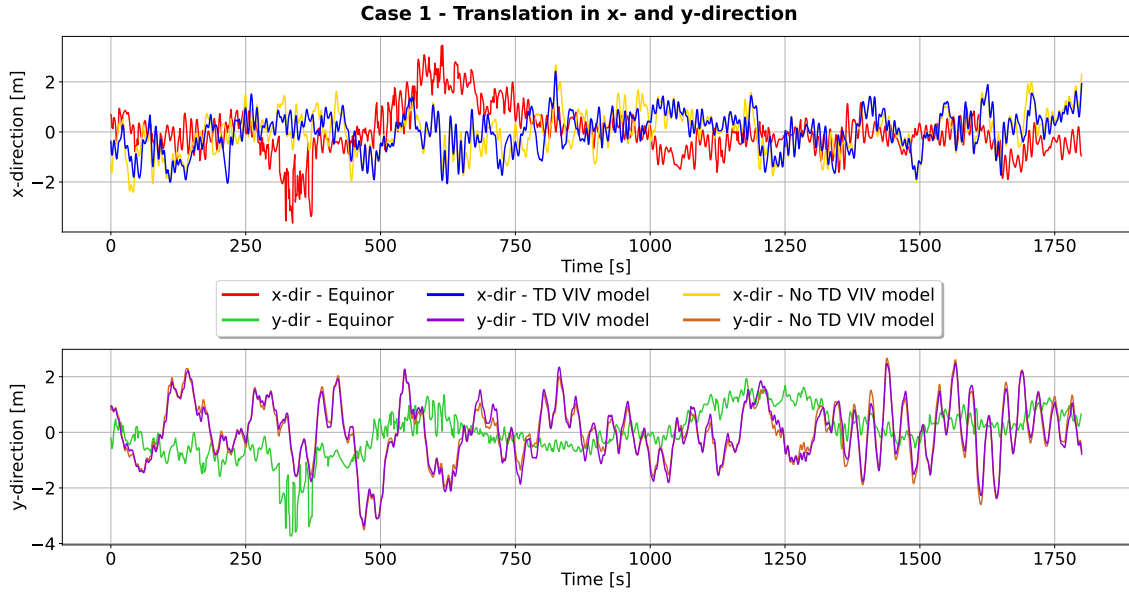


Figure 5.4: Translation in x- and y-direction for case 1. The full-scale measurements from Equinor and the SIMA results both with and without the TD VIV model are shown.

labels are also referred in the figure legend.

From the translation plots for case 1 it can be seen that translation in y-direction with and without the TD VIV model are almost perfectly overlapping. For the x-direction, slightly more discrepancies are occurring, but generally the motions are following the same pattern with and without the TD VIV model. This indicates little contribution in the structure motion from the additional VIV load terms in the TD VIV model. Compared to the full-scale measurements from Equinor in the x-direction, the general agreement is really good. The simulated motion overlaps well with the measurements and no significant oscillations are occurring in any of the x-direction plots. For the y-direction, the simulated motion is not capturing as accurately the measurement motion as for the x-direction. In the y-direction some oscillations around different periods are present, which are not as distinctly visible in the measurements motion. To easier visualize the frequency components of the time series, the frequency spectra for the translation in both x- and y-motion is found by FFT. The frequency spectra for case can be found in Fig. 5.5, which follows the same color scheme and labeling as the translation plots in Fig. 5.4.

In the frequency spectra, the same trends can be found as in the translation plots, however, the significant frequency components are much more prominent and can easily be distinguished. The natural periods for surge and sway motions as well as roll and pitch motions are also marked with dashed lines. It should be noted that the natural periods marked are the natural periods of the modelled floating wind turbine structure, not the stated natural periods from Equinor. The actual values of the natural periods are listed in Tab. 4.13. In the x-direction frequency spectra, good agreement between the full-scale measurements and simulated motions both with and without the TD VIV model can be seen, as was also seen in the translational plots. In the y-direction, clear peaks around the surge and sway natural periods and also roll and pitch natural periods can be

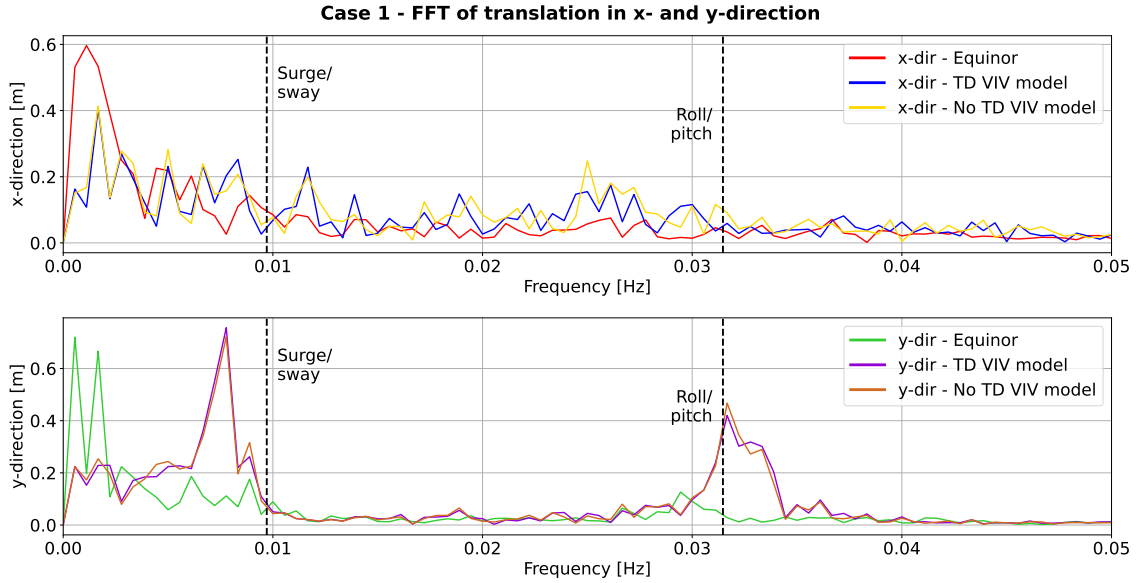


Figure 5.5: Fast Fourier transform of translation in x- and y-direction for case 1. The full-scale measurements from Equinor and the SIMA results both with and without the TD VIV model are shown.

seen. The reason for the peak around the surge and sway natural period is not coinciding directly with the period is most likely due a change in the natural periods due to the mean position of the floating wind turbine. When the structure is moved by environmental loads to a new mean position, the mooring lines are tightened and slacked according to the direction, and naturally the natural periods will be affected. The natural periods marked on the figure are based on a mean position in the global origin with no environmental loads present. Although the frequency peaks around the natural periods indicated VIM, the fact that motion without the TD VIV model produces almost identical peaks as the motion with the TD VIV model, the origin of the peaks are not from the VIV load terms in the TD VIV model, but rather captured by other aspects of the load models in SIMA. This indicates great potential for the TD VIV model as a VIM prediction tool, as the full-scale measurements for this case does not include any VIM in terms of significant peaks around the natural frequencies. In other words, the TD VIV model is not producing VIM for case 1, where the full-scale measurements neither include VIM.

The full-scale measurements of case 3 is the only case where tendencies to VIM can clearly be observed in the provided Equinor data. This makes case 3 a very interesting case to investigate in a greater extent. The translational motion in x- and y-directions are plotted in Fig. 5.6. The clear oscillation in the full-scale measurements y-direction can be seen in green. Although the oscillation is clearly visible, the oscillation amplitude is never above three meters, and the oscillation is not even consistent through the complete time series, but is gradually reducing the amplitude and eventually dies out completely at the end of the time series. This indicates mild VIM, meaning relatively small motions compared to the VIM amplitude potential. The motion is also very volatile as it is not consistent throughout the full 30 minutes. Although this motion classifies as VIM, it is not a completely VIM-dominating response.

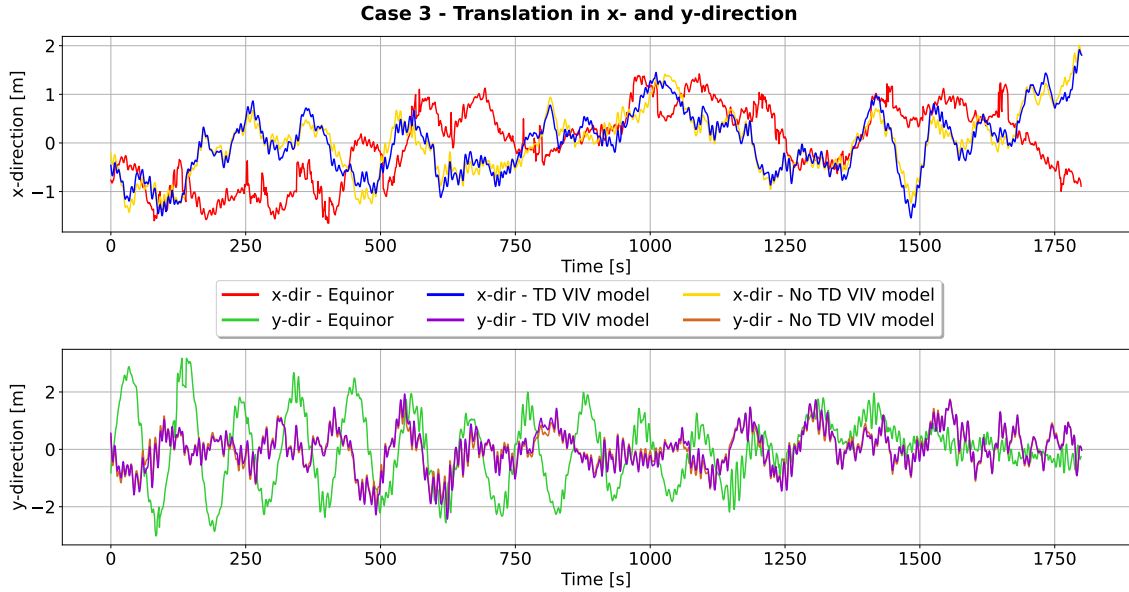


Figure 5.6: Translation in x- and y-direction for case 3. The full-scale measurements from Equinor and the SIMA results both with and without the TD VIV model are shown.

It is observed that in the y-direction the simulated motions with the TD VIV model almost completely correlates with the simulated motions without the TD VIV model. Again, this indicates that the VIV load terms in the TD VIV model are not contributing much to the total response of the floating wind turbine structure. Although the VIV load terms does not include much contribution to the response, it is observed that the total motion in the y-direction is actually decently captured anyways. The oscillation seen in the full-scale measurements is not as prominent in the simulations, however, it is present at least for certain periods of the total time series. In the x-direction the agreement between the simulated motion with and without the TD VIV model is also good. The agreement with the full-scale measurements is also very good. No clear periodic oscillations can be identified and the general motion behaves similarly for both the full-scale measurements and the simulations.

The frequency spectra of the translation in x- and y-directions for case 3 are plotted in Fig. 5.7. The oscillations observed in the y-direction in the translation plots can be seen as a major spike in the frequency spectra around the surge and sway natural periods. A smaller amplification in the frequency spectra around the same natural period is also observed in the simulated motions with and without the TD VIV model. Elsewhere, the agreement is good when comparing the full-scale measurements with the simulated motion with and without the TD VIV model in the y-direction. In the x-direction, generally good agreement is observed with the full-scale measurements and the simulated motions, both with and without the TD VIV model.

For case 3, the general agreement between the full-scale measurements and the simulated motions with the TD VIV model is good. Some contribution from the VIV load terms in the TD VIV model could be expected to capture the oscillations in y-direction around the natural surge and sway periods, however this is not case as the oscillations in the simulated motions with the TD VIV

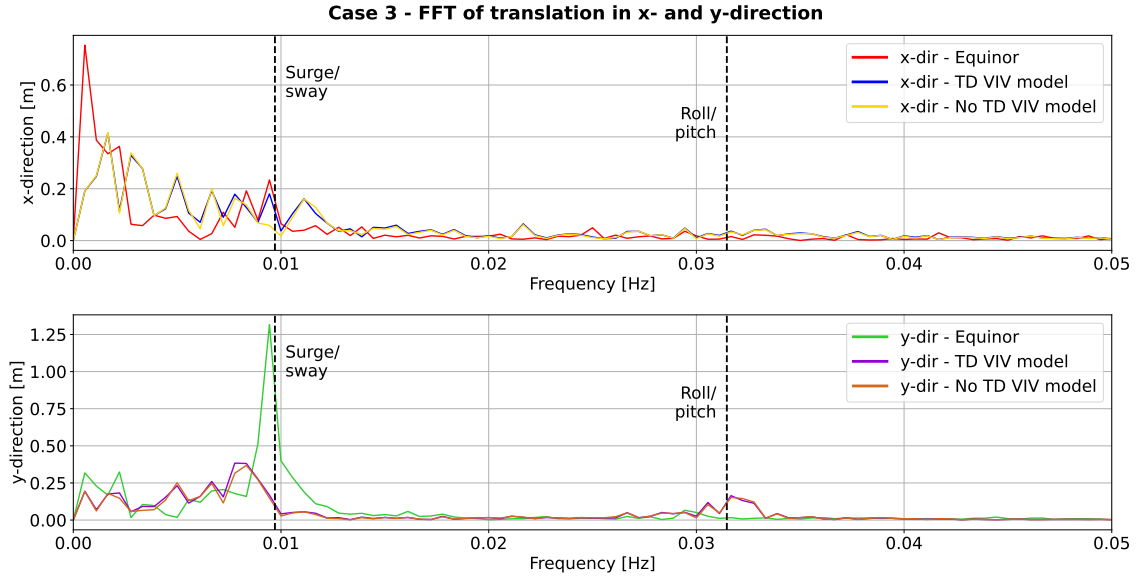


Figure 5.7: Fast Fourier transform of translation in x- and y-direction for case 3. The full-scale measurements from Equinor and the SIMA results both with and without the TD VIV model are shown.

model are also present without the TD VIV model. This makes a case for the TD VIV model to not capture the VIM onset completely accurate, as some VIM would be expected in this case. However, as discussed previously, the VIM in the full-scale measurements is not of a very dominant character, due to the relatively low oscillation amplitude, and consistency in the oscillations. This might be the reason why the VIV load terms in the TD VIV model are not capturing these oscillations. Another explanation might be the TD VIV model needs further calibration on the customizable hydrodynamic coefficients and parameters.

Another interesting case to look into is case 6. The translation in x- and y-direction are plotted in Fig. 5.8. In both x- and y-directions the agreement is good between simulations with and without the TD VIV model. Especially in the x-direction almost no deviation between the two can be identified, while for the y-direction some slight deviation is observed towards the end of the time series. Comparing the simulated results with the full-scale measurements, good agreement is found both in the x- and y-directions. Both present oscillations and general motion seems to match up good. To investigate the frequency components of the oscillations, the frequency spectra for case 6 is plotted in Fig. 5.9. Very good agreement between all of the plots can be seen pretty much throughout the frequency spectra both in the x- and y-directions. In the x-direction a very low-frequency component can be seen as a spike in frequency spectrum, but this component is not caused by VIM as it is far too low-frequency to align with any of the floating structure's natural periods. This low-frequency component is regardless present in most of the full-scale measurement cases and seems to be somewhat independent of the case in consideration. As a few examples the spike is visible in both Figs. 5.5 and 5.7. Reference is also made to App. B.1 where a complete set of all the motions and frequency spectra is attached. Apart from this low-frequency spike, the rest of the x-direction frequency spectra in Fig. 5.9 does not include any significant components for neither the measurements or simulations. In the y-direction, a small peak is observed around

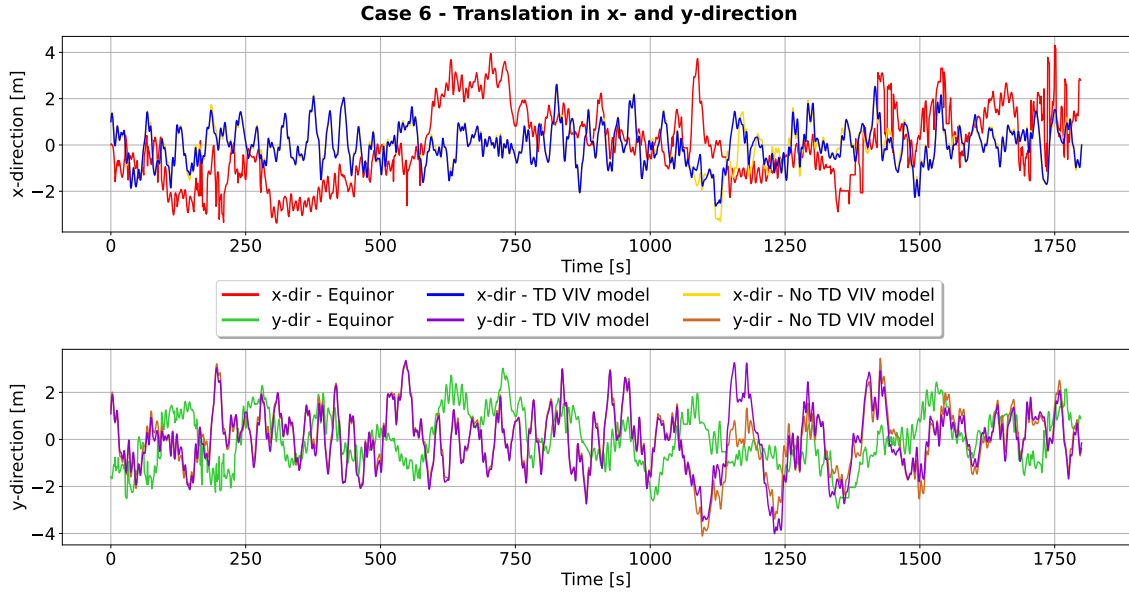


Figure 5.8: Translation in x- and y-direction for case 6. The full-scale measurements from Equinor and the SIMA results both with and without the TD VIV model are shown.

the surge and sway natural periods, both for the full-scale measurements and the simulations both with and without the TD VIV model. The agreement for all of the y-direction is in general very good between the measurements and simulations, especially for the low-frequency components, but the agreement is also fairly good for the components with slightly higher frequency components. Such a good agreement with the simulated motions and full-scale measurements really supports the potential of the TD VIV model to be used in VIM prediction. For this case, no clear VIM is experienced, and the VIV load terms does not contribute to any VIM in the simulated motions. The motions which are present in the full-scale measurements are accurately captured by the Morison's model in SIMA, without the TD VIV model, along with the wind and wave loads. Thus, the TD VIV model is accurately capturing the total motion of the structure, and the onset of VIM, which is none in this case, is also accurately captured. In other words, the TD VIV model is not producing VIM in cases it neither should not.

A final case worth investigating in some more detail is case 11. This case does also include tendencies to VIM, as for case 3, but not nearly as prominent. Nonetheless, it is interesting to see whether the TD VIV model is capturing the motions accurately. The translational motion in x- and y-directions are plotted in Fig. 5.10 for case 11. The VIM tendencies in the full-scale measurements can be seen as periodic oscillations in y-direction, most prominent of the second half of the time series. It is however observed that the simulated motions both with and without the TD VIV model is showing similar motion as the measurements in the y-direction. In fact, the motions with and without the TD VIV model are almost perfectly overlapping both in the x- and y-directions. In the x-direction the full-scale measurements does not include as much oscillation as the simulated motions, however, this does not originate from the TD VIV model as the motion is similar without the model.

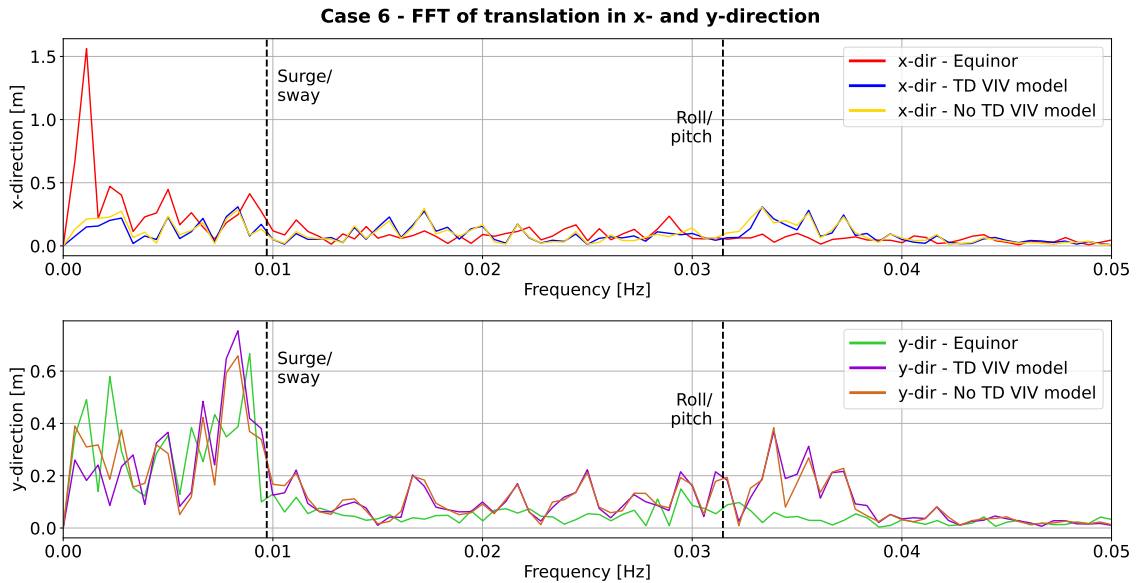


Figure 5.9: Fast Fourier transform of translation in x- and y-direction for case 6. The full-scale measurements from Equinor and the SIMA results both with and without the TD VIV model are shown.

The frequency spectra for the same case are also generated and are plotted in Fig. 5.11. The general agreement with and without the TD VIV model can clearly be seen also here as the two are mostly overlapping both in x- and y-directions. In the x-direction, small peaks are observed around the surge and sway, as well as the roll and pitch natural periods. These peaks are present both in the simulations with and without the TD VIV model, which suggests the motion is not produced by the VIV load terms in the TD VIV model. These peaks are however not present in the full-scale measurements. In the y-direction, similar peaks are observed around the same frequency components. In this direction, the peaks can however also be observed in the measurements, at least the peak around the surge and sway natural periods. This suggests that the simulations can accurately capture the motions for this case. The VIV load terms in the TD VIV model are not producing any VIM, which also is its ideal behaviour. All the motions present in the measurements are captured without the TD VIV model, and because the TD VIV model is producing very similar results as without it, the TD VIV model is again proving itself as an accurate VIM prediction tool.

A reminder is given that for the curious reader, a complete set of the translation plots and frequency spectra for all the cases is given in App. B.1. However, for all the other cases not discussed in detail here, similar behaviour as the one discussed can be found. For all cases the simulated motions with and without the TD VIV model are mostly overlapping or producing similar motions with similar frequency components. The simulated motions are also matching up good with the full-scale measurements for most of the cases. Even though the simulated motions are not necessarily perfectly replicating the full-scale measurements, generally the agreement is good. The fact that the TD VIV model is not producing any additional VIM which is not seen in the full-scale measurements is a very positive feature of the TD VIV model as a VIM prediction tool. This proves that the TD VIV model is able to predict accurate motions for cases where no to little VIM can be found.

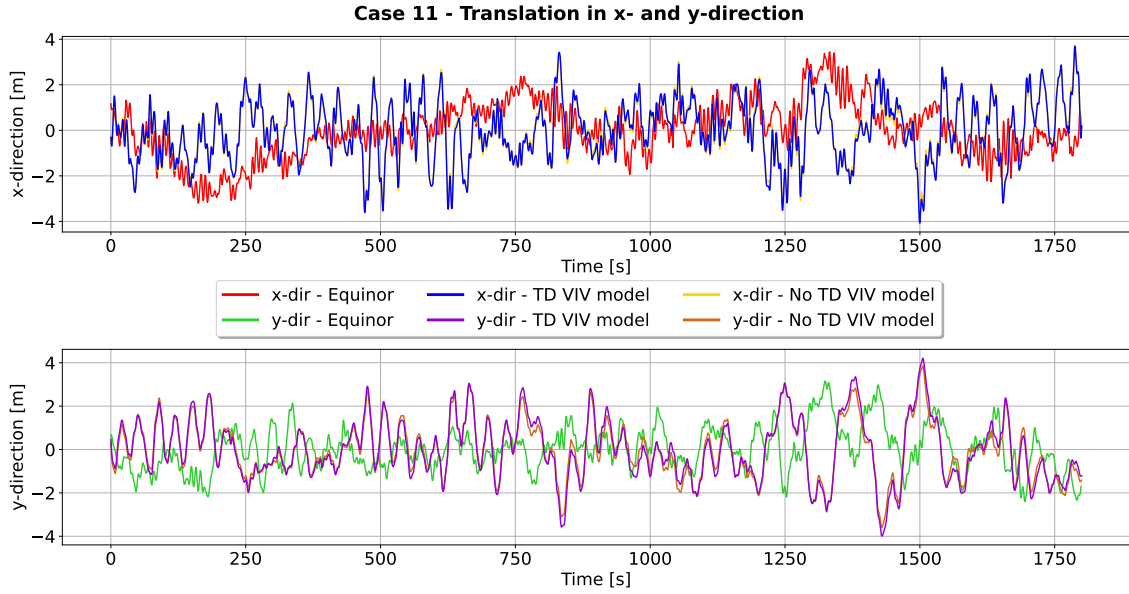


Figure 5.10: Translation in x- and y-direction for case 11. The full-scale measurements from Equinor and the SIMA results both with and without the TD VIV model are shown.

The ability of the model to predict accurate onset of VIM is difficult to validate with the provided cases. Only a few of the cases did in fact include tendencies of VIM, and for these cases the simulated motions without the TD VIV model was able to predict fairly accurate response. The only small exception was for case 3, where it could be argued that an ideal prediction tool would produce more VIM in the simulated motions, but as discussed the VIM was mild and not consistent so it would be difficult to capture perfectly in any way. It would be interesting to investigate simulated motions with the TD VIV model for cases including more VIM, if that can be obtained. This is also necessary to validate the TD VIV model as VIM prediction tool further and is recommended as further work.

In general, the validation of the TD VIV model against the full-scale measurements strengthened the potential of the TD VIV model to be used as a VIM prediction tool. For all the provided cases, the TD VIV model produces accurate motions as discussed in detail above. A calibration study on the customizable hydrodynamic coefficients and parameters of the TD VIV model was considered, but it was deemed unnecessary. The produced motion with the initial set of parameters gave satisfactory results, and a larger variety of case data with different environmental conditions are necessary to perform an accurate calibration study. This is however recommended as further work if more full-scale measurements or other case data can be obtained.



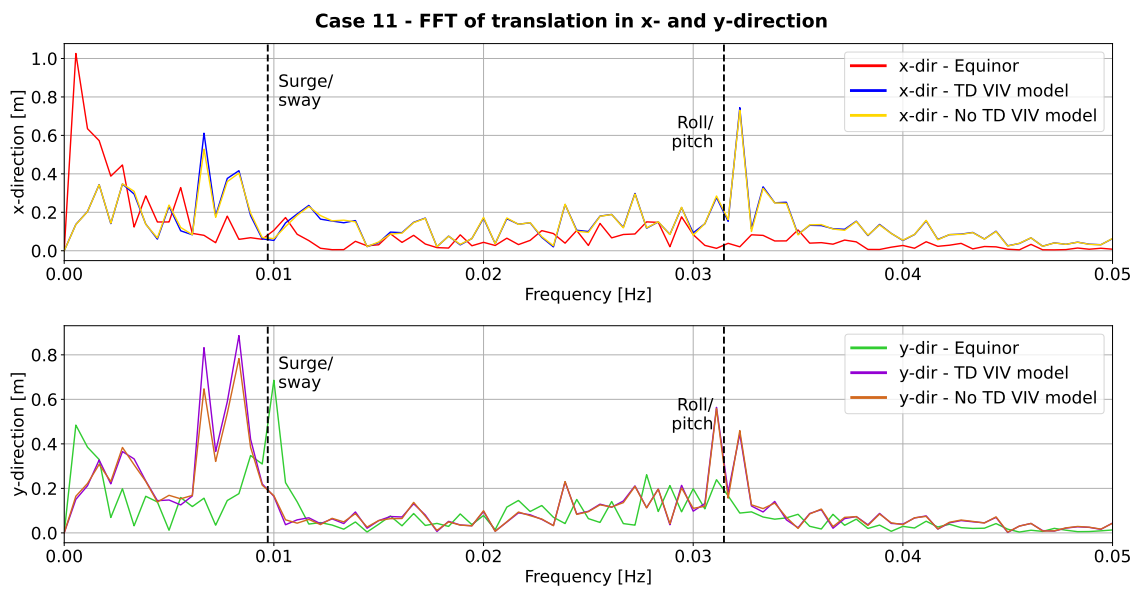


Figure 5.11: Fast Fourier transform of translation in x- and y-direction for case 11. The full-scale measurements from Equinor and the SIMA results both with and without the TD VIV model are shown.



# Chapter 6

## Case studies

With the TD VIV model validated against full-scale measurements, case studies were performed using the validated model. The case studies had two main objectives. The first was to investigate the respective importance of waves and wind on the VIM response using the TD VIV model. This was done to gain a better understanding of the importance of the different environmental loads with regards to onset of VIM, when using the TD VIV model as VIM prediction tool. The second objective was to investigate the effect on the fatigue life of the mooring system when analyzed with and without the use of the TD VIV model. This was done by applying a representative environmental condition over a full year on the modelled floating wind turbine structure and performing a fatigue analysis on the mooring system. This was done to investigate if the TD VIV model would produce any VIM of significance over a representative full year which would consequently affect the fatigue life of the mooring system.

### 6.1 Effect of wind and waves on VIM prediction

In the current section, the effect of wind and waves on the VIM prediction by the TD VIV tool will be investigated. The investigation was done by analyzing the same 11 cases as presented in Ch. 5. This was done as the 11 cases are already introduced and full-scale measurements and simulated response with and without the TD VIV model are already investigated. The 11 cases also include a variety of different environmental conditions so the respective effect of wind and waves on the VIM response can be analyzed individually for all of the cases. Each case was analyzed without wind, but including current and waves to investigate if the absence of wind had any effect on the VIM response of structure. The same procedure was done to investigate the effect waves. Each case was analyzed without the waves, both wind waves and swell waves, but including current and wind. The results from these analyses were then compared to the result from the analyses with the full environment including wind, waves and current. The results are presented in the same way as in Ch. 5 for the validation against the full-scale measurements. That is plots of the translation in x- and y-directions as well as frequency spectra of the translations to easier determine the different frequency components of the response and identify VIM response. In the following, a few interesting cases will be discussed in more detail, however, a complete set of the

results from the investigation on the effect of wind and waves on the VIM response can be found in App. B.2.

Firstly, case 1 is investigated. The translational motion in x- and y-directions are plotted in Fig. 6.1. Here, the simulated motion for the full environment, including all of wind, waves and current, are labeled "Full environment" and are plotted in blue and brown for the x- and y-direction respectively. The simulated motions without waves, but including current and wind are labeled "No wave" and are plotted in red and green for the x- and y-direction respectively. The simulated motions without wind, but including current and waves are labeled "No wind" and are plotted in orange and purple for the x- and y-direction respectively. Reference is also made to the figure legend. The results show that when the waves are removed, as expected the high-frequent response components in the wind wave and swell wave periods are also removed. However, the general response pattern is still very similar as the response obtained for the full environmental condition. This is shown by the mostly overlapping time series plots for the two conditions, and the observation is valid both in the x- and y-direction. However, when the wind is removed, the general response pattern is no longer recognizable. This indicates that wind is the governing loading on the structure response. It is observed that all of the motion when the wind is removed is mostly high-frequent around the wave periods.

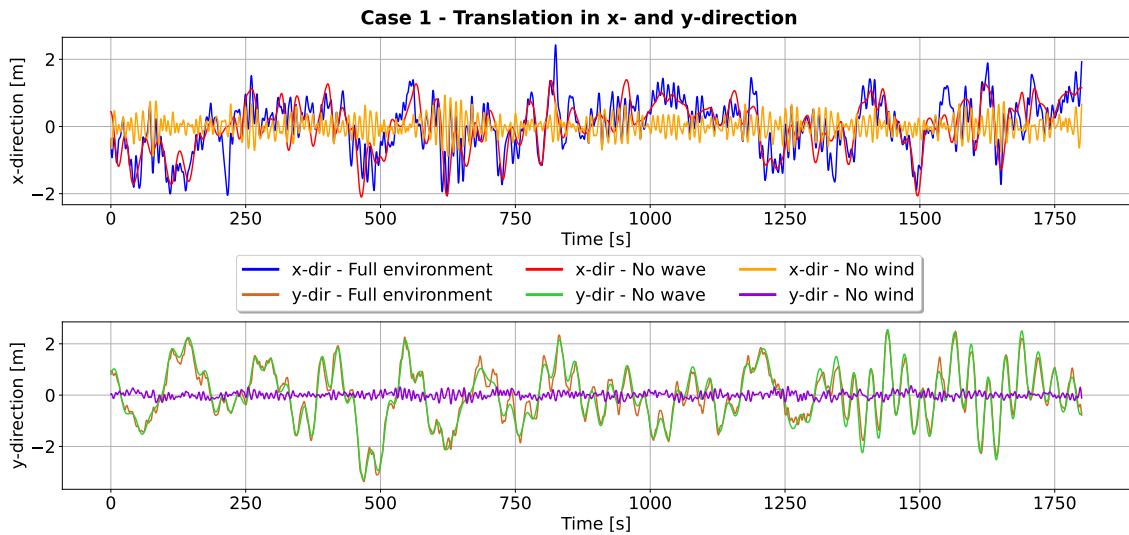


Figure 6.1: Translation in x- and y-direction for case 1. All lines show results with the TD VIV model for different metocean environments. Full environment consists of current, wind and waves.

The frequency spectra of the translational motion in x- and y-directions for case 1 are plotted in Fig. 6.2. The frequency components of the response around the wind wave and swell wave peak periods are not included in the frequency spectra as the main focus is on the VIM response. The VIM response generally occurs with much lower frequencies around the natural periods in surge and sway, eventually in roll and pitch. The frequency spectra does however show that the absence of waves does not affect the response in any noteworthy degree. This is seen by the mostly overlapping spectra for the full environment and the environment without waves, and holds for both x- and y-direction. This means no additional VIM is produced by the TD VIV model by removing the waves, which suggests that the TD VIV model is not greatly affected by the waves.

For the frequency spectra with no wind, almost no components can be observed at all. Again note that the response components caused by the waves lie outside of the plotted interval. It is observed that the absence of wind, as with the waves, does not produce any additional VIM. This also suggest that the wind has little contribution the VIM response for this case.

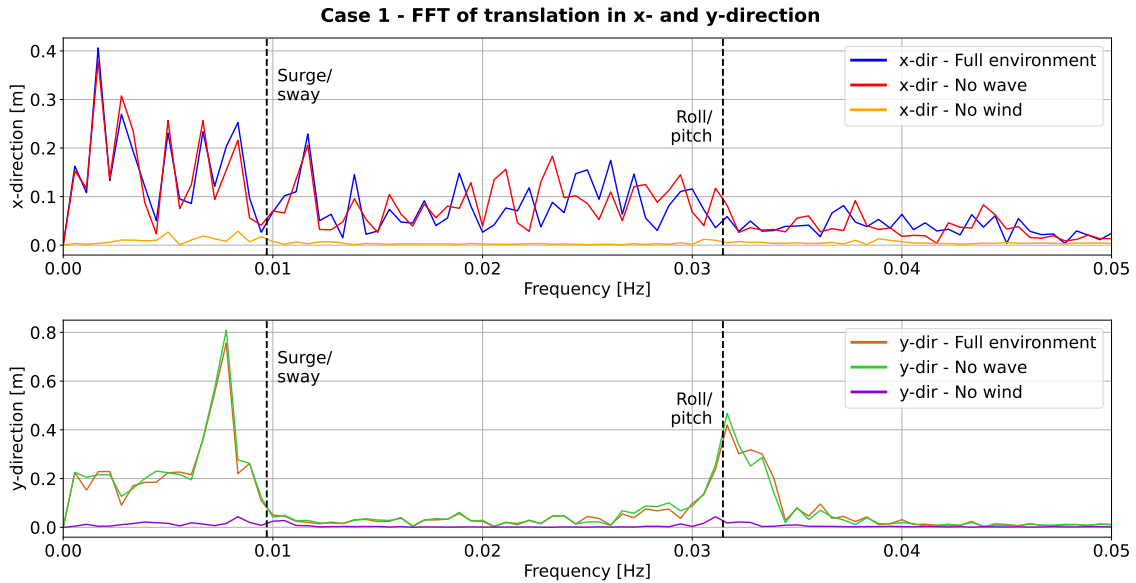


Figure 6.2: Fast Fourier transform of translation in x- and y-direction for case 1. All lines show results with the TD VIV model for different metocean environments. Full environment consists of current, wind and waves.

For case 2, some other interesting results are produced. The translation in x- and y-direction are plotted in Fig. 6.3. For the time series where the waves were removed, the same tendencies as seen in case 1 is also observed for case 2. The waves seem to have little influence on the overall response, as well as the VIM response. For the time series where the wind is removed, there is however observed a small amount of VIM both in the x- and y-directions. The VIM amplitude is very low, even significantly lower than the general response amplitude for the full environment, especially for the y-direction. Case 2 is one of the cases with the highest current speed so it would be expected to observe VIM for this case, if for any. The observed VIM when the wind was removed indicates that the wind does in fact affect the predicted VIM predicted by the TD VIV model.

The frequency spectra for case 2 are also produced and are plotted in Fig. 6.4. For the spectra without the wind, clear peaks around the surge and and sway natural periods can be seen. In x-direction the magnitude reaches around the same magnitude as the response for the full environment, while in the y-direction, the magnitude is smaller, but still visible on the spectrum. It is also observed that these peaks are dominating the response for this condition, and the fact that the response is around the natural period in surge and sway indicates VIM. This shows that the TD VIV model is actually producing VIM for this case when the wind is removed. Even though the VIM amplitude is low, the VIM is dominating the response and can be argued to be of significance. This is an interesting observation which should be noted. The frequency spectra for the condition with no waves also show no to little difference from the condition with the full environment. This supports the claim of little influence of waves on predicted VIM.

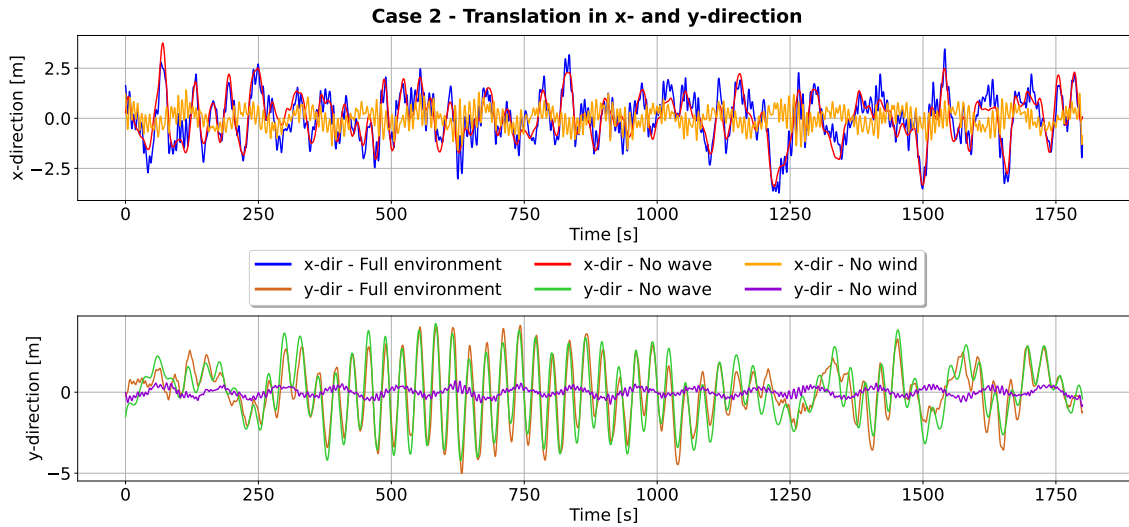


Figure 6.3: Translation in x- and y-direction for case 2. All lines show results with the TD VIV model for different metocean environments. Full environment consists of current, wind and waves.

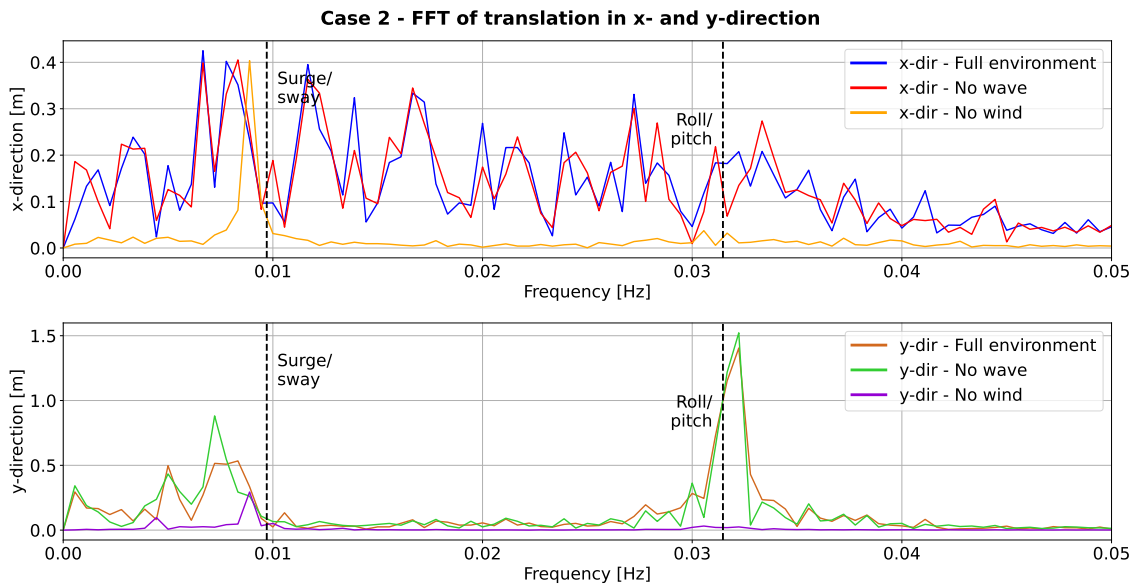


Figure 6.4: Fast Fourier transform of translation in x- and y-direction for case 2. All lines show results with the TD VIV model for different metocean environments. Full environment consists of current, wind and waves.

Case 3 is also worth looking into in some more detail. The translation in x- and y-directions are plotted in Fig. 6.5. For the condition without waves, the same tendencies as for both case 1 and case 2 can be seen both in x- and y-direction. In general the waves does not seem to affect the VIM prediction. For the condition without the wind however, VIM can be observed, but only in x-direction. The frequency spectra for this case are plotted in Fig. 6.6 and illustrates this more

clearly. It is observed that in the x-direction, the condition without wind has a dominating peak around the natural surge and sway periods. This indicates the VIM observed in the time series. In the x-direction, it is worth mentioning that a small peak around the same frequency is observed, but the magnitude is very low, and it was barely not even recognizable in the time series. The fact that only the x-direction gives significant VIM is interesting and could be a consequence of the current and wave directional combination. The nonexistent effect from the absence of the waves can also be observed in the frequency spectra.

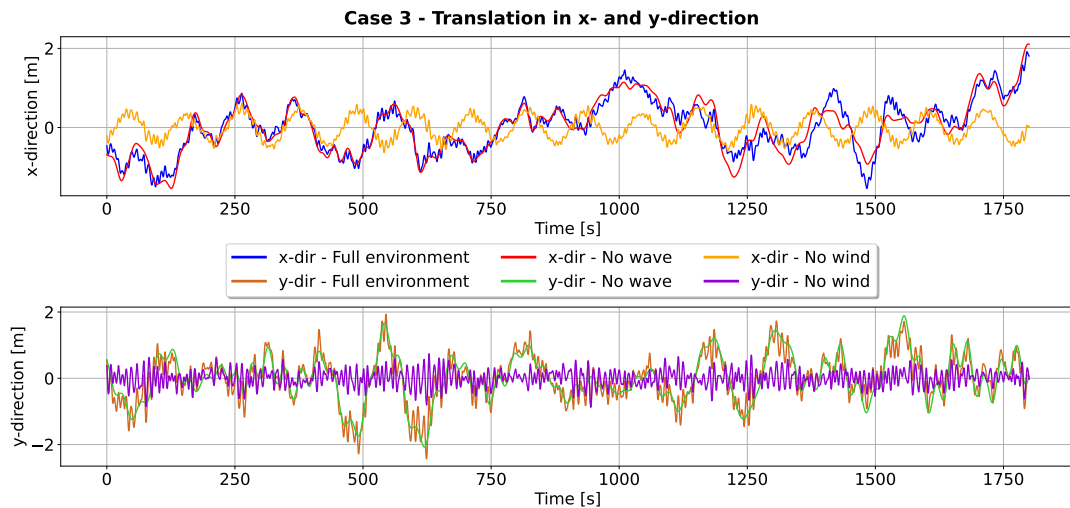


Figure 6.5: Translation in x- and y-direction for case 3. All lines show results with the TD VIV model for different metocean environments. Full environment consists of current, wind and waves.

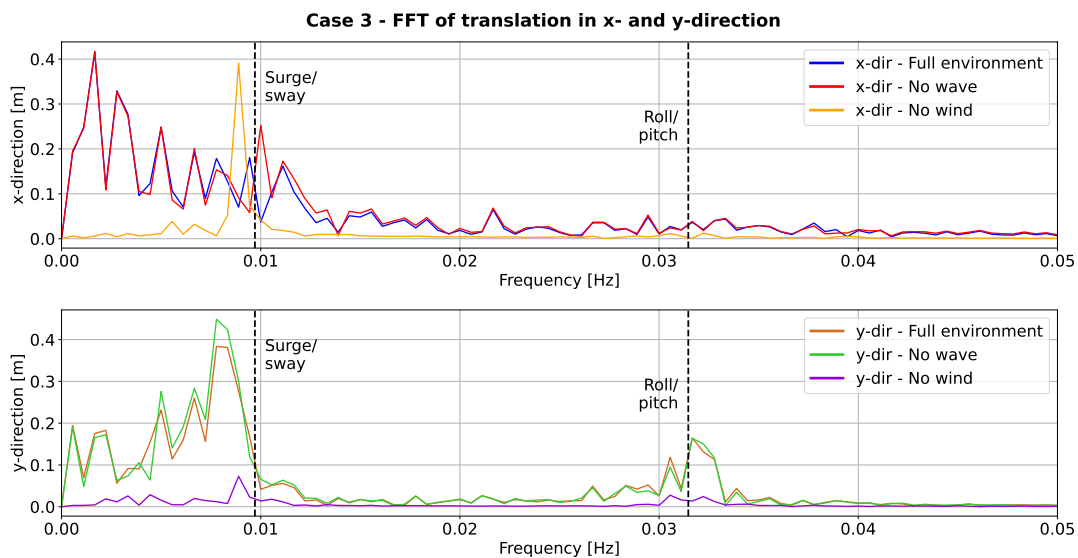


Figure 6.6: Fast Fourier transform of translation in x- and y-direction for case 3. All lines show results with the TD VIV model for different metocean environments. Full environment consists of current, wind and waves.

Case 8 is also briefly discussed here as significant VIM is observed in this case as well. The translational plot is shown in Fig. 6.7 and the frequency spectra in Fig. B.38. Again, the waves does not seem to have any effect on the VIM response in neither the x- or y-direction. The absence of the wind is however generating significant VIM, especially in the y-direction but also some in the x-direction, as seen by the oscillations in the time series. The frequency spectra also captures the VIM as peaks around the surge and sway natural periods. The magnitude of the peak in the y-direction is quite significant. Compared to case 3, where VIM was only observed in the x-direction, it is interesting that case 8 is mainly giving VIM in the y-direction. Obviously this could be due to the change in direction of the applied wave and current conditions, but an effect of the directional combinations of current and waves might also have an impact. In any case, the absence of wind is causing the TD VIV model to produce additional VIM not seen in the simulations with the full environment.

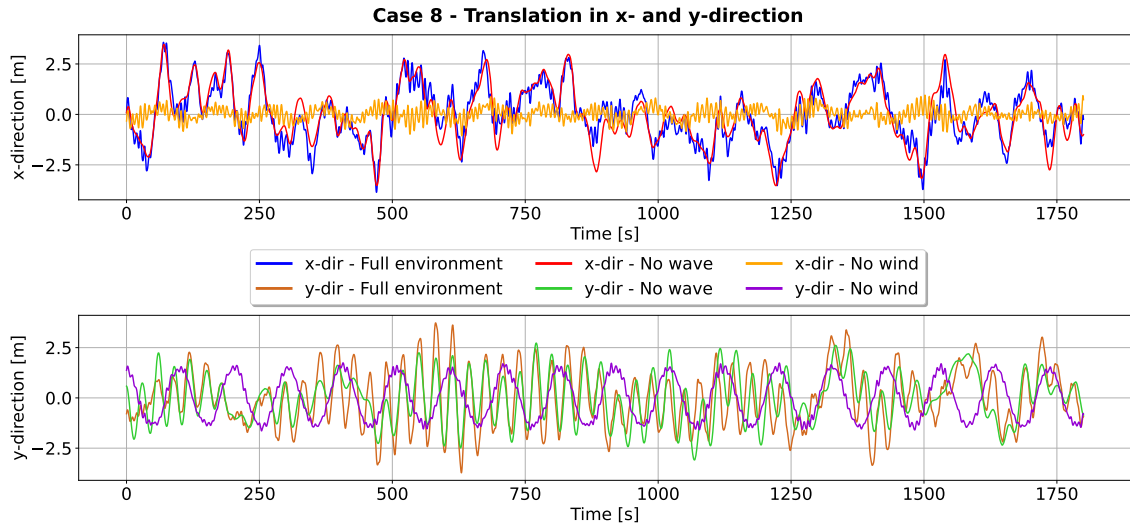


Figure 6.7: Translation in x- and y-direction for case 8. All lines show results with the TD VIV model for different metocean environments. Full environment consists of current, wind and waves.

The remainder of the cases not discussed in this section does not include any additional features of significance concerning the predicted VIM response. Most of the other cases did not produce any additional VIM, neither in x- and y-direction for neither the conditions with removed wind or removed waves. This indicates that in general, the waves does not affect the VIM prediction of the TD VIV model, while the wind for some certain cases has an effect. Especially the cases with the highest current speeds showed tendencies to VIM in the simulated motions when the wind was removed. A remainder is also given to the curious reader that a complete set of the translational plots and frequency spectra for all the cases investigating the effect of wind and waves on the VIM prediction can be found in App. B.2.



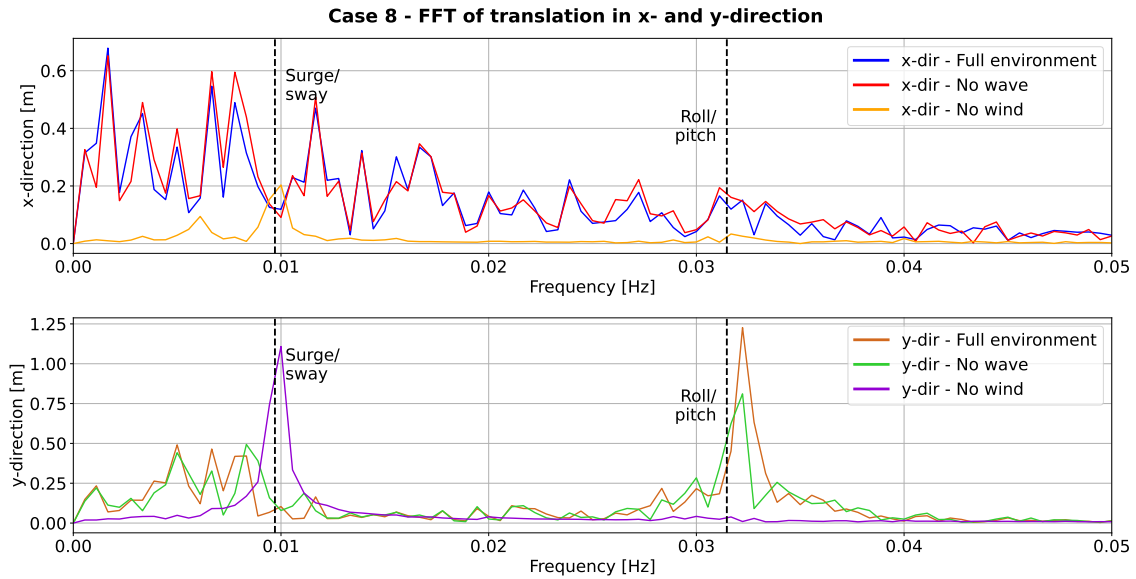


Figure 6.8: Fast Fourier transform of translation in x- and y-direction for case 8. All lines show results with the TD VIV model for different metocean environments. Full environment consists of current, wind and waves.

## 6.2 Representative full year environmental conditions

The objective of the second part of the case studies was to investigate the effect of the fatigue life on the mooring system when analyzed with and without the TD VIV model. It was investigated if the TD VIV model would predict significant VIM over a representative full year which would consequently reduce the lifetime of the mooring system compared to analyzes without the TD VIV model. To perform this investigation, a representative full year environmental condition first had to be established. This was done by considering probability distributions of the the different environmental parameters and creating ten intervals with equal probability of occurrence. Then the expected value within each interval was extracted and used to generate ten different full year environmental conditions. The detailed procedure and values are given in the following.

### 6.2.1 Wave condition

Firstly, a probability distribution for the wave statistics at the site of the Hywind Scotland wind park was obtained. This was found in the Hywind Buchan Deep metocean design basis [71]. Buchan Deep is the name of the site where the wind park is located. An annual Weibull distribution of significant wave height wave height was given. The general cumulative Weibull distribution was introduced in Ch. 5, specifically in Eq. 5.1. The Weibull parameter for the significant wave height at Buchan Deep are listed in Tab. 6.1 and the distribution is plotted in Fig. 6.9. The distribution is divided into ten intervals with equal probability of occurrence, which are also indicated in the figure. The expected value within each interval was then calculated and are also marked with red dots and its respective value in the figure. These ten values are then used to generate the representative full year environmental description.

Table 6.1: Weibull parameters for significant wave height at Buchan Deep.

Parameter	Value
$\varepsilon$	0.32
$\theta$	1.51
$\gamma$	1.301

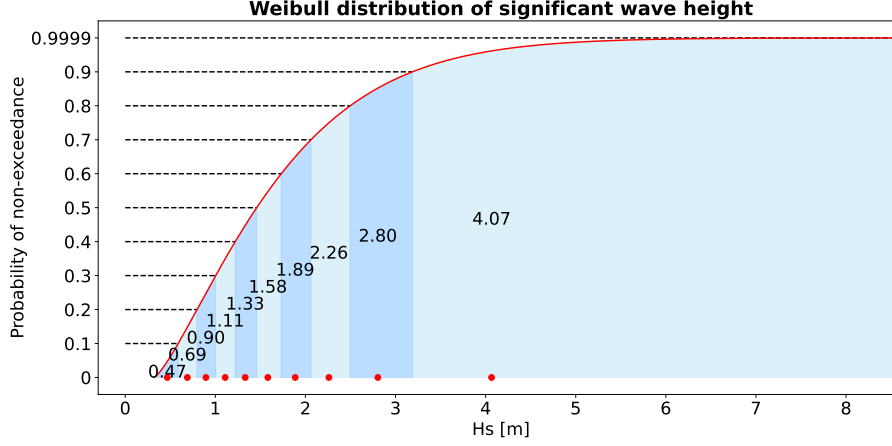


Figure 6.9: Weibull distribution of significant wave height at Buchan Deep.

The probability distribution for the peak period was found given the significant wave height for each individual value. A scatter plot of spectral peak period for given significant wave height at Buchan Deep is shown in Fig. 6.10. The probability distribution of peak period given significant wave height was given in [71] and defined as:

$$f_{T_p|H_s}(t_p|h_s) = \frac{1}{t_p \cdot \sigma \sqrt{2\pi}} \cdot \exp\left(-\frac{(\ln(t_p) - \mu)^2}{2 \cdot \sigma^2}\right), \quad (6.1)$$

where

$$\mu = a_1 + a_2 \cdot h_s^{a_3}, \quad (6.2)$$

and

$$\sigma^2 = b_1 + b_2 \cdot \exp(-b_3 \cdot h_s). \quad (6.3)$$

The values of the parameters  $a_1$ ,  $a_2$ ,  $a_3$ ,  $b_1$ ,  $b_2$  and  $b_3$  are listed in Tab. 6.2.

Table 6.2: Parameters in the peak period Weibull distribution given significant wave height.

Parameter	Value
$a_1$	1.307
$a_2$	0.567
$a_3$	0.369
$b_1$	0.005
$b_2$	0.119
$b_3$	0.425

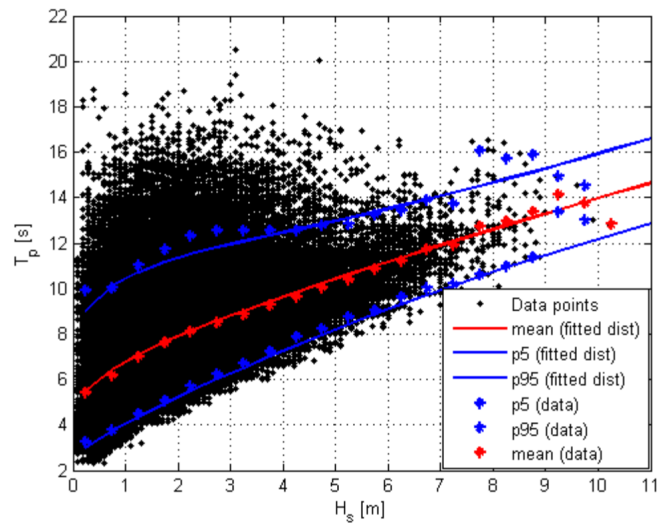


Figure 6.10: Spectral peak period for given significant wave height at Buchan Deep. The figure is from [71].

The all-year wave rose at Buchan Deep for the period 1958-2010 is also presented [71], and can be seen in Fig. 6.11. The wave rose shows the sample direction distribution of significant wave height over a full year. The direction convention follows the definition used in the full-scale measurement data, which were defined in Fig. 5.1. It is observed that the most dominant wave direction is 0 degrees, meaning waves coming from the north. This wave direction is the direction used in the representative full year environmental condition.

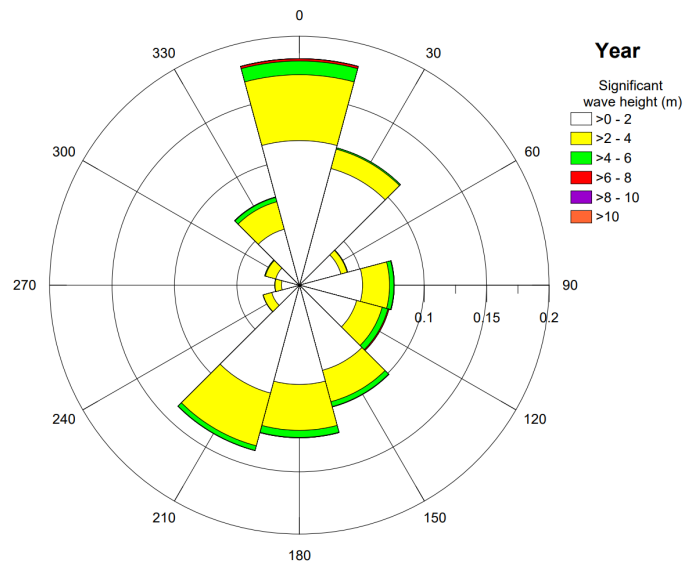


Figure 6.11: All-year wave rose at Buchan Deep for the period 1958 - 2010. The figure is from [71].

### 6.2.2 Wind condition

A similar procedure as for the wave condition is done for the wind condition. A probability distribution for the wind statics at Buchan Deep was obtained from the Hywind design basis [71]. The distribution was given as a Weibull distribution with parameters as listed in Tab. 6.3. The distribution is also plotted in Fig. 6.12, and divided into ten intervals. The intervals have equal probability of occurrence. The expected value within each interval is found and marked in the figure with red dots. The respective values are also included in the figure.

Table 6.3: Weibull parameters for wind speed at 10 meters above sea level at Buchan Deep.

Parameter	Value
$\varepsilon$	-0.41
$\theta$	10.03
$\gamma$	2.235

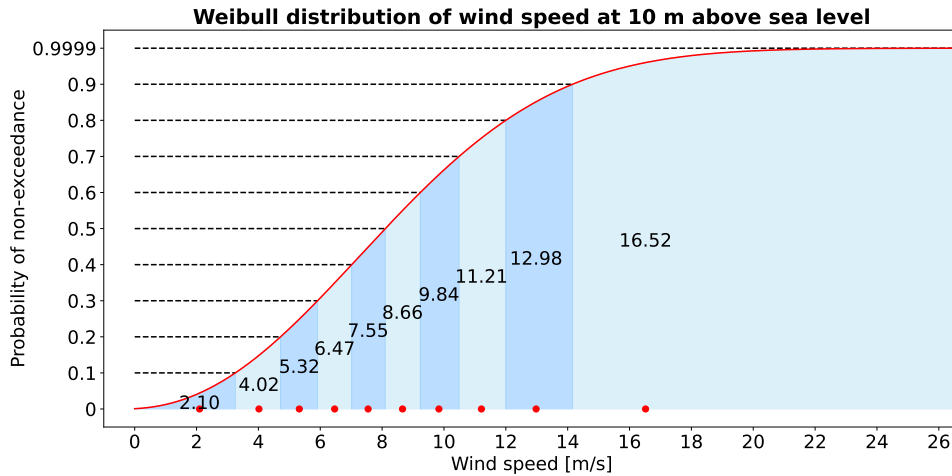


Figure 6.12: Weibull distribution of wind speed at 10 meters above sea level at Buchan Deep.

The hub height of the Hywind Scotland wind turbine is 98.4 meters above sea level, so the wind speed at the 10 meters above sea level has to be adjusted in order to represent the expected wind speed at the hub. This is done by using the wind profile defined in the design basis [71]. The wind profile was defined as:

$$U(z) = U_0 \cdot \left( 1 + C \cdot \ln \left( \frac{z}{z_r} \right) \right), \quad (6.4)$$

where

$$C = 5.73 \cdot 10^{-2} \cdot \left( 1 + 1.5 \cdot \frac{U_0}{U_{ref}} \right)^{\frac{1}{2}}. \quad (6.5)$$

Here,  $U(z)$  is the wind speed at  $z$  meters above sea level,  $z_r = 10$  meters is the reference elevation above sea level,  $U_0$  is the wind speed at the reference elevation,  $z_r$ , and  $U_{ref} = 10$  m/s is the reference wind speed. By inserting  $z = 98.4$  and the expected wind speed at 10 meters above sea level as  $U_0$ , the expected wind speed at 98.4 meters is found. This is done for all of the 10 probability intervals.

Next, the turbulence intensity had to be determined for the ten different wind conditions with equal probability of occurrence. The turbulence intensity,  $I_u$ , is given by:

$$I_u = 0.06 \cdot \left(1 + 0.43 \cdot \frac{U_0}{U_{ref}}\right) \cdot \left(\frac{z}{z_r}\right)^{-0.22} \quad \text{for } U_0 > 12.0 \text{ m/s}, \quad (6.6)$$

and

$$I_u = \frac{a \cdot \exp(0.09 \cdot U(z))}{U(z)} \quad \text{for } U_0 < 12.0 \text{ m/s}, \quad (6.7)$$

where  $U(z)$  is defined by the wind profile in Eq. 6.4. The  $a$ -parameter is defined as:

$$a = I_u \cdot \exp(-0.09 \cdot U(z)) \cdot U(z) \quad \text{for } U_0 = 12.0 \text{ m/s}. \quad (6.8)$$

The computed turbulence intensity for different wind speeds is compared to the turbulence intensity determined from measurements at 100 meters above sea level at station FINO 3, which is a research platform located in the German Bight in the North Sea. This is shown in Fig. 6.13. It is observed that the computed turbulence intensity shows good correlation with the measurements in the German Bight. Obviously this is not where the Hywind Scotland wind park is located, but the turbulence intensity is assumed to be the same for the two locations as no other data was obtained. Using this procedure, the turbulence intensity for the ten different probability intervals was calculated.

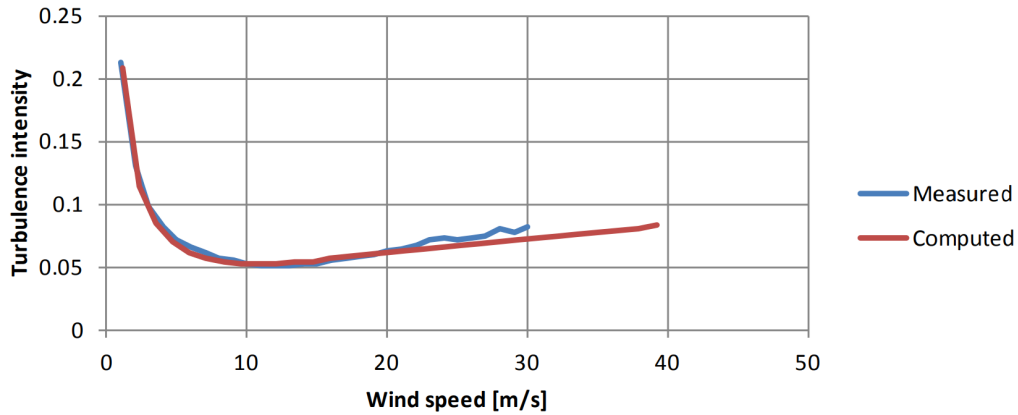


Figure 6.13: Computed turbulence intensity compared to turbulence intensity measurements at 100 m above sea level at FINO 3. The figure is from [71].

The direction of the representative full year wind condition was determined using the wind roses at Buchan Deep. The wind roses for the 1 hour average wind speed at different heights above sea level at Buchan Deep for the period 1958-2010 are shown in Fig. 6.14. The direction convention follows the definition used in the full-scale measurement data defined in Fig. 5.1. The wind roses shows the annual sample distribution of 1 hour average wind speed at the site. It is observed that 210 degrees is the most dominating wind speed both at 10 meters and 100 meters above sea level. This direction is therefore used as the wind direction in the representative full year environmental condition.

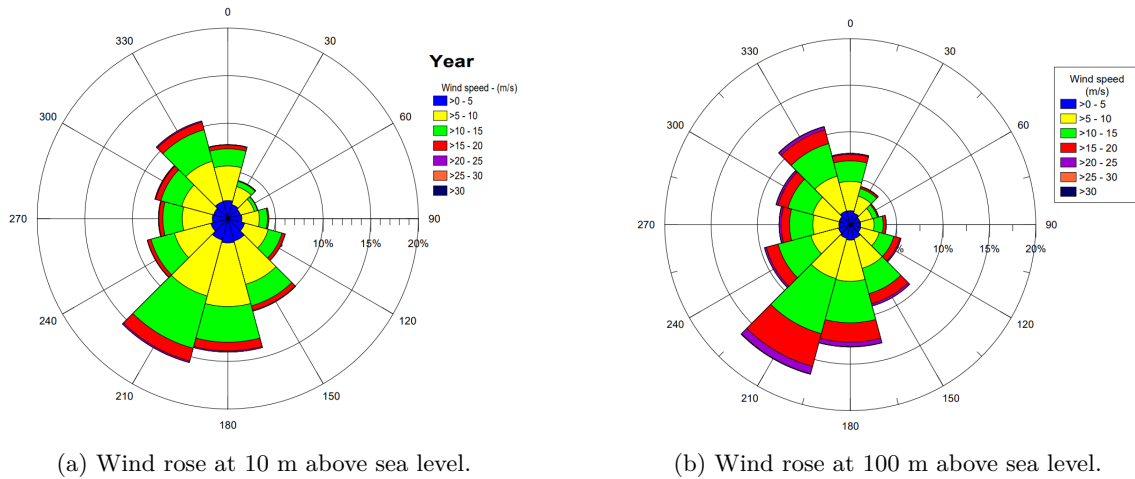


Figure 6.14: Wind roses for the 1 hour average wind speed at different height above sea level at Buchan Deep for the period 1958 - 2010. The figures are from [71].

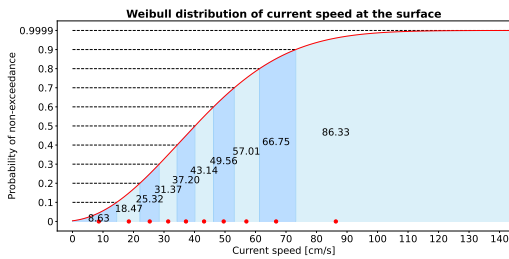
### 6.2.3 Current condition

A representative full year current condition also had to be established in order to obtain a representative full year environmental condition. The probability distribution for the current speed was included in the design basis for several depths [71]. The Weibull parameters for the different depths are listed in Tab. 6.4, and the distributions are plotted in Fig. 6.15. It is worth mentioning that the current distributions only contain data from November 2013 to March 2014. This does cover the winter season, which historically contains the harshest environmental conditions, so the estimate of using this data should be conservative. However, the current speeds might be overestimated over the full year by using this approach, which should be noted. This could for example lead to overestimated VIM produced by the TD VIV model. Even though a data set covering a full year would give more accurate conditions, it was not possible to obtain. The conservatism is therefore included and is worth remembering. The Weibull distributions are also divided into ten interval, each with equal probability of occurrence, which are indicated in the figure. Then, the expected value within each interval was calculated, and are marked on the probability distribution plot as red dots. The actual values are also included in the figure. These are the values that are used to create the representative full year current condition.

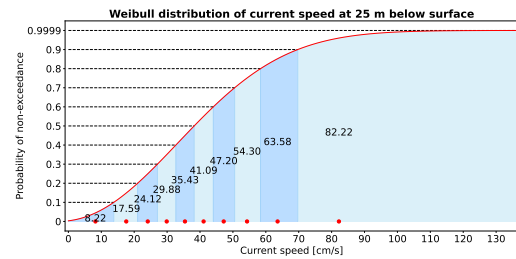
Table 6.4: Weibull parameters for current speed at different depths at Buchan Deep.

Parameter	Surface	-25 m	-40 m	-60 m	-70 m	-90 m
$\varepsilon$	-3.57	-3.40	-5.85	-7.45	-6.97	-3.97
$\theta$	51.90	49.43	50.36	49.80	47.93	40.48
$\gamma$	2.131	2.131	2.224	2.341	2.369	2.331

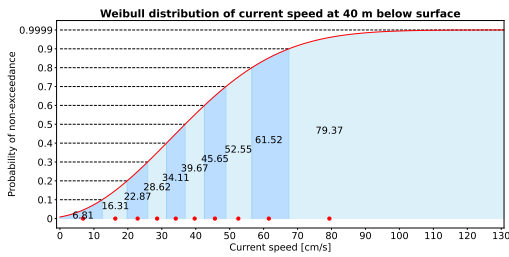
To obtain the current directions, the same procedure as for the wind and waves is applied. The current roses for different depths at Buchan Deep are shown in Fig. 6.16. A current rose at the surface was not included in the design basis [71]. The direction convention in the current roses also follows the definition used in the full-scale measurement data, which were defined in Fig. 5.1. As for the probability distributions, the current roses also only contain data from November 2013



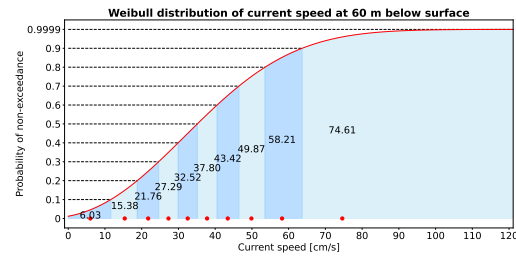
(a) Weibull distribution of current speed at the surface.



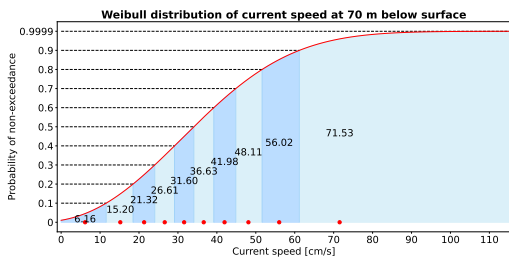
(b) Weibull distribution of current speed at 25 m below surface.



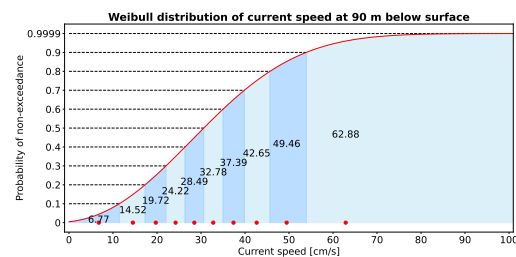
(c) Weibull distribution of current speed at 40 m below surface.



(d) Weibull distribution of current speed at 60 m below surface.



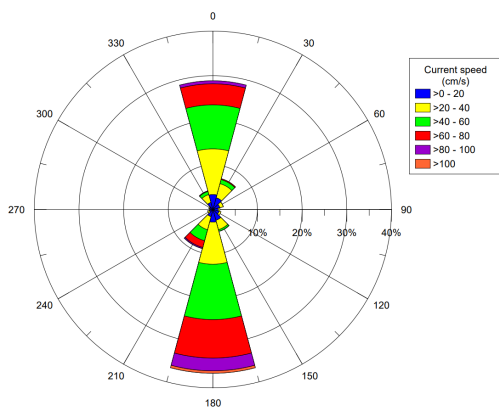
(e) Weibull distribution of current speed at 70 m below surface.



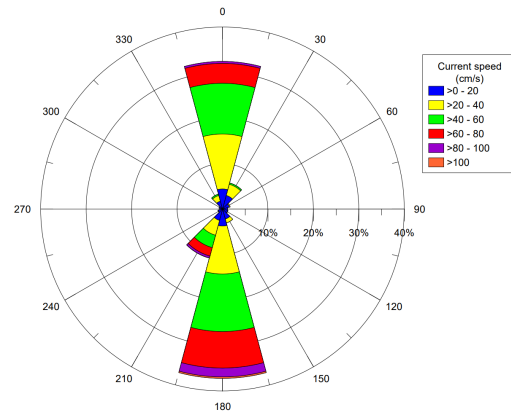
(f) Weibull distribution of current speed at 90 m below surface.

Figure 6.15: Cumulative Weibull distributions of current speeds at different depths at Buchan Deep. The distributions are divided in ten intervals with equal probability of occurrence and the expected value within each interval is presented.

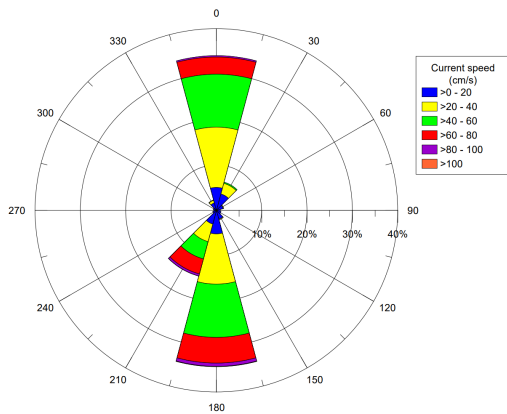
to March 2014. A clear trend in the current roses are observed due to the tide. The directions 0 degrees and 180 degrees are dominating the current roses with approximately equal contributions. This indicates that one of the directions are present when the ocean is ebbing, while the other direction is present when the ocean is flowing. In other words, the current direction should, for the most part at least, be consistent over the water depth. It is however observed that the most dominant direction varies with different depths. Therefore a single direction is chosen to represent the current direction through the whole water column when establishing the representative full year current condition. The direction of 180 degrees, meaning current coming from the north, was chosen as this direction was the dominant for three of the five current roses.



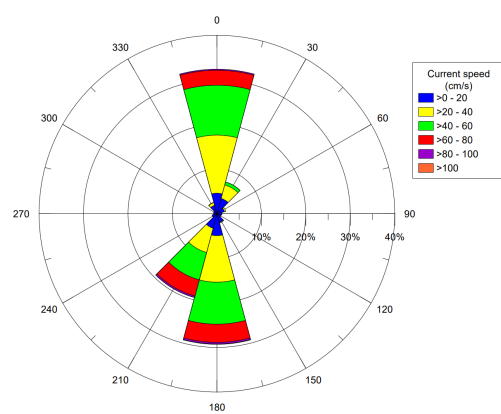
(a) Current rose at 25 m below the surface.



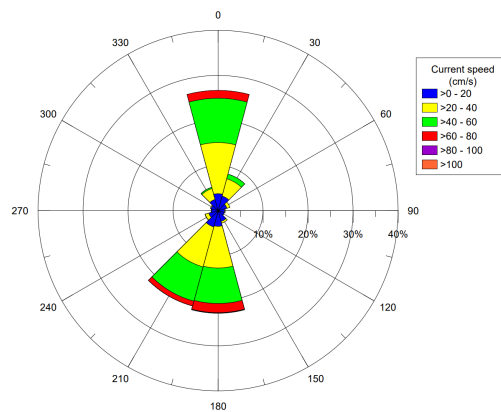
(b) Current rose at 40 m below the surface.



(c) Current rose at 60 m below the surface.



(d) Current rose at 70 m below the surface.



(e) Current rose at 90 m below the surface.

Figure 6.16: Current roses for different depths at Buchan Deep for the period November 2013 - March 2014. The figures are from [71].



### 6.2.4 Complete full year environmental condition

The representative full year wave, wind and current conditions have to be combined in order to establish a representative full year complete environmental condition. The correlation between the different environmental conditions is unknown so simplifications and assumptions have to be made. In addition, considerations regarding the computational cost of the analyses also have to be made. It was therefore decided to create ten different complete full year environmental conditions which in theory should have equal probability of occurrence. The mildest wave condition was combined with the mildest wave condition and the mildest current condition. The second mildest wave condition was combined with the second mildest wind condition and second mildest current condition, and so on all the way until the harshest conditions. This method of combining the different environmental conditions is obviously a huge simplification and this should be taken into account when the results are analysed. The different combined conditions are labeled from 1 to 10 where "full year environment 1" contains the mildest conditions with probability of non-exceedance from 0 to 0.1, while "full year environment 10" contains the harshest conditions with probability of non-exceedance from 0.9 to 0.9999. These ten different environments are listed in Tab. 6.5 for the wave and wind conditions, and Tab. 6.6 for the current conditions.

Table 6.5: Complete representative full year environmental conditions for wave and wind parameters.

Probability of non-exceedance	Wave				Wind	
	Hs [m]	Tp [s]	Dir. (Equinor) [deg]	Magn. [m/s]	Turb. intensity [%]	Dir. (Equinor) [deg]
0-0.1	0.47	5.97	0	2.41	10.60	210
0.1-0.2	0.69	6.35	0	4.68	6.84	210
0.2-0.3	0.90	6.65	0	6.26	5.96	210
0.3-0.4	1.11	6.93	0	7.65	5.56	210
0.4-0.5	1.33	7.19	0	8.99	5.36	210
0.5-0.6	1.58	7.47	0	10.38	5.28	210
0.6-0.7	1.89	7.79	0	11.86	5.29	210
0.7-0.8	2.26	8.15	0	13.62	5.40	210
0.8-0.9	2.80	8.64	0	15.90	5.65	210
0.9-0.9999	4.07	9.70	0	20.55	6.21	210

Table 6.6: Complete representative full year environmental conditions for current parameters.

Probability of non-exceedance	Current speed [m/s]						Current direction [deg]
	Surface	-25 m	-40 m	-60 m	-70 m	-90 m	
0-0.1	0.0863	0.0822	0.0681	0.0603	0.0616	0.0677	180
0.1-0.2	0.1847	0.1759	0.1631	0.1538	0.1520	0.1452	180
0.2-0.3	0.2532	0.2412	0.2287	0.2176	0.2132	0.1972	180
0.3-0.4	0.3137	0.2988	0.2862	0.2729	0.2661	0.2422	180
0.4-0.5	0.3720	0.3543	0.3411	0.3252	0.3160	0.2849	180
0.5-0.6	0.4314	0.4109	0.3967	0.3780	0.3663	0.3278	180
0.6-0.7	0.4956	0.4720	0.4565	0.4342	0.4198	0.3739	180
0.7-0.8	0.5701	0.5430	0.5255	0.4987	0.4811	0.4265	180
0.8-0.9	0.6675	0.6358	0.6152	0.5821	0.5602	0.4946	180
0.9-0.9999	0.8633	0.8222	0.7937	0.7461	0.7153	0.6288	180

### 6.3 Results and discussion of the full year environmental conditions

The 10 different representative full year environmental conditions were then analyzed in SIMA both with and without the TD VIV model. The procedure for analyzing the different conditions is the same as previously discussed and used for the full-scale measurements cases. The results are also presented in a similar manner as the previous results in this thesis. The translation in x- and y-directions are plotted as time series, and frequency spectra of the translations are also generated. In the following the most interesting results are presented and discussed in detail, but for the curious reader, a complete set of all the translational plots and frequency spectra for the representative full year environmental conditions can be found in App. B.3.

For the mildest environmental conditions, good agreement between the simulated motions with and without the TD VIV model is observed. This can for example be seen in Fig. 6.17, where the translation in x- and y-direction for full year environment 4 are plotted. It is observed that the simulated motions are almost perfectly overlapping, which indicates the VIV loads terms in the TD VIV model is not producing any additional VIM for this environmental condition. Similar time series as then ones shown for full year environment 4, can be seen for full year environment 1 through to full year environment 6. The frequency spectra for full year environment 6 are plotted in Fig. 6.18. For this condition, some minor discrepancies between the simulated motions with and without the TD VIV model is starting to appear, as seen in low-frequency part of the spectra especially for the y-direction. However, the discrepancies are small, and the magnitude of the peak around the surge and sway natural periods is actually larger without the TD VIV model than with it in the y-direction. This indicates that the VIV load terms in the TD VIV model are not actually producing any additional VIM, but the fact the discrepancies are presents suggest that it is not far from it. This becomes clear when the next full year environment is investigated.

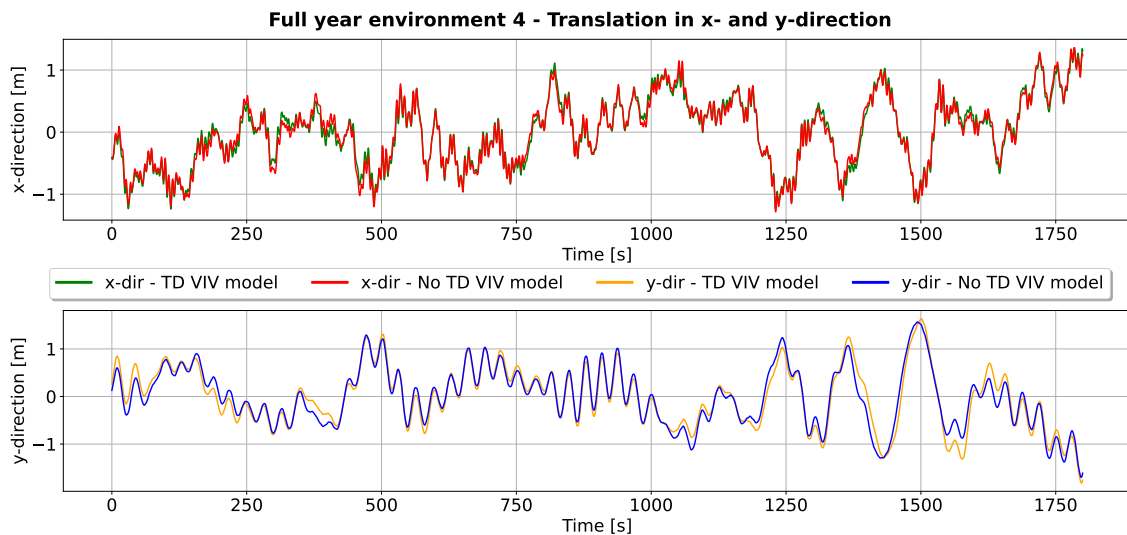


Figure 6.17: Translation in x- and y-direction for full year environment 4. Results both with and without the TD VIV model are shown.

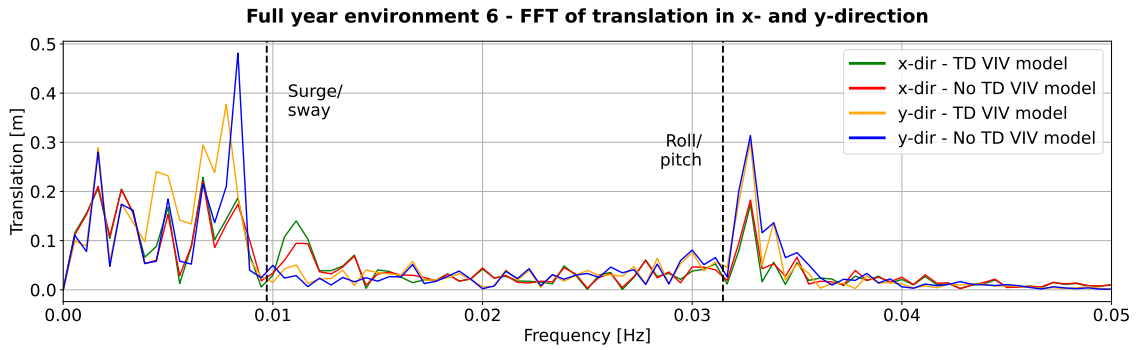


Figure 6.18: Fast Fourier transform of translation in x- and y-direction for full year environment 6. Results both with and without the TD VIV model are shown.

The translation in x- and y-directions for full year environment 7 are plotted in Fig. 6.19. Here it is observed that the simulated motions with the TD VIV model are no longer following the simulated motions without the TD VIV model as accurately as for the milder environmental conditions. This is mainly true for the y-direction, while in the x-direction, the simulated motions are still pretty similar with and without the TD VIV model. In the y-direction the oscillation amplitude seems to be increasing when the TD VIV model is used, which could indicate VIM. To look further into the frequency components, the frequency spectra for full year environment 7 are plotted in Fig. 6.20. In this plot, the difference between the results with and without the TD VIV model becomes quite obvious. In the y-direction, the peak around the surge and sway natural period is significantly larger for the analysis with the TD VIV model, than without it. A small additional peak in the x-direction is also observed around the same area in the frequency spectrum with the TD VIV model. These observations indicates additional VIM produced by the VIV load terms in

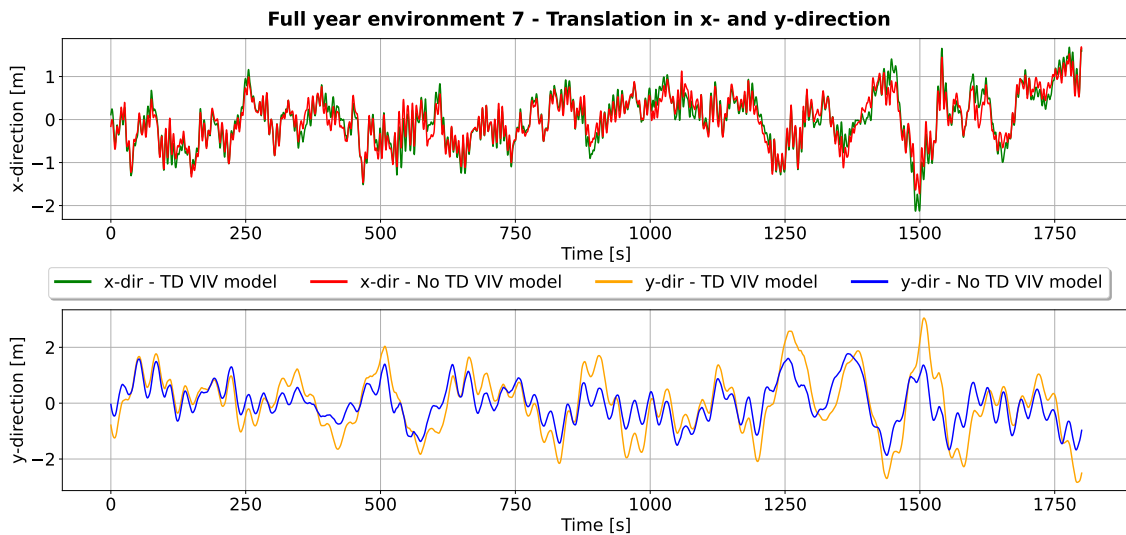


Figure 6.19: Translation in x- and y-direction for full year environment 7. Results both with and without the TD VIV model are shown.

the TD VIV model. The fact that additional VIM is predicted by the TD VIV model already on the seventh out of ten representative full year environmental conditions suggests that VIM might actually be a significant factor in response pattern of the floating wind turbines in the Hywind Scotland wind park. In fact, there are still three conditions with even higher current speeds than full year environment 7, where more VIM is expected. These conditions are looked into next.

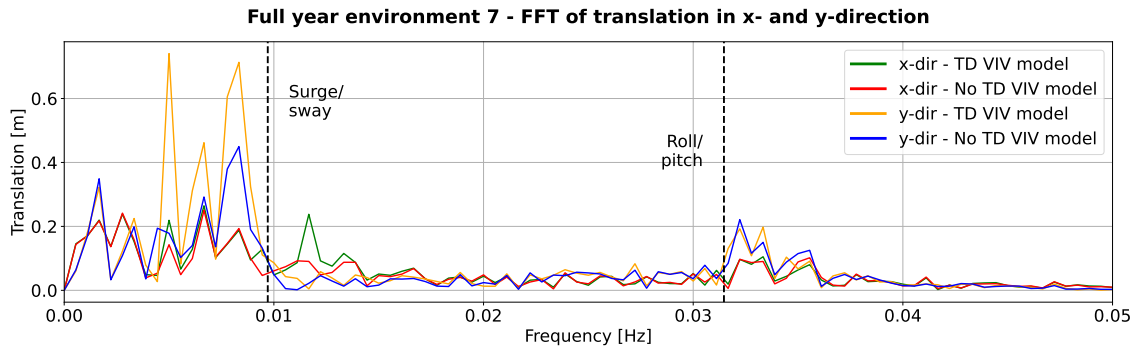


Figure 6.20: Fast Fourier transform of translation in x- and y-direction for full year environment 7. Results both with and without the TD VIV model are shown.

The frequency spectra for full year environment 8 and 9 and plotted in Figs. 6.21 and 6.22 respectively. It is observed that more and more VIM is produced, the harsher the environmental condition is. This is most likely due to the increase in current speed over the different environmental conditions. The VIM can be seen by the clear peaks around the natural surge and sway periods both in x- and y-directions with the TD VIV model. The VIM response is also observed to be more and more dominating in the total response pattern. This is seen by the increasing magnitude of the peaks. It is also observed that the peaks in the x- and y-directions are appearing at slightly different frequencies, but still around the natural frequencies in surge and sway. This is likely due to the way the mooring lines are tightened and slackened as a response to the incoming environmental loads in their respective directions. This would naturally change the natural frequencies, which could be why the peaks are not perfectly aligned with each other and with the marked natural frequencies. The marked natural frequencies were found when no environmental loads were applied and the floating wind turbine was located in the global origin, as described in Sec. 4.4.

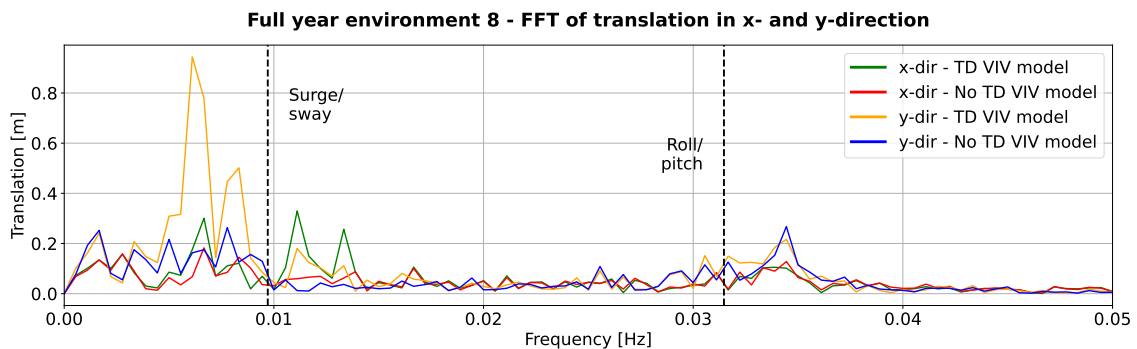


Figure 6.21: Fast Fourier transform of translation in x- and y-direction for full year environment 8. Results both with and without the TD VIV model are shown.

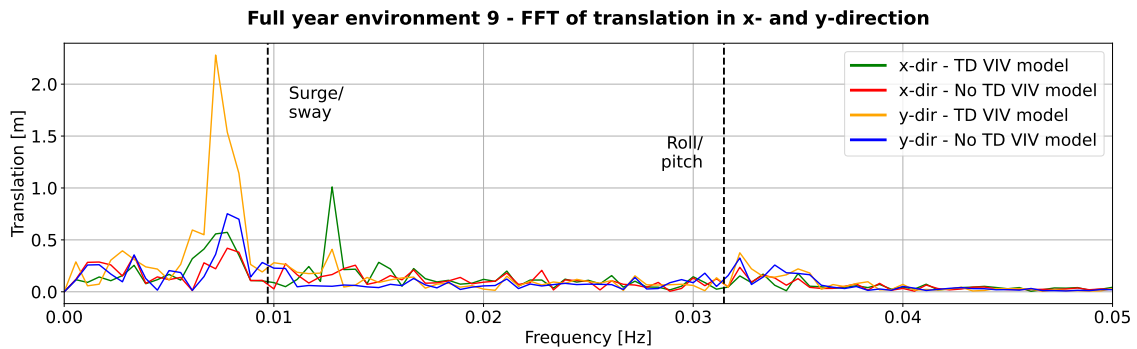


Figure 6.22: Fast Fourier transform of translation in x- and y-direction for full year environment 9. Results both with and without the TD VIV model are shown.

Finally, the results from the harshest environmental condition with the highest current speed is analyzed. The translation in x- and y-directions are plotted in Fig. 6.23. Here, very clear VIM can be observed, both in the x- and y-directions for the simulated motions with the TD VIV model. For the y-direction, VIM is totally dominating the response, with barely any other components visible in the motion time series. It is also worth mentioning the large oscillation amplitude which reaches up to over 7 meters at the maximum. This constitutes to a total displacement of around one spar floater diameter of 14.4 meters over half a oscillation period. In other words, quite substantial VIM. In the x-direction, VIM is also dominating the response, but at least in this direction, some other components are also visible. The oscillation amplitude in the x-direction is also significant, but considerably lower than in the y-direction.

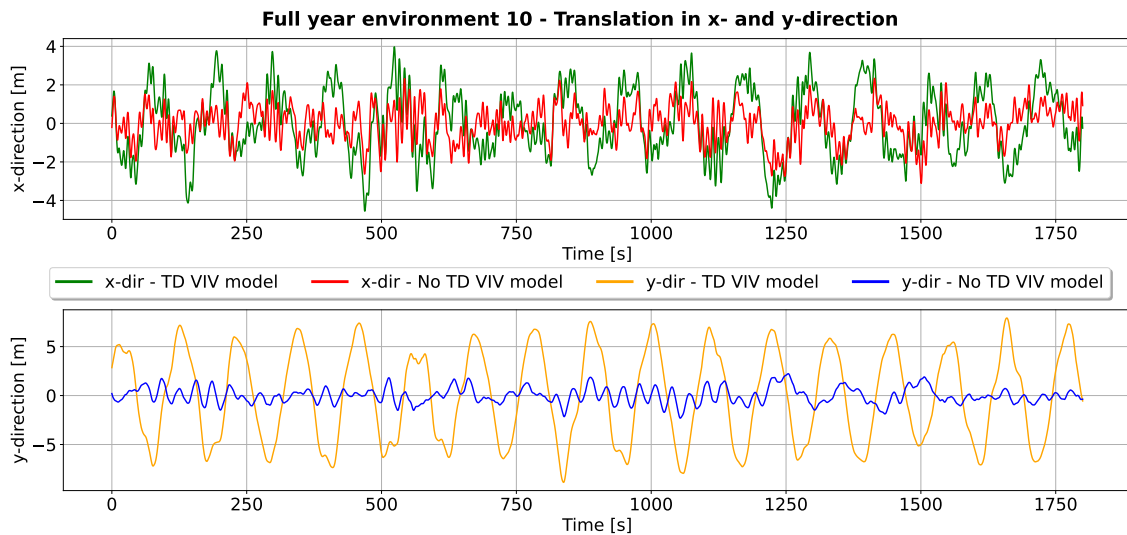


Figure 6.23: Translation in x- and y-direction for full year environment 10. Results both with and without the TD VIV model are shown.

The dominant VIM is also illustrated well in the frequency spectra, which are plotted in Fig. 6.24 for full year environment 10. It is observed that the peaks around the natural periods in surge and sway are dominating the spectra completely, both in the x- and y-directions, and it is hard to extract any other components. The large magnitude of the peaks are also worth mentioning. A reminder is given that each of the full year environments has equal probability of occurrence and should hence include a representative response pattern for 10 % of the time over a full year. This is quite a lot of time with predicted VIM, since VIM was observed already at full year environment 7. That means the TD VIV model is predicting the floating wind turbine is in fact experiencing VIM around 40 % of the time. This is a very significant portion of time and proves that VIM should be seriously considered in design and operation. The VIM is also expected to affect the fatigue life of the mooring system, which will be investigated in the following section.

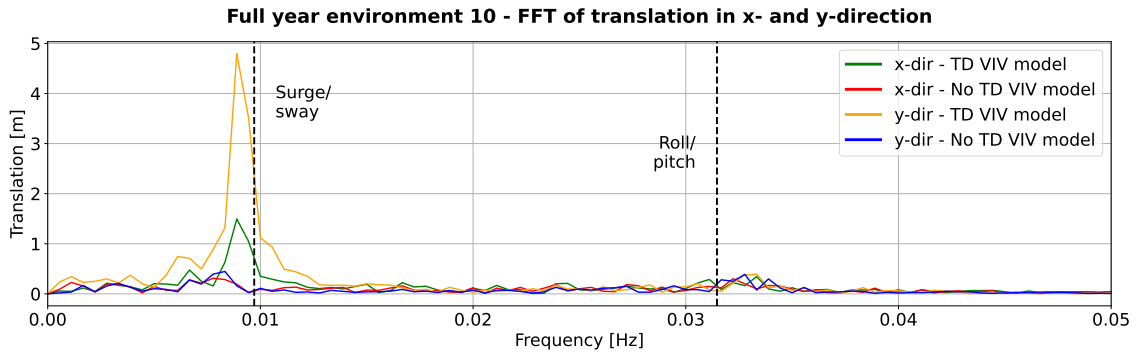


Figure 6.24: Fast Fourier transform of translation in x- and y-direction for full year environment 10. Results both with and without the TD VIV model are shown.

## 6.4 Effect on mooring system

The final objective of this work was to investigate the effect of the predicted VIM by the TD VIV model on the mooring system. As seen in the previous section, the TD VIV model does in fact predict quite a large amount of VIM, which is expected to have an effect on the mooring system. Both the effect on the ultimate limit state (ULS) design and fatigue life are investigated in the following.

### 6.4.1 Ultimate limit state

ULS corresponds to the maximum load-carrying capacity of a component or structure, in this case the mooring line. It can also refer to maximum allowable deformation or loading, including several factors of safety. In any way, the ULS design is based upon the maximum loading which the mooring line has to withstand. It is therefore interesting to investigate the stresses in the mooring lines. A single point on each of the mooring lines was selected as a critical point to be investigated. This was chosen as the point in the connection between the main mooring line and the bridles. Remember the mooring configuration of the floating wind turbine illustrated in Figs. 4.3 and 4.4. The stresses are retrieved from the element in the main mooring line closest to the bridles. It should however be noted, that larger stresses may appear in other parts of the mooring lines. However, due to the complexity of the mooring lines, which contains several hundred elements, and the variety of environmental conditions which could also change the critical point on the mooring line, a single point is selected. It is however reasonable to assume that this has high stresses as it

is at the top of the main mooring line. When the line transitions over to the bridles, the stresses are also divided on two different lines. The bridles have not been looked into in this investigation.

The maximum stresses in the mooring lines are expected to appear in the harshest environmental conditions. This is full year environment 10 when looking into the representative full year environmental condition. The time series of the stresses in the mooring lines for this environmental condition are presented in order to evaluate the effect of the VIM on the ULS design. The stresses in main mooring line 141, both with and without the TD VIV model, are plotted in Fig. 6.25. The stresses in main mooring line 142 are plotted in Fig. 6.26, while the stresses for main mooring line 143 are plotted in Fig. 6.27.

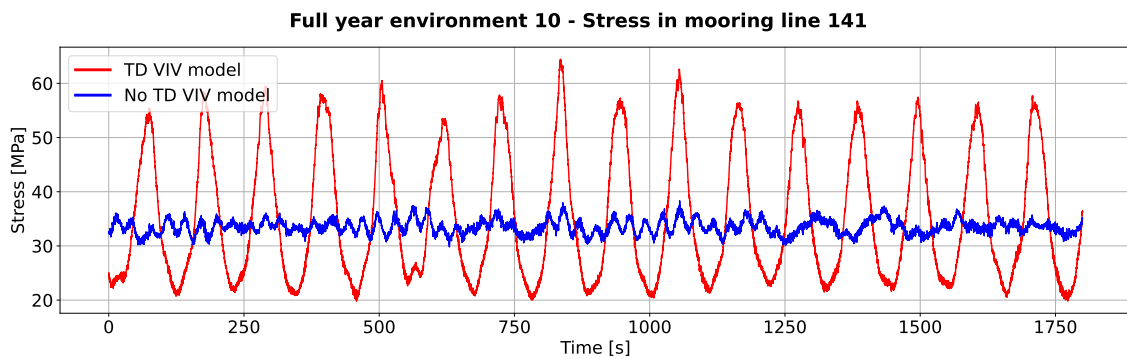


Figure 6.25: Stress in main mooring line 141 for full year environment 10 with and without the TD VIV model.

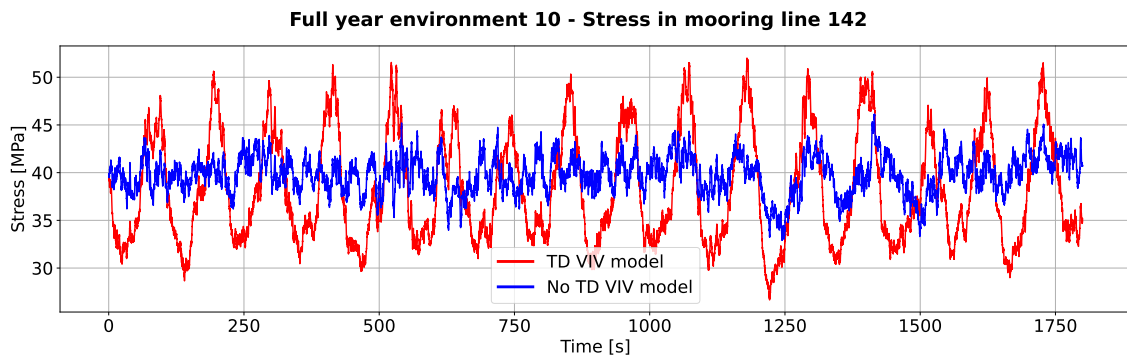


Figure 6.26: Stress in main mooring line 142 for full year environment 10 with and without the TD VIV model.

It is observed that VIM is affecting the stresses in the mooring lines quite significantly. Especially mooring line 141 and 143 have very obvious VIM correlation in the observed stresses. For these two mooring lines the VIM response is definitely dominating the maximum stresses in the mooring lines. For mooring line 142, VIM response is also determining the maximum stress, but not quite as dominating. The maximum stresses in the mooring lines for full year environment 10 with and without the TD VIV model are listed in Tab. 6.7. These maximum stresses represents the peak values observed in the time series plots. It is observed that for mooring line 141 the maximum stress is increasing with over 68 % when analyzed with the TD VIV model as compared to without

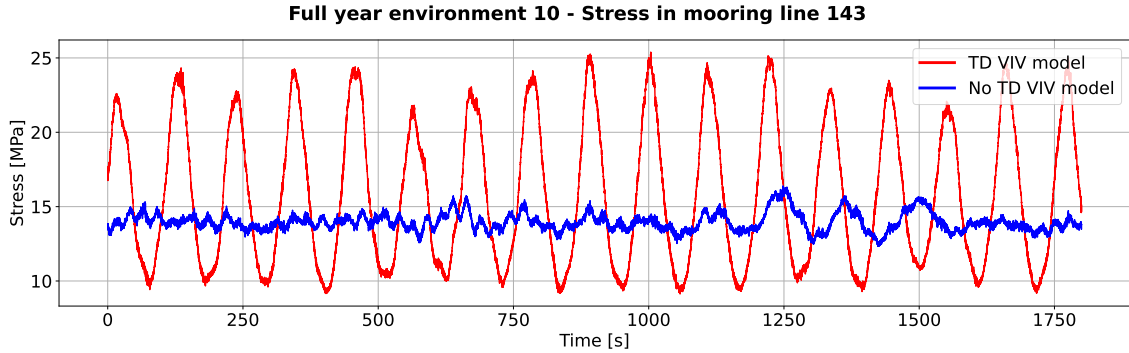


Figure 6.27: Stress in main mooring line 143 for full year environment 10 with and without the TD VIV model.

it. This is the mooring line with largest increase in maximum stress, but all of the lines does experience an increase as seen both from the table and time series plots. It is concluded that the use of the TD VIV model as a prediction tool does affect the maximum stresses in the mooring lines, and hence the ULS design. It is proved that the effect of the VIM predicted by the TD VIV model is captured in the stresses in the mooring lines, which strengthens the potential of the TD VIV model to be used as a VIM prediction tool.

Table 6.7: Maximum stresses in the mooring lines for full year environment 10 with and without the TD VIV model.

Mooring line	Maximum stress [MPa]		Increase [%]
	No TD VIV model	TD VIV model	
141	38.33	64.45	68.15
142	46.13	52.01	12.75
143	16.39	25.39	54.91

### 6.4.2 Fatigue life

The effect of VIM predicted by the VIV model was also investigated with respect to the fatigue life of the mooring lines. A fatigue analysis was performed using the results from the analyses on the representative full year environmental condition. The time series of the stresses in the mooring lines were used to calculate the total fatigue damage over a full year. This was done by utilizing the fact that each of the full year environmental conditions had equal probability of occurrence and hence would represent the stress response for ten percent of the time. The stresses were then rainflow counted and by use of the Miner summation, the fatigue lives for the mooring lines were calculated. The S-N curve used in the fatigue analysis was the offshore standard DNV-OS-E301 position mooring S-N curve for studless chain (open link) mooring lines [72], shown in Fig. 6.28.

The contribution to the total fatigue damage from the different full year environmental conditions are illustrated in Fig. 6.29 both with and without the TD VIV model for all of the three mooring lines. It is observed that without the TD VIV model, the fatigue damage distribution is spread out over the different full year environments. Some of the environments does include a bigger portion



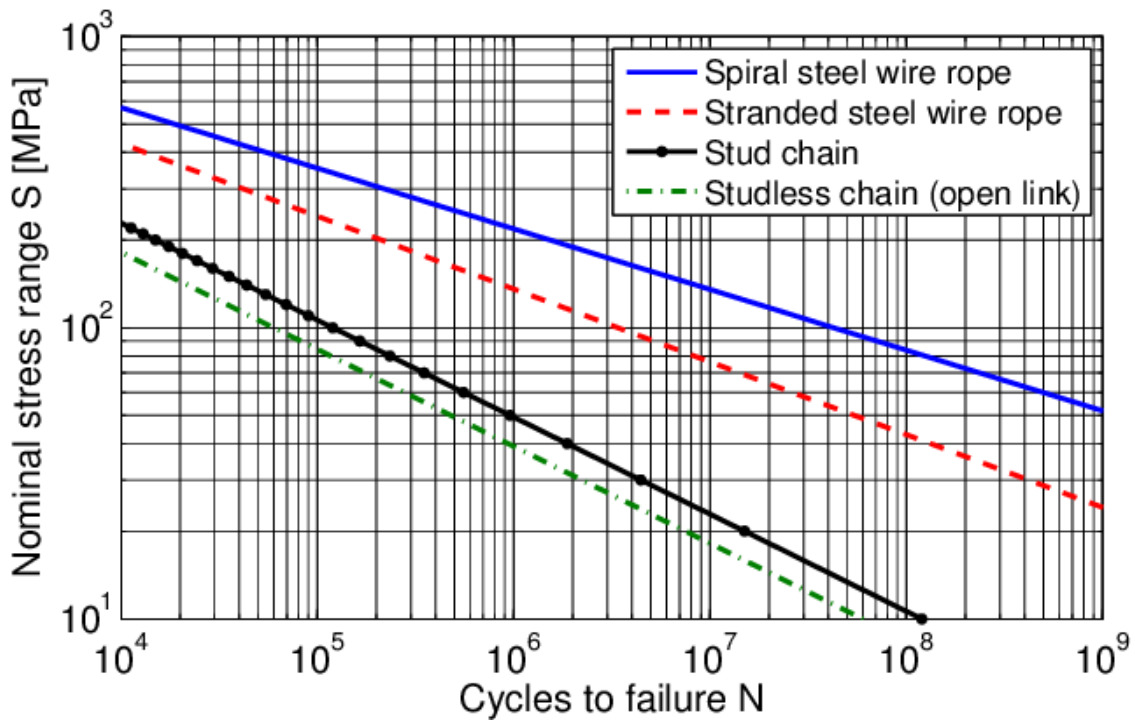
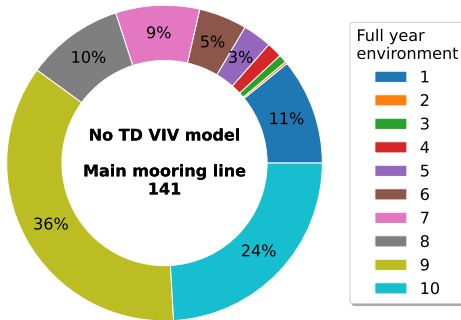


Figure 6.28: S-N curve for different mooring lines. The figure is from [73].

of the fatigue damage, such as full year environment 9 and 10, but still the other environments also constitutes a fair bit of the total fatigue damage. For mooring line 143 for example, full year environment 9 and 10 only contributes to 47% of the total fatigue damage. When the fatigue damage distribution is investigated with the TD VIV model a huge shift towards the harsher conditions containing VIM is observed. Now, the two environmental conditions full year environment 9 and 10 almost exclusively contains the fatigue damage contributions, especially for mooring lines 141 and 143. For mooring line 143 in particular, these three cases contains 97% of the total fatigue damage. This means that VIM is in fact increasing the total fatigue damage, and might actually be totally dominating the lifetime of the mooring lines.

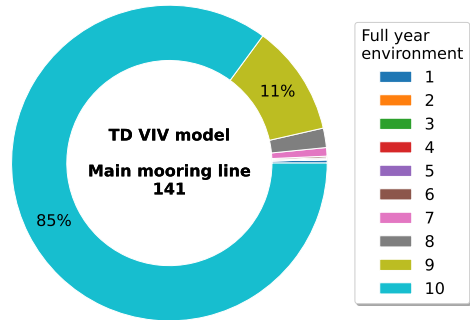
The total fatigue life of the mooring lines are calculated with and without the TD VIV model and are listed in Tab. 6.8. A significant reduction in fatigue life is observed for all of the mooring lines. The largest reduction is observed for mooring line 141 which has reduced fatigue life by a factor of 34. With the TD VIV model, this is the critical mooring line with the shortest fatigue life. When analyzed without the TD VIV model however, mooring line 142 is in fact the critical line. The critical mooring line obviously determines the fatigue life of the complete mooring system, in the sense that if one line fails, the mooring system has failed. The fatigue life of the mooring system without the TD VIV model was therefore 327.1 years, while with the TD VIV model, the fatigue life was 34.68 years. This corresponds to a reduction in fatigue life by a factor of 9.43 which is almost a complete order of magnitude. This is quite a significant reduction which underlines the importance of VIM prediction.

**Fatigue damage distribution**



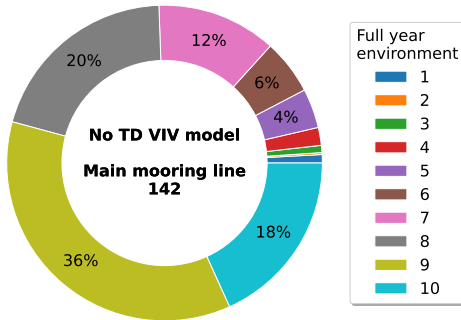
(a) Line 141 without the TD VIV model.

**Fatigue damage distribution**



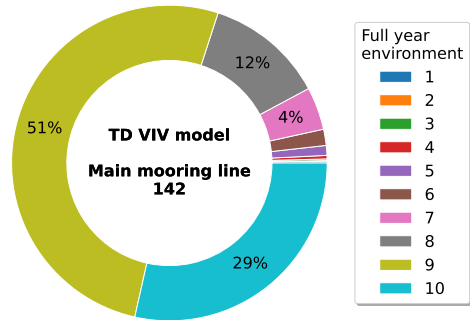
(b) Line 141 with the TD VIV model.

**Fatigue damage distribution**



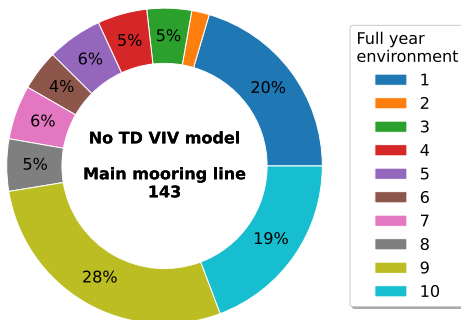
(c) Line 142 without the TD VIV model.

**Fatigue damage distribution**



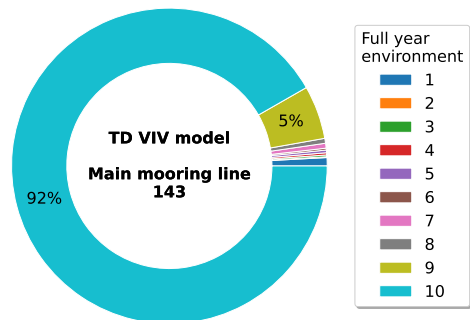
(d) Line 142 with the TD VIV model.

**Fatigue damage distribution**



(e) Line 143 without the TD VIV model.

**Fatigue damage distribution**



(f) Line 143 with the TD VIV model.

Figure 6.29: Fatigue damage distribution with and without the TD VIV model for all the mooring lines.

Table 6.8: Fatigue life for the different mooring lines with and without the TD VIV model.

Mooring line	Fatigue life [years]		Reduced by factor
	No TD VIV model	TD VIV model	
141	1179	34.68	34.00
142	327.1	74.55	4.39
143	15210	631.4	24.09
Critical	327.1	34.68	9.43

In addition, an overview of the floating wind turbine with incoming environmental directions and fatigue lifetimes with and without the TD VIV model indicated is illustrated in Fig. 6.30. Due to the fact that all the full year environmental conditions have the same incoming environmental directions, the directions can easily be displayed on the illustration. In this way, it is easier to visualize how the different environments are affecting the fatigue lives of the different mooring lines. The points on the mooring lines which are investigated are also indicated with red dots. Due to the fact that the current is coming in the same direction as mooring line 142 is aligned, means the IL direction defined in the same direction as mooring line 142. When the current is applied, it can be observed from the figure that mooring line 142 should be slackened. This is neglect the load from the incoming wind. Any reduction of fatigue life for mooring line 142 would mostly be due to IL VIM, as CF VIM would not affect the stresses in mooring line 142 in a significant manner. For the other two mooring lines, line 141 and 143, both IL and CF VIM are contributing to the reduced fatigue life. However, the fatigue lives of these lines are reduced more heavily, which suggests that the CF VIM contributions are the ones constituting the largest reductions.

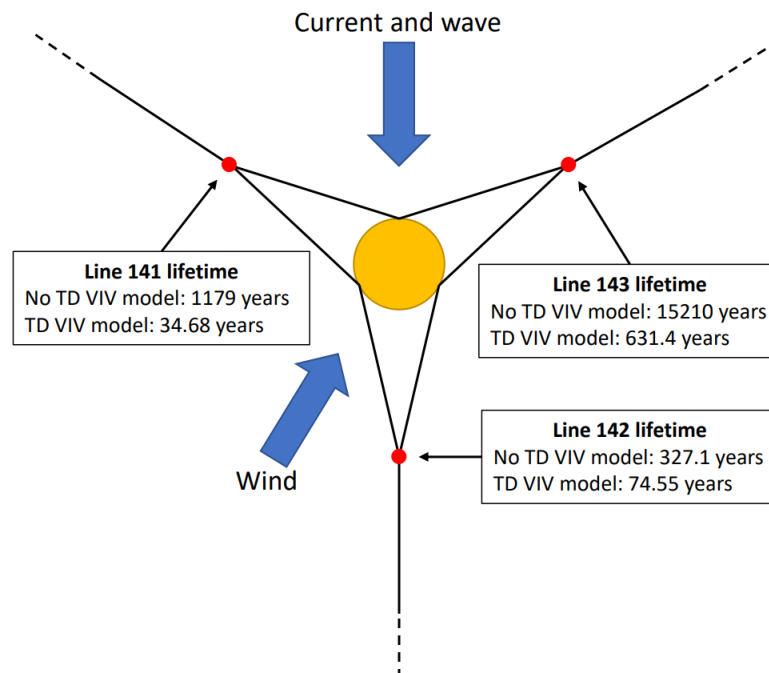


Figure 6.30: Overview of the floating wind turbine with incoming environmental directions and fatigue lifetimes with and without the TD VIV model indicated.

It is concluded that the VIM predicted by the TD VIV model is significantly affecting the fatigue life of the mooring system. Both CF and IL contributions are of significance, and all of the mooring lines on the floating wind turbine are experiencing reduced lifetime due to VIM. It is proved that the TD VIV model is able to predict reduction of fatigue life due to VIM, which is strengthening the models potential to be used as a VIM prediction tool. The importance of an accurate VIM prediction tool is also underlined as the effect of VIM with regards to reduced lifetime, is very significant with the use of the TD VIV model.

# Chapter 7

## Conclusions and further work

### 7.1 Conclusions

The main objective of this thesis was to investigate if a recently developed TD VIV prediction tool, here referred to as the TD VIV model, could be used as a VIM prediction tool. This was done by firstly validating the model against full-scale measurements. It was concluded that for the provided full-scale measurement cases, the TD VIV model predicted accurate motions with regards to VIM response. It was observed that the simulated motions with the TD VIV model were almost identical as the simulated motions without the TD VIV model for all of the full-scale cases. This suggested that the VIV load terms in the TD VIV model did not produce any additional motions, and in particular VIM, for the environmental conditions in the full-scale measurement cases. This also agreed well with the response patterns seen in the full-scale measurements themselves. Most of the full-scale measurements did in fact not include any VIM and only a few contained VIM tendencies. The fact that the TD VIV model did not produce any additional VIM for these cases strengthens the potential of the TD VIV model to be used as a VIM prediction tool.

Next, the relative importance of different environmental conditions were investigated with regards to onset of VIM with the TD VIV model. This was done by analyzing the same cases as the full-scale measurements covered, but without the wind or wave condition. The current was obviously still applied as the current condition is a vital component contributing to VIM response. It was found that waves had little to no contribution on the VIM response of the floating wind turbine. The simulated motions including and excluding the wave condition showed mostly similar response, when disregarding response components around the wave frequencies. Even though the analyzed cases contained waves with different values of significant wave height, peak period and direction for both wind waves and swell waves, no difference in the predicted VIM was observed when comparing results with and without waves. The wind was however found to do have an impact on the predicted VIM response. The same procedure as for the waves were performed with the wind, and it was found that the absence of wind did produce additional VIM for the cases with the highest current speeds. This VIM was not seen when analyzed with the complete environmental description. The VIM amplitude was not very large, but the VIM was still clearly visible in the translational time series plots, and consistent throughout the complete analysis time. It was concluded that the wind

condition does affect the VIM prediction of the TD VIV model for cases with significant current speeds. The wave condition was not found to affect the VIM prediction.

Finally, a representative full year environmental condition was established to investigate the effect of VIM on the mooring system ULS design and fatigue life. It was predicted by the TD VIV model that the analysed wind turbine concept at its respective location would be experiencing VIM around 40% of the time. This was both CF and IL VIM exclusively produced by the VIV load terms in the TD VIV model and was not captured in analyses when the TD VIV model was not used. The VIM amplitude was also significant and the motion was consistent. The effect of this VIM was captured in both the maximum stress in the mooring lines as well as in the fatigue life. The maximum stress in the mooring lines was found to increase with over 68% for the most affected mooring line when analyzed with the TD VIV model and VIM was produced, compared to without the TD VIV model and no VIM. This affects the ULS design and underlines the importance of an accurate VIM prediction tool. The fatigue life of the mooring system was also affected by the predicted VIM. Both CF and IL VIM was found to contribute to a fatigue life reduction. The complete mooring system had a reduction in fatigue life by a factor of 9.43. The worst individual line reduced the fatigue life with a factor of 34. This reduction in life time is quite significant and illustrates well the effect VIM can have on the mooring system, and the importance of accurate VIM prediction to capture these effects. The TD VIV model was proved to capture the effect of VIM on the mooring system which strengthens the potential of the TD VIV model to be used as a VIM prediction tool. It was concluded that the TD VIV model has great potential as a VIM prediction tool. but additional validation and possibly calibration is needed in order to confidently predict accurate VIM.

## 7.2 Recommendations for further work

The use of the TD VIV model as a VIM prediction tool was investigated in this thesis. The TD VIV model was validated against a few full-scale measurements cases and the relative importance of environmental conditions with regard to onset of VIM was investigated. A very simplified representative full year environmental descriptions was established to investigate the effect of VIM on the mooring system. Several assumptions and simplification were made in many aspects of the investigation as described in the main body of the thesis. In addition, not much other research on the topic of TD VIM prediction exists, and hence several recommendations for further work are given.

The TD VIV model should be validated against much more data than done in this thesis before it can be classified as an accurate tool for VIM prediction. More full-scale measurements should be obtained for a larger variety of environmental conditions and compared to results with the TD VIV model. Especially cases with higher current speeds and present VIM is of particular interest. The full-scale measurements investigated in this thesis all had relatively low current speeds and only small amounts of VIM. The validation of the TD VIV model for cases with actual VIM is therefore of great interest. Moreover, a calibration study could be performed on the hydrodynamic parameters of the TD VIV model given the results of the validation.

A more in depth investigation on the relative importance of the different environmental conditions could be performed. In this study, the same environmental conditions as for the full-scale measurement cases were used. It would be interesting to perform a similar study but with different environmental conditions. Fully customisable environmental conditions would make a great basis

for a thorough investigation of the relative importance of the different conditions. In addition, an investigation on the directional dependence of the different environmental conditions with regards to VIM response could be performed. In this thesis, full-scale measurement cases were utilized with actual measured environmental conditions. These included several different directions and magnitudes of the various parameters, and with only a few available cases, it was hard to draw conclusions on the directional dependencies. With fully customisable environmental conditions, several directions can be included or isolated and the effects from each of the different directions and parameters can be determined. This could also be linked up to the relative importance of CF and IL VIM and how they are influenced by different wave and wind directions. In general, more investigation on the CF and IL VIM components should be performed.

The representative full year environmental condition established in thesis was made with several assumptions and simplifications. A more accurate and detailed condition could be established in order to evaluate the effect of the VIM predicted by TD VIV model on the mooring system more accurate. In addition, the TD VIV model could be utilized on other concepts and the effect of the predicted VIM on these could be analyzed and compared to other concepts. In this thesis, the TD VIV model is also only tested on a single spar-type floating wind turbine concept. Other spar-type structures, other floating wind turbine concepts or even completely different floating structures could also be analysed with regards to VIM response with the TD VIV model. It is recommended that more research is initially focused on the spar-concept as this is a simple design, however, eventually other concepts such as semi-submersibles could also be looked into.





# References

- [1] Yin D, Passano E, Jiang F, Lie H, Wu J, Ye N, Sævik S, Leira BJ. State-of-the-art review of vortex-induced motions of floating offshore wind turbine structures. *Journal of Marine Science and Engineering*. 2022;10(8). Article 1021. doi: 10.3390/jmse10081021.
- [2] Bussemakers PJM. Validation of aero-hydro-servo-elastic load and motion simulations in BHawC/OrcaFlex for the Hywind Scotland floating offshore wind farm. Master's thesis, NTNU. 2020. <https://hdl.handle.net/11250/2780185>.
- [3] Sumer BM, Fredsøe J. *Hydrodynamics around cylindrical structures (Revised edition)*. Singapore: World Scientific Publishing Company. 2006.
- [4] Gerrard JH. The mechanics of the formation region of vortices behind bluff bodies. *Journal of Fluid Mechanics*. 1966;25(2):401–413. doi: 10.1017/S0022112066001721.
- [5] Chandrasekaran S. Vortex-induced vibration. In: *Woodhead publishing series in civil and structural engineering: Design of marine risers with functionally graded materials*, edited by Chandrasekaran S, chap. 3, pp. 59–90. Woodhead Publishing. 2021;.
- [6] Williamson CHK. Oblique and parallel modes of vortex shedding in the wake of a circular cylinder at low Reynolds numbers. *Journal of Fluid Mechanics*. 1989;206:579–627. doi: 10.1017/S0022112089002429.
- [7] Bloor MS. The transition to turbulence in the wake of a circular cylinder. *Journal of Fluid Mechanics*. 1964;19(2):290–304. doi: 10.1017/S0022112064000726.
- [8] Williamson CHK. The existence of two stages in the transition to three-dimensionality of a cylinder wake. *The Physics of Fluids*. 1988;31(11):3165–3168. doi: 10.1063/1.866925.
- [9] Schewe G. On the force fluctuations acting on a circular cylinder in crossflow from subcritical up to transcritical Reynolds numbers. *Journal of Fluid Mechanics*. 1983;133:265–285. doi: 10.1017/S0022112083001913.
- [10] Achenbach E, Heinecke E. On vortex shedding from smooth and rough cylinders in the range of Reynolds numbers  $6 \times 10^3$  to  $5 \times 10^6$ . *Journal of Fluid Mechanics*. 1981;109:239–251. doi: 10.1017/S002211208100102X.
- [11] Lienhard JH. *Synopsis of lift, drag, and vortex frequency data for rigid circular cylinders*. Bulletin 300. Technical Extension Service, Washington State University, Pullman, WA. 1966.
- [12] Potts DA, Marcollo H, Jayasinghe K. Strouhal Number for Vortex-Induced Vibration Excitation of Long Slender Structures. *Journal of Offshore Mechanics and Arctic Engineering*. 2022; 144(4). Article 041906. doi: 10.1115/1.4054426.
- [13] Roshko A. Experiments on the flow past a circular cylinder at very high Reynolds number. *Journal of Fluid Mechanics*. 1961;10(3):345–356. doi: 10.1017/S0022112061000950.

- [14] Thorsen MJ. Time domain analysis of vortex-induced vibrations. Ph.D. thesis, Norwegian University of Science and Technology. 2016.
- [15] Bishop RED, Hassan A. The lift and drag forces on a circular cylinder oscillating in a flowing fluid. In: *Proceedings of the Royal Society of London. Series A. Mathematical and Physical Sciences*, vol. 277. 1964; pp. 51–75. doi: 10.1098/rspa.1964.0005.
- [16] Gopalkrishnan R. Vortex-induced forces on oscillating bluff cylinders. *Tech. rep.*, Woods Hole Oceanographic Institution MA. 1993.
- [17] Feng CC. The measurement of vortex induced effects in flow past stationary and oscillating circular and D-section cylinders. Master’s thesis, University of British Columbia. 1968. doi: 10.14288/1.0104049.
- [18] SINTEF Ocean. VIVANA 4.20.2 Theory Manual. April 18, 2021.
- [19] Blevins RD, Coughran CS. Experimental investigation of vortex-induced vibration in one and two dimensions with variable mass, damping, and Reynolds number. *Journal of Fluids Engineering*. 2009;131(10). Article 101202. doi: 10.1115/1.3222904.
- [20] Fujarra AL, Rosetti GF, de Wilde J, Gonçalves RT. State-of-art on vortex-induced motion: A comprehensive survey after more than one decade of experimental investigation. In: *Proceedings of the ASME 2012 31st International Conference on Ocean, Offshore and Arctic Engineering*, vol. 4. Rio de Janeiro, Brazil. July 1–6, 2012; pp. 561–582. doi: 10.1115/OMAE2012-83561.
- [21] Okamoto T, Yagita M. The experimental investigation on the flow past a circular cylinder of finite length placed normal to the plane surface in a uniform stream. *Bulletin of JSME*. 1973; 16(95):805–814. doi: 10.1299/jsme1958.16.805.
- [22] Rooney DM, Rodichok J, Dolan K. Finite aspect ratio effects on vortex shedding behind two cylinders at angles of incidence. *Journal of Fluids Engineering*. 1995;117(2):219–226. doi: 10.1115/1.2817133.
- [23] Kawamura T, Hiwada M, Hibino T, Mabuchi I, Kumada M. Flow around a finite circular cylinder on a flat plate: Cylinder height greater than turbulent boundary layer thickness. *Bulletin of JSME*. 1984;27(232):2142–2151. doi: 10.1299/jsme1958.27.2142.
- [24] Gonçalves RT, Sakata K, Gambarine DM, Cicolin MM, Hirabayashi S, Assi GR. Experimental study on vortex-induced vibration of floating circular cylinders with low aspect ratio and different free-end corner shapes. In: *Proceedings of the ASME 2018 37th International Conference on Ocean, Offshore and Arctic Engineering*, vol. 2. Madrid, Spain. June 17–22, 2018; Article V002T08A035. doi: 10.1115/OMAE2018-77218.
- [25] Kaimal JC, Wyngaard JCJ, Izumi Y, Coté O. Spectral characteristics of surface-layer turbulence. *Quarterly Journal of the Royal Meteorological Society*. 1972;98(417):563–589. doi: 10.1002/qj.49709841707.
- [26] Jonkman, BJ. TurbSim User’s Guide v2.00.00. *National Renewable Energy Laboratory*. June 1, 2016.
- [27] Berge, Stig and Ås, Sigmund Kyrre. Compendium - Fatigue and fracture design of marine structures. NTNU. 2017.
- [28] Holmes S, Oakley Jr OH, Constantinides Y. Simulation of riser VIV using fully three dimensional CFD simulations. In: *Proceeding of the 25th International Conference on Offshore Mechanics and Arctic Engineering*, vol. 4. Hamburg, Germany. June 4–9, 2006; pp. 563–570. doi: 10.1115/OMAE2006-92124.

- [29] Chaplin J, Bearman PW, Cheng Y, Fontaine E, Graham J, Herfjord K, Huarte FH, Isherwood M, Lambrakos K, Larsen C, et al. Blind predictions of laboratory measurements of vortex-induced vibrations of a tension riser. *Journal of Fluids and Structures*. 2005;21(1):25–40. doi: 10.1016/j.jfluidstructs.2005.05.016.
- [30] Bourguet R, Karniadakis GE, Triantafyllou MS. Vortex-induced vibrations of a long flexible cylinder in shear flow. *Journal of Fluid Mechanics*. 2011;677:342–382. doi: 10.1017/jfm.2011.90.
- [31] Auburtin E, Kim J, Jang H, Lai L, McConochie J, Drobyshevski Y, van Haaften E. Current Forces on Prelude Hull and Water Intake Riser by CFD: Full Scale Model Using Two of the World’s Largest Supercomputers. In: *Proceedings of the ASME 2021 40th International Conference on Ocean, Offshore and Arctic Engineering*, vol. 1. Virtual, Online. June 21–30, 2021; Article V001T01A016. doi: 10.1115/OMAE2021-62276.
- [32] Triantafyllou M, Triantafyllou G, Tein YS, Ambrose BD. Pragmatic riser VIV analysis. In: *Paper presented at the 1999 Offshore Technology Conference*. Houston, Texas. May 3–6, 1999; doi: 10.4043/10931-MS.
- [33] Vandiver JK, Li L. SHEAR7 v4.4 Program Theoretical Manual. Department of Ocean Engineering, Massachusetts Institute of Technology: Cambridge, MA, USA. 2005.
- [34] Larsen CM, Zhao Z, Lie H. Frequency Components of Vortex Induced Vibrations in Sheared Current. In: *Proceedings of the ASME 2012 31st International Conference on Ocean, Offshore and Arctic Engineering*, vol. 5. Rio de Janeiro, Brazil. July 1–6, 2012; pp. 493–501. doi: 10.1115/OMAE2012-83092.
- [35] Finn L, Lambrakos K, Maher J. Time domain prediction of riser VIV. In: *Proceedings of the Fourth International Conference on Advances in Riser Technologies*. Aberdeen, Scotland. 1999; .
- [36] Cheng Y, Lambrakos KF. Time domain computation of riser VIV from vessel motions. In: *Proceedings of the 25th International Conference on Offshore Mechanics and Arctic Engineering*, vol. 4. Hamburg, Germany. June 4–9, 2006; pp. 829–838. doi: 10.1115/OMAE2006-92432.
- [37] Mainçon P. A Wiener-Laguerre model of VIV forces given recent cylinder velocities. *Mathematical Problems in Engineering*. 2011;2011. Article 414702. doi: 10.1155/2011/414702.
- [38] Birkhoff G, Zarantonello EH. *Jets, wakes, and cavities*. Academic Press Inc, New York. 1957.
- [39] Gabbai RD, Benaroya H. An overview of modeling and experiments of vortex-induced vibration of circular cylinders. *Journal of sound and vibration*. 2005;282(3-5):575–616. doi: 10.1016/j.jsv.2004.04.017.
- [40] Thorsen MJ, Sævik S, Larsen CM. A simplified method for time domain simulation of cross-flow vortex-induced vibrations. *Journal of Fluids and Structures*. 2014;49:135–148. doi: 10.1016/j.jfluidstructs.2014.04.006.
- [41] Thorsen MJ, Sævik S, Larsen CM. Fatigue damage from time domain simulation of combined in-line and cross-flow vortex-induced vibrations. *Marine Structures*. 2015;41:200–222. doi: 10.1016/j.marstruc.2015.02.005.
- [42] Thorsen MJ, Sævik S, Larsen CM. Time domain simulation of vortex-induced vibrations in stationary and oscillating flows. *Journal of Fluids and Structures*. 2016;61:1–19. doi: 10.1016/j.jfluidstructs.2015.11.006.
- [43] Thorsen MJ, Sævik S, Larsen CM. Non-linear time domain analysis of cross-flow vortex-induced vibrations. *Marine Structures*. 2017;51:134–151. doi: 10.1016/j.marstruc.2016.10.007.

- [44] Ulveseter JV, Sævik S, Larsen CM. Time domain model for calculation of pure in-line vortex-induced vibrations. *Journal of Fluids and Structures*. 2017;68:158–173. doi: 10.1016/j.jfluidstructs.2016.10.013.
- [45] Ulveseter JV, Thorsen MJ, Sævik S, Larsen CM. Stochastic modelling of cross-flow vortex-induced vibrations. *Marine Structures*. 2017;56:260–280. doi: 10.1016/j.marstruc.2017.08.001.
- [46] Ulveseter JV, Thorsen MJ, Sævik S, Larsen CM. Time domain simulation of riser VIV in current and irregular waves. *Marine Structures*. 2018;60:241–260. doi: 10.1016/j.marstruc.2018.04.001.
- [47] Ulveseter JV, Thorsen MJ, Sævik S, Larsen CM. Simulating fundamental and higher harmonic VIV of slender structures. *Applied Ocean Research*. 2019;90. Article 101856. doi: 10.1016/j.apor.2019.101856.
- [48] Kim SW, Sævik S, Wu J, Leira BJ. Time domain simulation of marine riser vortex-induced vibrations in three-dimensional currents. *Applied Ocean Research*. 2022;120. Article 103057. doi: 10.1016/j.apor.2022.103057.
- [49] Kim SW, Sævik S, Wu J, Leira BJ. Prediction of deepwater riser VIV with an improved time domain model including non-linear structural behavior. *Ocean Engineering*. 2021;236. Article 109508. doi: 10.1016/j.oceaneng.2021.109508.
- [50] Kim SW, Sævik S, Wu J, Leira BJ. Simulating high-mode vortex-induced vibration of a riser in linearly sheared current using an empirical time-domain model. *Journal of Offshore Mechanics and Arctic Engineering*. 2021;143(4). Article 041901. doi: 10.1115/1.4049246.
- [51] Passano E, Grytøyr G, Haslum H, Lie H, Yin D. Simulation of VIM of an offshore floating wind turbine. In: *Proceedings of the ASME 41st International Conference on Ocean, Offshore and Arctic Engineering*, vol. 8. Hamburg, Germany. June 5–10, 2022; Article V008T09A025. doi: 10.1115/OMAE2022-79006.
- [52] DNV. DNV-RP-C205 Environmental Conditions and Environmental Loads. September, 2019.
- [53] DNV. DNV-ST-0119 Floating wind turbine structures. June, 2021.
- [54] ISO. ISO 19001-7:2013 Petroleum and natural gas industries — Specific requirements for offshore structures — Part 7: Stationkeeping systems for floating offshore structures and mobile offshore units. May, 2013.
- [55] Equinor. Hywind Scotland. <https://www.equinor.com/energy/hywind-scotland>. Accessed: 31.10.22.
- [56] Equinor. Equinor and ORE Catapult collaborating to share Hywind Scotland operational data. <https://www.equinor.com/news/archive/2019-11-28-hywind-scotland-data>. Accessed: 31.10.22.
- [57] Jacobsen A, Godvik M. Influence of wakes and atmospheric stability on the floater responses of the Hywind Scotland wind turbines. *Wind Energy*. 2021;24(2):149–161. doi: 10.1002/we.2563.
- [58] Chen P, Jia C, Ng C, Hu Z. Application of SADA method on full-scale measurement data for dynamic responses prediction of Hywind floating wind turbines. *Ocean Engineering*. 2021; 239. Article 109814. doi: 10.1016/j.oceaneng.2021.109814.
- [59] Statoil. Hywind Scotland Pilot Park - Environmental Statement. April, 2015.
- [60] Equinor. Hywind Scotland data description. Internal document. 2022.
- [61] SINTEF Ocean. SIMO 4.24.0 User Guide. 2022.
- [62] SINTEF Ocean. SIMO 4.24.0 Theory Manual. 2022.

- 
- [63] SINTEF Ocean. RIFLEX 4.24.0 User Guide. 2022.
- [64] SINTEF Ocean. RIFLEX 4.24.0 Theory Manual. 2022.
- [65] SINTEF Ocean. RIFLEX 4.24.0 Input Reference. 2022.
- [66] Sudhakar S, Nallayarasu S. Influence of heave plate on hydrodynamic response of spar. In: *Proceedings of the ASME 2011 30th International Conference on Ocean, Offshore and Arctic Engineering*, vol. 1. Rotterdam, The Netherlands. June 19–24, 2011; pp. 437–447.
- [67] Orcina Ltd. OrcaFlex 11.3e documentation. 2023.
- [68] Jonkman J, Butterfield S, Musial W, Scott G. Definition of a 5-MW reference wind turbine for offshore system development. *Tech. rep.*, National Renewable Energy Lab.(NREL). Golden, CO, United States. 2009.
- [69] Jonkman J. Definition of the Floating System for Phase IV of OC3. *Tech. rep.*, National Renewable Energy Lab.(NREL). Golden, CO, United States. 2010.
- [70] Offshore Renewable Energy. Floating turbine design cases. <https://pod.ore.catapult.org.uk/data-collection/floating-turbine-design-cases>. Accessed: 09.06.23.
- [71] Mathiesen M, Meyer AK, Kvingedal B. Hywind Buchan Deep Metocean Design Basis. May, 2014.
- [72] DNV. Offshore Standard DNV-OS-E301 Position Mooring. October, 2008.
- [73] Thies PR, Johanning L, Smith GH. Lifecycle fatigue load spectrum estimation for mooring lines of a floating marine energy converter. In: *Proceedings of the ASME 2012 31st International Conference on Ocean, Offshore and Arctic Engineering*, vol. 2. Rio de Janeiro, Brazil. 1–6 July. 2012; pp. 667–676. doi: 10.1115/OMAE2012-84101.



# Appendices





# Appendix A

## TurbSim example input file

### A.1 turbsim\_case1.inp

```
1 -----TurbSim v2.00.* Input File-----
2 Example input file for TurbSim.
3 -----Runtime Options-----
4 False      Echo          - Echo input data to <RootName>.ech (flag)
5 2318573    RandSeed1       - First random seed (-2147483648 to 2147483647)
6 RANLUX     RandSeed2       - Second random seed (-2147483648 to 2147483647) for
7           ↳ intrinsic pRNG, or an alternative pRNG: "RanLux" or "RNSNLW"
8 False     WrBHHTIP      - Output hub-height turbulence parameters in binary form?
9           ↳ (Generates RootName.bin)
10 False    WrFHHTIP     - Output hub-height turbulence parameters in formatted
11          ↳ form? (Generates RootName.dat)
12 False    WrADHH       - Output hub-height time-series data in AeroDyn form? (
13          ↳ Generates RootName.hh)
14 False    WrADFF       - Output full-field time-series data in TurbSim/AeroDyn
15          ↳ form? (Generates RootName.bts)
16 True     WrBLFF       - Output full-field time-series data in BLADED/AeroDyn
17          ↳ form? (Generates RootName.wnd)
18 False    WrADIWR      - Output tower time-series data? (Generates RootName.twr)
19 False    WrFMTHFF     - Output full-field time-series data in formatted (
20          ↳ readable) form? (Generates RootName.u, RootName.v, RootName.w)
21 False    WrACT        - Output coherent turbulence time steps in AeroDyn form?
22          ↳ (Generates RootName.cts)
23 True     Clockwise    - Clockwise rotation looking downwind? (used only for
24          ↳ full-field binary files - not necessary for AeroDyn)
25 0        ScaleIEC     - Scale IEC turbulence models to exact target standard
26          ↳ deviation? [0=no additional scaling; 1=use hub scale uniformly; 2=use
27          ↳ individual scales]
28 -----Turbine/Model Specifications-----
29 39        NumGrid.Z    - Vertical grid-point matrix dimension
30 49        NumGrid.Y    - Horizontal grid-point matrix dimension
31 0.05      TimeStep     - Time step [seconds]
32 3000      AnalysisTime - Length of analysis time series [seconds] (program will
33          ↳ add time if necessary: AnalysisTime = MAX(AnalysisTime, UsableTime+
34          ↳ GridWidth/MeanHHWS) )
35 "ALL"     UsableTime   - Usable length of output time series [seconds] (program
36          ↳ will add GridWidth/MeanHHWS seconds unless UsableTime is "ALL")
37 98.4      HubHt        - Hub height [m] (should be > 0.5*GridHeight)
38 196.00    GridHeight   - Grid height [m]
```

```

26 | 250.00   GridWidth       - Grid width [m] (should be >= 2*(RotorRadius+ShaftLength
    | ↪ ))
27 | 0        VFlowAng        - Vertical mean flow (uptilt) angle [degrees]
28 | 0        HFlowAng        - Horizontal mean flow (skew) angle [degrees]
29 |
30 | -----Meteorological Boundary Conditions-----
31 | "IECKAI" TurbModel      - Turbulence model ("IECKAI","IECVKM","GP_LLJ","NWCUP","
    | ↪ SMOOTH","WFUPW","WF_07D","WF_14D","TIDAL","API","USRINP","TIMESR", or "
    | ↪ NONE")
32 | "unused" UserFile      - Name of the file that contains inputs for user-defined
    | ↪ spectra or time series inputs (used only for "USRINP" and "TIMESR" models
    | ↪ )
33 | "3"     IECstandard     - Number of IEC 61400-x standard (x=1,2, or 3 with
    | ↪ optional 61400-1 edition number (i.e. "1-Ed2"))
34 | 8.83    IECturbc        - IEC turbulence characteristic ("A","B","C" or the
    | ↪ turbulence intensity in percent) ("KHTEST" option with NWCUP model, not
    | ↪ used for other models)
35 | "NIM"   IEC_WindType    - IEC turbulence type ("NIM"=normal, "xETM"=extreme
    | ↪ turbulence, "xEWMI"=extreme 1-year wind, "xEWM50"=extreme 50-year wind,
    | ↪ where x=wind turbine class 1, 2, or 3)
36 | default ETMc           - IEC Extreme Turbulence Model "c" parameter [m/s]
37 | default WindProfileType - Velocity profile type ("LOG";"PL"=power law;"JET";"H2L
    | ↪ "Log law for TIDAL model;"API";"USR";"TS";"IEC"=PL on rotor disk, LOG
    | ↪ elsewhere; or "default")
38 | "unused" ProfileFile   - Name of the file that contains input profiles for
    | ↪ WindProfileType="USR" and/or TurbModel="USRVKM" [-]
39 | 99.00   RefHt           - Height of the reference velocity (Uref) [m]
40 | 8.49    URef            - Mean (total) velocity at the reference height [m/s] (or
    | ↪ "default" for JET velocity profile) [must be 1-hr mean for API model;
    | ↪ otherwise is the mean over AnalysisTime seconds]
41 | default ZJetMax        - Jet height [m] (used only for JET velocity profile,
    | ↪ valid 70-490 m)
42 | default PLExp          - Power law exponent [-] (or "default")
43 | default Z0             - Surface roughness length [m] (or "default")
44 |
45 | -----Non-IEC Meteorological Boundary Conditions-----
46 | default Latitude      - Site latitude [degrees] (or "default")
47 | 0.05    RICH_NO        - Gradient Richardson number [-]
48 | default UStar         - Friction or shear velocity [m/s] (or "default")
49 | default ZI            - Mixing layer depth [m] (or "default")
50 | default PC_UW         - Hub mean u'w' Reynolds stress [m^2/s^2] (or "default"
    | ↪ or "none")
51 | default PC_UV         - Hub mean u'v' Reynolds stress [m^2/s^2] (or "default"
    | ↪ or "none")
52 | default PC_VW         - Hub mean v'w' Reynolds stress [m^2/s^2] (or "default"
    | ↪ or "none")
53 |
54 | -----Spatial Coherence Parameters-----
55 | default SCMod1        - u-component coherence model ("GENERAL", "IEC", "API",
    | ↪ "NONE", or "default")
56 | default SCMod2        - v-component coherence model ("GENERAL", "IEC", "NONE",
    | ↪ or "default")
57 | default SCMod3        - w-component coherence model ("GENERAL", "IEC", "NONE",
    | ↪ or "default")
58 | default InCDec1       - u-component coherence parameters for general or IEC
    | ↪ models [-, m^-1] (e.g. "10.0 0.3e-3" in quotes) (or "default")
59 | default InCDec2       - v-component coherence parameters for general or IEC
    | ↪ models [-, m^-1] (e.g. "10.0 0.3e-3" in quotes) (or "default")
60 | default InCDec3       - w-component coherence parameters for general or IEC
    | ↪ models [-, m^-1] (e.g. "10.0 0.3e-3" in quotes) (or "default")
61 | default CohExp        - Coherence exponent for general model [-] (or "default
    | ↪ ")

```

```
62 |-----Coherent Turbulence Scaling Parameters-----|
63 |"C:/Yiwork_NREL/OffshoreWind/Turbsim/Test/EventData" CTEventPath - Name of the
64 |↪ path where event data files are located
65 |"Random" CTEventFile - Type of event files ("LES", "DNS", or "RANDOM")
66 |true Randomize - Randomize the disturbance scale and locations? (true/
67 |↪ false)
67 |1.0 DistScl - Disturbance scale [-] (ratio of event dataset height to
68 |↪ rotor disk). (Ignored when Randomize = true.)
68 |0.5 CTLy - Fractional location of tower centerline from right [-]
69 |↪ (looking downwind) to left side of the dataset. (Ignored when Randomize
70 |↪ = true.)
69 |0.5 CTLz - Fractional location of hub height from the bottom of
70 |↪ the dataset. [-] (Ignored when Randomize = true.)
70 |30.0 CTStartTime - Minimum start time for coherent structures in RootName.
71 |↪ cts [seconds]
71 |-----|
72 |-----|
73 |! NOTE: Do not add or remove any lines in this file!
74 |-----|
```



## Appendix B

# Complete set of results

### B.1 Validation against full-scale measurements

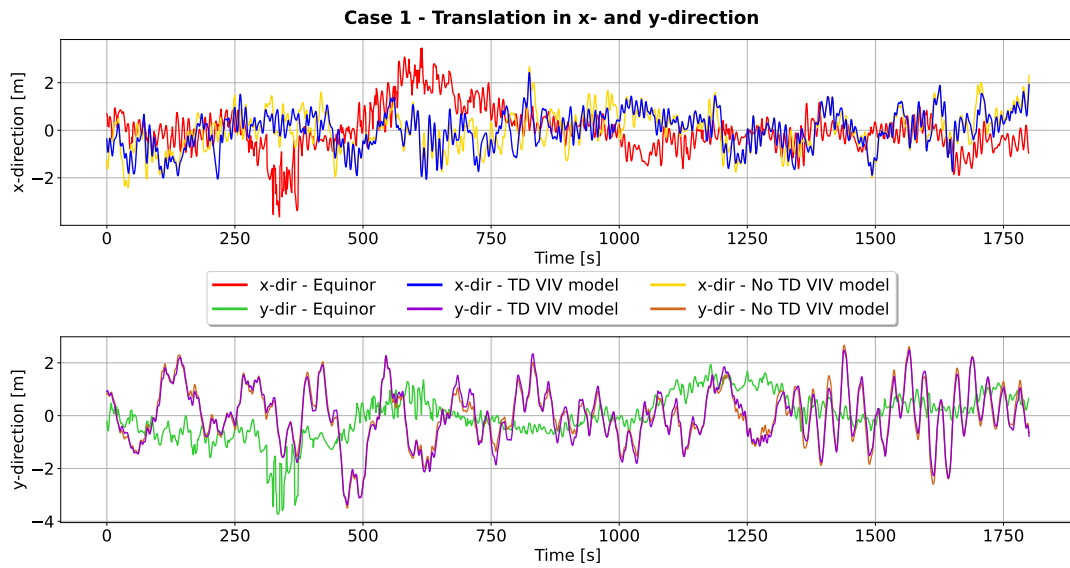


Figure B.1: Translation in x- and y-direction for case 1. The full-scale measurements from Equinor and the SIMA results both with and without the TD VIV model are shown.

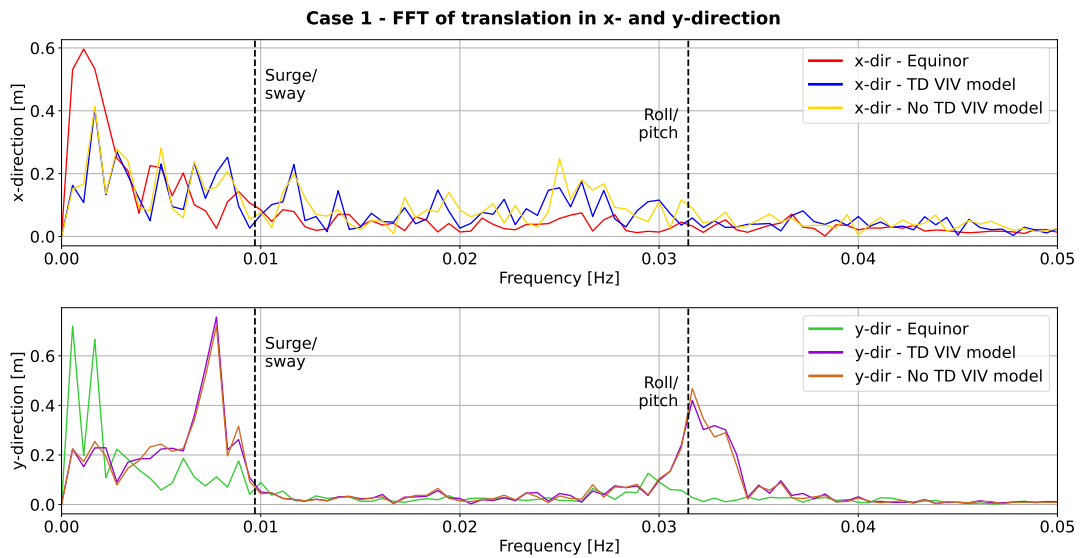


Figure B.2: Fast Fourier transform of translation in x- and y-direction for case 1. The full-scale measurements from Equinor and the SIMA results both with and without the TD VIV model are shown.

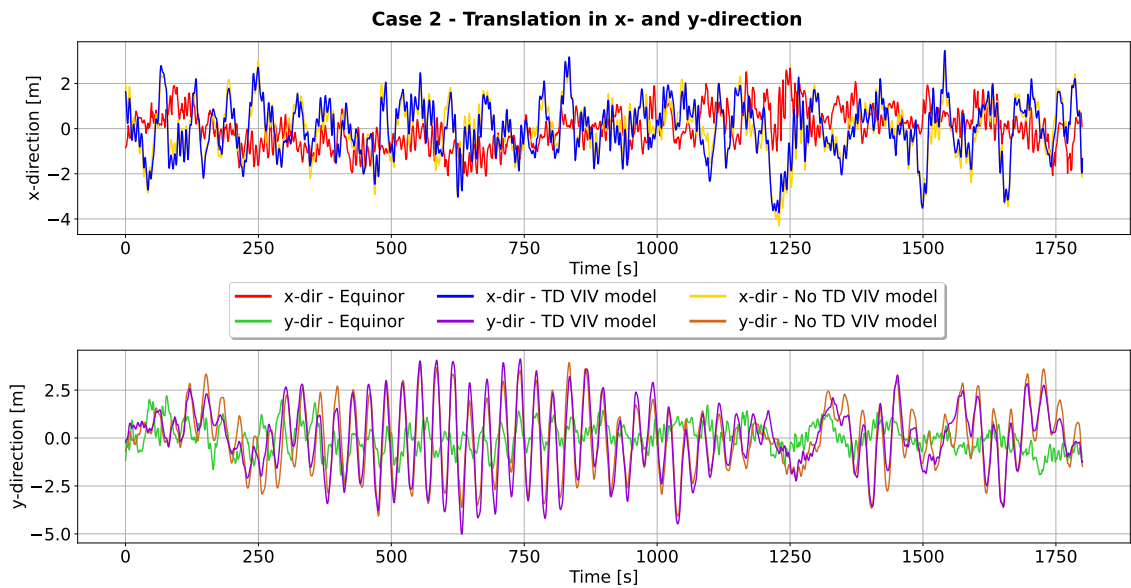


Figure B.3: Translation in x- and y-direction for case 2. The full-scale measurements from Equinor and the SIMA results both with and without the TD VIV model are shown.

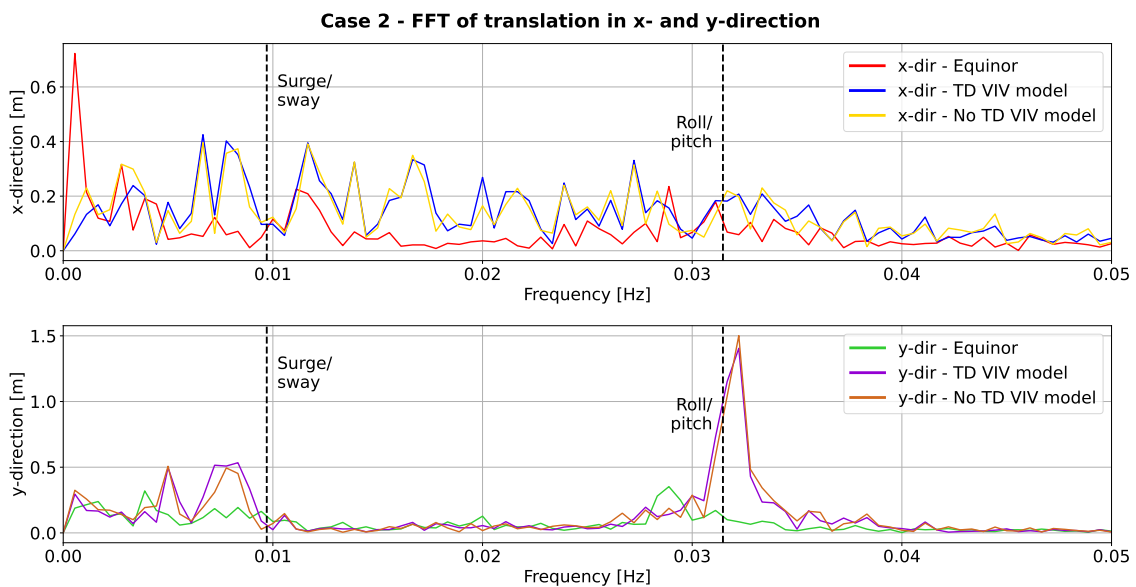


Figure B.4: Fast Fourier transform of translation in x- and y-direction for case 2. The full-scale measurements from Equinor and the SIMA results both with and without the TD VIV model are shown.

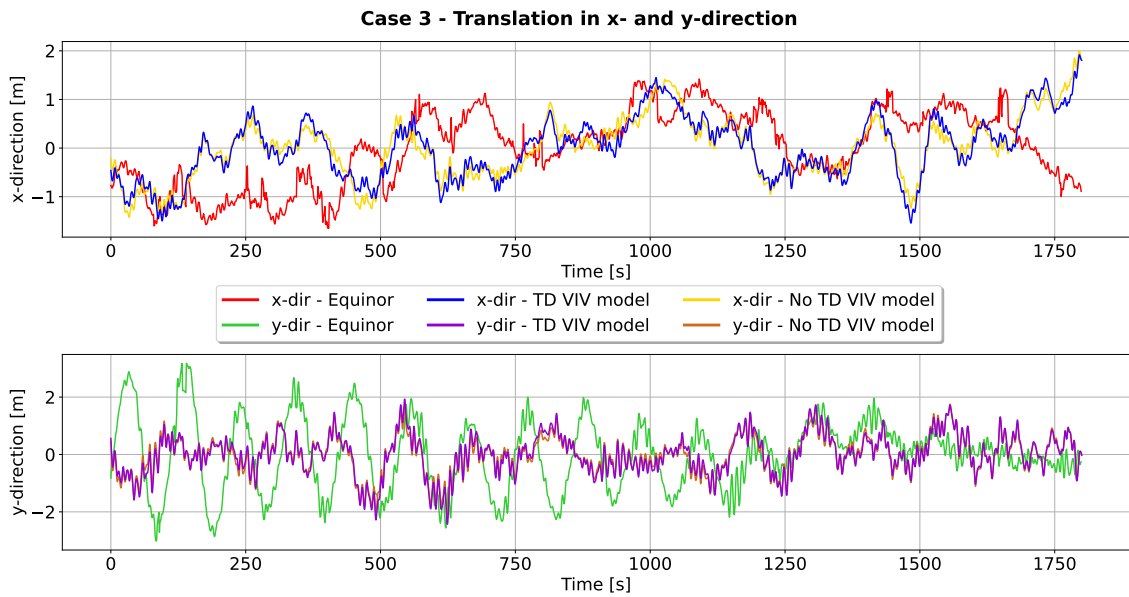


Figure B.5: Translation in x- and y-direction for case 3. The full-scale measurements from Equinor and the SIMA results both with and without the TD VIV model are shown.

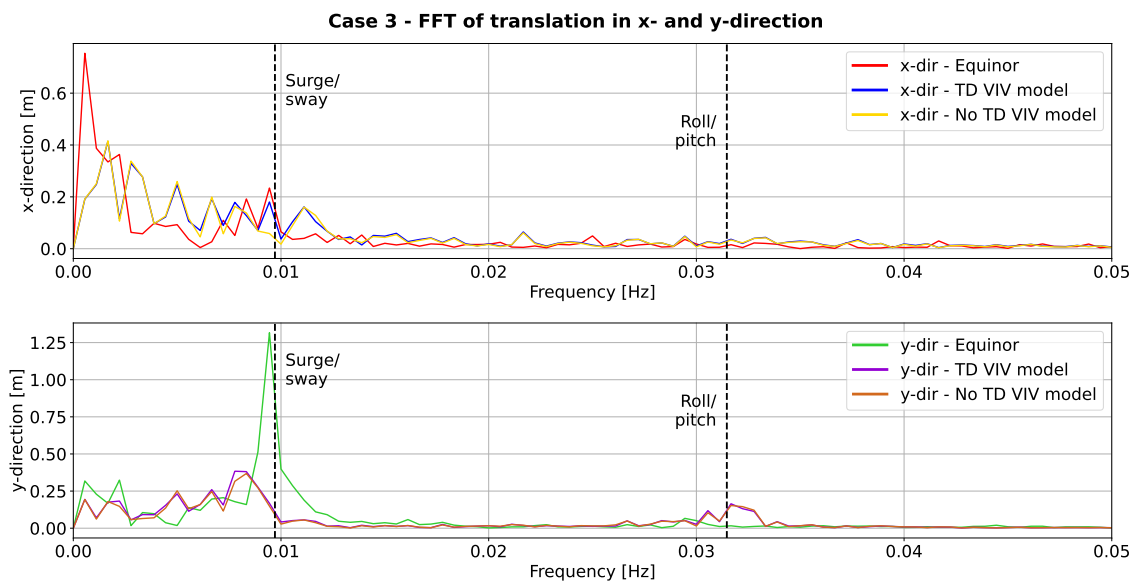


Figure B.6: Fast Fourier transform of translation in x- and y-direction for case 3. The full-scale measurements from Equinor and the SIMA results both with and without the TD VIV model are shown.



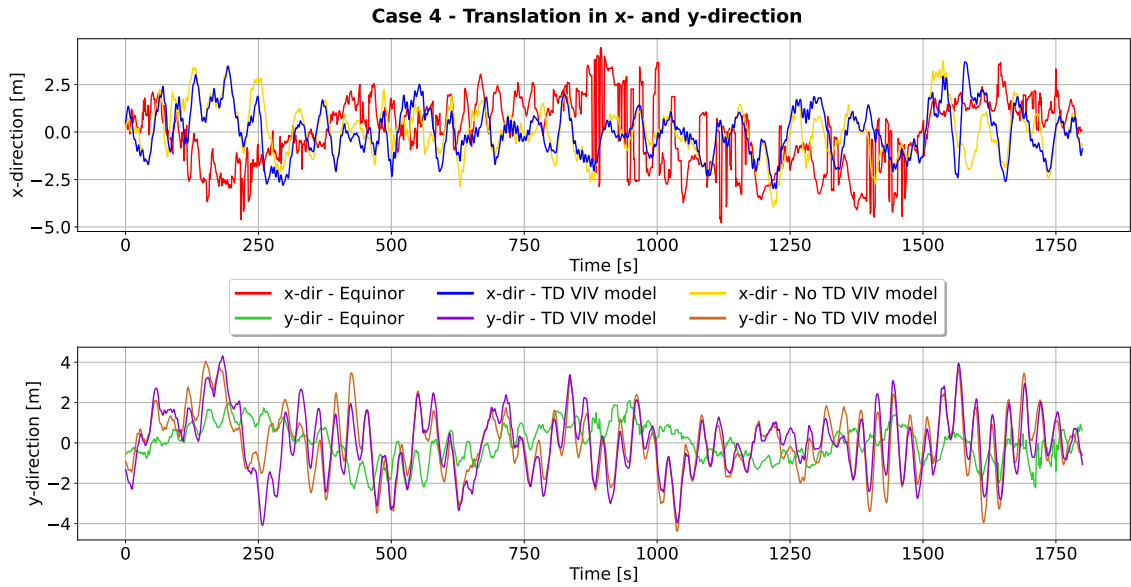


Figure B.7: Translation in x- and y-direction for case 4. The full-scale measurements from Equinor and the SIMA results both with and without the TD VIV model are shown.

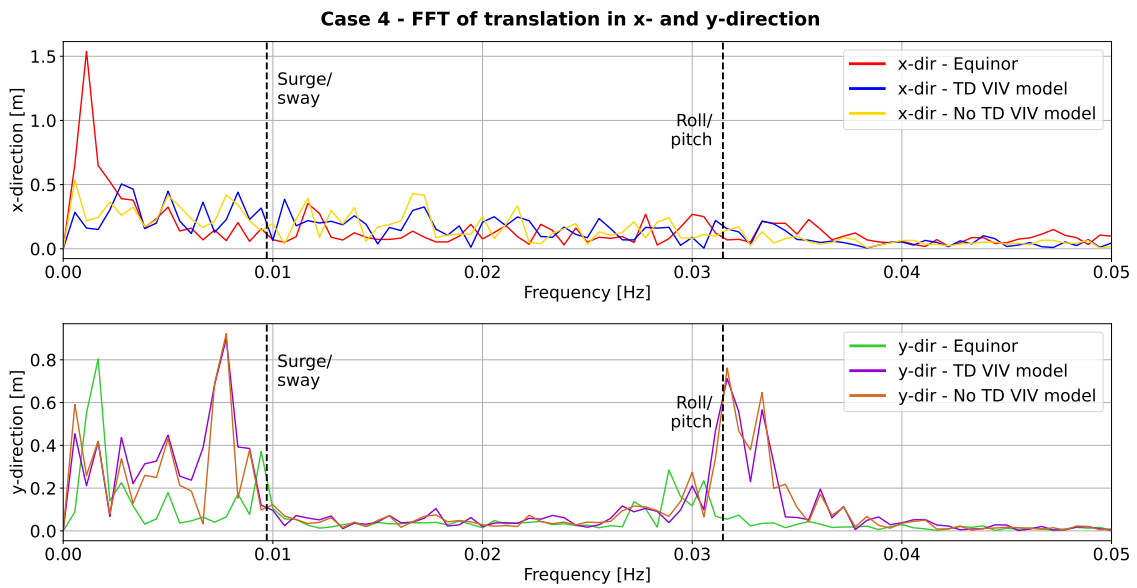


Figure B.8: Fast Fourier transform of translation in x- and y-direction for case 4. The full-scale measurements from Equinor and the SIMA results both with and without the TD VIV model are shown.

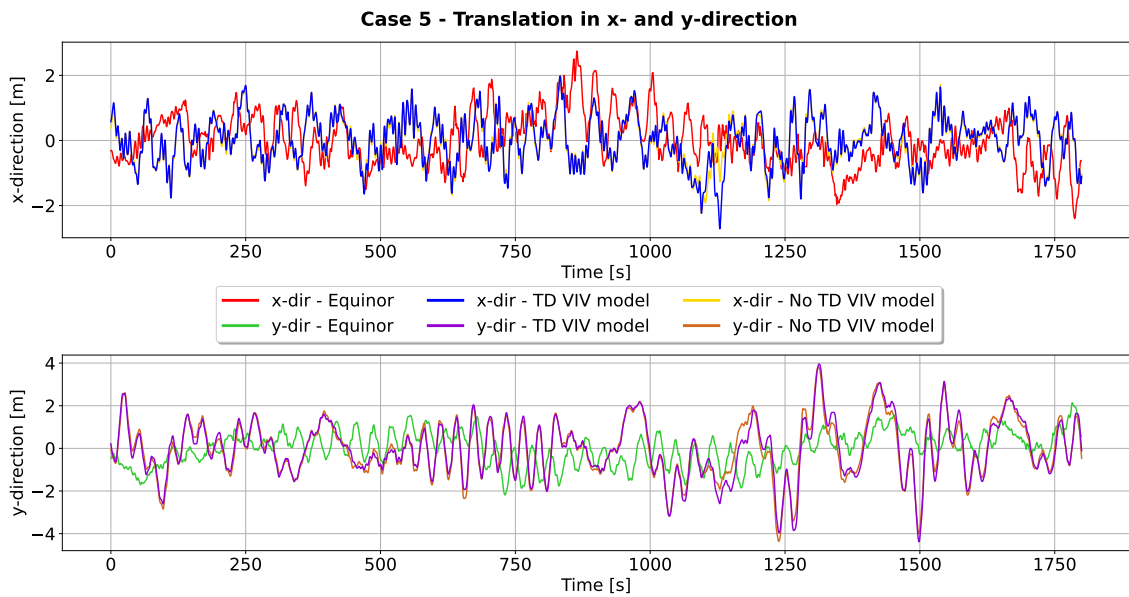


Figure B.9: Translation in x- and y-direction for case 5. The full-scale measurements from Equinor and the SIMA results both with and without the TD VIV model are shown.

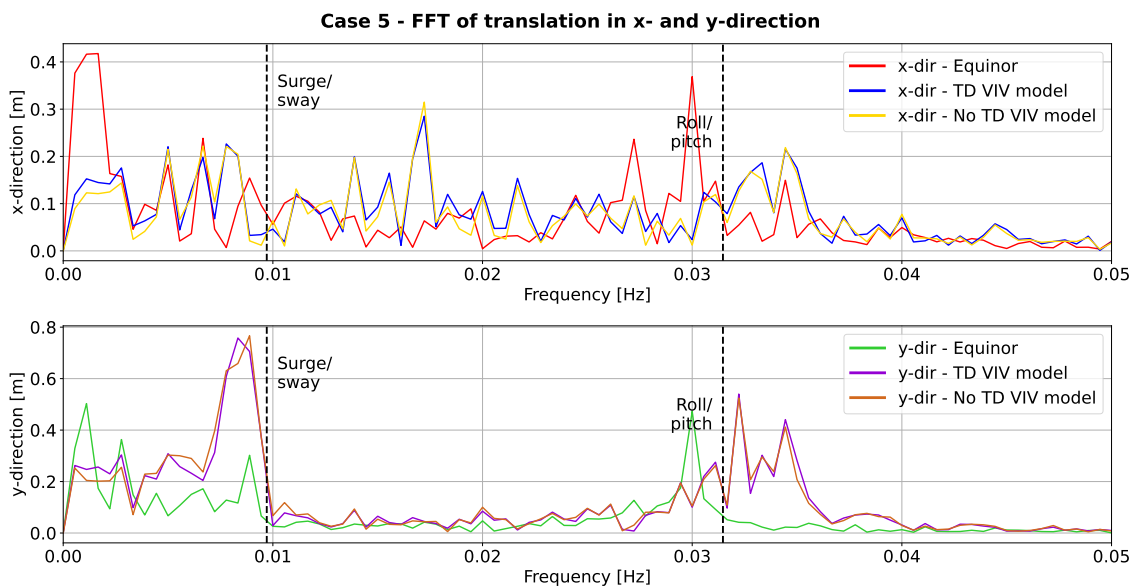


Figure B.10: Fast Fourier transform of translation in x- and y-direction for case 5. The full-scale measurements from Equinor and the SIMA results both with and without the TD VIV model are shown.

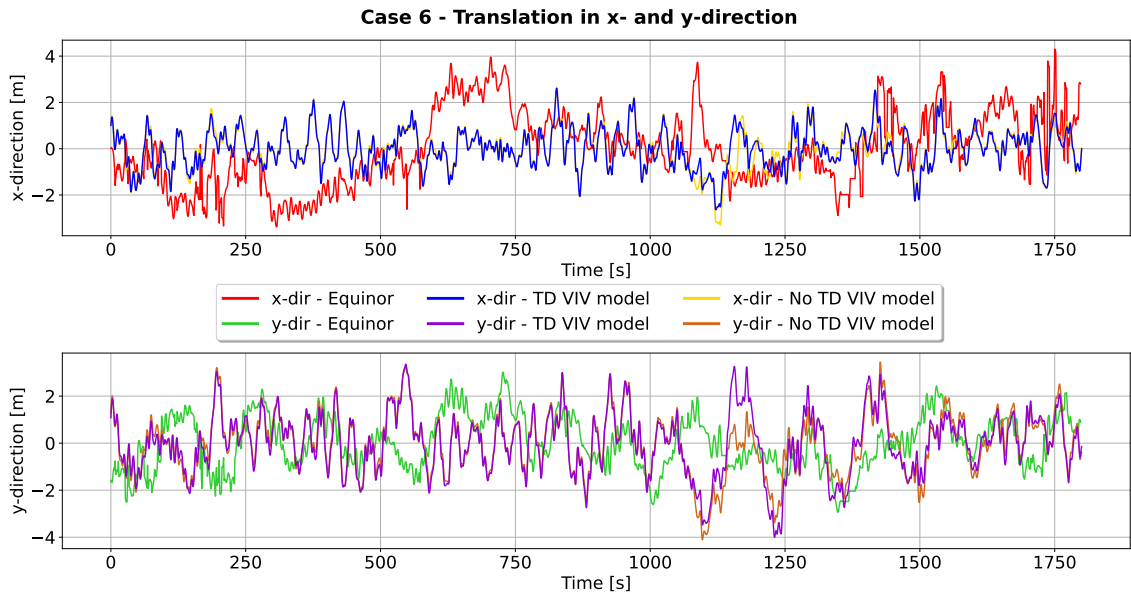


Figure B.11: Translation in x- and y-direction for case 6. The full-scale measurements from Equinor and the SIMA results both with and without the TD VIV model are shown.

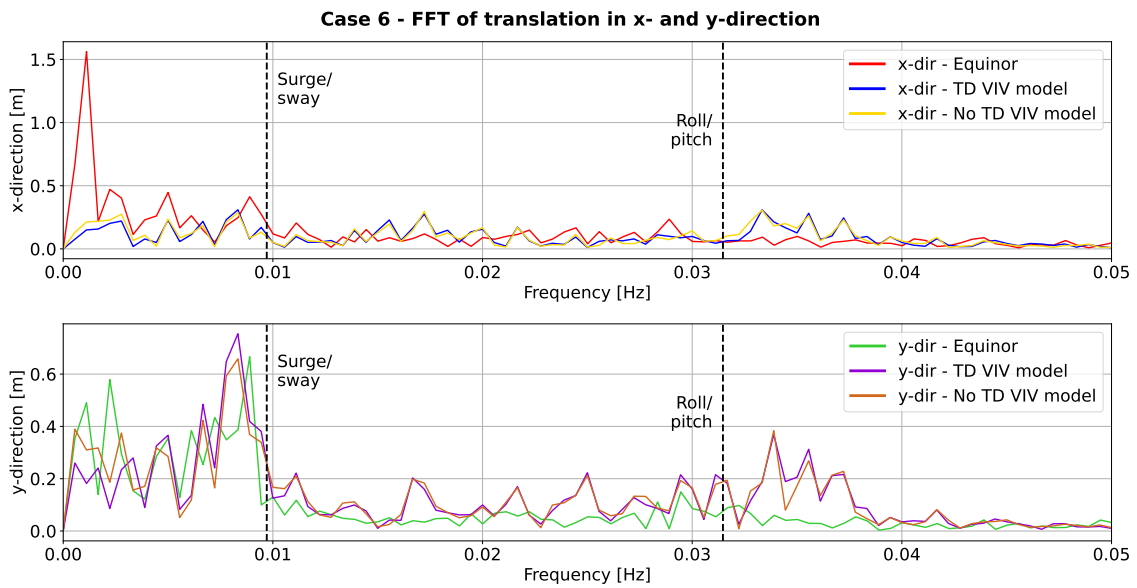


Figure B.12: Fast Fourier transform of translation in x- and y-direction for case 6. The full-scale measurements from Equinor and the SIMA results both with and without the TD VIV model are shown.

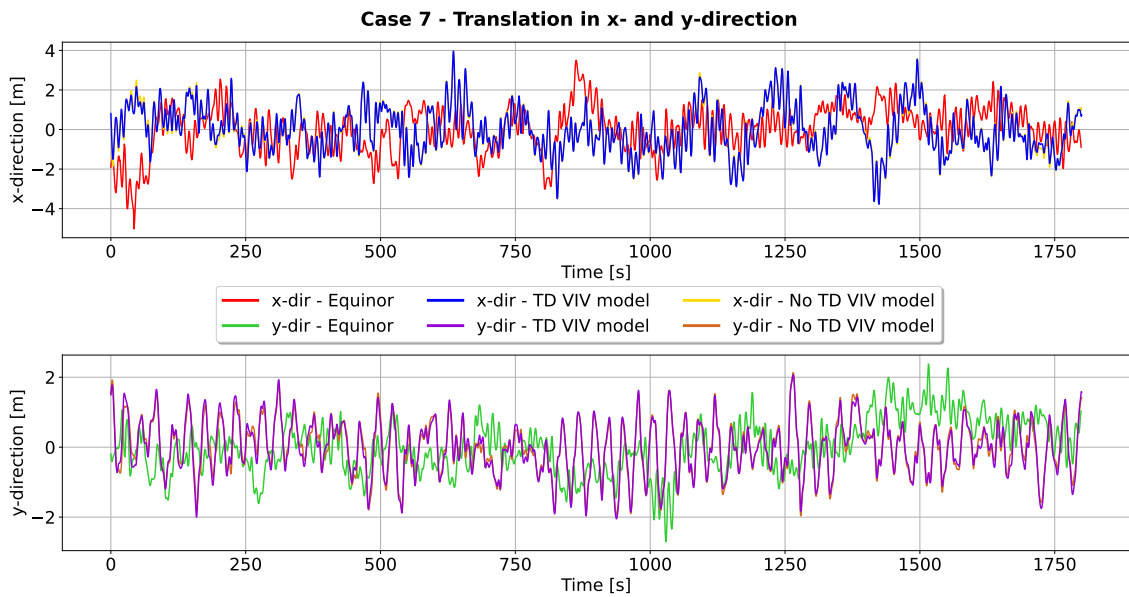


Figure B.13: Translation in x- and y-direction for case 7. The full-scale measurements from Equinor and the SIMA results both with and without the TD VIV model are shown.

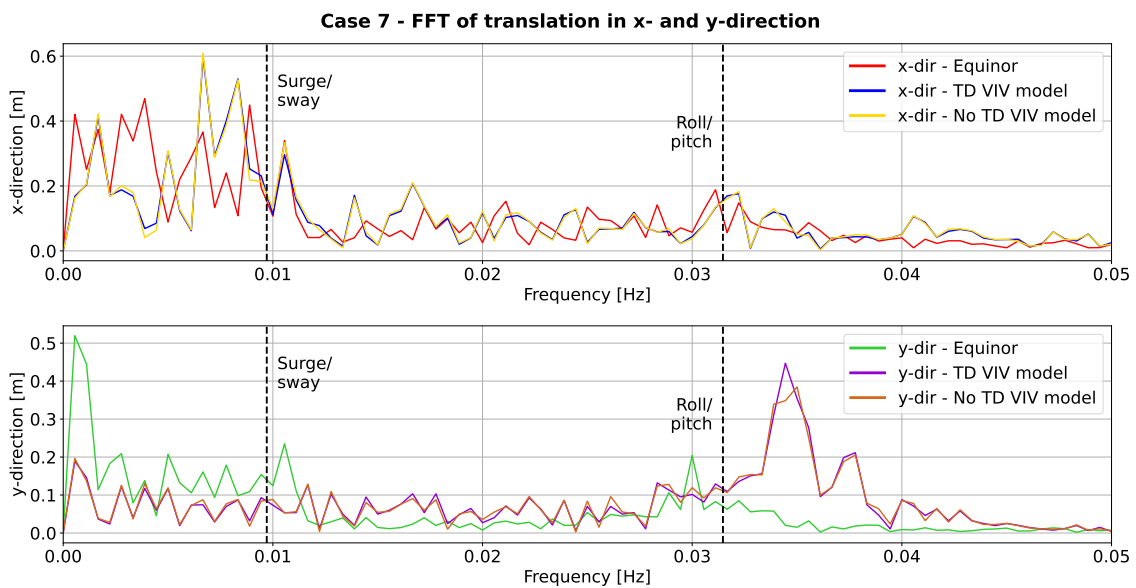


Figure B.14: Fast Fourier transform of translation in x- and y-direction for case 7. The full-scale measurements from Equinor and the SIMA results both with and without the TD VIV model are shown.

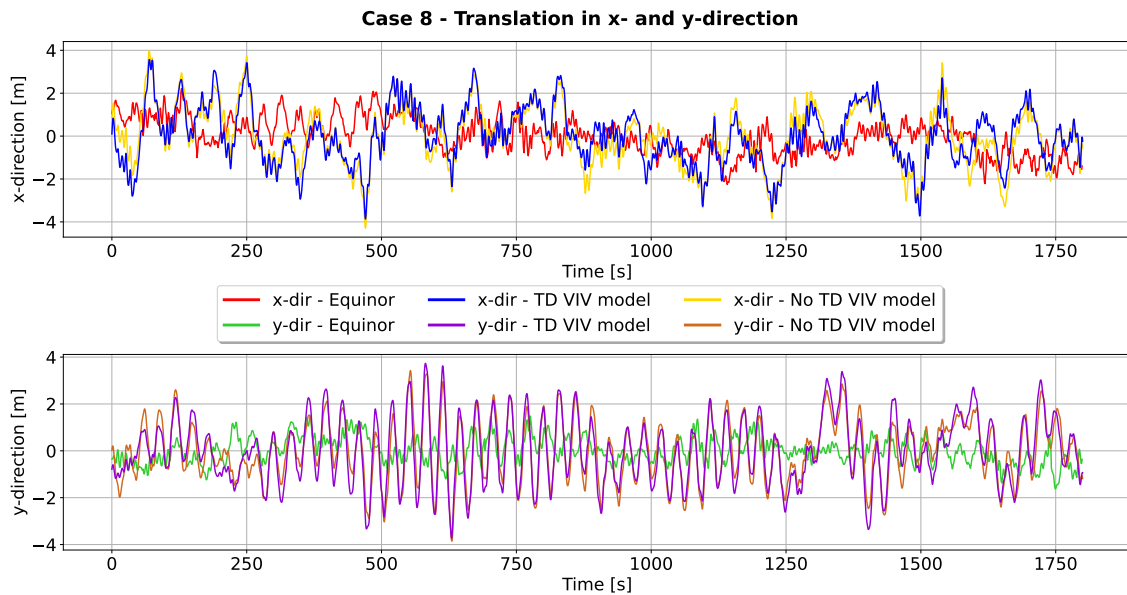


Figure B.15: Translation in x- and y-direction for case 8. The full-scale measurements from Equinor and the SIMA results both with and without the TD VIV model are shown.

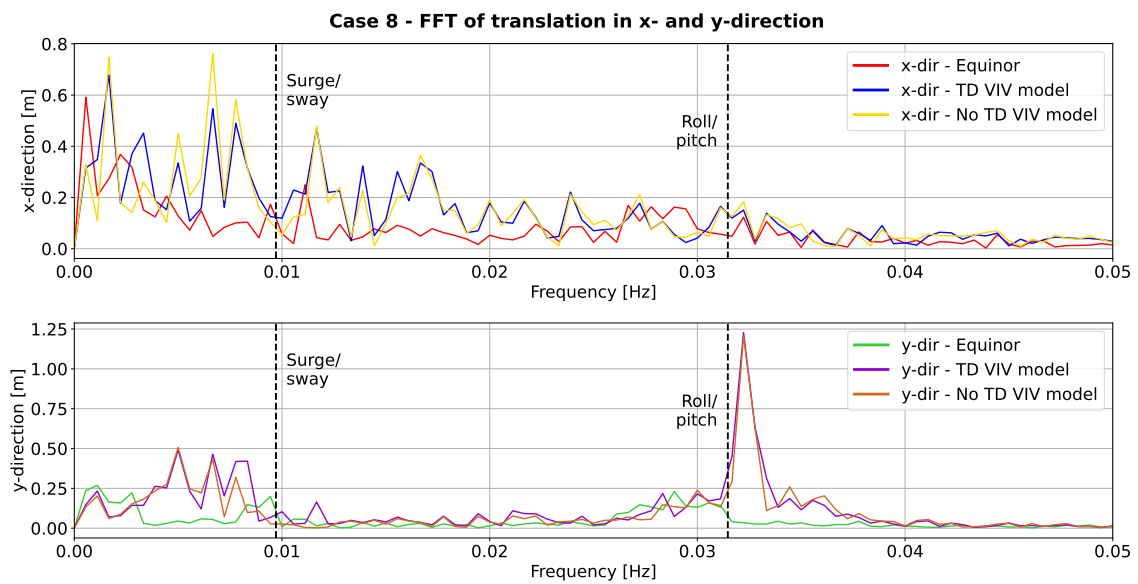


Figure B.16: Fast Fourier transform of translation in x- and y-direction for case 8. The full-scale measurements from Equinor and the SIMA results both with and without the TD VIV model are shown.

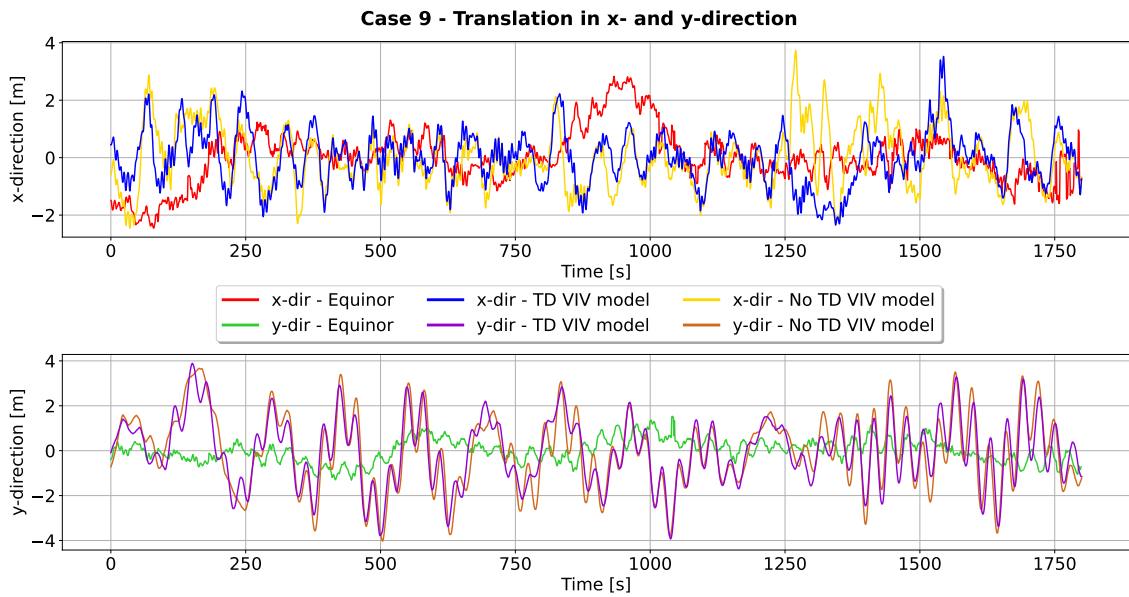


Figure B.17: Translation in x- and y-direction for case 9. The full-scale measurements from Equinor and the SIMA results both with and without the TD VIV model are shown.

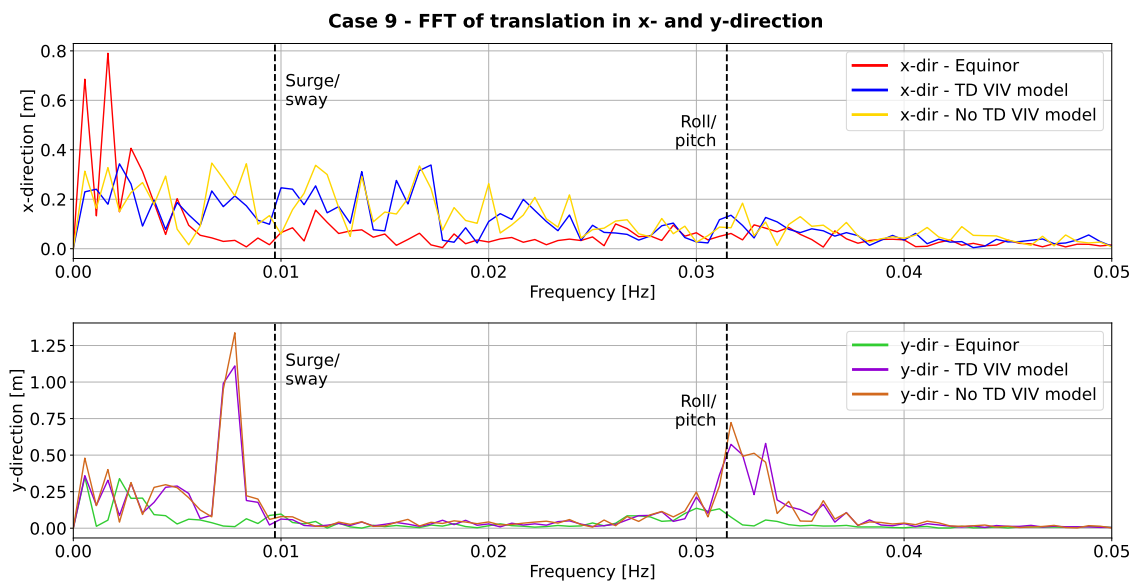


Figure B.18: Fast Fourier transform of translation in x- and y-direction for case 9. The full-scale measurements from Equinor and the SIMA results both with and without the TD VIV model are shown.

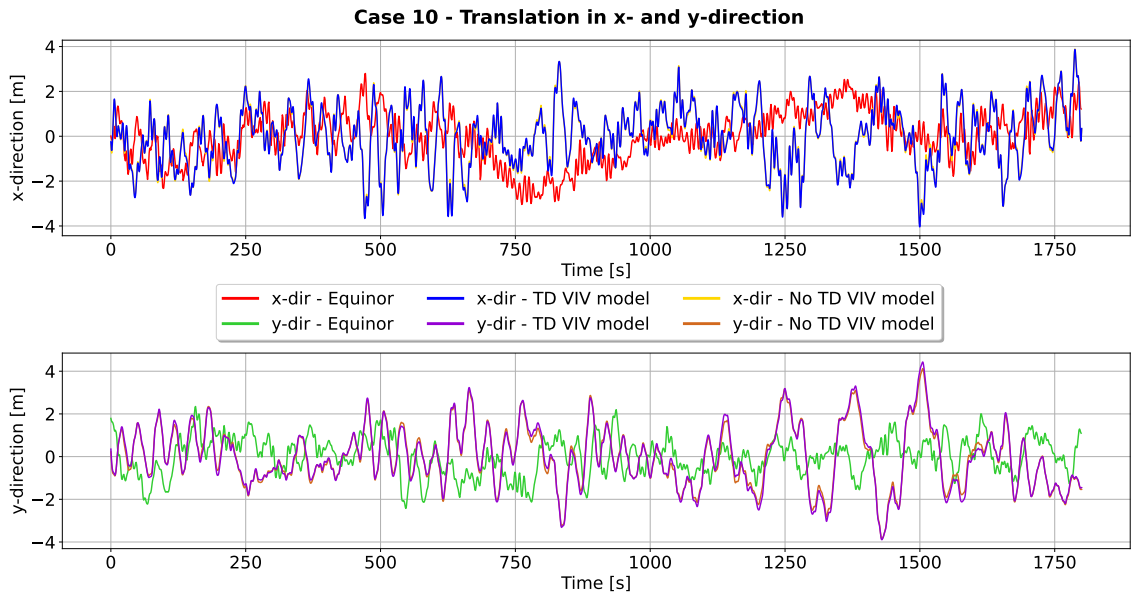


Figure B.19: Translation in x- and y-direction for case 10. The full-scale measurements from Equinor and the SIMA results both with and without the TD VIV model are shown.

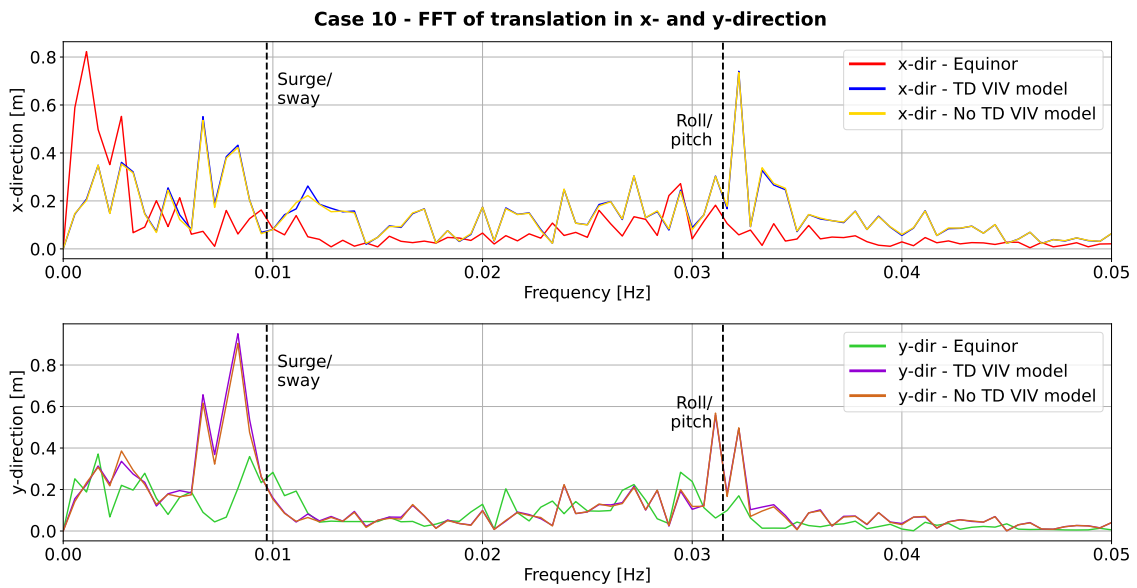


Figure B.20: Fast Fourier transform of translation in x- and y-direction for case 10. The full-scale measurements from Equinor and the SIMA results both with and without the TD VIV model are shown.

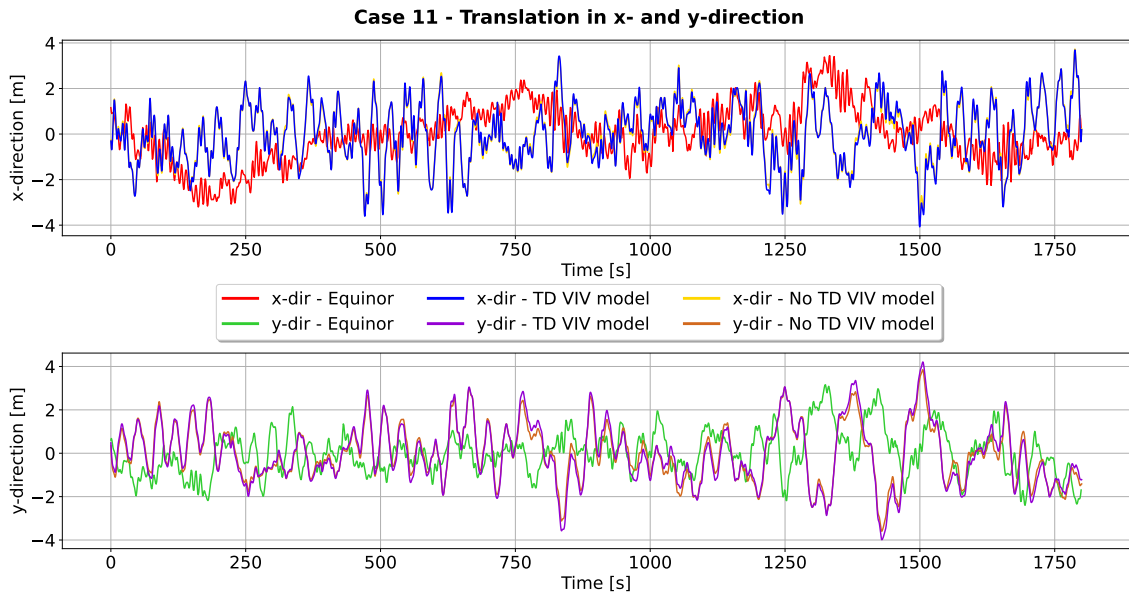


Figure B.21: Translation in x- and y-direction for case 11. The full-scale measurements from Equinor and the SIMA results both with and without the TD VIV model are shown.

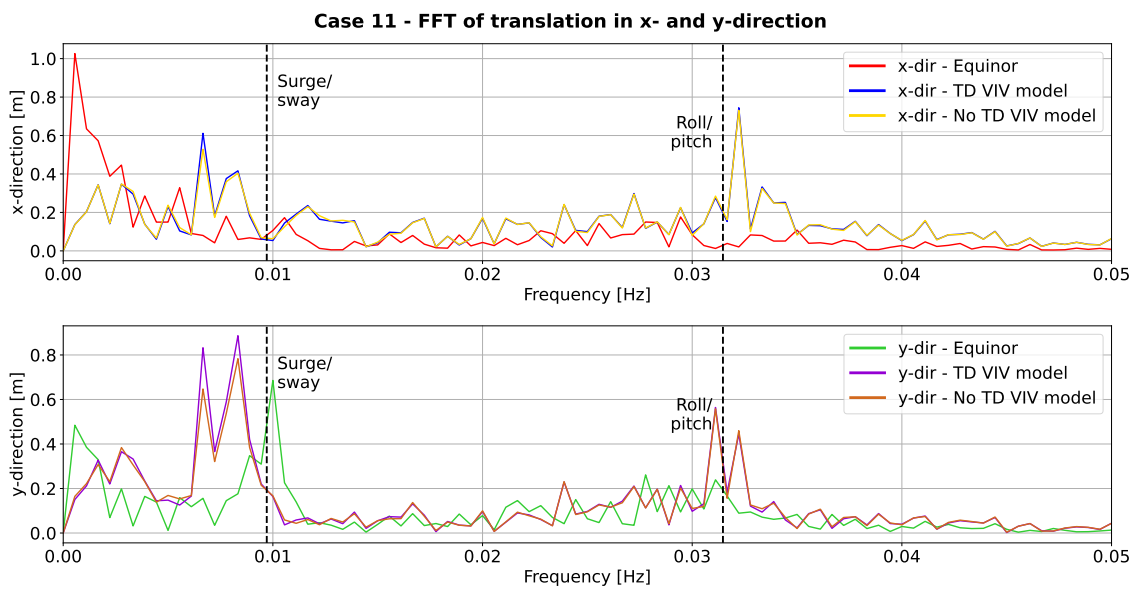


Figure B.22: Fast Fourier transform of translation in x- and y-direction for case 11. The full-scale measurements from Equinor and the SIMA results both with and without the TD VIV model are shown.



## B.2 Effect of wind and waves on VIM response

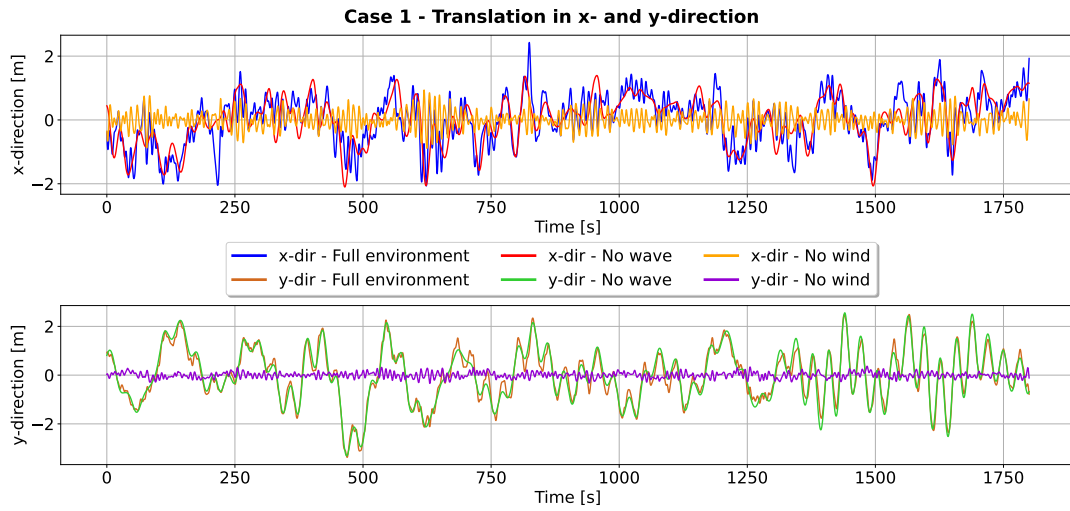


Figure B.23: Translation in x- and y-direction for case 1. All lines show results with the TD VIV model for different metocean environments. Full environment consists of current, wind and waves.

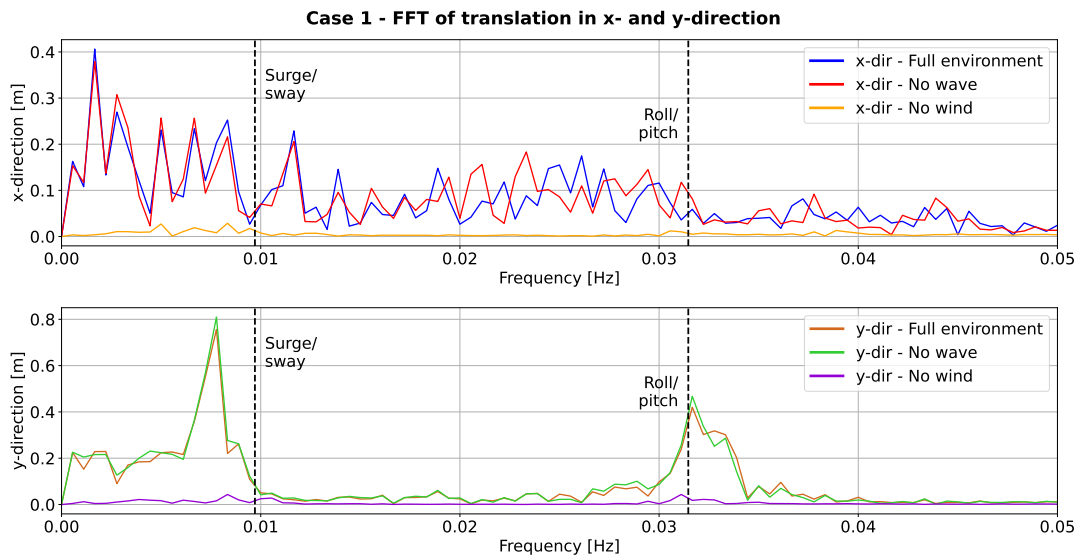


Figure B.24: Fast Fourier transform of translation in x- and y-direction for case 1. All lines show results with the TD VIV model for different metocean environments. Full environment consists of current, wind and waves.

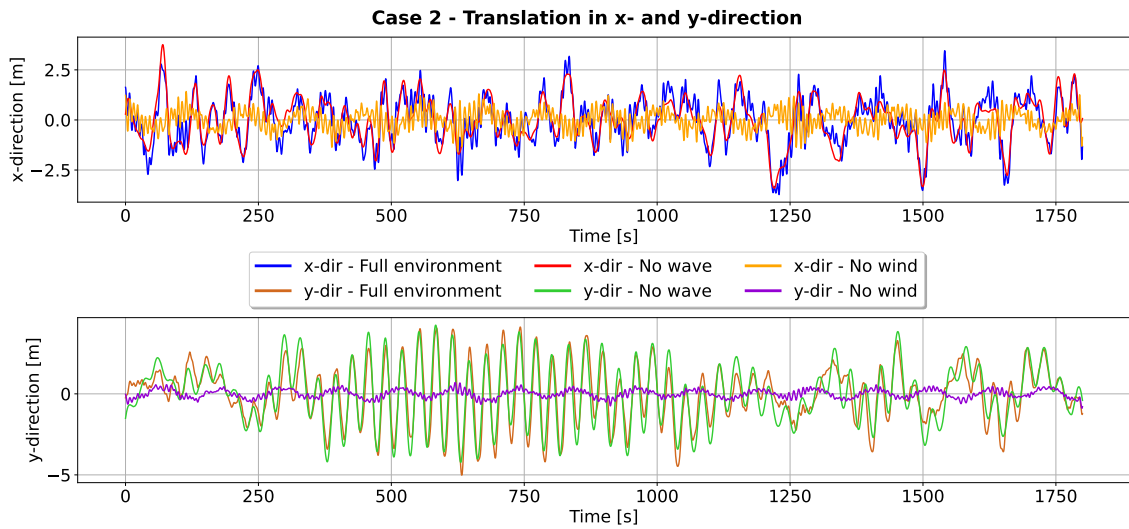


Figure B.25: Translation in x- and y-direction for case 2. All lines show results with the TD VIV model for different metocean environments. Full environment consists of current, wind and waves.

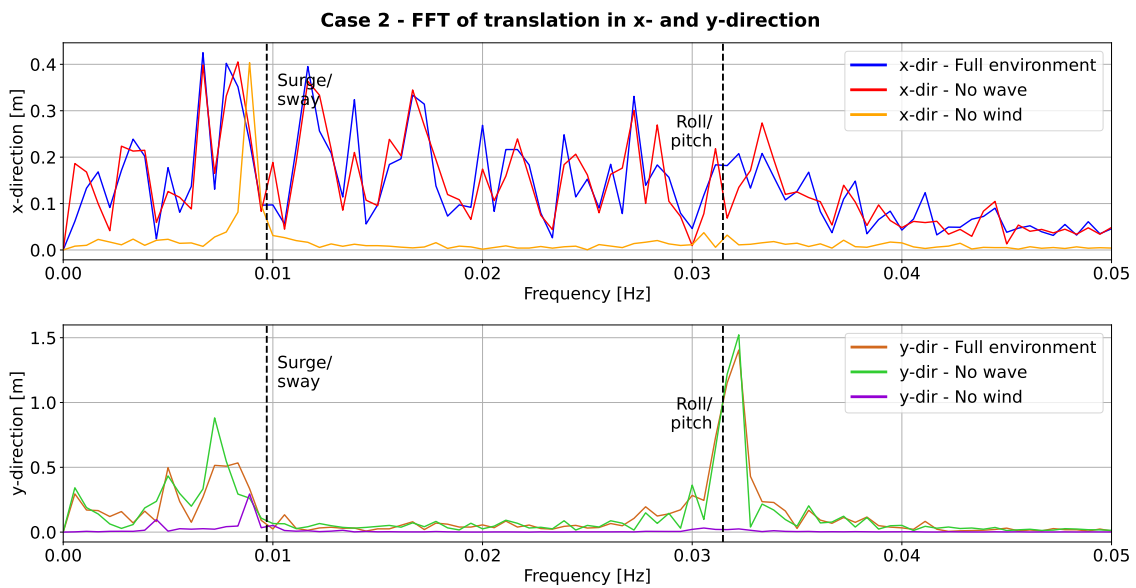


Figure B.26: Fast Fourier transform of translation in x- and y-direction for case 2. All lines show results with the TD VIV model for different metocean environments. Full environment consists of current, wind and waves.

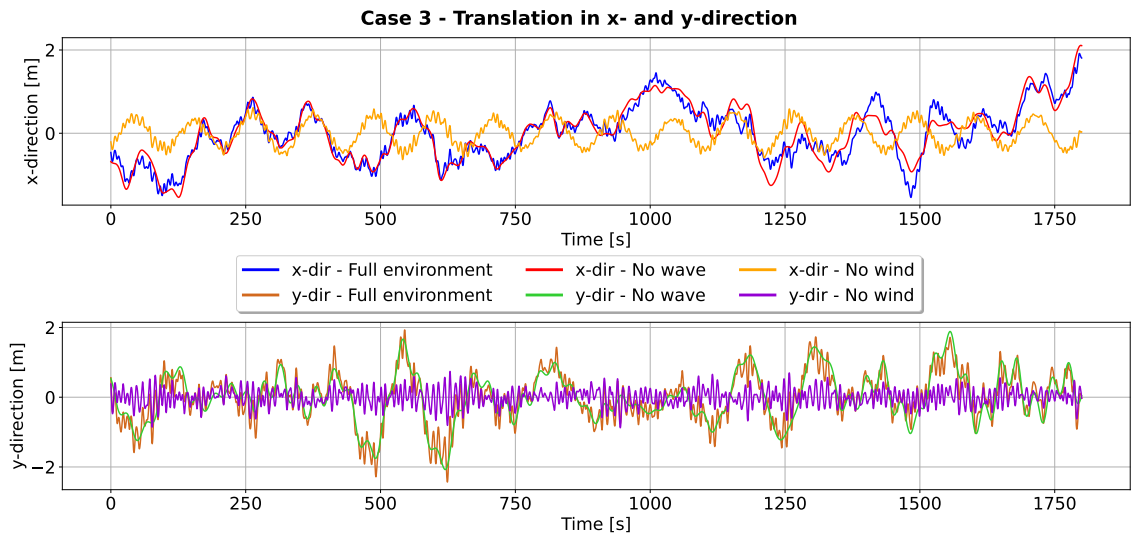


Figure B.27: Translation in x- and y-direction for case 3. All lines show results with the TD VIV model for different metocean environments. Full environment consists of current, wind and waves.

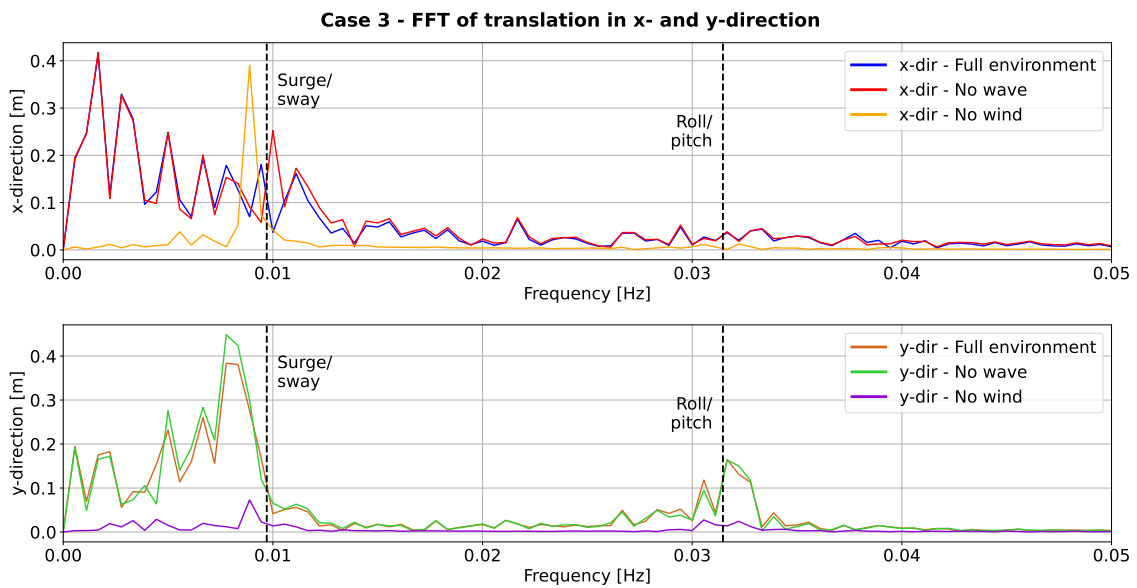


Figure B.28: Fast Fourier transform of translation in x- and y-direction for case 3. All lines show results with the TD VIV model for different metocean environments. Full environment consists of current, wind and waves.

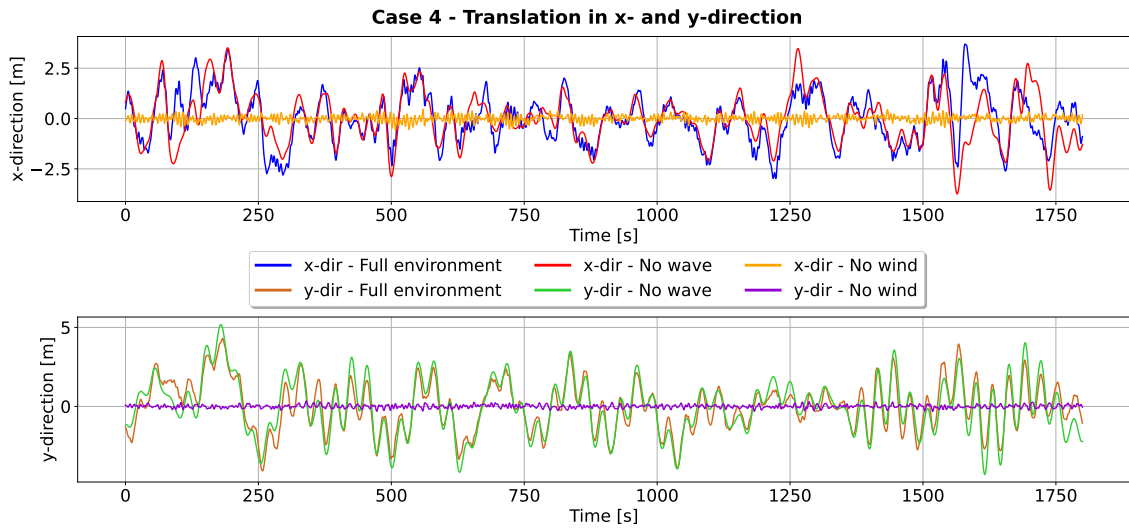


Figure B.29: Translation in x- and y-direction for case 4. All lines show results with the TD VIV model for different metocean environments. Full environment consists of current, wind and waves.

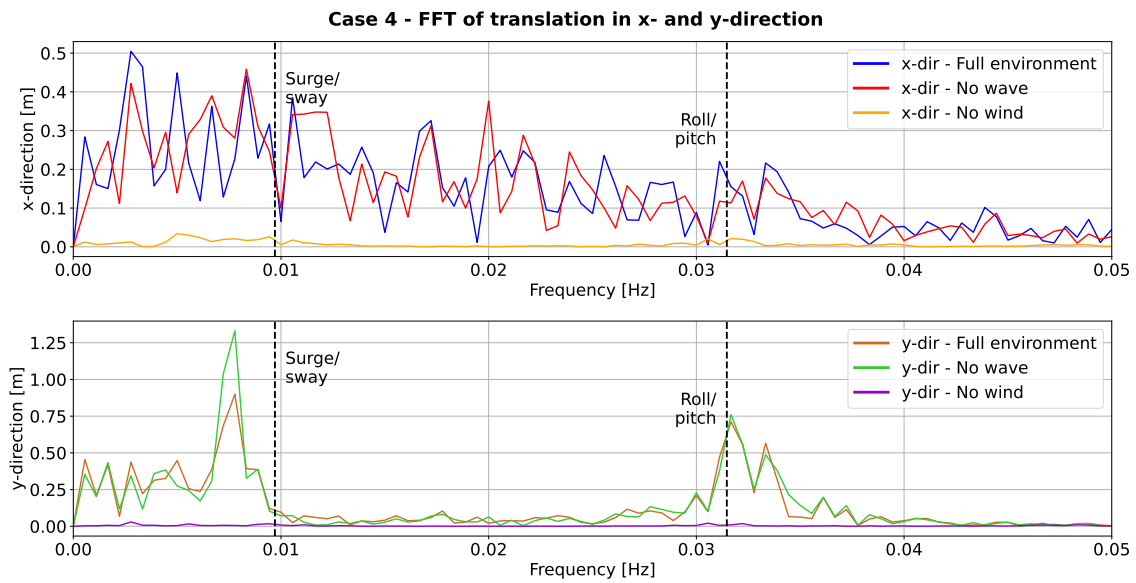


Figure B.30: Fast Fourier transform of translation in x- and y-direction for case 4. All lines show results with the TD VIV model for different metocean environments. Full environment consists of current, wind and waves.

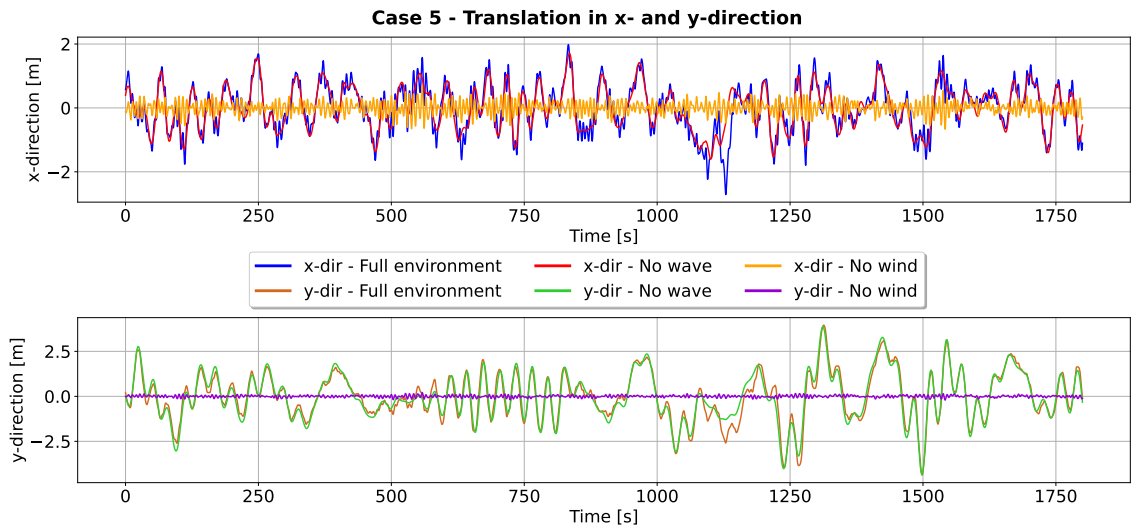


Figure B.31: Translation in x- and y-direction for case 5. All lines show results with the TD VIV model for different metocean environments. Full environment consists of current, wind and waves.

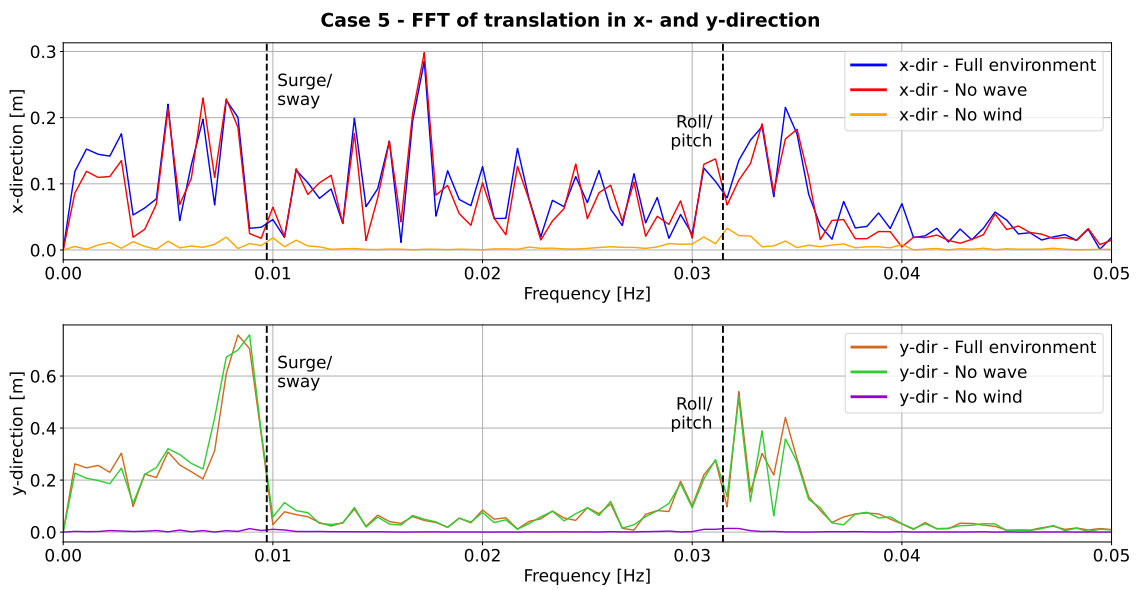


Figure B.32: Fast Fourier transform of translation in x- and y-direction for case 5. All lines show results with the TD VIV model for different metocean environments. Full environment consists of current, wind and waves.

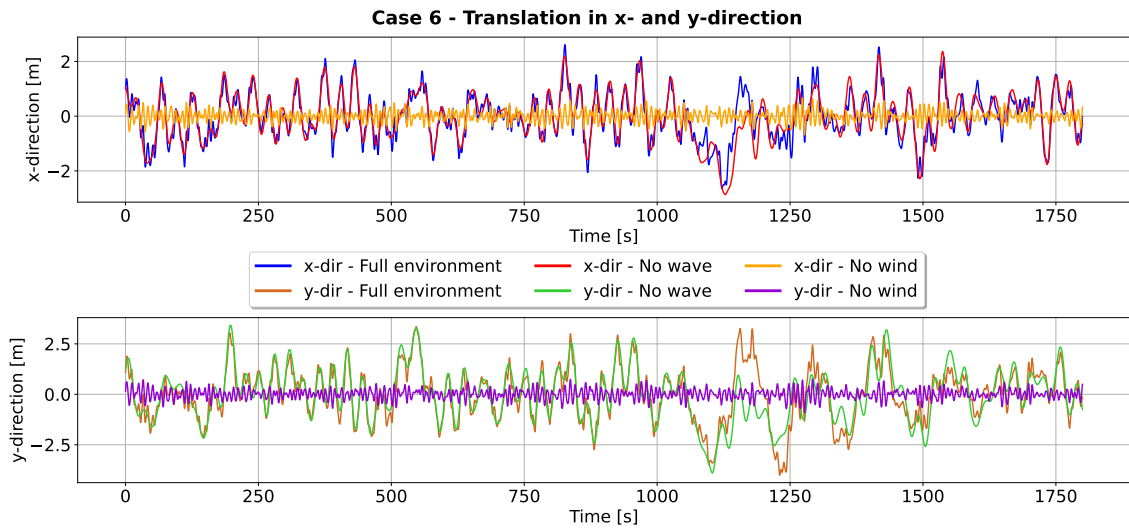


Figure B.33: Translation in x- and y-direction for case 6. All lines show results with the TD VIV model for different metocean environments. Full environment consists of current, wind and waves.

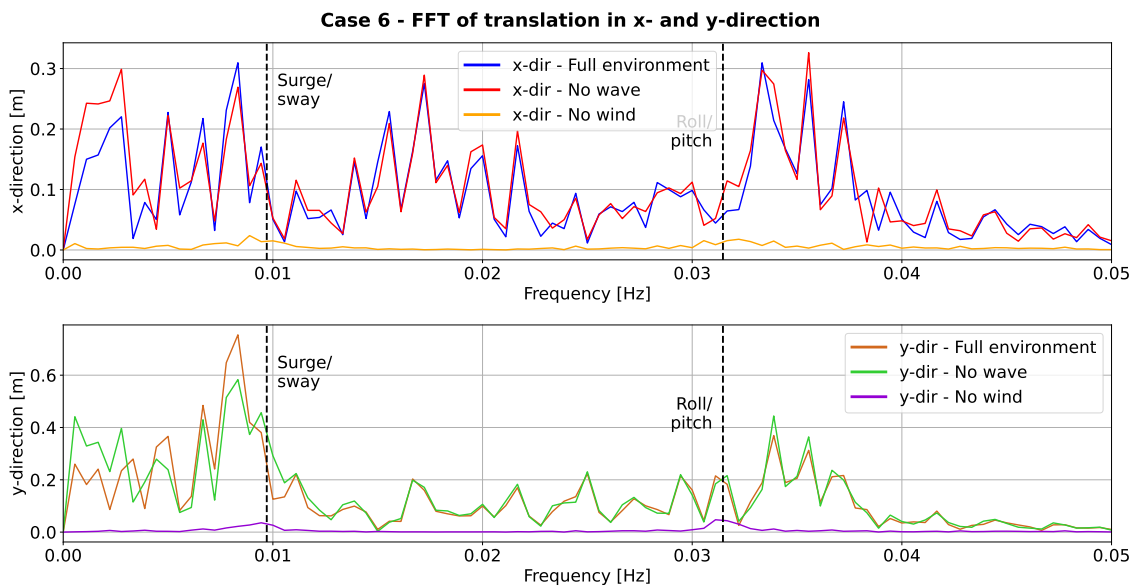


Figure B.34: Fast Fourier transform of translation in x- and y-direction for case 6. All lines show results with the TD VIV model for different metocean environments. Full environment consists of current, wind and waves.

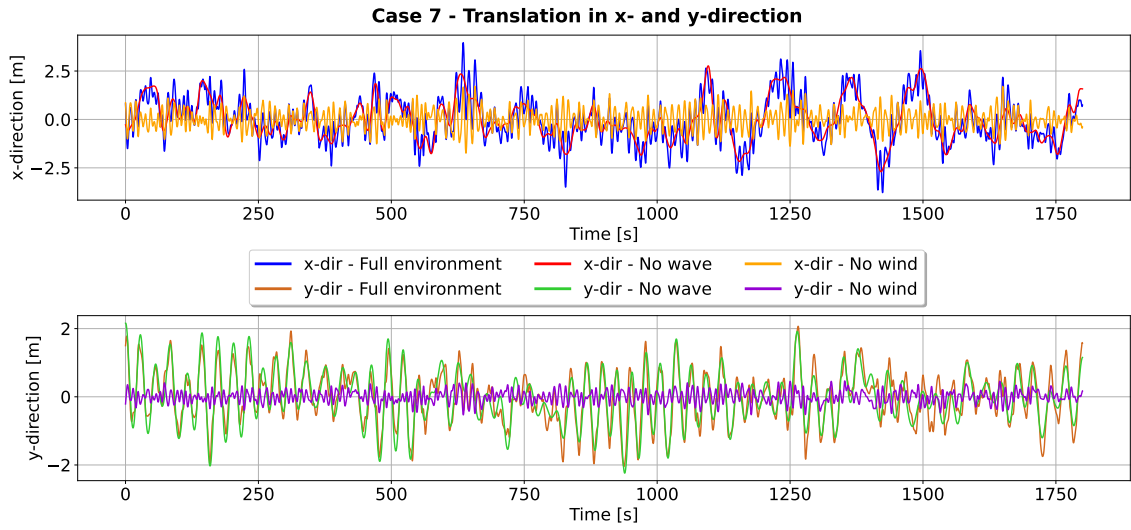


Figure B.35: Translation in x- and y-direction for case 7. All lines show results with the TD VIV model for different metocean environments. Full environment consists of current, wind and waves.

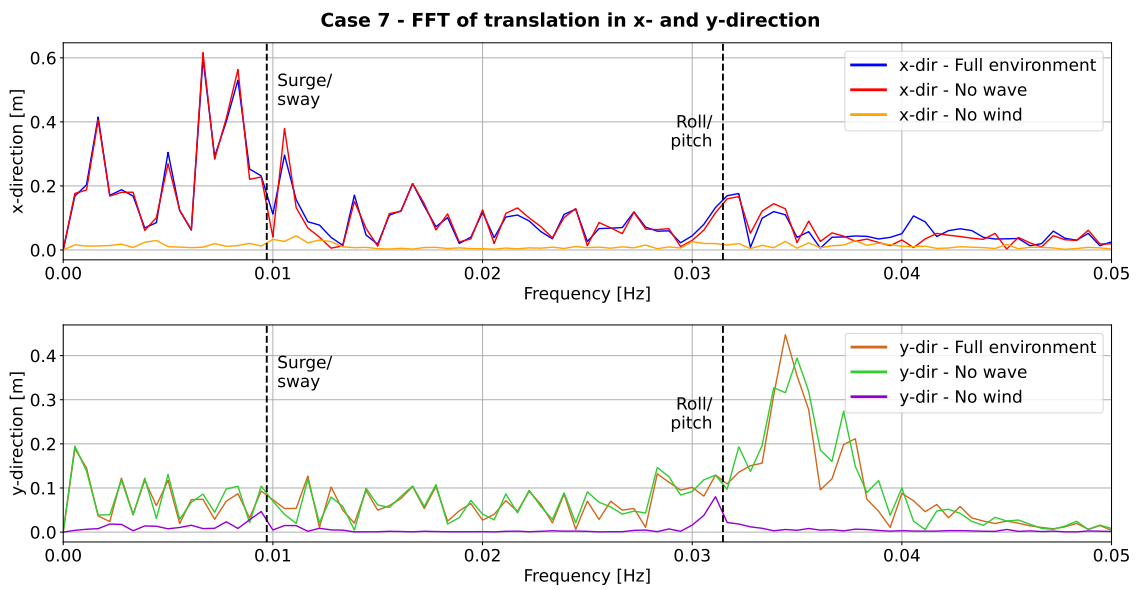


Figure B.36: Fast Fourier transform of translation in x- and y-direction for case 7. All lines show results with the TD VIV model for different metocean environments. Full environment consists of current, wind and waves.

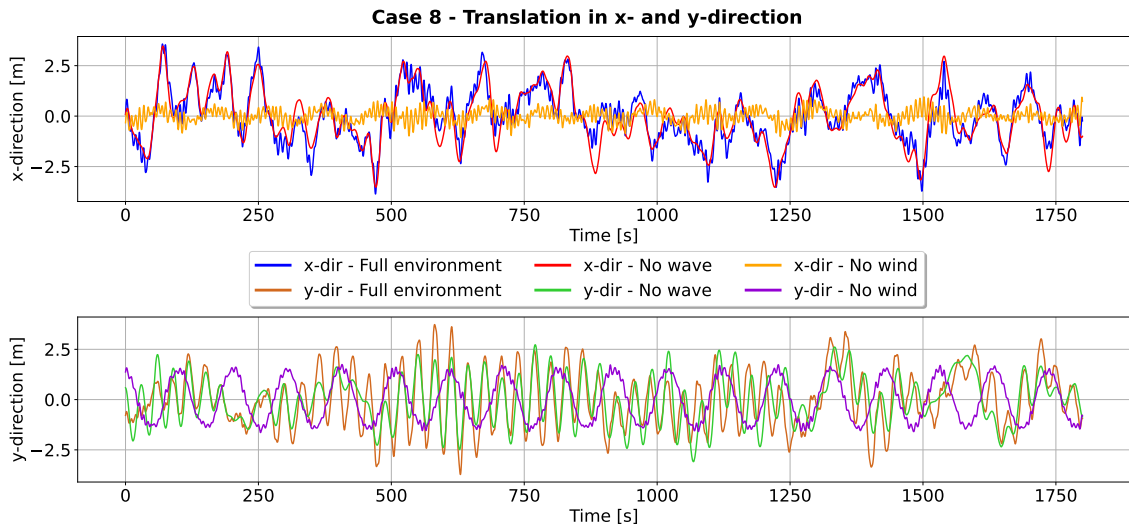


Figure B.37: Translation in x- and y-direction for case 8. All lines show results with the TD VIV model for different metocean environments. Full environment consists of current, wind and waves.

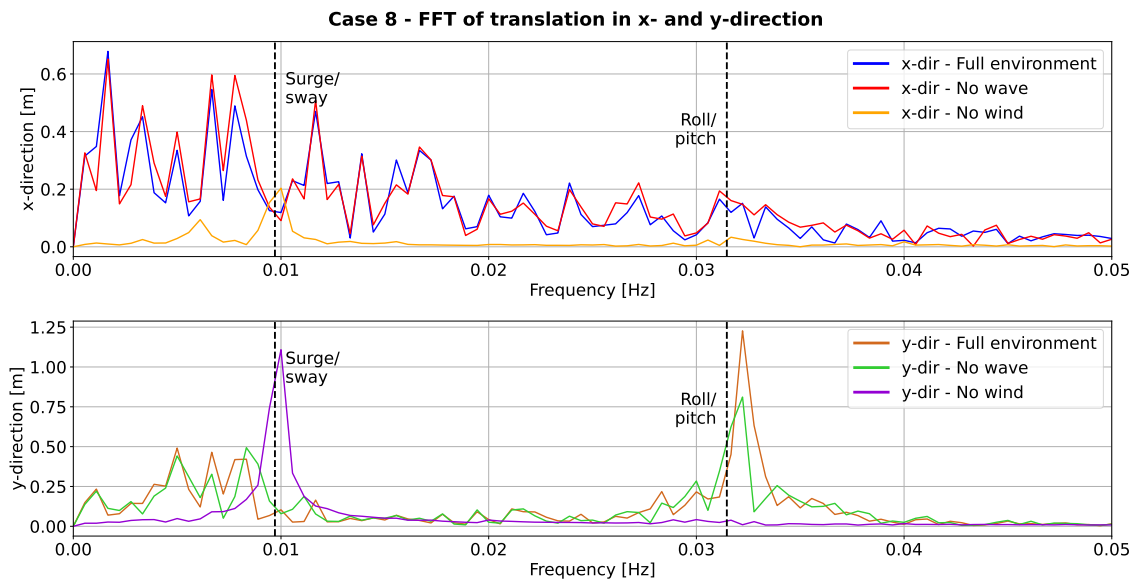


Figure B.38: Fast Fourier transform of translation in x- and y-direction for case 8. All lines show results with the TD VIV model for different metocean environments. Full environment consists of current, wind and waves.



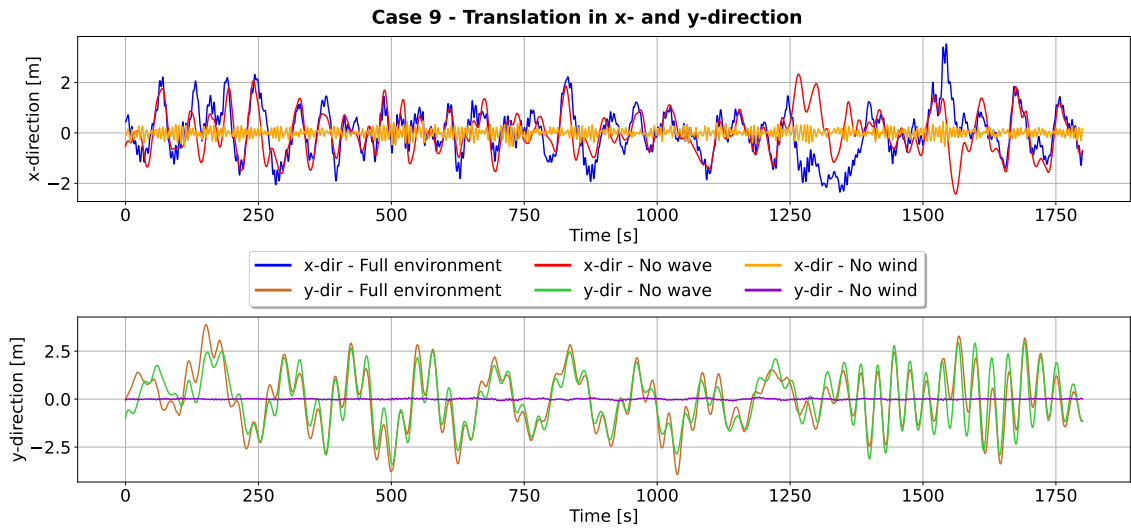


Figure B.39: Translation in x- and y-direction for case 9. All lines show results with the TD VIV model for different metocean environments. Full environment consists of current, wind and waves.

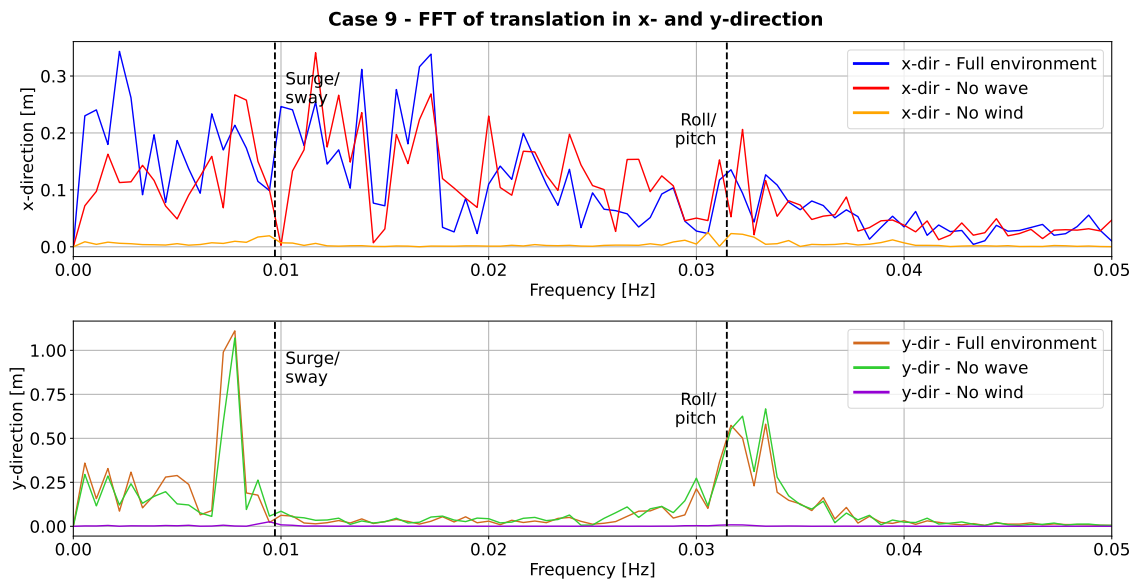


Figure B.40: Fast Fourier transform of translation in x- and y-direction for case 9. All lines show results with the TD VIV model for different metocean environments. Full environment consists of current, wind and waves.

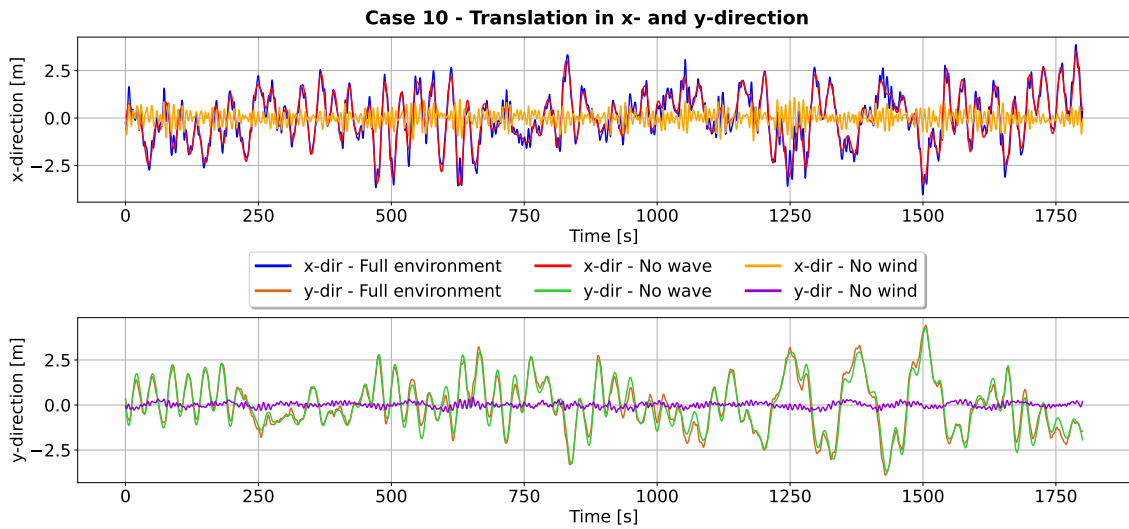


Figure B.41: Translation in x- and y-direction for case 10. All lines show results with the TD VIV model for different metocean environments. Full environment consists of current, wind and waves.

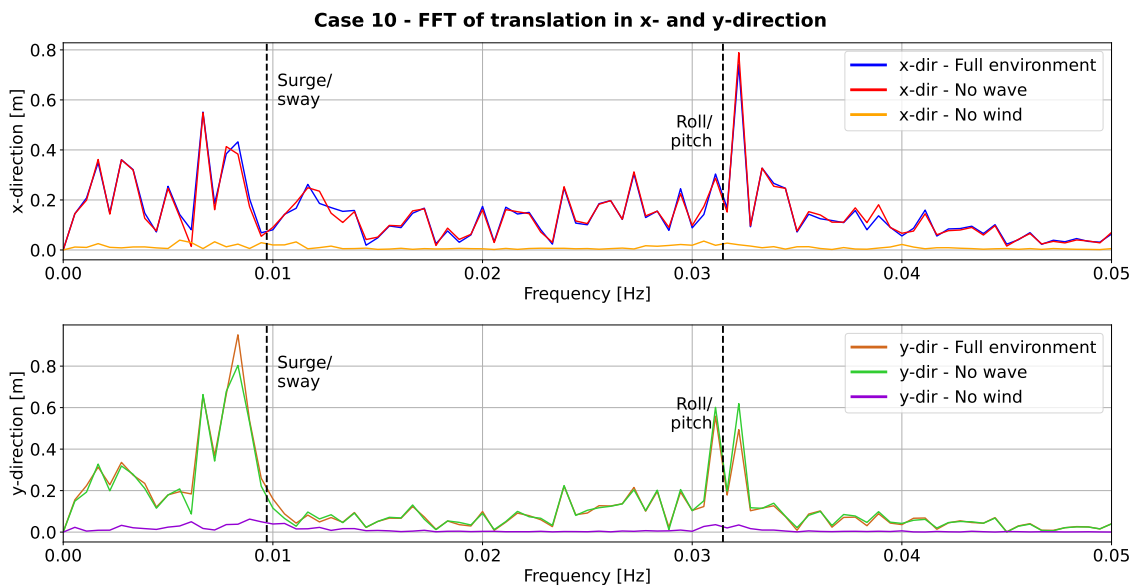


Figure B.42: Fast Fourier transform of translation in x- and y-direction for case 10. All lines show results with the TD VIV model for different metocean environments. Full environment consists of current, wind and waves.

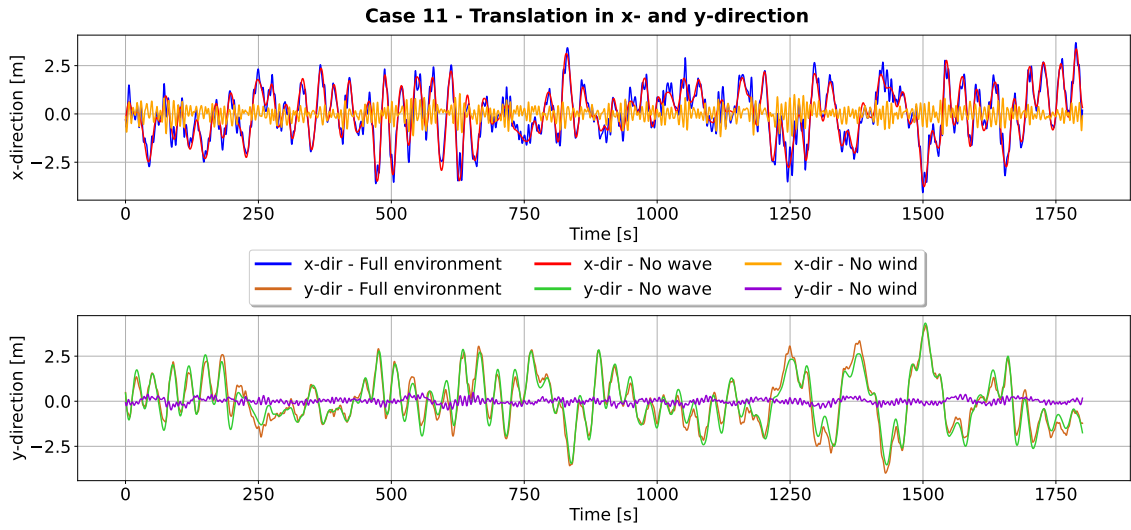


Figure B.43: Translation in x- and y-direction for case 11. All lines show results with the TD VIV model for different metocean environments. Full environment consists of current, wind and waves.

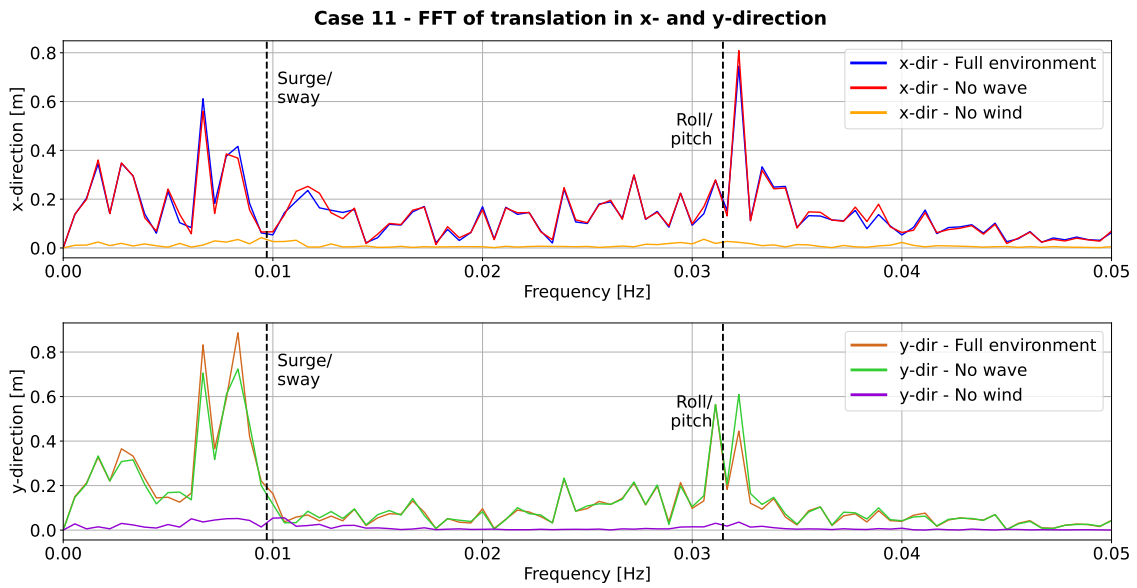


Figure B.44: Fast Fourier transform of translation in x- and y-direction for case 11. All lines show results with the TD VIV model for different metocean environments. Full environment consists of current, wind and waves.

### B.3 Full year environmental condition

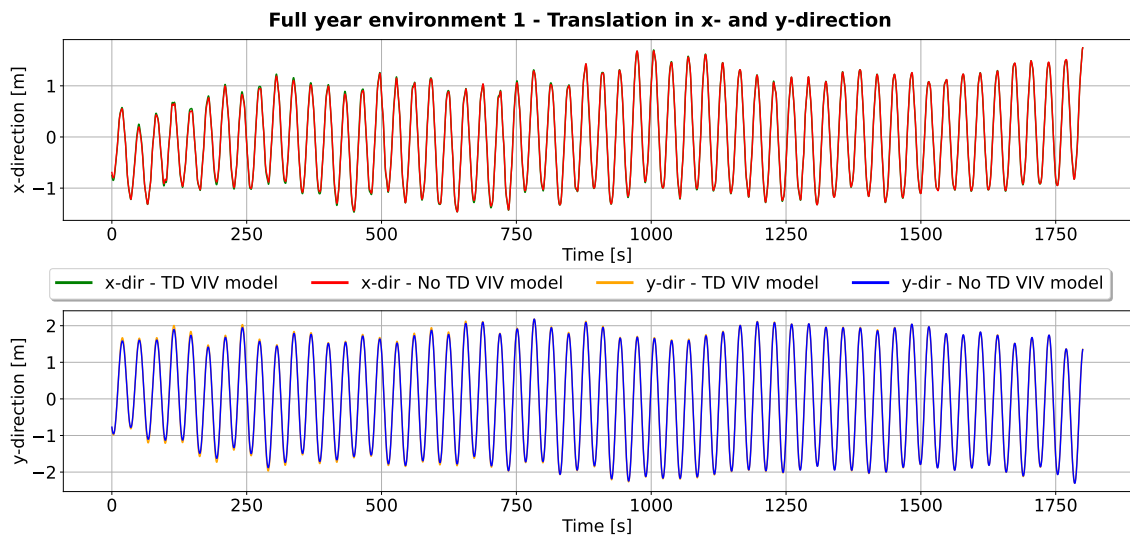


Figure B.45: Translation in x- and y-direction for full year environment 1. Results both with and without the TD VIV model are shown.

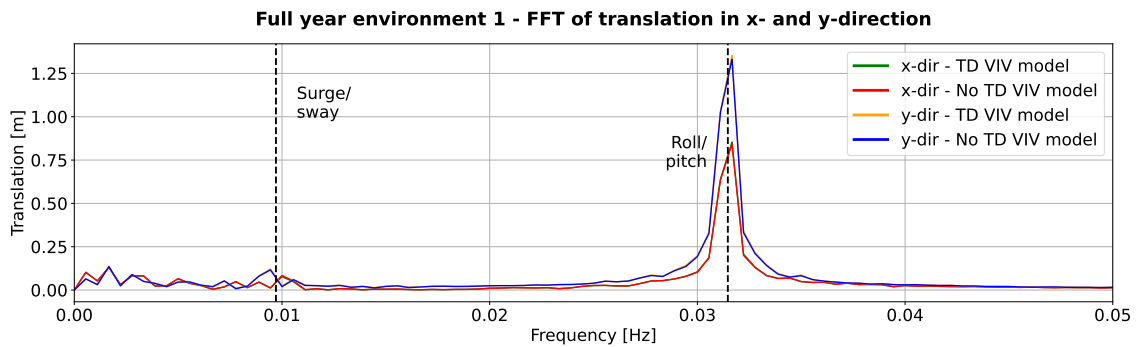


Figure B.46: Fast Fourier transform of translation in x- and y-direction for full year environment 1. Results both with and without the TD VIV model are shown.

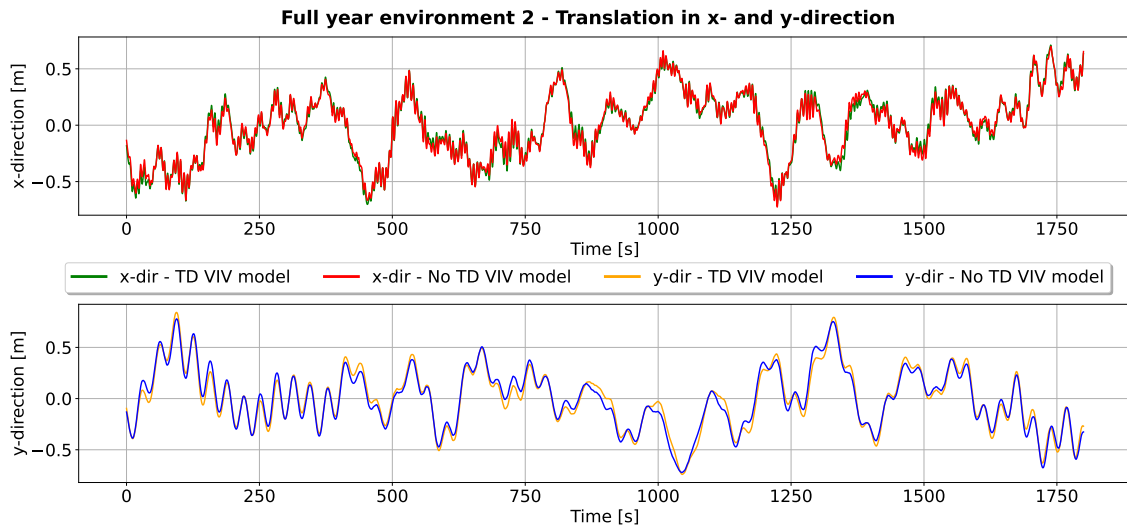


Figure B.47: Translation in x- and y-direction for full year environment 2. Results both with and without the TD VIV model are shown.

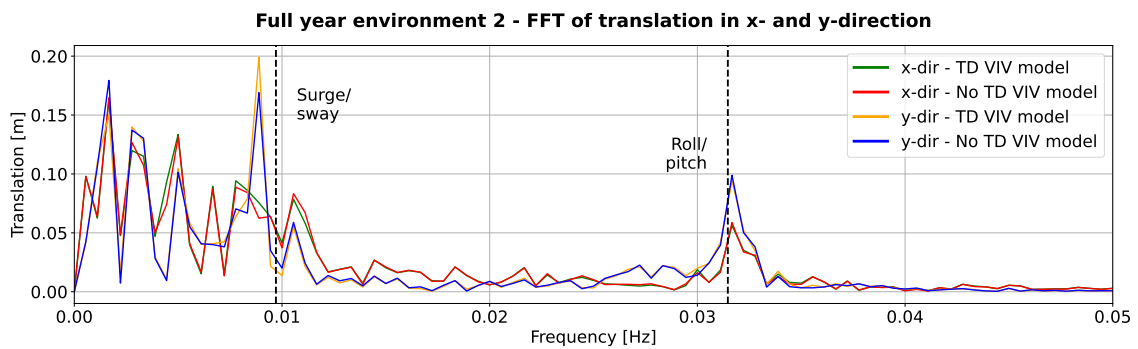


Figure B.48: Fast Fourier transform of translation in x- and y-direction for full year environment 2. Results both with and without the TD VIV model are shown.

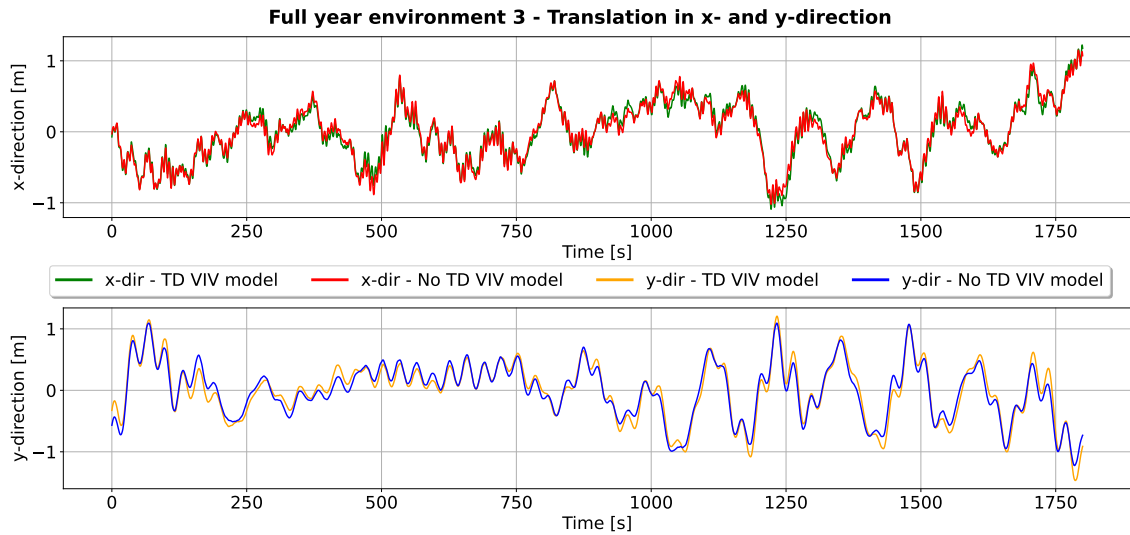


Figure B.49: Translation in x- and y-direction for full year environment 3. Results both with and without the TD VIV model are shown.

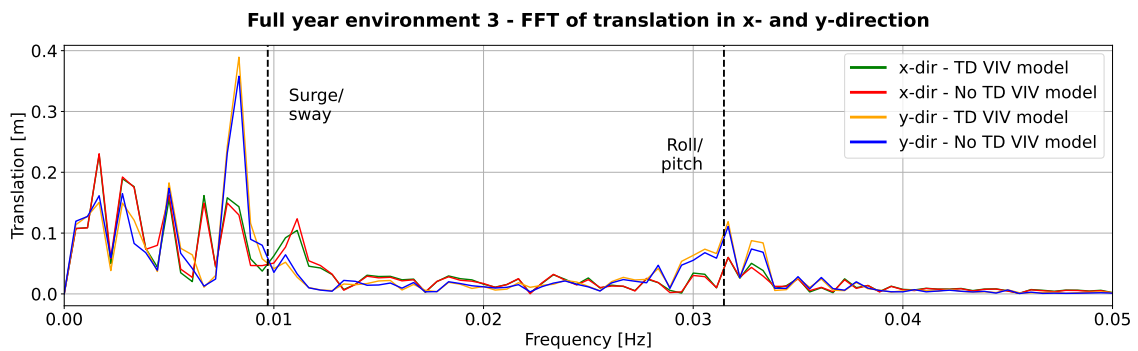


Figure B.50: Fast Fourier transform of translation in x- and y-direction for full year environment 3. Results both with and without the TD VIV model are shown.

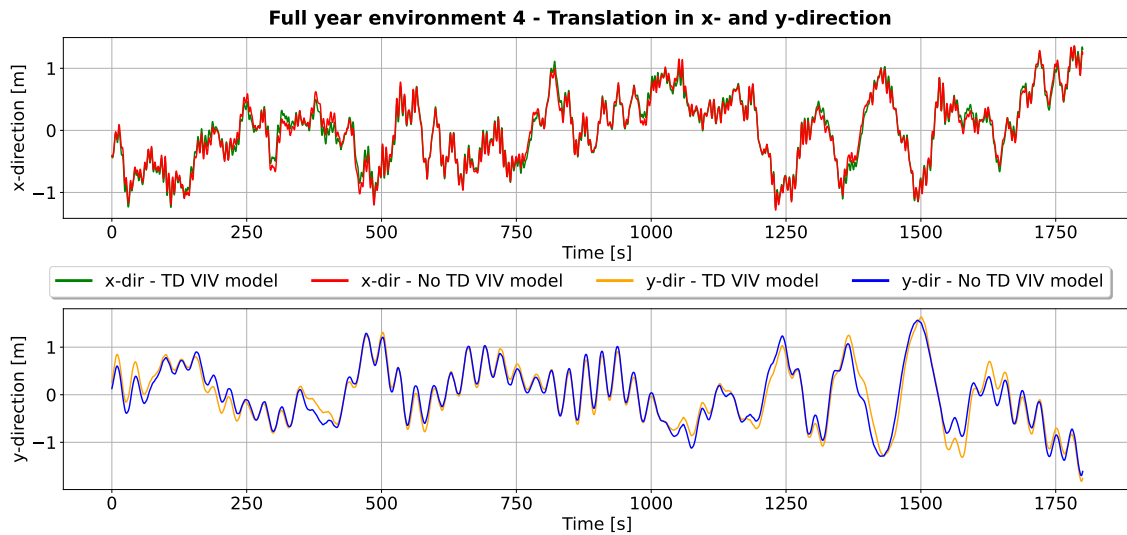


Figure B.51: Translation in x- and y-direction for full year environment 4. Results both with and without the TD VIV model are shown.

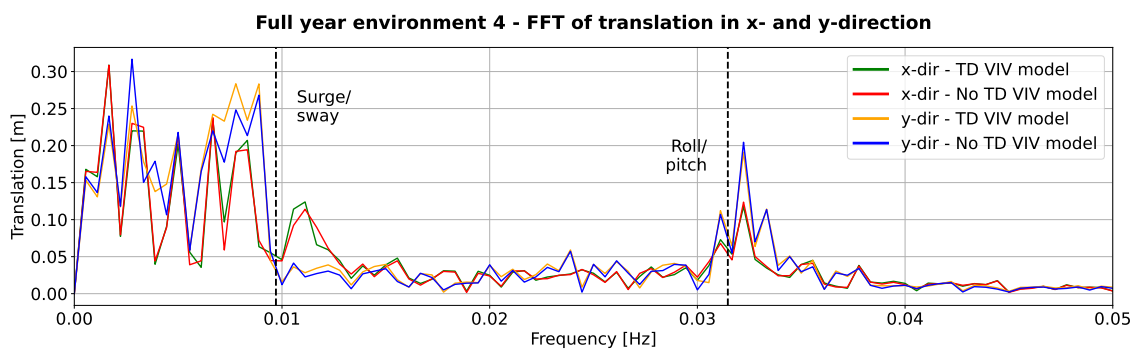


Figure B.52: Fast Fourier transform of translation in x- and y-direction for full year environment 4. Results both with and without the TD VIV model are shown.

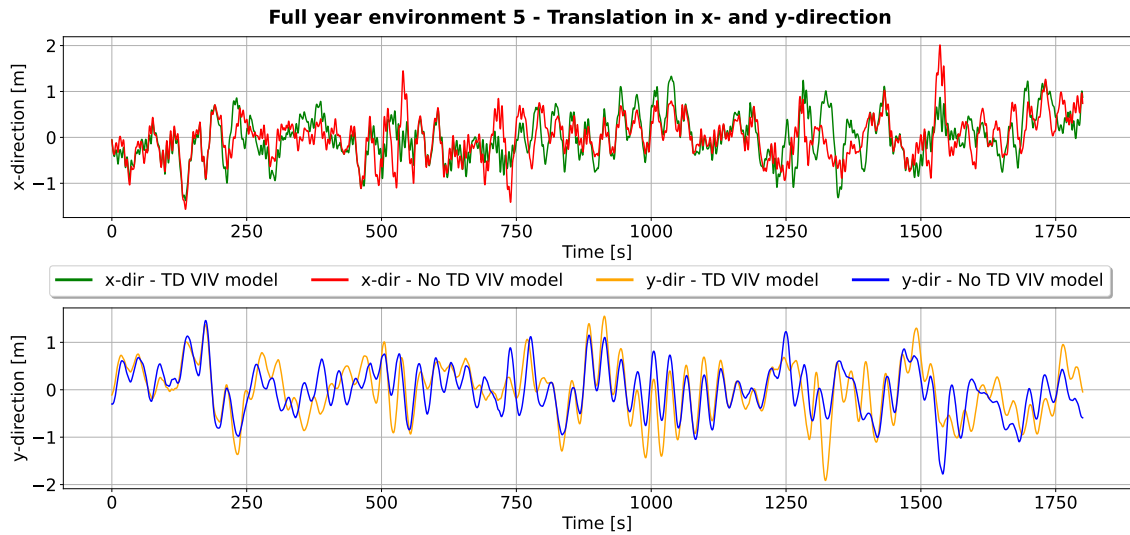


Figure B.53: Translation in x- and y-direction for full year environment 5. Results both with and without the TD VIV model are shown.

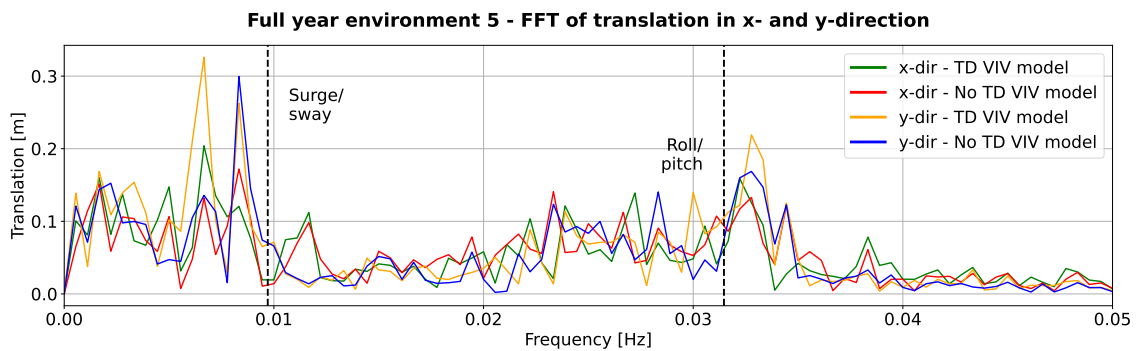


Figure B.54: Fast Fourier transform of translation in x- and y-direction for full year environment 5. Results both with and without the TD VIV model are shown.



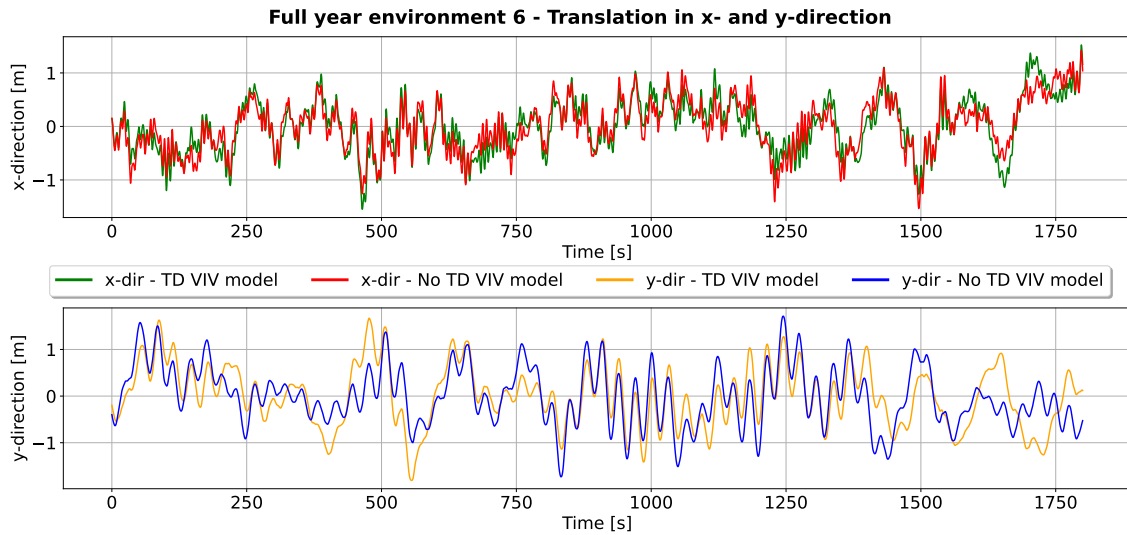


Figure B.55: Translation in x- and y-direction for full year environment 6. Results both with and without the TD VIV model are shown.

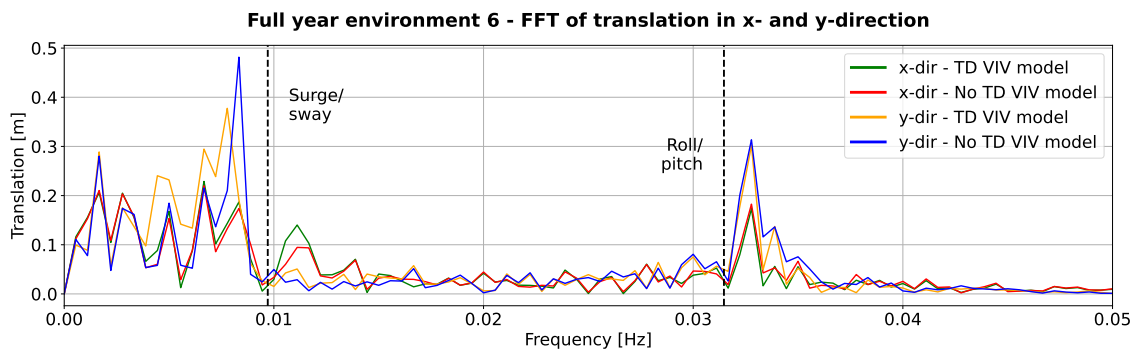


Figure B.56: Fast Fourier transform of translation in x- and y-direction for full year environment 6. Results both with and without the TD VIV model are shown.

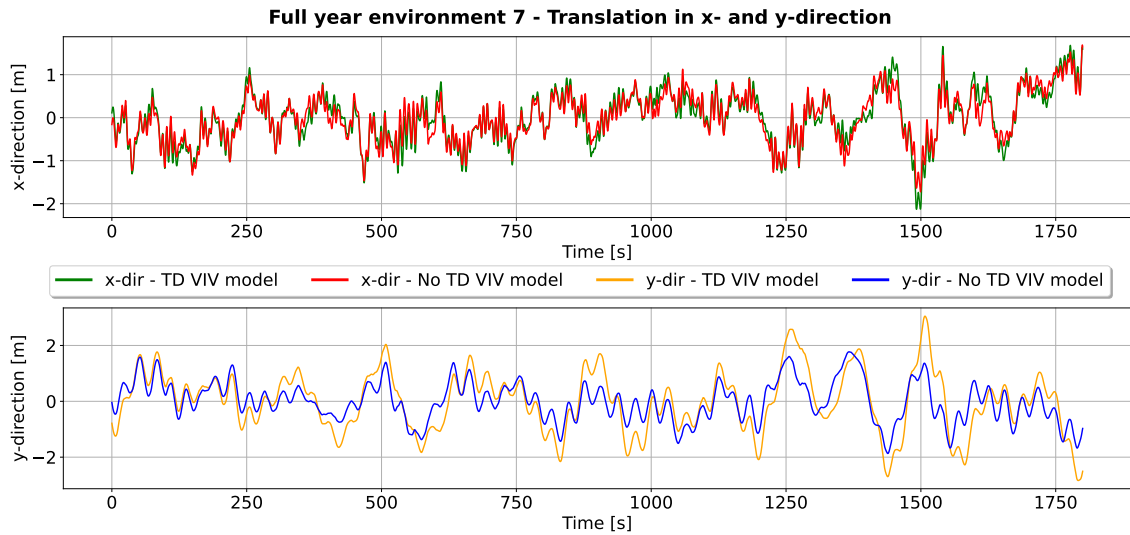


Figure B.57: Translation in x- and y-direction for full year environment 7. Results both with and without the TD VIV model are shown.

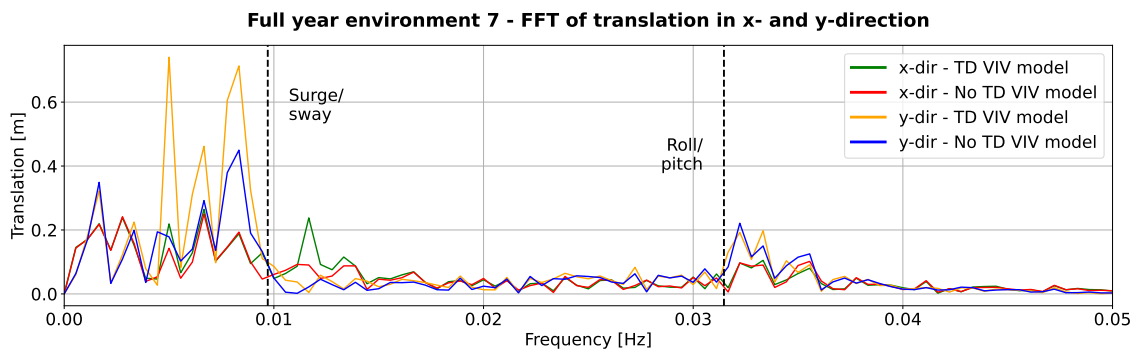


Figure B.58: Fast Fourier transform of translation in x- and y-direction for full year environment 7. Results both with and without the TD VIV model are shown.

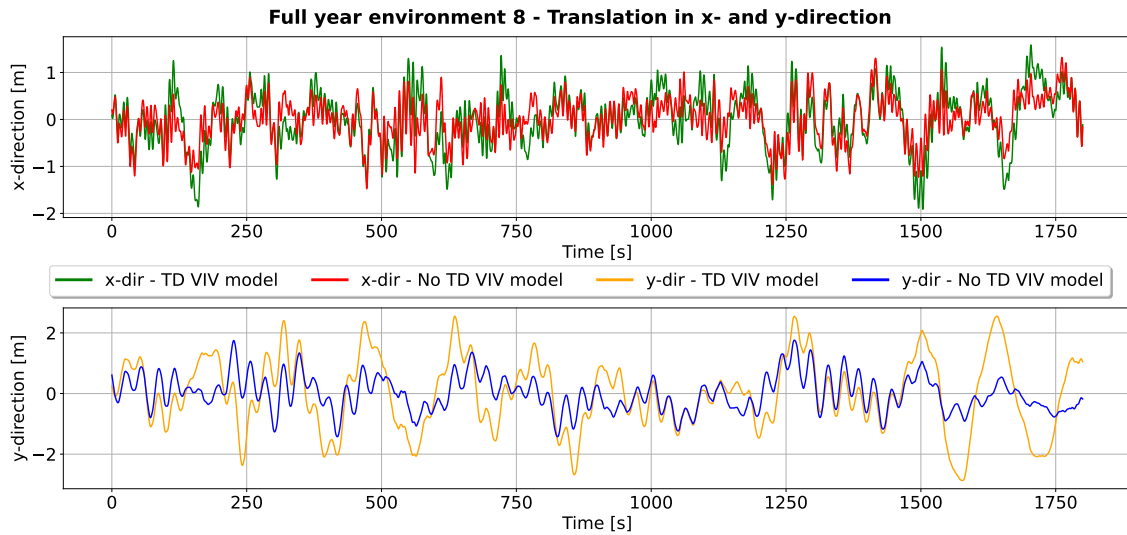


Figure B.59: Translation in x- and y-direction for full year environment 8. Results both with and without the TD VIV model are shown.

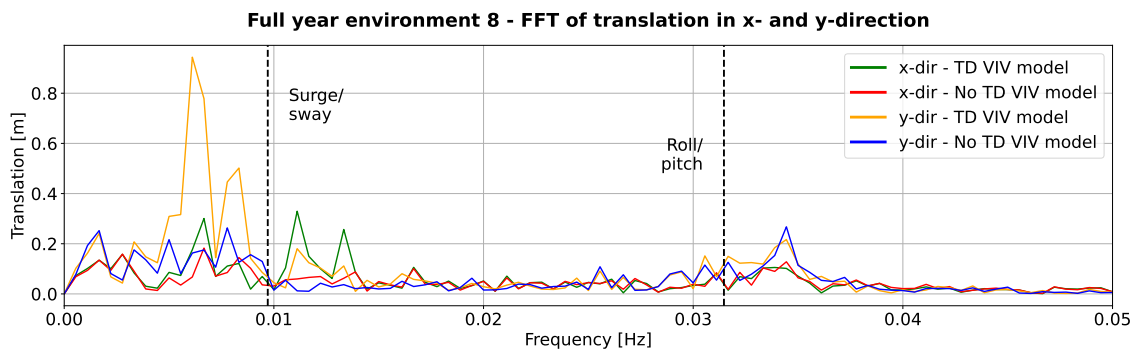


Figure B.60: Fast Fourier transform of translation in x- and y-direction for full year environment 8. Results both with and without the TD VIV model are shown.

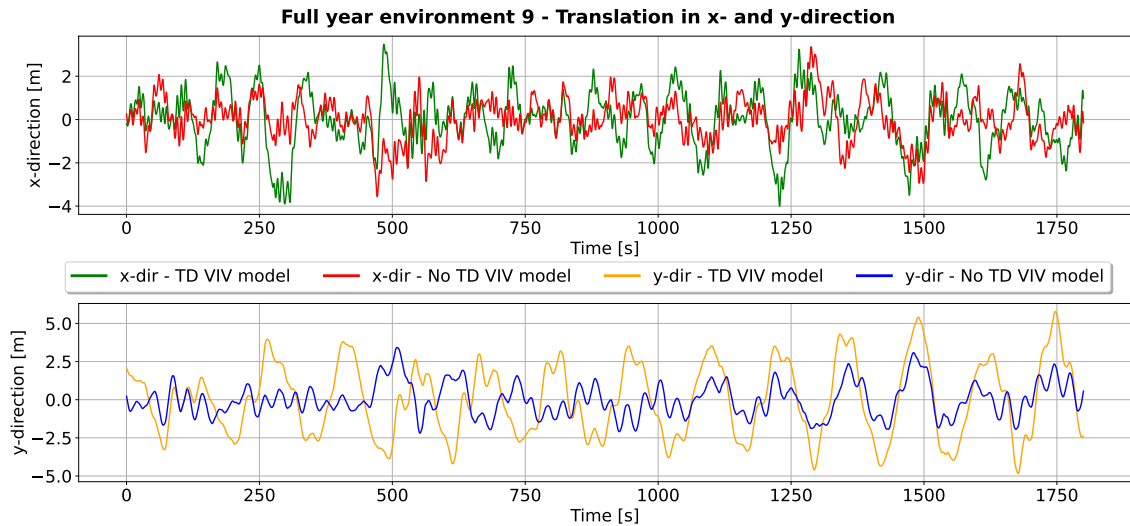


Figure B.61: Translation in x- and y-direction for full year environment 9. Results both with and without the TD VIV model are shown.

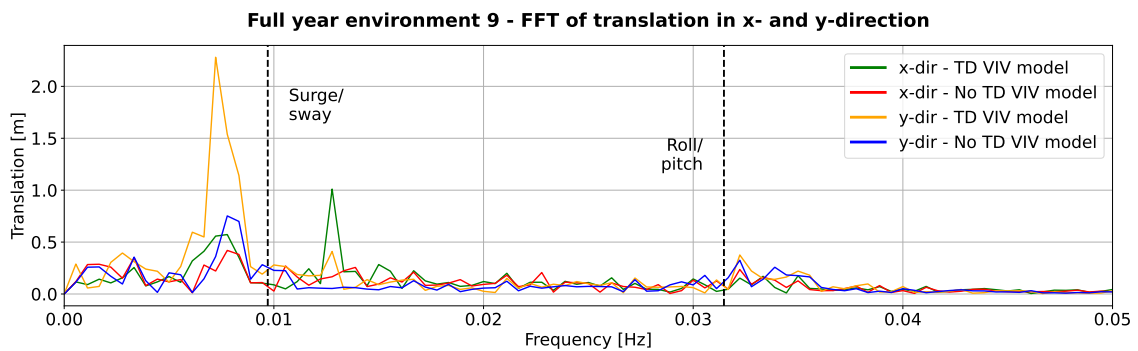


Figure B.62: Fast Fourier transform of translation in x- and y-direction for full year environment 9. Results both with and without the TD VIV model are shown.

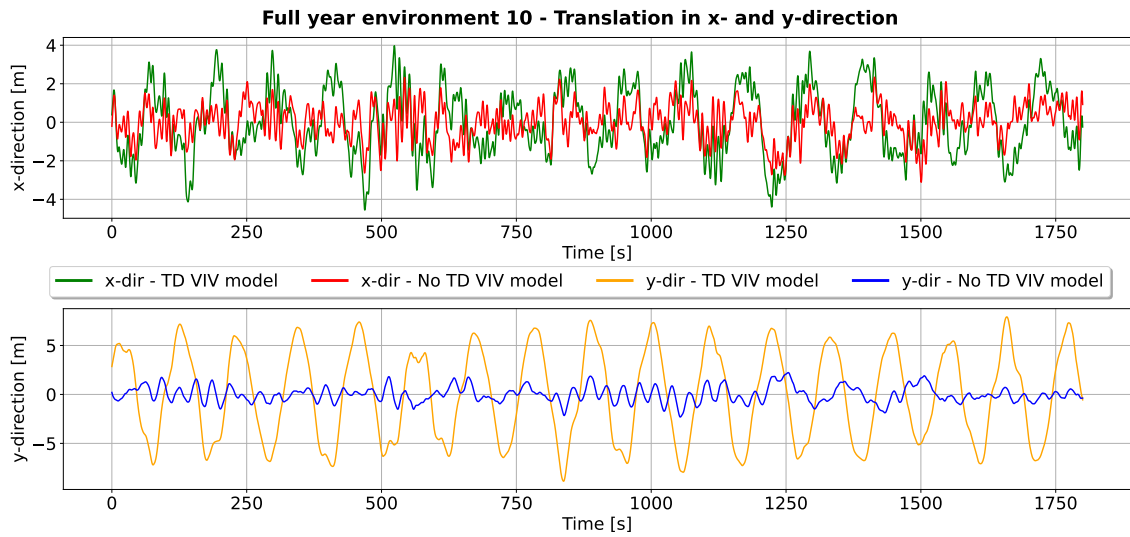


Figure B.63: Translation in x- and y-direction for full year environment 10. Results both with and without the TD VIV model are shown.

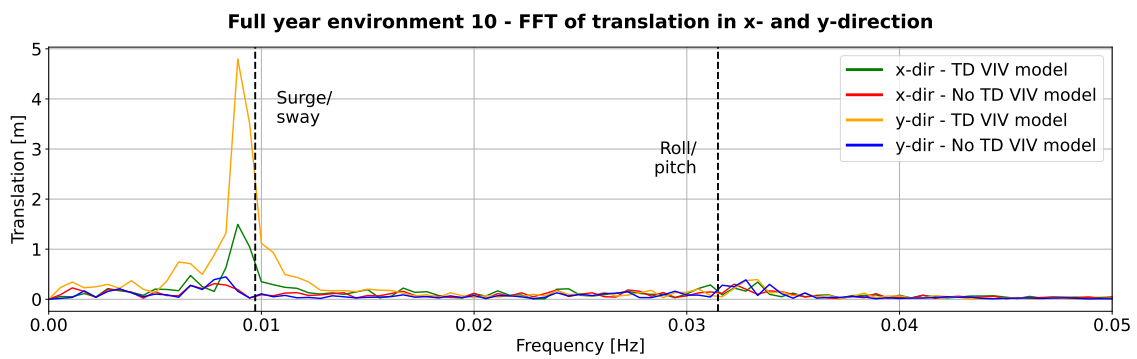


Figure B.64: Fast Fourier transform of translation in x- and y-direction for full year environment 10. Results both with and without the TD VIV model are shown.



 **NTNU**

Norwegian University of  
Science and Technology